Universidad de Salamanca
Departamento de Fisica Aplicada

Doctoral Thesis

Micromagnetic study of magnetic domain wall motion: thermal effects and spin torques

A thesis submitted in fulfilment of the requirements for the degree of doctor of philosophy (Ph.D.) in Applied Physics and Technology at the University of Salamanca

Candidate
Simone Moretti

Supervisor
Dr. Eduardo Martinez

D. Eduardo Martínez Vecino, profesor titular de Universidad, miembro del Área de Electromagnetismo del Departamento de Física Aplicada de la Universidad de Salamanca,

CERTIFICA

Que la presente Memoria, titulada “Micromagnetic study of magnetic domain wall motion: thermal effects and spin torques” ha sido realizada bajo su dirección en el Área de Electromagnetismo del Departamento de Física Aplicada de la Universidad de Salamanca por Simone Moretti, y constituye su Tesis para optar al Grado de Doctor en Física.

En Salamanca, 23 de Octubre de 2017

D. Simone Moretti

D. Eduardo Martínez Vecino
Profesor Titular de Universidad

Abstract

Magnetic domain walls represent the boundary between two differently aligned magnetic domains. In ferromagnetic nanostrips, they can be efficiently displaced by electrical current as a consequence of the spin transfer torque mechanism. This effect inspired a number of potential applications for logic and memory devices, which are based on the reliable control and manipulation of domain walls. These applications represent a promising alternative to CMOS based devices, which are reaching their limit in scalability. At the same time, the achievement of low-energy devices, based on domain walls, could have important consequences on the energy consumption of the Information and Communication Technology sector and, consequently, on carbon emissions and climate change. Apart from that, domain wall dynamics is also interesting from a fundamental point of view since domain walls can be displaced by several means such as electrical current, thermal gradients, spin waves etc. Furthermore, advances in material deposition opened the possibility of creating magnetic ultrathin films with a thickness of few angstroms, where the interfacial interactions with the neighbouring layers play a significant role and they can give rise to new interesting effects such as perpendicular magnetic anisotropy or the presence of the Dzyaloshinskii-Moriya interaction. Moreover, these systems are promising for the study of chiral and topological magnetism due to the presence of topologically protected patterns such as Skyrmions or chiral domain walls.

In this thesis we analyse two aspects of domain wall motion in ferromagnetic nanostructures by means of micromagnetic simulations. In the first part we analyse the influence of Joule heating and thermal gradients on domain wall dynamics. It is well known that, apart from the spin transfer torque, electrical currents also produce heating as a consequence of Joule effect. Thus, on the one hand it is important to analyse the effect of Joule heating in order to establish the real contribution of the spin transfer torque. On the other hand, Joule heating and thermal gradients can be also used to efficiently displace magnetic domain walls, although the theory behind this effect is still under debate. These studies were performed with a novel micromagnetic software which couples heat and magnetization dynamics.

In the second part, we analyse the domain wall dynamics in ultrathin systems with perpendicular magnetic anisotropy and Dzyaloshinskii-Moriya interaction. This part includes a collaboration with an experimental group from the University of Leeds (UK) and it is devoted to the fitting of the experimental data for the field and current driven domain wall motion. In particular, we analyse the role of disorder in these systems, which

represents a critical issue towards the realization of domain wall devices. Finally, we analyse the dependence of the domain wall depinning field with the damping parameter. The main conclusions are summarized in Part IV.

Acknowledgement

It is really difficult to write this chapter after almost 4 years of this wonderful and intense experience in Salamanca. I feel like I started my PhD yesterday but so many things happened and there are so many people I should thank. Due to a professional deformation, I shall give some numbers to better define “a lot of things”: 4 years, 3 first-author publications, 4 secondments (2 times in Leeds, Zurich, Paris), 5 conferences around the world (New Orleans, San Diego, Barcelona, Assisi, Dublin), 3 summer schools (Madrid, Cluj-Napoca, Spetses), 8 project meetings also around the world (Zurich, Paris, Leeds, Turin, Mainz), online courses, onsite courses, approximatively 40 flights, a lot (a lot!) of code lines, equations, calculations, corrections, a lot of *cañas*, *pinchos*, *pintas*, *chuletones* and, finally, 1 thesis. All of this would not have been possible (and it would not have been such a great experience) without the help of the many people I met during this experience.

A big thank you to my supervisor Eduardo Martinez, who introduced me into the world of magnetism and micromagnetic simulations. For his patience in reading, re-reading, re-re-reading, re-re- ... -reading all my papers and this thesis. For his corrections, his ideas and his support. All this work would not have been possible without his supervision.

I would like to thank all the members of the electromagnetism group here at the University of Salamanca: Luis Lopez, Luis Torres, Victor, Marce, Nacho, Ana, Auxi, Pablo, Michele, Ricardo, Nerea and Rocío for the coffee break at 11.00, the group meetings and for the friendly and welcoming environment. Luis Torres in particular for his middle-morning singing, cheering up our office. I would like to thank Luis Lopez for his help, for the discussions about physics, science and the academic world, for countless lunches (with also Michele, Rocío, Eduardo, David and Julian) speaking about science, politics, movies, football and music. I would like to thank Victor for his help with MuMax and Comsol. I want to thank also Javier Gomez, a former computer scientist of our group, who helped me with CUDA and many other computer issues. A special thanks to Michele, who started with me this PhD experience. We shared a lot of trips, flights, lunches, dinners, rooms, (coding) pain and interesting discussions. It would have been much more difficult (and less funny) without his company and help. I would like to thank also Noel Perez, a former PhD student of our group, who helped me a lot at the beginning of the PhD in developing the code. I would not be here without his help. He went teaching in high-school and I think they are very very lucky to have him. Thanks to Ricardo for his presence in our office and for the Spanish and informatics tips. A special thanks also to Rocío and Julian from the postdoc office, who supported me during the thesis writing. For their genuine friendship, the countless questions about physics I asked, for the *pequeño* break at 17.30 and all the nice discussions we had.

I would like to thank Salvatore and Riccardo, who spent some time here in Salamanca during these years. For the late discussions with Salvo at the whiteboard about the beauty of physics, the ping-pong matches (which Salvo lost), the conferences and all the nice moments together.

A big thank you to all the WALL people, professors and students, for the friendly and stimulating environment. In particular all the other ESR: Michele, Samridh, Ali, Bhaskar, Benjamin, Kowsar, Risalat, Yuting, Guru and Fabienne. Thank you for the nice time at all our project meetings and the interesting discussions about physics. Thanks to Risalat, Kowsar, Thomas Moore and Chris Marrows from the University of Leeds for the nice time I spent there, for your warm welcome in your (cold!) office. Thank you for your patience in explaining me the experiments and for the nice discussions about the results. In particular thanks to Tom for reading and commenting this thesis and for his report. Thanks to Gianfranco for his work as coordinator, for his friendship and guidance (and for the NBA match in New Orleans!). Thanks to Rolf Allenspach and all his group at IBM Zurich for the nice time at IBM and all the discussions about physics and the academic/industry world. Thanks to Ales Hrabec, André Thiaville, Vincent Jeudy and all the people from the magnetism group at LPS in Paris for the nice time I spent there and for the nice discussions about the experimental results.

I would like to thank also Giovanni Carlotti, for his constant help, for reading the thesis and for his report.

An immense thank you to the Addicts to O'Hara crew (now spread around the world) David, Indy, Vincent, Pablo, Michele, Riccardo, Maria, Mar, Elise, Sarah, Luca, Julian, Jose, Carla and Steph for the countless nights in O'Hara, Chupiteria (at 1.00am) etc., the dinners, the pints, the futobolines and all the *legendary* moments we shared.

Thanks to Vicente (el *barista madridista*) for the coffees after lunch, the magic tricks and his lessons about *fútbol*. Alberto and Jere from Fray Luis for (other) coffees and many lunches in summer. Thanks to all the football teams, the Saturday morning team and the Science team, who are too many to be listed here. Thanks to my family and all the friends who supported me or visited me from Italy, in particular Mom, Dad, Bro, Luca, Andrea, Laura and Annalisa.

Thank you to all the friends of Comunione e Liberazione and Escuela de Comunidad here in Salamanca and Madrid: Don Pablo, Carlos, Dani, Bea, Elena B., Ana, Blanca, Gabriella, Martina, Raquel, Fran, Elena G., Samu, Tommaso, Kenya and Davide for their presence and friendship.

Last but not least, I would like to thank the European Commission who provided the financial support for this project within the Marie Curie Initial Training Network WALL. In these uncertain times where some people doubt about the goodness of European Union we had the privilege to experience his benefits and the good it represents.

Contents

List of Figures

List of Tables

List of Acronyms

DW, DWs	Domain Wall, Domain Walls
STT, STTs	Spin Transfer Torque, Spin Transfer Torques
CMOS	Complementary Metal Oxide Semiconductor
RAM	Random Access Memory
MRAM	Magnetic Random Access Memory
JH	Joule heating
TG	Thermal gradient
SH	Spin Hall
PMA	Perpendicular Magnetic Anisotropy
DMI	Dzyaloshinskii-Moriya Interaction
SLT	Slonczewski Like Torque
ZLT	Zhang-Li Like Torque
LL	Landau Lifshitz
LLG	Landau Lifshitz Gilbert
LLB	Landau Lifshitz Bloch
ET	Entropic Torque
μ**STT**	Magnonic Spin Transfer Torque
TIDF	Thermally Induced Dipolar Field
CIDWM	Current Induced Domain Wall Motion
UCS	Uniform Cross Section
NUCS	Non Uniform Cross Section
CC	Collective Coordinates
1D	One Dimensional
FM	Ferromagnetic
HM	Heavy Metal

Chapter 1

Introduction

1.1 Magnetism

Electromagnetism is one of the fundamental forces in nature and it concerns the interactions between electrical charges and magnetic moments. Known since ancient times, it has deeply changed our world at least three times, as recently stated by Prof. Michael Coey at the last International Conference of Magnetism (INTERMAG) in Dublin: the first time with the invention of the magnetic compass allowing the geographical exploration of the earth. The second time, during the last couple of centuries, with the ”electrification” of the world and all the related inventions such as electrical light, computers, smartphones, radio, televisions etc. And the third, more recently, with the invention of the hard disk allowing massive storage of digital information and benchmarking the start of the ”information” revolution.

Apart from its technological relevance, magnetism has fascinated scientists among centuries with a variety of magnetic phenomena that needed an explanation, which, often, implied significant advances in fundamental research. The mere existence of magnetic materials, for instance, can be explained only in the context of quantum mechanics since it is related to the electron spin, firstly postulated in the context of nuclear physics and eventually introduced theoretically within the Dirac equation. The mechanism of the spontaneous symmetry breaking, used to explain the ferromagnetic order, has inspired Peter Higgs in the development of his theory for the Higgs boson, which won him the Nobel Prize for physics in 2013. Topologically protected magnetic patterns, such as Skyrmions or chiral domain walls, represent interesting systems to analyse topological phases of matter, whose discovery was awarded with the Nobel prize for physics in 2016. Bose-Einstein condensates of magnons (the fundamental excitation of magnetic systems) were observed experimentally [1] and they also represent a promising candidate to analyse this exotic state of matter.

In short, magnetism is a bridge between fundamental and applied research, where technology-driven investigations can lead to important fundamental discoveries and *vice versa*. An important research field, born within the broader field of magnetism, is the field of Spintronics, which is the topic of this thesis.

1.2 Spintronics

Spintronics stands for spin-transport electronics and it concerns the study of the coupled transport of charge and spin in magnetic nanostructures. The name wants to extend the concept of electronics, devoted to the study of charge transport alone. The relevance of this new field of research was recognized in 2007, when Albert Fert and Peter Grünberg were awarded with the Nobel prize in physics for their discovery of the Giant Magneto-Resistance. This phenomenon has had an enormous impact on our technology since it is at the basics of the hard disk drive memory. Fert and Grunberg separately discovered that if an electrical current passes through a multilayer stack made of two magnetic layers separated by a thin non-magnetic layer, the amount of current that passes through the stack strongly depends on the relative orientation of the two magnetic layers. In particular, if the two layer have parallel magnetization the stack has low resistance (more current), while if the layers have anti-parallel magnetization, the stack has high resistance (low current). In other words, they discovered that magnetization can affect electrical currents. This effect eventually led to the realization of the hard disk drive memory, where the ”0” and ”1” bits correspond to low or high current respectively. However, further investigations pointed out that also the opposite was true: due to the very same interaction, also electrical currents can affect the magnetization. This latter effect, called spin-transfer torque (STT), has inspired new concepts of technological devices, which include, for instance, the STT-MRAM memories (recently commercialized as alternative to conventional CMOS based RAM), Racetrack memory [2] and domain walls logic devices [3]. While for STT-MRAM the STT is used to switch the magnetic state, Racetrack memories and domain wall logic devices are based on the reliable manipulations of magnetic domain walls.

1.3 Magnetic domain walls

Magnetic domain walls (DWs) represent the boundary between two differently aligned magnetic domains. They can be efficiently displaced by electrical currents and they have potential for new kind of logic and memory devices. In racetrack memories, for instance, the information is encoded in the magnetization of the domains. The STT moves the DW towards a reading or writing head which can read or write the magnetic configuration. Trains of DWs can be packed into a single ferromagnetic nanostrip and they can be displaced coherently. Due to fast DW motion and the low dimension of the DWs, these memories have potential for high-speed, high-density magnetic memories. However, they still present issues related, for instance, to the reliable control of the DW motion, to material lithography or to the high currents needed to achieve considerable DW velocities.

Nonetheless, this class of magnetic memories still constitutes a promising candidate to substitute hard-disk drive and CMOS based memories, which are reaching their limit of scalability. Furthermore, current research is focused on achieving DW motion with minimal electrical currents. Low energy memories and low energy logic devices, based on DWs, could reduce the energy consumption of the Information and Communication Technology sector, with important consequences on carbon emissions and climate change.

Apart from their technological relevance DWs are also interesting from a fundamental point of view since they can be displaced by several means such as thermal gradients, electrical fields, magnons, etc. Additionally, recent advances in material deposition opened the possibility of creating magnetic ultrathin films with a thickness of few angstroms, where the interfacial interactions with the neighbouring layers play a significant role and they can give rise to new interesting effects [4]. These systems triggered the interesting research field of interfacial magnetism [4].

1.4 About this thesis

In this thesis we study two aspect of DW dynamics by means of micromagnetic simulations.

In part II we analyse the influence of Joule heating (JH) and thermal gradients on DW dynamics in in-plane magnetized systems. In fact, it is well known that when an electrical current flows through a ferromagnet, apart from the STT, it also generates heating as a consequence of Joule effect. Thus, on the one hand, it is important to understand the effect of JH in order to evaluate properly the STT contribution, while, on the other hand, it is interesting to investigate whether heating effects can be used to efficiently control the DW dynamics. This latter field, generally called spin caloritronics, is getting an increasing interest due to its potential for ultralow dissipation devices (since no electron motion is involved) or as a candidate for heat harvesting. Spin caloritronics aims more generally to the study of spin and heat coupling while DW motion by thermal gradients represents a specific aspect within this broader field. In this part we develop a novel micromagnetic framework in order to couple heat and magnetization dynamics self-consistently. This framework is used to analyse the influence of JH on current-induced DW dynamics [5, 6] (Chapter 6 and 7) and to investigate the effects of a localized thermal gradients on DWs [7] (Chapter 8). A more detailed introduction can be found at the beginning of part II (Chapter 5).

In part III we analyse the DW dynamics in ultrathin films by means of the micromagnetic software MuMax [8]. The modelling of DW motion in these structures present new issues with respect to in-plane magnetized systems. In particular, the role of disorder is still under debate and its inclusion into the micromagnetic modelling represents an open challenge. This part benefits of the collaboration with an experimental group from the University of Leeds and it is focused on the fitting of their experimental results for the DW dynamics. Chapter 11 analyses the field and current driven DW dynamics in Pt/Co/$\mathrm{Pt_xAu_{1-x}}$, where x varies between 0 and 1. In this chapter, a particular emphasis is devoted to show the role of disorder in DW dynamics. Finally, in Chapter 12 we analyse the damping dependence of the DW depinning field in ultrathin films [9]. Also in this case, a more detailed introduction can be found at the beginning of part III (Chapter 10).

Additionally, part I provides a global theoretical background. It describes basic concepts of magnetism in Chapter 2, the main aspects of the micromagnetic theory in Chapter 3 and its numerical implementation in Chapter 4. It can be skipped by a reader familiar with magnetism and micromagnetics and consulted when necessary.

The results presented in this thesis were mainly adapted from some of the scientific articles published by the author (list of publications). For this reason, each part and each chapter are self-consistent and they can be read separately. For the same reason, many concepts are repeated especially in the introduction and when describing the simulation methods. A scheme of the thesis structure is shown in Fig. 1.1. This thesis was carried out within the Marie Curie Initial Training Network "WALL", funded by the European Commission with the FP7 program, which is gratefully acknowledged for the financial support.

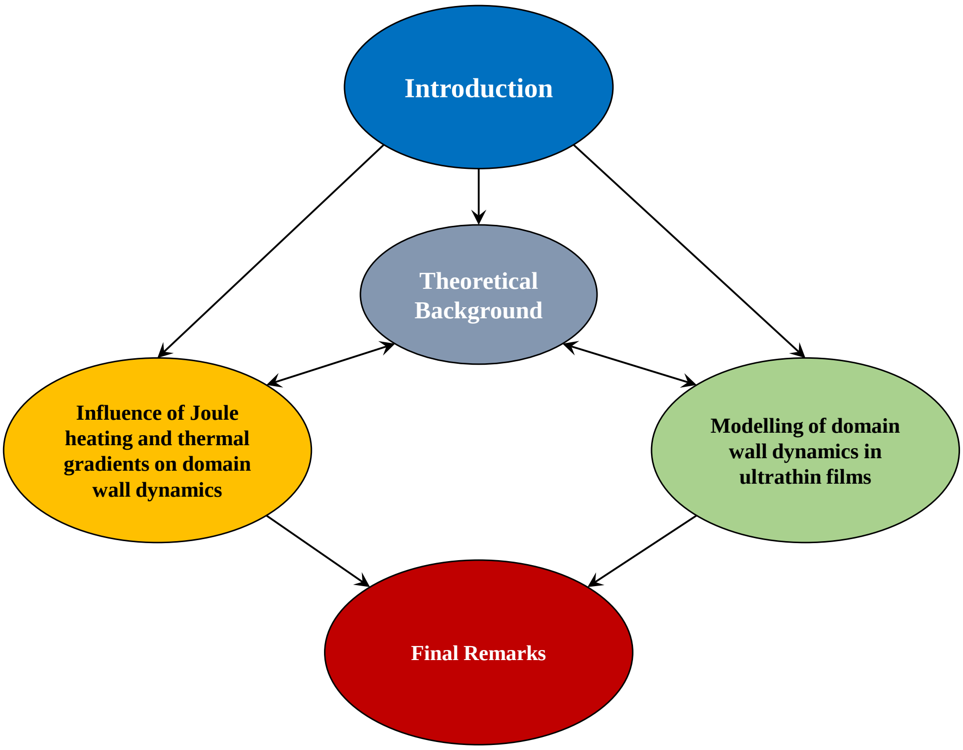

Figure 1.1: Thesis structure.

Part I

Theoretical Background

Chapter 2

Basic concepts of magnetism

This chapter provides a brief overview about magnetism in condensed matter. We will introduce the concept of magnetic moment and we will describe the main magnetic interactions. Different types of magnetic order will be presented, with particular emphasis on paramagnetism and ferromagnetism. Finally, we will introduce magnetic domains and domain walls. Far from being exhaustive, the aim of this chapter is simply to set the basics and the context for the micromagnetic theory, which will be presented in the next chapter.

2.1 Magnetic materials

As commonly perceived, magnetic materials are materials that can generate a magnetic field around them. This field originates from magnetic dipoles (or magnetic moments) related to the material's atoms and electrons. As electrical charges are sources of electrical fields, magnetic moments are sources of magnetic fields. In general, as stated in Maxwell's equations, the source of magnetic fields are electrical currents and, in fact, magnetic moments can be classically linked to bounded current loops, i.e., current loops that are confined inside the material, such as the electrical current associated to electrons orbiting around the nucleus. However, this classical picture is not enough to explain the existence of magnetic materials and the origin of magnetic moments is mainly linked to electrons spin, an intrinsic angular momentum, whose origin is quantum mechanical. The magnetic moment per unit volume is defined as the magnetization $\mathbf{M}$ of a material. All atoms can have magnetic moments but if their interaction is negligible, their directions is random, and the average magnetization is null. A net magnetization can be induced by external means, such as an external magnetic field, or it can be an intrinsic "spontaneous" feature. Materials with spontaneous magnetization are called Ferromagnets. Typical ferromagnetic materials are Co, Fe and Ni. The existence of spontaneous magnetization is due to additional interactions between magnetic moments which favour their alignment, as it will be discussed in the following.

2.2 Magnetic moments

Orbital angular momentum

Magnetic moments are the fundamental object of magnetism. From a classical point of view, magnetic moments can be related to electrical current loops. If a current I flows through an infinitesimal current loop placed in a magnetic field $\mathbf{B}$, as sketched in Fig. 2.1(a), the Lorentz force will exert a torque on the circuit which can be written as [10]

$$d\mathbf{T} = d\boldsymbol{\mu} \times \mathbf{B}\,, \tag{2.1}$$

where the magnetic moment $d\boldsymbol{\mu}$ is defined as $d\boldsymbol{\mu} \equiv I d\mathbf{S}$ and $d\mathbf{S}$ represents the surface vector with modulus equal to the surface area and direction normal to the surface plane. It follows that the magnetic moment has units of $\mathrm{A} \cdot \mathrm{m}^2$. For a finite loop in a uniform magnetic field $\mathbf{B}$

$$\boldsymbol{\mu} = I \int d\mathbf{S} \qquad \text{and} \qquad \mathbf{T} = \boldsymbol{\mu} \times \mathbf{B}\,. \tag{2.2}$$

Furthermore, by calculating the work done by the Lorentz force, it is possible to demonstrate [10] that the energy of a magnetic moment inside a magnetic field is given by

$$E = -\boldsymbol{\mu} \cdot \mathbf{B}\,, \tag{2.3}$$

which is minimized when the magnetic moment is parallel to the magnetic field. This energy term, related to the interaction of a magnetic moment with an external magnetic field, is known as **Zeeman** energy (see Section 2.3.2). At the same time, the current loop generates a magnetic field, which can be written as [11]

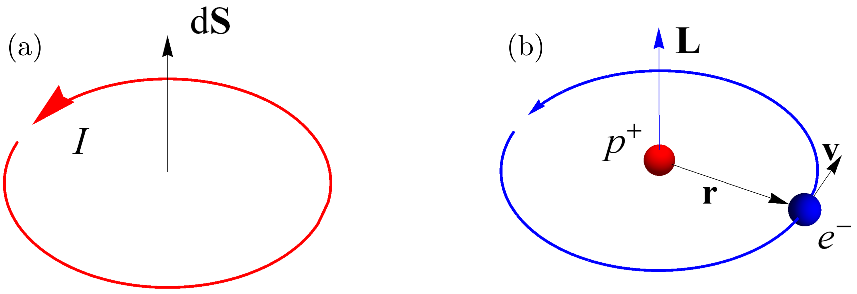

Figure 2.1: (a) Sketch of current loop. (b) Sketch of electron orbiting around a proton and its orbital angular momentum.

$$\mathbf{B}(\mathbf{r}) = \frac{\mu_0}{4\pi}\left[\frac{3\mathbf{r}(\mathbf{r}\cdot\boldsymbol{\mu})}{r^5} - \frac{\boldsymbol{\mu}}{r^3}\right], \tag{2.4}$$

if $r \gg R$, with R being the radius of the current loop. The field generated by the magnetic moment (Eq. (2.4)) is equivalent to a dipole field and it is shown in Fig. 2.2. Since an electrical current corresponds to moving charges, there is always an orbital angular momentum related to a current loop and, therefore, to a magnetic moment. In atoms, the magnetic moment $\boldsymbol{\mu}$ related to an electron orbiting around the nucleus, has the same direction of its angular momentum $\mathbf{L}$, namely

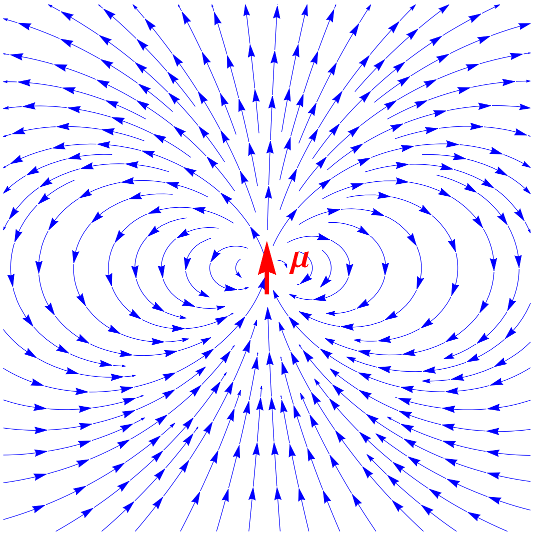

Figure 2.2: Dipolar field generated by a magnetic moment, according to Eq. (2.4).

$$\boldsymbol{\mu} = \gamma \mathbf{L}\,, \tag{2.5}$$

where γ is a proportionality constant, relating angular momentum and magnetic moment, known as the gyromagnetic ratio. Consider, for instance, an electron orbiting around a proton as sketched in Fig. 2.1(b). Within the Bohr atomic model, the electron in its ground state has angular momentum $m_e v r = \hbar$. The electrical current due to its motion is $I = -e/\tau$, where e is the elementary charge (positive) and τ the orbital period given by $\tau = 2\pi r/v$. Thus, its magnetic moment is

$$\mu = I\pi r^2 = -\frac{e}{2m_e} m_e v r = -\frac{e}{2m_e} L = -\frac{e\hbar}{2m_e} \equiv -\mu_B\,, \tag{2.6}$$

where $\mu_B = 9.274 \times 10^{-24}$ Am^2 is the Bohr magneton, which represents a useful unit for atomic magnetic moments. From Eq. (2.6), we see that the electron gyromagnetic ratio, related to the orbital angular momentum, is $\gamma = -e/2m_e$. Hence, **a magnetic moment is always associated with angular momentum.** Moreover, since torque corresponds to rate of change of angular momentum, by combining Eq. (2.2) and Eq. (2.5), we have that

$$\mathbf{T} = \frac{d\boldsymbol{L}}{dt} = \boldsymbol{\mu} \times \mathbf{B} \quad \Rightarrow \quad \frac{d\boldsymbol{\mu}}{dt} = \gamma\boldsymbol{\mu} \times \mathbf{B}\,, \tag{2.7}$$

which implies that a magnetic moment in an external magnetic field $\mathbf{B}$, will not align towards the magnetic field but it will precess around the field direction, conserving its energy (Eq. (2.3)) as described in Fig. 2.3. The precession frequency $2\pi f_L = \gamma B$ can be calculated from Eq. (2.7) and it is known as Larmor frequency.

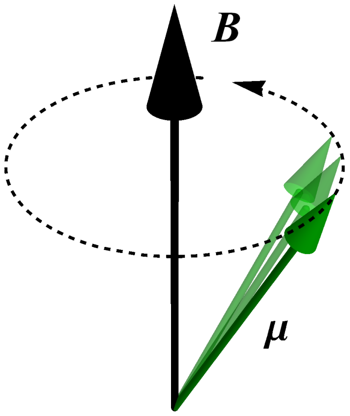

Figure 2.3: Magnetic moment $\boldsymbol{\mu}$ precessing around the magnetic field $\mathbf{B}$.

Spin angular momentum

This classical description, relating magnetic moments to orbital angular momentum (and helpful to understand some of their basic properties), is, however, not enough to explain the existence of magnetic materials. In fact, the average magnetization of a certain system can be calculated as (see Appendix A)

$$\mathbf{M} = \frac{\langle\boldsymbol{\mu}\rangle}{\Delta V} = -\frac{1}{\mu_0 \Delta V}\frac{\partial F}{\partial \mathbf{H}}\,, \tag{2.8}$$

where F is the system free energy and $\mu_0\mathbf{H} = \mathbf{B}$ is the external field. In other words, the magnetization is proportional to the variation of the system energy when we apply an external field. However, Eq. (2.7) shows that the energy of the system is conserved since the magnetic moments will precess around the field, conserving their initial energy. Therefore, no magnetization can be induced in a material according to classical mechanics. This statement, with a more rigorous demonstration, is known as the Bohr-Van Leeuwen theorem. The demonstration relies on the fact that the effect of a magnetic field on N particles can be included into the system energy by replacing the particles momentum $\mathbf{p}_i$ with $\mathbf{p}_i - q\mathbf{A}$ [12], where q is the particle charge and $\mathbf{A}$ the vector potential, from which the magnetic field can be calculated as $\mathbf{B} = \nabla \times \mathbf{A}$ [12]. Since $F = -k_B T N \log \mathcal{Z}$ and $\mathcal{Z} = \int_{-\infty}^{\infty} \exp\left[E_i/(k_B T)\right] d\mathbf{r} d\mathbf{p}$, where $\mathcal{Z}$ is the partition function (see Appendix A), the shift can be reabsorbed into the integral and F does not depend on $\mathbf{A}$ (see Ref. [13, 10] for more details). Hence, no magnetization can be induced according to classical mechanics. The existence of magnetization can only be explained in the context of quantum mechanics. In particular, according to quantum mechanics, electrons not only have orbital angular momentum but they also possess an intrinsic angular momentum called **spin**.

Spin was firstly introduced ad-hoc to explain the fine-splitting of the hydrogen atom spectrum and, later on, was used to successfully explain the Stern and Gerlach experiment, showing the quantization of the atom angular momentum. Mathematically, it finally appeared in the Dirac equation for a relativistic electron. Spin angular momentum ($\mathbf{S}$) has its own quantum number s and its component can have one of $(2s + 1)$ values in the range $\hbar s, \hbar(s-1), .., -\hbar s$. This intrinsic angular momentum is a specific property for each particle such as mass or charge. For electrons, $s = 1/2$ so that the spin components can only take the values $\pm\hbar/2$. The quantum number associated with a specific spin component is usually indicated as m_s, which for electrons is $m_s = \pm 1/2$. The magnetic moment associated with the spin angular momentum can be calculated in the framework of the Dirac equation. For electrons, the component of the electron magnetic moment along a certain direction of spin is

$$\mu_s = g \mu_B m_s \,, \tag{2.9}$$

where g is the g-factor and for electrons is approximatively $g \simeq -2$ [10]. [1] The minus sign is due to the electron negative charge as in Eq. (2.6). Note that, since $g = -2$, the electron magnetic moment is $\pm\mu_B$ even if $m_s = \pm 1/2$. It follows that the energy of an electron in a magnetic field B is $E = -g\mu_B m_s B$.

With the introduction of spin magnetic moments, the effect of a magnetic field cannot be reduced to a shift of the particles momentum (which would include the effect of the orbital angular momentum) but a new energy term ($E = g\mu_B m_s B$) must be added to the Hamiltonian and the existence of magnetic materials can be explained. Nevertheless, despite their quantum mechanical origin, many properties of magnetic materials can be explained by a semi-classical approach, assuming the existence of such intrinsic magnetic moments and considering the interactions as classical [13].

---

[1] In some textbooks the spin magnetic moment is expressed as $\mu_s = -g_s \mu_B m_s$, where g_s is the spin g-factor $g_s \simeq 2 = |g|$. The important point is that the spin magnetic moment is opposite to the spin angular momentum, as orbital magnetic moment is opposite to orbital angular momentum.

Material	μ (μ_B)	T_C (K)
Fe	2.22	1043
Co	1.72	1388
Ni	0.6	627
Gd	7.63	292
Dy	10.2	88

Table 2.1: Magnetic moment and Curie temperature for typical ferromagnetic materials.

Classically, we can assume that the electron has a magnetic moment given by

$$\boldsymbol{\mu} = \frac{g\mu_B}{\hbar}\mathbf{S}\,, \tag{2.10}$$

where $\mathbf{S}$ is a vector of modulus $\hbar/2$.

Hund's rules

We have seen that electrons orbiting around a nucleus have spin and orbital angular momentum. The magnetic moment of a certain atom will depends on the spin and orbital angular momentum of all its electrons. For instance, if an atom have two electrons with opposite spins and opposite angular momentum it will have zero magnetic moment since they will cancel each others. In general, the electrons' configuration in atoms follows (for the ground state) the Hund's rules, which is a set of empirical rules that allow to estimate the spin and orbital configuration that minimize the atom's energy. First rule is that the electrons in a certain orbital try to maximize the total spin $\mathbf{S}$. This will minimize Coulomb energy due to the exchange interaction (see Section 2.3.1). Second rule is that electrons will try to maximize the total orbital angular momentum $\mathbf{L}$. As a consequence, depending on the number of "unpaired" spins, atoms will have different net magnetic moments. Table 2.1 shows the atomic magnetic moments and the Curie temperature of typical ferromagnets [14]. The Curie temperature represents a critical temperature above which the material is no longer ferromagnetic (see Section 2.4). The first three elements are transition metals, while the last two are rare earth. The atomic magnetic moments is often a non-integer value due to additional effect such as spin-orbit couplings or non-localized electrons in metals (see Ref. [10] for more details). The magnetic behaviour of a certain material does not depends simply on the value of its atomic magnetic moments but it is also strongly affected by the interactions among them, as indicated by the Curie temperature on the last column. For instance Dy has a high magnetic moment but a very low Curie temperature, meaning that its magnetic moments interact weakly. In fact, if magnetic moments do not interact (or interact weakly), their direction will be random due to thermal agitation and the net magnetization will be null.

2.3 Magnetic interactions

Therefore magnetic interactions between magnetic moments play an important role in the magnetic behaviour of materials. In the following we shall describe the most relevant ones.

2.3.1 Exchange interaction

The exchange energy for a system of N spins has the form

$$E_{\text{exch}} = -\sum_{i,j} J_{ij} \mathbf{S_i} \cdot \mathbf{S_j} \,, \tag{2.11}$$

where J_{ij} is the exchange integral, which favours parallel or anti-parallel alignment of spins depending on its sign. The sum in i goes over all the spins of the system, i.e, $i = 1, ..., N$, while the sum in j typically goes over the nearest neighbours of the i^{th} spin, since exchange is a short range interaction, being related to the overlapping of the electron wave-functions. Indeed, exchange interaction has a quantum mechanical origin and it is related to the fact that, according to quantum mechanics, identical particles (such as electrons in materials) must have symmetric or anti-symmetric wave-functions depending on their spin. For electrons the wave-function must be anti-symmetric so two electrons cannot have the same quantum numbers (also known as Pauli exclusion principle) and, therefore, if two electrons have the same spin, they cannot be in the same position, thus minimizing Coulomb energy. In other words, the exchange interaction can be seen as a consequence of Pauli exclusion principle and Coulomb interactions. J_{ij} is the exchange integral which is related to the spatial overlapping of the i and j electron wave functions [10]. Exchange is a very important interaction and it is the main reason for the ferromagnetic behaviour since it can favour parallel or anti-parallel spin alignment. There are different kind of exchange in materials. Direct exchange is when the electrons of neighbouring atoms interact directly through exchange. However, this implies that the electrons wave functions of different atoms overlap, which often is not the case. Indirect exchange is when the exchange interaction between localized moments is mediated by another atoms or by electrons (see Ref. [10] for more details). This latter case is particularly important since it occurs in metals, where exchange is mediated by conduction electrons. Such exchange is also called itinerant exchange or RKKY (Ruderman-Kittel-Kasuya-Yosida).

2.3.2 Zeeman interaction

The Zeeman interaction represents the interaction of a magnetic moment with an external magnetic field. Its energy has the form

$$E_{\text{Zeemam}} = -\boldsymbol{\mu} \cdot \mathbf{B} \,, \tag{2.12}$$

as already introduced in Section 2.2. The name is due to the Zeeman effect, which consists in the splitting of an atom spectral lines into different components in an external magnetic field. Classically, it can be seen as the consequence of the Lorentz force on an infinitesimal current loop as described in Section 2.2. However, the same interaction holds for spin magnetic moment.

2.3.3 Spin-orbit interaction

The spin-orbit interaction represents the interaction between the spin **S** and the orbital angular momentum **L** of electrons. This interaction is particularly important since it gives rise to a rich variety of phenomena such as magneto-crystalline anisotropy (see Section 3.2.2) or the Dzyaloshinskii-Moriya interaction (see Section 3.6.2). Also the spin-orbit interaction has a quantum-mechanical origin and it can be fully described only in the context of relativistic quantum mechanics. However, also in this case, a semi-classical approach can provide an intuitive explanation: consider an electron orbiting around a nucleus. In the reference frame of the orbiting electron the nucleus is moving around the electron with velocity **v** equal to the electron velocity in the rest frame of the nucleus. Thus, the nucleus is generating a magnetic field $\mathbf{B} = (\mathbf{E} \times \mathbf{v})/c^2$ [10]. Since the electrical field can be written as

$$\mathbf{E} = -\nabla V(r) = -\frac{dV(r)}{dr}\frac{\mathbf{r}}{r}\,, \tag{2.13}$$

and, from Zeeman interaction, $E = -\boldsymbol{\mu}_s \cdot \mathbf{B}$, it follows that

$$E_{\mathrm{SO}} = -\frac{1}{2}\boldsymbol{\mu}_s \cdot \mathbf{B} = \frac{1}{2}\frac{g\mu_B}{rm_e\hbar c^2}\frac{dV(r)}{dr}\mathbf{S} \cdot \mathbf{L}\,, \tag{2.14}$$

which represents the spin-orbit energy. The 1/2 factor is a correction factor which comes from the proper relativistic calculation.

2.3.4 Dipolar interaction

Dipolar interaction represents the interaction between a magnetic moment and the magnetic field generated by another magnetic moment. Such interaction is particularly important in macroscopic systems since it is responsible for the formation of magnetic domains (see Section 3.2.3). The dipolar energy of two magnetic moments $\boldsymbol{\mu}_1$ and $\boldsymbol{\mu}_2$ placed a distance $|\mathbf{r}|$ apart has the form [10]

$$E_{\mathrm{dipolar}} = \frac{\mu_0}{4\pi r^3}\left[\boldsymbol{\mu}_1 \cdot \boldsymbol{\mu}_2 - \frac{3}{r^2}(\boldsymbol{\mu}_1 \cdot \mathbf{r})(\boldsymbol{\mu}_2 \cdot \mathbf{r})\right]. \tag{2.15}$$

The field generated by a single dipole is given by Eq. (2.4) and it is shown in Fig. 2.2.

2.4 Magnetic order

Depending on the dominant magnetic interactions, materials can present different types of magnetic phases. In particular, materials can be classified as:

- **Paramagnetic**: Paramagnetic materials have no net magnetization in the absence of magnetic field. However, they present a net magnetization, parallel to the magnetic field, if an external field is applied: $\mathbf{M} = \chi \boldsymbol{H}$, where $\chi > 0$ is the magnetic susceptibility and $\mathbf{H} = \mathbf{B}/\mu_0$ is the external field. In paramagnetic materials magnetic moments do not interact significantly among them.

- **Diamagnetic**: Diamagnetic materials are similar to paramagnetic materials but the magnetization is opposite to the applied field: $\chi < 0$.

- **Ferromagnetic**: Ferromagnetic materials present a spontaneous magnetization even in the absence of an external magnetic field, if $T < T_C$. Their response to an external field is highly non-linear and it is characterized by a hysteresis loop as shown in Fig. 2.5(a). However, the total magnetization of a ferromagnetic object can be null due to the presence of different magnetic domains (see Section 3.2.3). Ferromagnetic behaviour is due to exchange interaction which favour parallel alignment of the magnetic moments.

- **Antiferromagnetic**: materials with antiferromagnetic order present no net magnetization but their response to an external field is non-linear. This is because in anti-ferromagnets the exchange interaction favours anti-parallel alignment of the magnetic moments. Thus, contrary to paramagnet, the moments strongly interact even if the net magnetization is zero.

- **Ferrimagnetic**: ferrimagnets present both anti-ferromagnetic and ferromagnetic behaviours. They are characterized by at least two sub-lattices which present separately ferromagnetic behaviour. However, they interact anti-ferromagnetically. The net magnetization is given by the difference between the magnetization of the different sub-lattices.

In this thesis, we will mainly deal with ferromagnetic materials, which will be analysed in more details in what follows. Nonetheless, in order to introduce ferromagnetic models, it is convenient to first analyse paramagnetic materials.

2.4.1 Paramagnetism

Paramagnetic materials have positive susceptibility $\chi > 0$. Paramagnetism is essentially a competition between the Zeeman interaction (Eq.(2.3)), which wants to align the magnetic moments along the magnetic field, and thermal agitation, which makes them fluctuates randomly. As previously commented, the average magnetization of a certain system can be calculated as (see Appendix A)

$$M = -\frac{1}{\mu_0 \Delta V}\left(\frac{\partial F}{\partial H_z}\right) , \tag{2.16}$$

where $F = -k_B T N \log \mathcal{Z}_i$ is the free energy of the system and N is the total number of moments. $\mathcal{Z}_i$ is the single particle partition function, which, for a classical magnetic moment in an external magnetic field along the z direction (sketched in Fig. 2.4) is given by

$$\begin{aligned} \mathcal{Z}_i &= 2\pi \int_0^{\pi} \exp\left(\beta\mu_0 H_z \mu \cos\theta\right) \sin\theta d\theta \\ &= 2\pi \int_{-1}^{1} \exp\left(\beta\mu_0 H_z \mu x\right) dx = \frac{4\pi}{a} \sinh a \,, \end{aligned} \tag{2.17}$$

where $a = \beta\mu_0\mu H_z$ and $\beta = (k_B T)^{-1}$, with k_B being the Boltzmann constant and T is the temperature of the system. θ represents the angle between the magnetic moment and the external field, as depicted in Fig. 2.4. From Eq. (2.16) it follows that

$$M = -\frac{1}{\mu_0 \Delta V}\left(\frac{\partial F}{\partial H_z}\right) = M_0\left(\coth a - 1/a\right) = M_0 L(a)\,, \tag{2.18}$$

where $M_0 = N\mu/(\Delta V)$ is the maximum possible magnetization, coinciding with all the moments aligned with the magnetic field. $L(a)$ is known as the Langevin function. The magnetic susceptibility is defined as

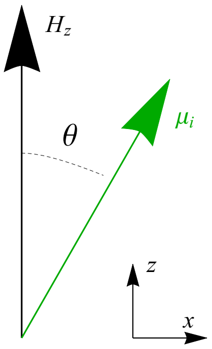

Figure 2.4: Magnetic moment $\boldsymbol{\mu}_i$ inside a magnetic field H_z pointing along z. The energy of the magnetic moment is $E = -\mu_0 \boldsymbol{\mu}_i \cdot \mathbf{H} = -\mu_0 \mu_i H_z \cos\theta$.

$$\chi \equiv \frac{\partial M}{\partial H_z} = M_0 \frac{\mu_0 \mu}{k_B T} \frac{\partial L(a)}{\partial a}\,, \tag{2.19}$$

which, for $a \ll 1$[2], becomes

$$\chi \sim M_0 \frac{\mu_0 \mu}{3 k_B T} = \frac{n \mu_0 \mu^2}{3 k_B T}\,, \tag{2.20}$$

---

[2] Note that for an external magnetic field of $\mu_0 H_z = 1$ T, $\mu = \mu_B$ and $T = 300$ K, $a \sim 0.002$.

since $\partial L(a)/\partial a \sim 1/3 - a^2/15 + \mathcal{O}(a^3)$. $n = N/\Delta V$ is the density of particles. Repeating the same calculation for quantum mechanical moments $\mu = \pm 1/2$ yields $M = M_0 \tanh a$, and for a generic moment related to the spin quantum number J

$$\frac{M}{M_0} = \frac{2J+1}{2J} \coth\left(\frac{2J+1}{2J} a\right) - \frac{1}{2J} \coth\left(\frac{a}{2J}\right) \equiv B_J(a) \,, \tag{2.21}$$

which is known as the Brillouin function.

The paramagnetic theory predicts that no magnetization is possible with zero applied field and that strong magnetic fields are needed in order to achieve a small increase in the materials magnetization. However, this is in contrast with everyday experience which shows that materials can be magnetic even without any applied field. This latter class of material are classified as ferromagnets. As anticipated, ferromagnetic materials present a spontaneous magnetization even in the absence of magnetic field and their response to an external field is highly non-linear. While in paramagnets, in the absence of an external field, the magnetic moments point randomly since any configuration is energetically equivalent, in ferromagnets additional interactions favour specific configurations even if $H_z = 0$.

2.4.2 Ferromagnetism

Ferromagnetism is the most common example of magnetic order. In everyday experience we all have seen magnets attached to a fridge or we have played with magnets at least once. In these systems, the exchange interaction (see Section 2.3.1) favours a parallel alignment of the atomic magnetic moments. A typical feature of ferromagnetic materials is **hysteresis**, i.e., the magnetization as function of the applied field follows a characteristic curve depicted in Fig. 2.5 (a). The value of the magnetization for a given applied field, not only depends on the applied field but also on the previous state of the system. Furthermore, as anticipated, the system has a remanent magnetization M_r even if $H_z = 0$. The external field needed to have $M = 0$ is known as coercive field H_c. The value of the magnetization at very large fields is defined as the saturation magnetization (or spontaneous magnetization) $M_s = M_0$. In reality, this definition is not very accurate. The saturation magnetization of a ferromagnet is more generally defined as the remanent magnetization of a single magnetic domain. [3] If properly measured, M_s is independent on the sample size and it depends on temperature as depicted in Fig. 2.5 (b). M_s decreases with temperature and it is zero if $T > T_C$, where T_C is the Curie temperature above which the system behaves as a paramagnet (for $H_z = 0$).

---

[3] As it will discussed in Section 2.5 ferromagnets break into different domains of uniform magnetization. Due to this fact the value of M_r depends on the sample size and the domains configuration. In the absence of field, ferromagnets can also present zero net magnetization. However by measuring M_s at large fields and extrapolating the value at $H = 0$, it is possible to obtain the remanent magnetization for the single domain, which is taken as the definition of M_s [13].

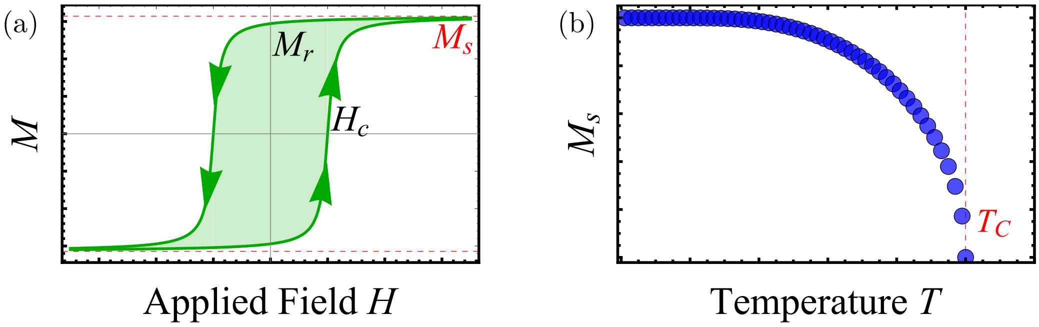

Figure 2.5: (a) Hysteresis curve for ferromagnetic materials. Magnetization (M) vs Applied Field (H). (b) M_s as function of temperature for a typical ferromagnet.

Weiss Model

A first theory for ferromagnetic materials was introduced by Pierre-Ernest Weiss who extended the theory of paramagnetism by replacing the external applied field H_z with $H_z \rightarrow H_z + \lambda M$. He hypothesized the existence of an additional internal magnetic field (λM), proportional to the magnetization itself, which gives rise to the spontaneous magnetization. Within the Weiss model (see Ref. [11] for more details)

$$a = \frac{\mu_0 \mu}{k_B T}(H_z + \lambda M)\,, \tag{2.22}$$

and, extending Eq. (2.21), the average magnetization becomes

$$M/M_0 = m = B_J\left(\frac{\mu_0 \mu}{k_B T}(H_a + \lambda M)\right)\,. \tag{2.23}$$

Thus, the magnetic susceptibility $\chi = M_0 \partial m/\partial H_a$ becomes

$$\chi = M_0 B_J'(a) \frac{\mu_0 \mu}{k_B T - \mu_0 \mu \lambda M_0 B_J'(a)}\,, \tag{2.24}$$

where $B_J'(a)$ stands for $\partial B_J(a)/\partial a$. For small a around $a \sim 0$, namely for high temperatures, the susceptibility can be written as

$$\chi = \frac{\mu_0 \mu M_s}{k_B}\frac{1}{T - T_C}\,, \tag{2.25}$$

which is known as the Curie-Weiss law valid only for $T > T_C$. Within the Weiss model, T_C is given by

$$T_C = \frac{\mu_0 \mu \lambda M_s}{k_B}\,. \tag{2.26}$$

Eq. (2.25) and (2.26) were calculated by considering $J = 1/2$. Above T_C thermal agitation is stronger than the internal field and the system is paramagnetic. A critical phase change, between ferromagnetic and paramagnetic order, occurs at $T = T_C$. Note that the Curie-Weiss law is not valid for $T < T_C$, since it predicts a negative susceptibility. For $T < T_C$ one should use the more general Eq. (2.24). Eq. (2.23) can be solved numerically to obtain m as function of temperature. The result of this calculation is shown in Fig. 2.6(a) for $J = 1/2$ and $J = \infty$ (classical spins). The corresponding susceptibility is shown in Fig. 2.6(b). A critical behaviour is observed at $T = T_C$ where the system undergoes to a phase change and the susceptibility diverges (see Ref. [10, 11] for more details about critical phenomena). The Weiss model reproduces qualitatively well the behaviour of the saturation magnetization as function of temperature.

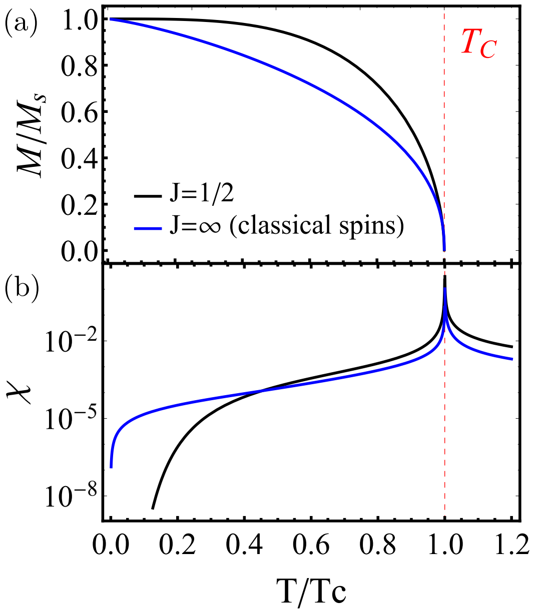

Figure 2.6: (a) Normalized magnetization as function of temperature. (b) Magnetic susceptibility as function of temperature.

Heisenberg Model

The origin of the internal field, proposed *ad-hoc* by Weiss, is the exchange interaction, which, as described in Section 2.3.1, has energy

$$E_{\text{exch}} = -\sum_{i,j} J_{ij} \mathbf{S_i} \cdot \mathbf{S_j} \,, \tag{2.27}$$

where J_{ij} is the coupling constant between the i^{th} and j^{th} spins. This model for the spin-spin interaction is known as Heisenberg model, who first introduced it. It is possible to further simplify Eq. (2.27) by adopting a mean-field approximation, which consider an average spin, $\langle \mathbf{S} \rangle$, acting on $\mathbf{S}_i$, instead of the single $\mathbf{S}_j$. Within this approach, Eq. (2.27) becomes

$$E_i = -2\sum_j J_{ij}\mathbf{S_i}\cdot\langle\mathbf{S}\rangle - \mu_0\frac{g\mu_B}{\hbar}\mathbf{S_i}\cdot\mathbf{H}_a, \tag{2.28}$$

where we have also included the Zeeman energy of the external magnetic field $\mathbf{H}_a$. The factor 2 comes from the double sum in Eq. (2.27) (each coupling should be considered twice). Thus, it is possible to write

$$E_i = -\mu_0\frac{g\mu_B}{\hbar}\mathbf{S}_i\cdot(\mathbf{H}_a + \frac{2}{\mu_0}\frac{\hbar}{g\mu_B}\sum_j J_{ij}\langle\mathbf{S}\rangle)\,. \tag{2.29}$$

Since the exchange interaction is restricted to neighbouring spins and the coupling J_{ij} is usually assumed to be equal for all neighbours, Eq. (2.29) becomes

$$E_i = -\mu_0\frac{g\mu_B}{\hbar}\mathbf{S}_i\cdot(\mathbf{H}_a + \frac{2pJ}{\mu_0}\frac{\hbar}{g\mu_B}\langle\mathbf{S}\rangle)\,, \tag{2.30}$$

where p is the number of nearest neighbours and J the coupling strength. The second term on the right-hand side of Eq. (2.30) is proportional to the mean magnetic moment and it can be associated with the internal field introduced by Weiss, proportional to the magnetization. Thus, the Weiss model can be seen as a mean field approximation of the Heisenberg model. In fact, from Eq. (2.30) it is possible to link the strength of the Weiss internal field (λ) with the strength of the exchange interaction J.

A more advanced description of the magnetization as function of temperature can obtained within the Heisenberg model, by considering all the magnetic excitations (magnons) at a given temperature. More details can be found in Ref. [13, 10, 14].

Furthermore, Weiss or Heisenberg model consider ferromagnetism as the consequence of the interactions between localized magnetic moments. However, it is known that electrons in metals are de-localized and they hybridize in bands. The susceptibility of the free-electron model (useful to describe many properties of metals) is known as Pauli-susceptibility. Ferromagnetism in metals occurs due to a spontaneous split of electronics bands between up and down spins, which cause that the electrons at the Fermi level are all spin-polarized. Also in this case, the splitting originates from exchange interaction and it depends on the competition between the increase in the kinetic energy due to moving the spins from one spin band to another, and the reduction of Coulomb energy due to exchange interaction. This criterion is formalized as the Stoner criterion (see Ref. [10] for more details about the Stoner criterion and Pauli susceptibility).

2.5 Magnetic domains

We have seen that exchange interaction can give rise to the presence of a spontaneous magnetization. However, ferromagnetic samples often present no net magnetization since they ”break” into magnetic domains with different uniform magnetization. As a consequence, the total net magnetization is zero. Advances in microscopic techniques, have led to the possibility of observing directly the magnetization patterns at the microscales. Fig. 2.7, taken from Ref. [15], shows real magnetization patterns of typical ferromagnetic samples. As anticipated, the magnetization breaks into different magnetic domains. This behaviour cannot be explained in terms of exchange interaction, which would favour a uniform magnetization. In fact, dipolar interaction is actually responsible for the formation of domains. The dipolar fields generated by each magnetic moment (Fig. 2.2) interact with the magnetization and lead to the formation of domains. This mechanism will be better described in the next chapter. The boundary between two domains represents a magnetic domain wall, whose dynamics represents the main topic of this thesis. The structure and the motion of magnetic domain walls will be described in more details in the next parts.

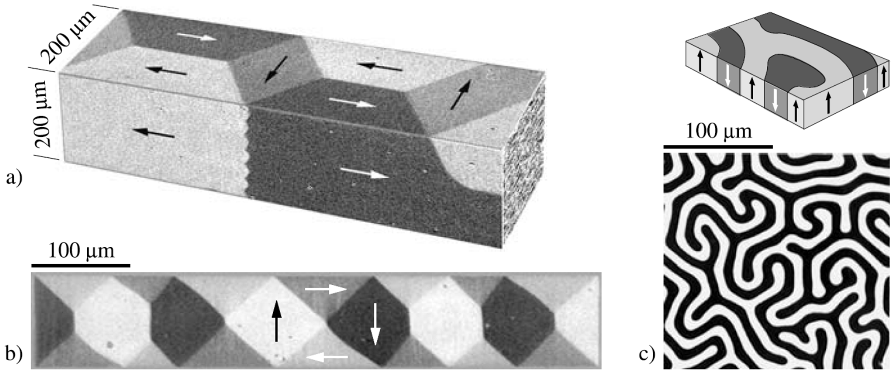

Figure 2.7: Figure taken from Ref. [15]. Domains observed with magneto-optical methods. (a) Image from two sides of an iron whisker, combined in a computer to simulate a perspective view. (b) Domains in an FeNi alloy. (c) Domains in a single-crystal garnet together with sketch of the domains structures.

In this chapter we have described the properties of ferromagnetic materials in terms of localized moments, which interact mainly through exchange interaction. However, at the micro- and nano-scale we have to deal with an extremely high number of magnetic moments, whose motion can be highly irregular and the description of ferromagnetic materials in terms of this microscopic approach would be extremely complicated and it would require a significant computational effort. Additionally, at these scales, other interactions (apart from Zeeman and exchange) become relevant and need to be included in the modelling. As a consequence, depending on the scale at which we are interested, we need to use a different approach and a different modelling. Fig. 2.8, also taken from Ref. [15], shows different approaches, used to describe magnetic object and magnetic behaviours, depending on the scale at which we are interested. This chapter belongs to the first level (”Atomic Level Theory”), while the next chapter will describe the ”Micromagnetic Analysis”, mainly used within this thesis to describe the magnetic domain wall dynamics.

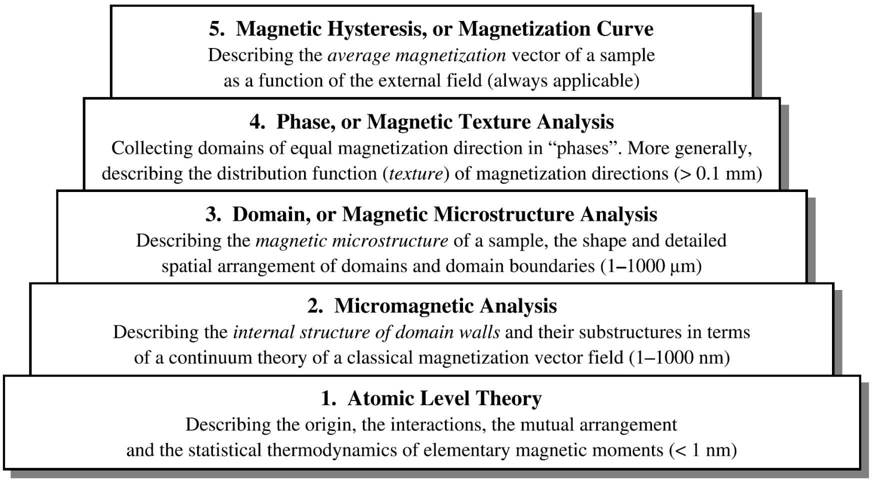

Figure 2.8: Figure taken from Ref. [15]. Different approaches to describe magnetic systems. The value in parenthesis indicates the length scales at which the model is applicable.

Chapter 3

Micromagnetic Theory

This chapter describes the micromagnetic formalism, mainly used in this thesis to analyse the domain wall dynamics. We will derive the Landau-Lifshitz-Gilbert equation, which describes the magnetization dynamics at the micro- and nano-scales. The theory will be extended in order to include the effects of electrical currents and thermal fluctuations. Furthermore, we will present the Landau-Lifshitz-Bloch equation, used to analyse the magnetization dynamics for temperature close to the Curie temperature. Additionally, we will describe magnetic ultrathin films and the energy terms related to interfacial interactions, such as surface anisotropy and Dzyaloshinskii-Moriya interaction. Finally, we will describe magnetic domain walls in nanostrips and we will introduce the collective-coordinate model, a useful tool to analyse the domain wall dynamics.

3.1 The continuum approximation

In the previous chapter, magnetic materials were described from a microscopic point of view by considering the magnetic moments of single atoms interacting mainly through exchange interaction. However, as anticipated, at micro- and nano-scales we have to deal with an extremely high numbers of magnetic moments and the description of the magnetization within this atomistic approach would be extremely complicated and it would require a considerable computational effort. Additionally, at these scale, we are not really interested in the dynamics of the single magnetic moments, rather we would like to know the behaviour of the macroscopic magnetization, averaging out all those degrees of freedom which are somehow superfluous. Furthermore, in the previous chapter, the spontaneous magnetization was explained in terms of the Zeeman and exchange interactions. However, these energies alone are not enough to explain typical magnetization patterns observed in magnetic materials at the micro-scales, such as the magnetic domains shown in Fig. 2.7 and Fig. 3.1(a). In these systems, the magnetizations spontaneously breaks into regions of uniform magnetization called **magnetic domains**. The boundary between different domains is a **domain wall**. As anticipated, this effect is mainly due to dipolar energy. In fact, exchange is short-range interaction (typically involving nearest neighbours) and, in large systems also dipolar and spin-orbit interactions became relevant.

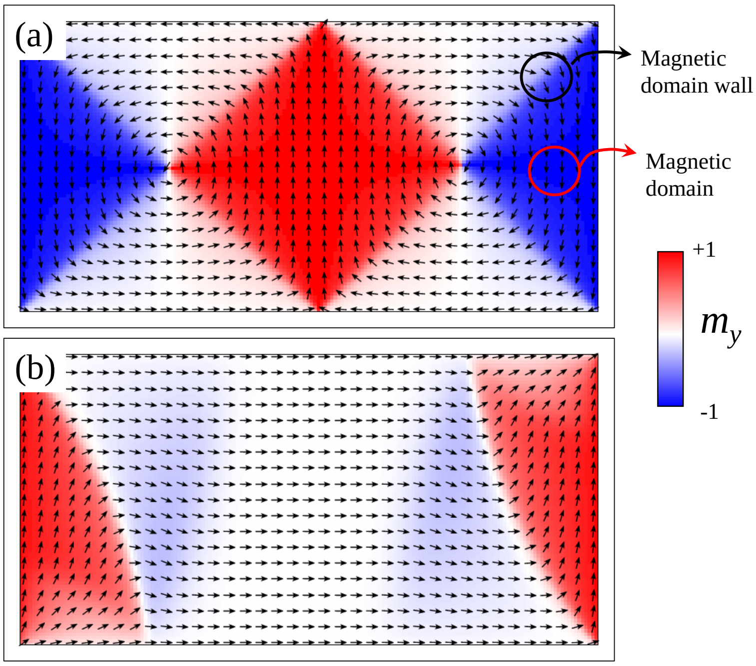

Figure 3.1: (a) Magnetic domains and domain walls. Due to magnetostatic energy the system spontaneously breaks into this magnetization pattern. (b) S-state state obtained by relaxing the system from a different initial magnetic configuration.

The most efficient approach to describe the magnetization at these scales relies on considering the magnetization as a continuous function of space $\mathbf{M}(\mathbf{r})$. The magnetization at each point represents an average over an certain volume elementary ΔV, sketched in Fig. 3.2, where ΔV must be small enough such that the magnetization can be considered uniform within ΔV, and it must be large enough in order to contain a significant number of elementary magnetic moments. This approach implies an assumption about time-scales: in particular, it is assumed that the time-scale at which the magnetic moments inside the volume ΔV reach their thermodynamic equilibrium value $\mathbf{M}$, with respect to a given local value $\mathbf{M}(\mathbf{r})$, is much shorter than the time-scale at which the system as a whole reaches its equilibrium configuration $\mathbf{M}(\mathbf{r})$. In other words, the dynamics of the elementary moments inside each cell is much faster than the dynamics of the average magnetization. We will relax this assumption in Section 3.8.

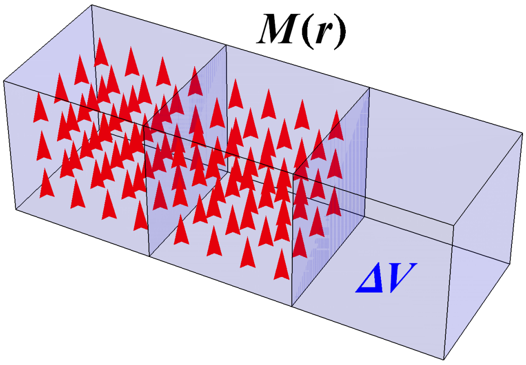

Figure 3.2: Sketch of the elementary volumes ΔV containing a large number of single spins $\mathbf{S}_i$. The magnetization at each point $\mathbf{M}(\mathbf{r})$ is defined as an average over ΔV.

The theory, developed accordingly, was introduced by W.F. Brown and it is known as **micromagnetic theory** or **continuum theory of magnetically ordered materials** [16]. Within this approach, the internal energy E of the system, instead of being a function of the single magnetic moments, is a functional of the magnetization $E[\mathbf{M}(\mathbf{r})]$. The ground state of the system is an energy minimum and, therefore, it has to satisfy

$$\delta E[\delta \mathbf{M}(\mathbf{r})] = 0\,, \tag{3.1}$$

where $\delta E[\delta \mathbf{M}(\mathbf{r})] = 0$ indicates the variation of the system energy for a generic infinitesimal variation of the magnetization $\delta \mathbf{M}(\mathbf{r})$. The approach is analogous to the minimization of the action integral which leads to the Euler-Lagrange equations describing the dynamics of the system. Here, instead of a balance of force in time (equations of motion) we have a balance of forces (and torques) in space (equilibrium equations). Thus, it is important to identify the different contribution to the system energy.

3.2 Micromagnetic energies

3.2.1 Exchange energy

Exchange interaction represents a very important contribution to the magnetic energy. As described in Section 2.3.1, the exchange interaction has a quantum mechanical origin and it is related to Pauli exclusion principle and Coulomb interaction. It can favours parallel or anti-parallel alignment of the magnetic moments and it leads to the existence of a spontaneous magnetization $M_s(T)$ in ferromagnets. Far from the Curie temperature, the external field dependence of $M_s(T)$ is negligible. Hence, at a certain temperature, the value of $M_s(T) = |\mathbf{M}(\mathbf{r})|$ depends only on the dynamics of the elementary magnetic moments inside the elementary cell. As anticipated, this dynamics, dominated by the exchange interaction between the magnetic moments, is much faster than the dynamics of the average $\mathbf{M}(\mathbf{r})$. As a consequence, the modulus of the magnetization in each cell reaches its equilibrium value much faster than the time needed by the overall magnetization to reach its final configuration. Thus, the main effect of exchange is that the magnetization $\mathbf{M}(\mathbf{r})$ of each elementary cell can be written as

$$\mathbf{M}(\mathbf{r}) = M_s \mathbf{m}(\mathbf{r})\,, \tag{3.2}$$

where $\mathbf{m}(\mathbf{r})$ is a unitary vector and M_s is the saturation magnetization of the material, which is considered constant at a given temperature. This approach is valid for $T \ll T_C$. Nevertheless, we can expect an effect of the exchange interaction if the magnetization of neighbouring cells is not aligned. For a small misalignment between neighbouring spins, Eq. (2.11) can be re-written as

$$\begin{aligned} E_{\text{exch}} &= -\sum_{ij} J_{ij} S^2 \cos\phi_{ij} \\ &= -\sum_{ij} J_{ij} S^2 (1 - \frac{\phi_{ij}^2}{2} + \mathcal{O}(\phi_{ij}^4))\,, \end{aligned} \tag{3.3}$$

where ϕ_{ij} indicates the angle between the i^{th} and j^{th} spins, whereas r_{ij} represents the distance between them, as sketched in Fig. 3.3.
Using the fact that $\phi_{ij} = |\mathbf{m_i} - \mathbf{m_j}|$, where $\mathbf{m}_{ij}$ are unitary vectors along $\mathbf{S}_{ij}$, and that $|\mathbf{m_i} - \mathbf{m_j}| \approx (\mathbf{r}_{ij} \cdot \nabla)\mathbf{m}$, Eq. (3.3) becomes

$$E_{\text{exch}} = \text{constant} + \sum_{ij} \frac{J_{ij} S^2}{2} [(\mathbf{r_{ij}} \cdot \nabla)\mathbf{m}]^2\,. \tag{3.4}$$

By assuming a simple cubic lattice and the same coupling constant J_{ij} for all neighbours, the exchange energy for the elementary volume ΔV finally reads like

$$\begin{aligned} \Delta E_{\text{exch}} &= A[(\nabla m_x)^2 + (\nabla m_y)^2 + (\nabla m_z)^2]\Delta V \\ &= A|\nabla \mathbf{m}|^2 \Delta V \end{aligned} \tag{3.5}$$

where $|\nabla \mathbf{m}|^2$ stands for $(\nabla m_x)^2 + (\nabla m_y)^2 + (\nabla m_z)^2$. $A = k2JS^2/a$ is the exchange constant, which has units of J/m, a is the lattice constant and k depends on the type of lattice ($k = 1$ for simple cubic, $k = 2$ for bcc and $k = 4$ for fcc). Exchange energy favours uniform magnetic patterns for which $|\nabla \mathbf{m}|^2 = 0$.

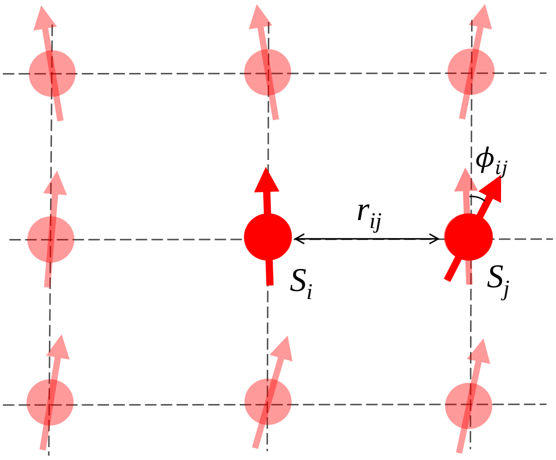

Figure 3.3: Sketch of exchange interaction between spins in a cubic lattice.

3.2.2 Anisotropy energy

The micromagnetic exchange energy is isotropic [1], namely, the magnetization alignment has no preferred direction in space. However, magnetic materials often present certain preferred directions (easy-axes) along which the magnetization is aligned more easily. The anisotropy energy refers to the energy that the system gains or loses depending on the magnetization direction. There are different kinds of anisotropies depending on the mechanisms that give rise to the favourable alignment directions. A common type of anisotropy is the magneto-crystalline anisotropy, i.e., the magnetization is aligned preferably along certain directions of the lattice, which are related to the crystal structure. The origin of magneto-crystalline anisotropy is the spin-orbit interaction (Eq. (2.14)) which wants to align spin and orbital angular momenta. This interaction is further influenced by the crystal field which fixes the directions of the orbital angular momentum and, therefore, it determines the direction of the anisotropy [11].

In micromagnetics the anisotropy energy is described phenomenologically as a certain function of the magnetization direction and the easy axis (or axes) direction:

$$\Delta E_{\text{anis}} = f(\mathbf{m}(\mathbf{r}), \hat{\mathbf{u}})\Delta V \,, \tag{3.6}$$

where $\mathbf{m}(\mathbf{r}) = \mathbf{M}(\mathbf{r})/M_s$ and $\hat{\mathbf{u}}$ represents the anisotropy direction.

---

[1] In general, the atomistic exchange coupling J_{ij} between different lattice directions could be different and, therefore, anisotropic.

Uniaxial anisotropy

For instance, if the anisotropy has only one preferred direction, the anisotropy energy can be written as

$$\Delta E_{\text{anis}} = K_u \left(1 - (\mathbf{m}(\mathbf{r}) \cdot \hat{\mathbf{u}})^2\right) \Delta V \,. \tag{3.7}$$

This kind of anisotropy is usually called uniaxial anisotropy. K_u represents the uniaxial anistropy constant and it has units J/m^3. A 3-dimensional (3D) representation of the uniaxial anisotropy energy is shown in Fig. 3.4(b) for $\hat{\mathbf{u}} = (0,0,1)$, in comparison with an isotropic energy shown in Fig. 3.4(a). The energy has a minimum along the z direction.

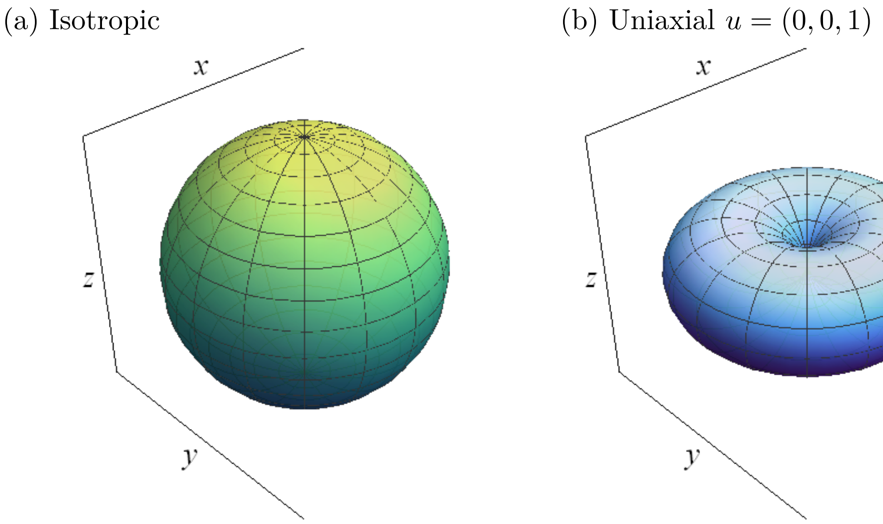
(a) Isotropic

(b) Uniaxial $u = (0,0,1)$

Figure 3.4: (a) 3D representation of an isotropic energy, any direction of the magnetization has the same energy. (b) 3D representation of uniaxial anistropy energy along the z direction. The energy has minima along the z axis.

Since $\mathbf{m}(\mathbf{r})$ is unitary we can write in polar coordinates $\mathbf{m}(\mathbf{r}) = (\sin\theta\cos\phi, \sin\theta\sin\phi, \cos\theta)$, where the angles θ and ϕ are defined in Fig. 3.5(a). $0 < \theta < \pi$ while $0 < \phi < 2\pi$. Thus, in polar coordinates

$$\Delta E_{\text{anis}} = K_u \sin^2\theta \,. \tag{3.8}$$

The corresponding energy is plotted in Fig. 3.5(b). The energy has two minima for $\theta = 0$ and $\theta = \pi$, i.e., when the magnetization is fully aligned along the z direction (the direction of the anisotropy). Another kind of magneto-crystalline anisotropy is the cubic

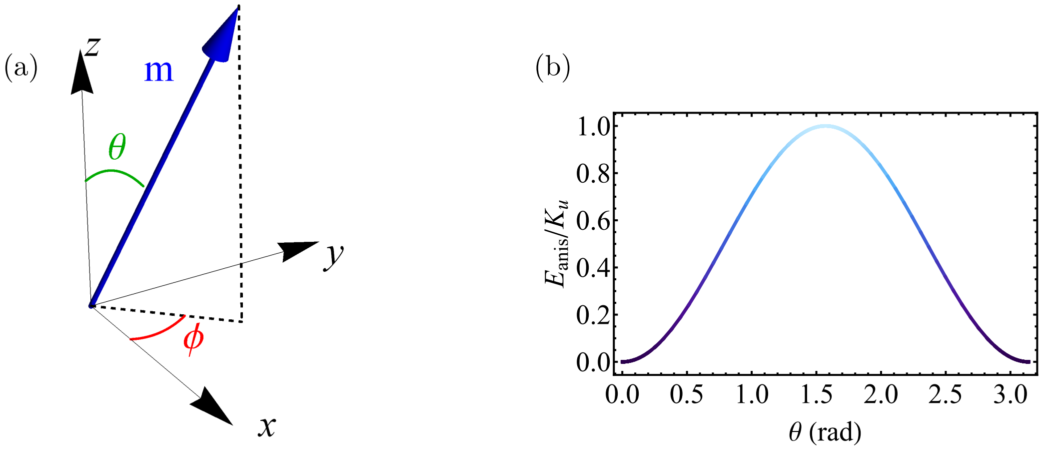

Figure 3.5: (a) Definition of the angles θ and ϕ. (b) Uniaxial anisotropy energy for $\hat{\mathbf{u}} = (0, 0, 1)$.

anisotropy which is minimized when the magnetization lies along one of the three main cubic axes (see Ref. [11] for more details).

Other types of anisotropies are the shape anisotropy, related to magnetostatic interactions and described in Section 3.2.3, and surface anisotropy, related to interfacial effects in ultrathin films and described in Section 3.6.

3.2.3 Magnetostatic energy

The magnetostatic energy is the energy of the magnetic moments in the magnetic field generated by themselves. As shown in Section 2.3.4, the energy of two magnetic moments is given by Eq. (2.15), however, it would be extremely complicated to calculate the energy of all the magnetic moments in the system. A more convenient approach is to use Maxwells' equations to calculate the magnetic field generated by a certain magnetic configuration [11]. Maxwells' equations for the magnetic field, in the absence of external electrical currents, read like

$$\begin{aligned} \nabla \cdot \mathbf{H_M}(\mathbf{r}, t) &= \rho_M \,, & (3.9) \\ \nabla \times \mathbf{H_M}(\mathbf{r}, t) &= 0 \,, & (3.10) \end{aligned}$$

where $\mathbf{H}_M = \mathbf{B}/\mu_0 - \mathbf{M}$ and $\rho_M = -\nabla \cdot \mathbf{M}(\mathbf{r})$. The subscript M indicated that the field is generated by the magnetization itself. Mathematically, Eq. (3.9) and (3.10) have the same form of the electrostatic Maxwells' equations relating charges and electrical field (note that the analogy holds only in this particular case where there are no free electrical currents). In this case, ρ_M plays the role of magnetic density charge. Thus, it is possible to write

$$\mathbf{H}_M = -\nabla \phi \,, \tag{3.11}$$

which satisfies $\nabla \times \mathbf{H}_M = 0$. Then, by using Eq. (3.9) we see that

$$\nabla^2 \phi = -\rho_M \, , \tag{3.12}$$

which yields the solution

$$\phi(\mathbf{r}) = -\frac{1}{4\pi} \int \frac{\nabla \cdot \mathbf{M}(\mathbf{r}')}{|\mathbf{r} - \mathbf{r}'|} d^3 r' \, , \tag{3.13}$$

where the integral is over the entire space. However, at the sample boundaries, $\mathbf{M}(\mathbf{r})$ changes abruptly, generating quasi-singular behaviours. In the limit that it passes suddenly to zero outside the material, Eq. (3.13) can be rewritten as

$$\begin{aligned} \phi(\mathbf{r}) &= -\frac{1}{4\pi} \int_V \frac{\nabla \cdot \mathbf{M}(\mathbf{r}')}{|\mathbf{r} - \mathbf{r}'|} d^3 r' + \frac{1}{4\pi} \int_S \frac{\mathbf{n} \cdot \mathbf{M}(\mathbf{r}')}{|\mathbf{r} - \mathbf{r}'|} d\Sigma' \\ &= \frac{1}{4\pi} \int_V \frac{\rho_M(\mathbf{r}')}{|\mathbf{r} - \mathbf{r}'|} d^3 r' + \frac{1}{4\pi} \int_S \frac{\sigma_M(\mathbf{r}')}{|\mathbf{r} - \mathbf{r}'|} d\Sigma' \end{aligned} \tag{3.14}$$

where the first integral is performed over the volume and the second over the surface (Σ) of the magnetic object. $\mathbf{n}$ represents the unit vector normal to the surface of the object and $\sigma_M = \mathbf{M} \cdot \mathbf{n}$ indicates the magnetic surface charges. The magnetic potential (Eq. (3.14)) allows to calculate the magnetostatic field $\mathbf{H}_M$, generated by a given magnetization pattern $\mathbf{M}(\mathbf{r})$.

In case of uniform magnetization, the second term of Eq. (3.14) depends only on the sample geometry and it acts against the magnetization $\mathbf{M}(\mathbf{r})$. Indeed, $\mathbf{H}_M$ is also known as demagnetizing field since it wants to avoid volume and surface charges generated by the magnetization, so it tries to ”demagnetize” the sample. Furthermore, it gives rise to a shape anisotropy in the material since the magnetization will be preferably aligned along directions which reduce the magnetic charges. Magnetostatic energy is the main responsible for the formation of magnetic domains, as shown in Fig 3.1. Exchange and anisotropy want to align all the spins along a certain direction but this would lead to the generation of magnetostatic charges at the sample's boundaries and, therefore, an increase in the magnetostatic energy. Thus, the system prefers to breaks into domains, paying a cost in exchange energy, but decreasing the total system energy. The exchange interaction is much stronger but it dominates only at small distances, while dipolar interaction is a large distance interaction since the dipolar field decreases as $1/r^3$.

The magnetic energy related to the magnetostatic field $\mathbf{H}_M$, for a single element ΔV is [13, 11]

$$\Delta E_M = -\frac{\mu_0}{2} \mathbf{M}(\mathbf{r}) \cdot \mathbf{H}_M(\mathbf{r}) \Delta V \, , \tag{3.15}$$

where $\mathbf{H}_M$ is the solution of Eq. (3.11). This energy has the same form of the Zeeman energy but the factor $1/2$ comes from the fact that the magnetic field is generated by the magnetization itself. Eq. (3.15) can be derived according to the following arguments: consider an elementary volume ΔV which contains a large number of atomistic magnetic moments. The energy of the single moment $\mathbf{m}_0$, which occupy a random position in ΔV, is

$$E_i = -\mu_0 \mathbf{m}_0 \cdot (\mathbf{H}_M - \lambda)\,, \tag{3.16}$$

where $\mathbf{H}_M = \sum_i \mathbf{h}_i / \Delta V$ is the average field generated by the all magnetic moments in ΔV and λ is a correction factor since the field generated by $\mathbf{m}_0$ must be subtracted to $\mathbf{H}_M$. This contribution is small and it will be neglected in what follows. Thus the total energy in the elementary volume ΔV is

$$\Delta E_M = -\frac{1}{2}\mu_0 \sum_i \mathbf{m}_i \cdot \mathbf{H}_M\,, \tag{3.17}$$

where the factor 1/2 must be included since each magnetic moment appears twice in the sum (one time as source of the field and one time as test moment). For a continuous magnetization

$$\Delta E_M = -\frac{1}{2}\mu_0 \sum_i \frac{\mathbf{m}_i}{\Delta V} \cdot \mathbf{H}_M \Delta V = -\frac{\mu_0}{2} \mathbf{M}(\mathbf{r}) \cdot \mathbf{H}_M \Delta V\,, \tag{3.18}$$

which corresponds to Eq. (3.15). As commented, the demagnetizing energy favours magnetization patterns which avoid magnetic charges, for instance by trying to align the magnetization along the edges of the magnetic object, as in Fig. 3.1(b). If magnetic charges cannot be avoided it will favour magnetization patterns that close the magnetic flux.

Demagnetizing factors

For certain geometries it is possible to calculate analytically the surface charges and the demagnetizing field generated by a uniform magnetization. For instance, in the case of an ellipsoid one finds that the demagnetizing field $\mathbf{H}_M$, calculated from an uniform magnetization $\mathbf{M}$, is also uniform inside the ellipsoid and it is opposed to $\mathbf{M}$:

$$\mathbf{H}_m = -\bar{\bar{N}}\mathbf{M}\,, \tag{3.19}$$

where $\bar{\bar{N}}$ is the demagnetizing tensor, which depends on the ellipsoid axes. It can be written in its diagonal form [11],

$$\bar{\bar{N}} = \begin{pmatrix} N_x & 0 & 0 \\ 0 & N_y & 0 \\ 0 & 0 & N_z \end{pmatrix}\,. \tag{3.20}$$

The demagnetizing factors along each axis obey to the constrain $N_x + N_y + N_z = 1$ [11]. For instance, for a sphere, $N_x = N_y = N_z = 1/3$ due to its symmetry.

Shape anisotropy

As anticipated in Section 3.2.2, the magnetostatic energy gives rise to a shape anistropy. Namely, the magnetization aligns preferably along certain directions which depend on the sample shape. More specifically, the magnetization will align preferably along directions that generates less magnetic charges and minimize the magnetostatic energy. These directions, in turns, depend on the sample geometry. Generally, it will try to avoid to be perpendicular to surfaces of the magnetic object since it would generate surface magnetic charges. For instance, for an elongated object as the one sketched in Fig. 3.6, the magnetization prefers to be aligned along the x direction since it will generate fewer magnetic charges. However, within this configuration with uniform magnetization, the magnetic charges (at the surfaces along the x direction) are quite far from each other and this would also increase the magnetostatic energy. Thus, in reality, the magnetization can also try to rotate close to the surface, as in Fig. 3.1(b), increasing the exchange energy but further reducing the magnetostatic energy by avoiding surface charges.

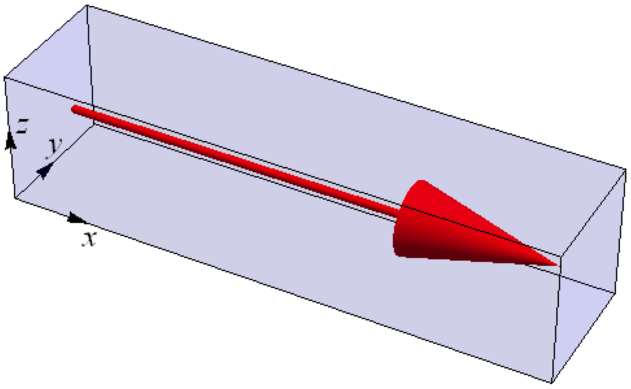

Figure 3.6: Sketch of shape anisotropy. The magnetization prefers to aligns along the larger axis of the sample since it will generates fewer magnetic surface charges .

3.2.4 Zeeman energy

The Zeeman energy corresponds to the energy related to an external magnetic field. Eq. (2.3) for a single magnetic moment can be generalized for a continuous magnetization as follows: according to Eq. (2.3) the energy of an ensemble of magnetic moment in the elementary volume ΔV, in a magnetic field $\mathbf{H}_a$, can be written as

$$\begin{aligned}\Delta E_{\text{Zeeman}} &= -\mu_0 \sum_i \boldsymbol{\mu}_i \cdot \mathbf{H}_a = -\mu_0 \sum_i \frac{\boldsymbol{\mu}_i}{\Delta V} \cdot \mathbf{H}_a \Delta V \\ &= -\mu_0 \mathbf{M}(\mathbf{r}) \cdot \mathbf{H}_a \Delta V \,, \end{aligned} \tag{3.21}$$

where we have used the fact that by definition $\sum_i \boldsymbol{\mu}_i/\Delta V = \mathbf{M}(\mathbf{r})$. As indicated by Eq. (3.21), the Zeeman energy favours magnetization patterns which are aligned with the external magnetic field.

3.3 Energy minimization

The total energy of the system is given by the sum of the different energy terms in each elementary volume ΔV. By transforming the sum into an integral over the entire magnetic object, the total energy reads like

$$E = \int_V \left[A|\nabla \mathbf{m}|^2 + f(\mathbf{m}(\mathbf{r}), \hat{\mathbf{u}}) - \frac{1}{2}\mu_0 M_s \mathbf{m} \cdot \mathbf{H}_M - \mu_0 M_s \mathbf{m} \cdot \mathbf{H}_a \right] dV, \tag{3.22}$$

where we have included exchange, anisotropy, magnetostatic and Zeeman energies respectively. The stable state (or states) of a magnetic object are given by the competition between these different energy terms. The system energy $E(\mathbf{m})$ can have several local minima, which satisfy the condition $\delta E(\delta \mathbf{m}) = 0$. In other words, the system can have several meta-stable states and, depending on its initial configuration, it can collapse on one state or another. A clear example is the "s-state" state shown in Fig. 3.1(b). The ground state of the system is shown in Fig. 3.1(a), which is obtained by relaxing the system from a random initial magnetization. However, if the initial state is a uniform magnetization along the x direction, the system collapse into the "s-state" state shown in Fig. 3.1(b). The mechanism is sketched in Fig. 3.7. The energy of the state "A" is lower than the energy of state "B", but the initial state of the system is closer to the local minimum corresponding to the s-state and, therefore, the system collapses into this latter one. Eventually, for $t \to \infty$, the system will collapse into its ground state.

Furthermore, the energy landscape can be modified by an external magnetizing field. As described in Section 3.2.4, the Zeeman energy favours magnetization patterns aligned with the external field. This mechanism can also explain the hysteresis loop: upon application of an external field, the initial state of the system (opposite to the external field) becomes a meta-stable state. Increasing the applied field keeps changing the energy landscape but the magnetization does not change until a critical field (the coercive field) at which the energy barrier is completely lifted and the system spontaneously "jumps" into the new global minimum (see Fig. 2.5(a)).

Each energy minimum has to satisfy Eq. (3.1), which can be calculated explicitly with the energy terms that we have introduced. Since for exchange interaction $\mathbf{M}(\mathbf{r}) = M_s \mathbf{m}(\mathbf{r})$, at $T \ll T_C$, the energy can be considered as a functional of the unitary vector $\mathbf{m}(\mathbf{r})$ and the minimization is performed with the constrain $|\mathbf{m}(\mathbf{r})| = 1$. The variation of the system energy (Eq. (3.22)) is given by

$$\delta E(\delta \mathbf{m}(\mathbf{r})) = \int_V \left(2A\nabla \mathbf{m} \cdot \nabla \delta \mathbf{m} + \frac{\partial f}{\partial \mathbf{m}} \delta \mathbf{m} - \mu_0 M_s \mathbf{H}_M \cdot \delta \mathbf{m} - \mu_0 M_s \mathbf{H}_a \cdot \delta \mathbf{m} \right) dV \,, \tag{3.23}$$

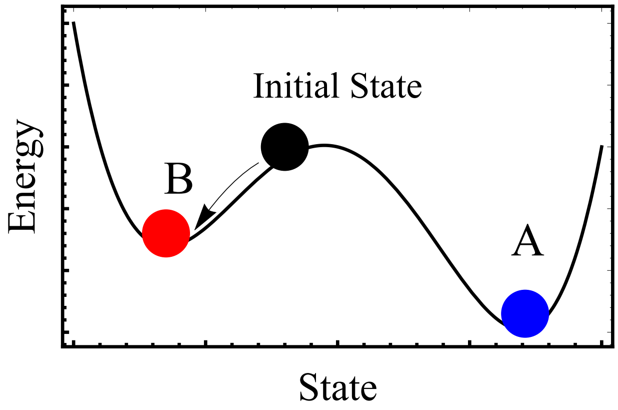

Figure 3.7: Sketch of the energy landscape between the "flower" state B and the domains state A. Despite the total energy is lower in the domains state, the system can collapse in a local minimum.

where $\nabla\mathbf{m}$ stands for $\nabla m_x + \nabla m_y + \nabla m_z$ and $\nabla\mathbf{m}\cdot\nabla\delta\mathbf{m} = \nabla m_x \cdot \nabla\delta m_x + \nabla m_y \cdot \nabla\delta m_y + \nabla m_z \cdot \nabla\delta m_z$. Additionally, we used the reciprocity theorem (see Appendix A) for the variation of the demagnetizing energy. Note, in fact, that a variation of $\mathbf{m}$ generates a change in $\mathbf{H}_M$ as well. By using the fact that $\nabla\cdot(a\mathbf{b}) = a\nabla\cdot\mathbf{b} + \mathbf{b}\cdot\nabla a$ and transforming the divergence integral into a surface integral, Eq. (3.23) can be rearranged as

$$\begin{aligned}\delta E(\delta\mathbf{m}(\mathbf{r})) &= -\int_V \left(2A\nabla\cdot(\nabla\mathbf{m}) - \frac{\partial f}{\partial\mathbf{m}} + \mu_0 M_s \mathbf{H}_M + \mu_0 M_s \mathbf{H}_a\right)\cdot\delta\mathbf{m}\; dV \\ &\quad +2\oint_S A\left(\frac{\partial\mathbf{m}}{\partial n}\cdot\delta\mathbf{m}\right)\, da \\ &= -\int_V \left(\mu_0 M_s \mathbf{H}_{\text{eff}}\cdot\delta\mathbf{m}\right)\, dV + 2\oint_S A\left(\frac{\partial\mathbf{m}}{\partial n}\cdot\delta\mathbf{m}\right)\, da \qquad (3.24)\end{aligned}$$

where the first integral is over the volume and the second over the surface of the magnetic object. $\partial\mathbf{m}/\partial n$ represents the derivative across the direction normal to the body surface and $\mathbf{H}_{\text{eff}}$ is defined as

$$\mathbf{H}_{\text{eff}} = -\frac{1}{\mu_0 M_s}\frac{\delta\mathcal{E}(\mathbf{m})}{\delta\mathbf{m}} = -\frac{1}{\mu_0 M_s}\left(\nabla\frac{\partial\mathcal{E}}{\partial(\nabla\mathbf{m})} - \frac{\partial\mathcal{E}}{\partial\mathbf{m}}\right), \qquad (3.25)$$

where $\mathcal{E}(\mathbf{m})$ is the energy density per unit of volume, namely the integrand of Eq. (3.22). Since $\delta\mathbf{m}$ must obey the constrain $|\mathbf{m}| = 1$, a generic variation $\delta\mathbf{m}$ must have the form $\delta\mathbf{m} = \mathbf{m}\times\delta\boldsymbol{\theta}$ and Eq. (3.24) can be re-written as

$$\delta E(\delta\mathbf{m}(\mathbf{r})) = -\int_V \mu_0 M_s\left(\mathbf{H}_{\text{eff}}\times\mathbf{m}\right)\cdot\delta\boldsymbol{\theta}\; dV + 2\oint_S A\left(\frac{\partial\mathbf{m}}{\partial n}\times\mathbf{m}\right)\cdot\delta\boldsymbol{\theta}\; da\,. \qquad (3.26)$$

Since the minima of the functional must satisfy the condition $\delta E = 0$ for any arbitrary variation $\delta\boldsymbol{\theta}$, Eq. (3.26) implies that equilibrium states must satisfy the following conditions:

$$\begin{aligned} \mathbf{m} \times \mathbf{H}_{\text{eff}} &= 0 \qquad \forall \mathbf{r} \in V\,, & (3.27)\\ \mathbf{m} \times \frac{\partial \mathbf{m}}{\partial n} &= 0 \qquad \forall \mathbf{r} \in S\,, & (3.28) \end{aligned}$$

which represent an important result of this chapter and state the mathematical conditions that an equilibrium configuration has to satisfy. Eq. (3.27) means that, at equilibrium, the magnetization $\mathbf{m}(\mathbf{r})$ in each elementary volume is aligned with the local field $\mathbf{H}_{\text{eff}}(\mathbf{r})$.

3.4 The Landau-Lifshitz-Gilbert equation

Eq. (3.27) and (3.28) give the conditions that must be satisfied by the system's equilibrium states but they tell us nothing about the magnetization dynamics, i.e, the temporal evolution of the magnetization towards such equilibrium. Nevertheless, Eq. (3.27) has the same form of Eq. (2.7), which was derived for a single magnetic moment in an external magnetic field. Also in that case the equilibrium corresponds to the condition $\boldsymbol{\mu} \times \mathbf{B} = 0$, when magnetic moment and applied field are aligned. However, Eq. (2.7) also describes the dynamics of the magnetic moment when it is not aligned with the field. We expect that a similar equation holds for the dynamics of the magnetization $\mathbf{m}$ of each elementary volume ΔV. The main difference is that, instead of the external field, we must use the effective field $\mathbf{H}_{\text{eff}}$. Thus, combining Eq. (3.27) and Eq. (2.7), it is possible to write for the magnetization dynamics

$$\frac{d\mathbf{m}}{dt} = -\gamma_0 \left(\mathbf{m} \times \mathbf{H}_{\text{eff}}\right)\,, \tag{3.29}$$

where $\gamma_0 = |\gamma\mu_0| = 2.21 \times 10^5$ rad $\cdot$ m $\cdot$ A^{-1} $\cdot$ s^{-1} is the gyromagnetic ratio in units of (rad $\cdot$ m $\cdot$ A^{-1} $\cdot$ s^{-1}).

As for the single magnetic moment, Eq. (3.29) predicts that the magnetization $\mathbf{m}$ precesses indefinitely around the effective field without aligning. However, in real systems, such motion is not observed and the magnetization does align along the effective field. This is because there are other mechanisms that can dissipate the magnetic energy (which would be conserved according to Eq. (3.29)). Typically, the main contribution to energy dissipation is considered to be the spin-orbit interactions which allows for energy transfer between spin and lattice system [17]. Other energy dissipation mechanisms include two magnons scattering in disordered systems and spin-pumping in ultrathin multilayers [18]. Such energy dissipation can be included phenomenologically into Eq. (3.29) by adding a damping term proportional to the rate of change of the magnetization ($\alpha d\mathbf{m}/dt$). Considering the constraint $|\mathbf{m}| = 1$, the most general damping term that it is possible to add is $\alpha(\mathbf{m} \times d\mathbf{m}/dt)$ and Eq. (3.29), augmented with an additional dissipation term, becomes

$$\frac{d\mathbf{m}}{dt} = -\gamma_0 \mathbf{m} \times \mathbf{H}_{\text{eff}} + \alpha \left(\mathbf{m} \times \frac{d\mathbf{m}}{dt} \right) , \tag{3.30}$$

where α is a phenomenological constant known as Gilbert damping. Eq. (3.30) is known as Landau-Lifshitz-Gilbert equation and it is equivalent to a previous form introduced by Landau and Lifshitz which reads like

$$\frac{d\mathbf{m}}{dt} = -\gamma_0' \mathbf{m} \times \mathbf{H}_{\text{eff}} - \alpha_{LL} \left(\mathbf{m} \times \left(\mathbf{m} \times \mathbf{H}_{\text{eff}} \right) \right) . \tag{3.31}$$

As anticipated, the two forms are equivalent upon a redefinition of the parameters. In fact, Eq.(3.30) can be transformed into the LL form by calculating explicitly the term $\mathbf{m} \times d\mathbf{m}/dt$, namely

$$\mathbf{m} \times \frac{d\mathbf{m}}{dt} = -\gamma_0 \mathbf{m} \times \left(\mathbf{m} \times \mathbf{H}_{\text{eff}} \right) - \alpha \frac{d\mathbf{m}}{dt} , \tag{3.32}$$

where we have used the fact that $\mathbf{m} \cdot (d\mathbf{m}/dt) = 0$ since $d\mathbf{m}/dt$ is perpendicular to $\mathbf{m}$. Therefore, Eq. (3.30) can be written as

$$\frac{d\mathbf{m}}{dt} = -\frac{\gamma_0}{1+\alpha^2} \mathbf{m} \times \mathbf{H}_{\text{eff}} - \frac{\gamma_0 \alpha}{1+\alpha^2} \mathbf{m} \times \left(\mathbf{m} \times \mathbf{H}_{\text{eff}} \right) . \tag{3.33}$$

Eq. (3.30) and Eq. (3.31) are equivalent by re-defining $\alpha_{LL} = \gamma_0 \alpha/(1+\alpha^2)$ and $\gamma_0' = \gamma_0/(1+\alpha^2)$. The difference in the gyromagnetic ratio is small since terms of order α^2 are usually negligible due to the fact that $\alpha \ll 1$. The first term on the RHS of Eq. (3.33) corresponds to magnetic precession while the second term represents the transverse relaxation towards the effective field. The torques affecting the magnetization vector $\mathbf{m}$ are depicted in Fig. 3.8(a). The precessional torque is perpendicular to both $\mathbf{H}_{\text{eff}}$ and $\mathbf{m}$, while the damping torque has a component along the effective field, driving the magnetization towards $\mathbf{H}_{\text{eff}}$ as sketched in Fig. 3.8(b). Eq. (3.33) represents another important result of this chapter and it will be extensively used among this thesis in order to analyse the magnetization dynamics.

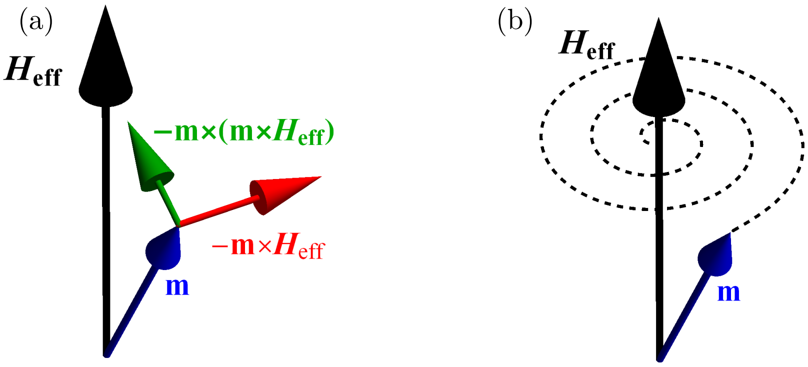

Figure 3.8: (a) Torques affecting the magnetization vector $\mathbf{m}$. (b) Magnetization dynamics due to the precessional and damping torques.

3.4.1 Length-scales

It is instructive to look at the typical length-scales of the micromagnetic theory. In particular, in micromagnetics there is a characteristic length-scale, known as **exchange length**, defined as [15]

$$l_{ex} = \sqrt{\frac{2A}{\mu_0 M_s^2}}, \qquad \text{or} \quad l_w = \sqrt{\frac{A}{K_u}}. \tag{3.34}$$

l_{ex} is the characteristic length-scale when the system is dominated by magnetostatic interaction (shape anisotropy) while l_w is the characteristic length scale when magnetocrystalline anisotropy dominates. The exchange length represents the length-scale over which magnetization changes. It originates from a competition between exchange and anisotropy energies: exchange would like to have a wide change of the magnetization in order to minimize the exchange energy (proportional to $|\nabla \mathbf{m}|^2$) but this would cost more anisotropy energy, since the domain wall (the region where the magnetization changes between two domains) is typically misaligned with the anisotropy directions (contrary to the domains). As a consequence, the magnetization varies over a length-scale which is given by the competition between these energy terms. Objects smaller than the exchange length will be most probably uniformly magnetized since they cannot host a magnetic domain wall due to their dimensions. In system where where magnetostatic and anisotropy energies are comparable, it is possible to define an effective exchange length given by

$$l_{ex} = \sqrt{\frac{A}{K_0}}\,, \tag{3.35}$$

where K_0 is an effective anisotropy which includes the magneto-crystalline and shape anisotropy contributions. More details about the calculation of the exchange length will be discussed in Section 3.9.3.

The competition between magnetostatic and anisotropy interactions can be quantified by the dimensionless parameter k defined as

$$k = \frac{2K_u}{\mu_0 M_s^2} = \frac{H_{an}}{M_s}\,. \tag{3.36}$$

If $k \geq 1$ the system is classified as an *hard* magnet, dominated by anisotropy interaction, while if $k \ll 1$ the system is classified as *soft* magnet, dominated by magnetostatic interaction and shape anisotropy.

3.4.2 Time-scales

After describing the typical length-scales, it is also interesting to look at the characteristic time-scales of Eq. (3.33). The Larmor frequency, introduced in the previous chapter for a single magnetic moment in an external field, describes the precession frequency of the magnetic moment around the effective field. It holds also for the magnetization vector $\mathbf{m}$ and it is given by $2\pi f_L = \gamma_0 H_{\text{eff}}$. In order to calculate the damping relaxation time it is convenient to assume a small displacement along the equilibrium configuration such that $\mathbf{m} = \mathbf{m}_0 + \delta\mathbf{m}$ and $\delta\mathbf{m} \perp \mathbf{m}_0$. By using Eq. (3.33) and neglecting the precessional torque, it is possible to obtain $\delta m(t) = \delta m_0 \exp{(-t/\tau)}$, where $\delta m = |\delta\mathbf{m}|$ and δm_0 is the initial displacement. The transverse relaxation time τ is given by $\tau = 2\pi(\gamma_0 \alpha m_0 H_{\text{eff}})^{-1}$. The Larmor frequency and the transverse relaxation frequency $(1/\tau)$ are plotted in Fig. 3.9 for $(0.001 < \mu_0 H < 1)$ T, which is the range of the typical magnetic fields related to the interactions described in the previous sections. The transverse relaxation is slower than the precessional dynamics and its frequency varies between 1 MHz $< f_T <$ 1 GHz for $\alpha = 0.01$, while the Larmor frequency has a range 100 MHz $< f_L <$ 100 GHz. However, the transverse relaxation depends on damping and the two frequencies coincide if $\alpha = 1$.

3.5 Spin Transfer Torque

According to the Landau-Lifshitz-Gilbert (LLG) equation, the only way to modify a magnetic state is by applying an external magnetic field. However, also electrical current can be used to excite the magnetization dynamics. This effect was firstly predicted theoretically by Berger [19] and Slonczewski [20], and, later on, it was confirmed experimentally during the last couple of decades (see Ref. [21, 22] and reference therein). The

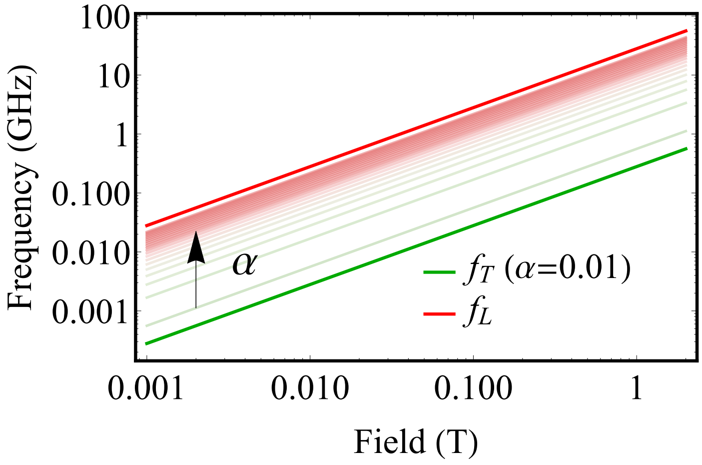

Figure 3.9: Larmor frequency f_L and transverse relaxation frequency f_T as function of the effective field. The transverse relaxation further depends on damping.

effect is known as **spin transfer torque** (STT) since it corresponds to a torque on the magnetization which is due to a transfer of angular momentum between the conduction electrons and the local magnetization.

An electrical current corresponds to a flux of electrons. Each electron carries a magnetic moment $\mu = \pm\mu_B$ that can interact with the local magnetization via exchange interaction. As a consequence, on the one hand the electrons' spin is aligned with the magnetization and the current becomes spin-polarized (namely there is also a spin-current associated with the electrical current since all the electron have the same spin alignment). On the other hand, the current affects the local magnetization when it differs from the spin-polarization direction. The effect was proposed by Slonczewski [20] and Berger [19] for different systems: Slonczewski considered a system of two uniform magnetic layers separated by a thin non magnetic layer as sketched in Fig. 3.10(a). The current is flowing perpendicular to the stack. Electrons become spin polarized in the first magnetic layer and they interact with the magnetization of the upper layer. In between, the non-magnetic spacer isolates the two magnetic layers from mutual exchange interaction. The spacer must be thin enough so that the current does not lose its spin-polarization. On the other hand, Berger considered a system in which the current is flowing in a single ferromagnetic layer with a **non-uniform** magnetization pattern as sketched in Fig. 3.10(b). Also in this case, the current gets spin polarized and the spin-polarization follows the magnetic texture, exchanging angular momentum with the local magnetization.

Despite the microscopic mechanism being the same, it is useful to divide the STT into these two kinds of torque (Slonczewski or Berger STT) since, phenomenologically, they are included into the LLG equation into different forms. The main difference between the two approaches is that in the case of Slonczewski the spin-polarization is assumed to remain fixed in the upper FM layer, while in the case of Berger it is assumed to follow the magnetization pattern.

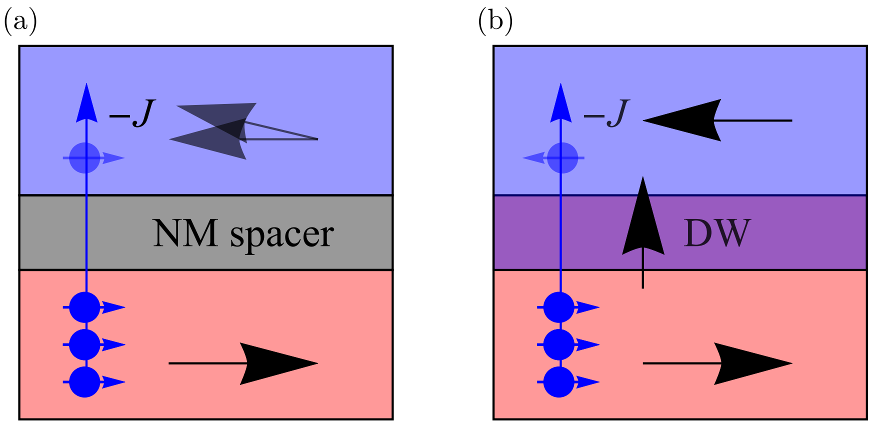

Figure 3.10: (a) Slonczewski system. (b) Berger system.

Slonczewski-like STT

More details about the microscopic description of the Slonczewski-like torque (SLT) can be found in Ref. [21, 22]. From a phenomenological point of view, it is possible to include its contribution by adding the following torque [21] to the LLG equation

$$\boldsymbol{\tau}_{SLT} = \frac{|g|}{2}\frac{\mu_B JP}{M_s|e|d}\left[\mathbf{m}\times(\mathbf{m}\times\mathbf{m}_p)\right] , \tag{3.37}$$

where J is the electrical current density, e is the electron charge and $|g|$ the g-factor introduced in the first chapter. $0 < P < 1$ represents the current polarization. $P = 1$ means that all electrons are spin-polarized. $\mathbf{m}_p$ indicates the magnetization of the fixed layer and it determines the polarization direction of the spin-current. As commented, within the Slonczewski approach, $\mathbf{m}_p$ is considered fixed. In reality, the spin-current loses its polarization as it interacts with the top layer and, therefore, its efficiency is inversely proportional to the free layer thickness d, which appears in Eq. (3.37). When transforming the LLG equation into its LL form, the SLT becomes

$$\boldsymbol{\tau}_{SLT} = \frac{|g|}{2}\frac{\mu_B JP}{M_s|e|d}\left[\mathbf{m}\times(\mathbf{m}\times\mathbf{m}_p) - \alpha\mathbf{m}\times\mathbf{m}_p\right] . \tag{3.38}$$

The SLT has the same form of the damping torque in the LLG equation and it can give rise to interesting effects. For instance, for a certain current density it will completely balance the damping torque leading to magnetic auto-oscillations. This mechanism is used indeed in spin torque nano-oscillators [23]. For large enough currents, it can efficiently switch the magnetization of the free layer as used in MRAM memories [24, 25].

Berger-like (Zhang-Li) STT

The original description of Berger, regarding the STT mechanism when an electrical current flows through a non-uniform magnetic texture, has been further extended by Zhang and Li in Ref. [26]. Other authors proposed similar forms of the STT for this case, starting from a theoretical or phenomenological approach [27, 28], which eventually can be interpreted as the Zhang-Li form. Thus, the STT within this geometry, is usually called Zhang-Li STT. More details about the microscopic mechanisms can be found in Ref. [19, 27, 26, 28]. The Zhang-Li torque (ZLT) can be included into the LLG equation by adding the following torque [26]

$$\begin{aligned}\boldsymbol{\tau}_{ZLT} &= -\frac{|g|}{2}\frac{\mu_B P}{|e|M_s(1+\xi^2)}\left\{\mathbf{m}\times[\mathbf{m}\times(\mathbf{J}\cdot\nabla)\mathbf{m}]+\xi\mathbf{m}\times(\mathbf{J}\cdot\nabla)\mathbf{m}\right\}\\ &= \frac{|g|}{2}\frac{\mu_B P}{|e|M_s(1+\xi^2)}\left\{-(\mathbf{J}\cdot\nabla)\mathbf{m}-\xi\mathbf{m}\times(\mathbf{J}\cdot\nabla)\mathbf{m}\right\}\end{aligned} \tag{3.39}$$

where we have used the fact that $\mathbf{m}\cdot(\mathbf{J}\cdot\nabla)\mathbf{m}=0$ since $|\mathbf{m}|=1$. $\mathbf{J}=\mathbf{J}(\mathbf{r},t)$ is the electrical current density, which, in general, can depend on time t and on the position $\mathbf{r}$ along the sample. ξ is the non-adiabatic factor ($0\leq\xi<1$). Following the description of Tatara et al. [27], the first term represents the transfer of angular momentum between the conduction electrons and the local magnetization. Namely it assumes that the current polarization follows adiabatically the local magnetization, exchanging its total angular momentum. The second term represents the linear momentum transfer, which considers the transfer of linear momentum between conduction electrons and the local magnetization and it accounts for the fact that the electrons polarization might not entirely follow the local magnetization. When transforming the LLG equation into the LL form, the ZLT becomes

$$\boldsymbol{\tau}_{ZLT}=\frac{|g|}{2}\frac{\mu_B P}{|e|M_s(1+\xi^2)}\left\{(1+\xi\alpha)(\mathbf{J}\cdot\nabla)\mathbf{m}+(\xi-\alpha)\mathbf{m}\times(\mathbf{J}\cdot\nabla)\mathbf{m}\right\}\,. \tag{3.40}$$

The ZLT can efficiently move a magnetic domain wall in nanostrips (see Section 3.9.3). Remarkably, the direction of motion only depends on the sign of the current. In particular, the DW moves along the direction of the electrons flow, opposite to the electrical current. This mechanism has paved the way for promising applications based on DW motion such as race-track memories [2] or DW logic devices [3].

Finally, it is important to remark that the exploitation of the STT has been possible due to significant advances in material deposition and lithography. For instance, in the Slonczewski case, it is important that the spacer is smaller than the spin-diffusion length, otherwise the current would completely lose its polarization. Also the free layer must be thin since the efficiency of the SLT depends inversely on the free layer thickness.

3.6 Ultrathin Films and Interfacial Phenomena

Further advances in material deposition introduced the possibility of creating ferromagnetic (FM) films, with a thickness t of few atomic layers, i.e, $(0.5 \leq t \leq 3)$ nm. These kind of systems are usually called **ultrathin** films. At these scales materials properties can vary significantly due to structural changes of the FM sample and/or interfacial effects due to the neighbouring layers. For instance the Curie temperature T_C or the saturation magnetization M_s can decreases significantly in ultrathin films [4]. A typical ultrathin multilayer stack is sketched in Fig. 3.11. In the previous sections the FM properties were mainly dominated by bulk effects, whereas here interfaces and neighbouring layers start playing an important role. Typical capping layers include heavy metals (HM) with large spin-orbit coupling such as Platinum (Pt), Tantalum (Ta) or Tungsten (W) or metal oxides such as Aluminium oxide ($\mathrm{AlO_x}$). Typical FM layers are Cobalt (Co) or an alloy of Cobalt-Iron-Boron (CoFeB).

Indeed, a rich variety of interfacial phenomena has been discovered over the last years and a significant research effort is now focused on these kind of systems. Their interest is twofold: on the one hand, they are interesting from a technological point of view since magnetic domain walls in this system are smaller and faster and, therefore, they could lead to smaller and faster devices. On the other hand, they are also intriguing from a theoretical point of view since they posed a series of theoretical challenges in order to understand the mechanisms responsible for the observed magnetization dynamics (chiral domain wall, domain wall motion against the electron flow, etc.). A detailed review about interfacial effects can be found in Ref. [4]. In the following, we shall introduce some of the most relevant interfacial effects. Part III of this thesis will be devoted to analysing the domain wall motion in these kind of systems.

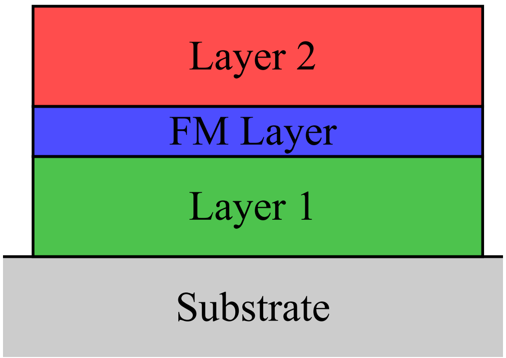

Figure 3.11: Sketch of a typical multilayer stack.

3.6.1 Surface anisotropy

An important interfacial effect is the surface anisotropy. Due to spin-orbit interaction with the neighbouring layers, the FM sample can present uniaxial anisotropy along the z direction (perpendicular to the film). Being an interfacial effect, the surface anisotropy is inversely proportional to the thickness of the FM layer. Thus, the overall uniaxial anisotropy K_u, introduced in Section 3.2.2, is given by

$$K_u = \frac{K_S}{t} + K_{MC}\,, \tag{3.41}$$

where K_S is the surface anisotropy and K_{MC} is the magneto-crystalline anisotropy, related to bulk effects. In thin films the shape anisotropy strongly favours in-plane magnetization and, therefore, the effective anisotropy (surface plus shape anisotropy) along the z direction, in the limit $K_{MC} = 0$, is given by (see also Section 3.9.3 for a calculation of the effective anisotropy):

$$K_0 = \frac{K_S}{t} - \frac{1}{2}\mu_0 M_s^2\,, \tag{3.42}$$

where the second term corresponds to the shape anisotropy due to the demagnetizing field. As a consequence, the out-of-plane magnetization (along the z axis) is stable only for small thickness, satisfying $K_0 > 0$, while, after a certain threshold, when $K_0 < 0$, the film magnetization turns in-plane. The value of $K_0 t$ as function of thickness is plotted in Fig. 3.12 for typical PMA material. When $K_0 t < 0$, the system turns in-plane. Being perpendicular to the film, this anisotropy is usually called perpendicular magnetic anisotropy (PMA). Fig. 3.12(b) and (c) show the two possible orientation of the magnetization in these systems: in-plane or out-of-plane depending on the value of K_0.

3.6.2 Dzyaloshinskii-Moriya interaction

Another important interfacial effect is the Dzyaloshinskii-Moriya interaction (DMI). This interaction was firstly proposed for bulk materials with broken inversion (crystal) symmetry. For these systems, Dzyaloshinsky firstly pointed out that the combination of spin-orbit interaction and broken inversion symmetry could give rise to an antisymmetric exchange interaction with the following energy [29, 30]

$$E_{\mathrm{DMI}} = \sum_{ij} \mathbf{D}_{ij} \cdot (\mathbf{S}_i \times \mathbf{S}_j)\,, \tag{3.43}$$

where $\mathbf{D}_{ij}$ represents the DMI vector, whose strength and direction depend on the spin-orbit coupling and the crystal symmetry. In Ref. [30] Moriya showed how to calculate the DMI vector $\mathbf{D}_{ij}$ for localized moments. In 1980, Fert and Levy mentioned that doping FM samples with high spin-orbit materials, such at Pt or Au, could lead to the presence of a significant DMI due to the scattering of conduction electron and the material impurities [31]. Later on, in 1998, Crépieux et al. showed that DMI could also

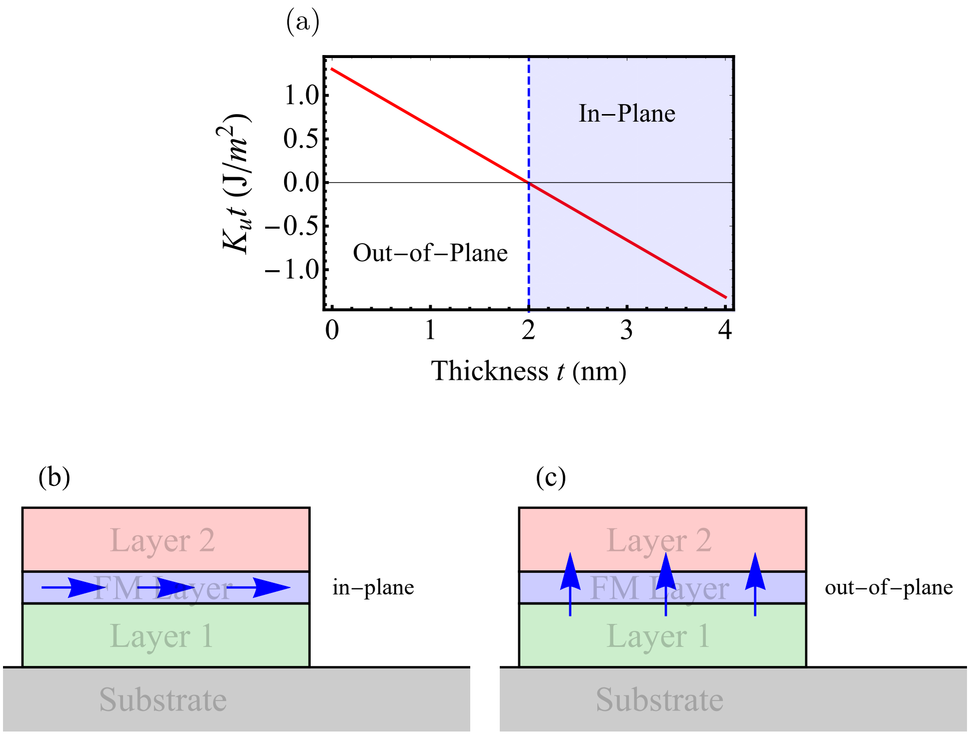

Figure 3.12: (a) $K_0 t$ as function of the FM layer thickness. Sketch of (b) in-plane magnetized system and (c) out-of-plane magnetized system.

occur in ultrathin multilayers as the one shown in Fig. 3.11 [32]. In this context, the DMI originates from the spin-orbit interaction between the atoms of the capping layers and the atoms of FM layer as sketched in Fig. 3.13. The broken symmetry is induced by placing different materials as the top and bottom layers. This kind of DMI is usually called interfacial-DMI in order to differentiate it from the bulk case. In this context [32]

$$\mathbf{D}_{ij} = D\,(\mathbf{r}_{ij} \times \hat{\mathbf{z}})\,, \tag{3.44}$$

where z is the direction of the broken symmetry, D the strength of the interfacial DMI and $\mathbf{r}_{ij}$ is the distance between the i and j spins as sketched in Fig. 3.13. In order to minimize the DMI energy, $\mathbf{S}_i \times \mathbf{S}_j$ must be parallel or anti-parallel to $\mathbf{D}_{ij}$, depending on the sign of D. Thus, the DMI promotes anti-parallel spins configurations and favours non-uniform magnetization patterns.

In the context of micromagnetics, Thiaville et al. [33], following the same approach shown for the exchange interaction in Section 3.2.1, derived the interfacial-DMI energy

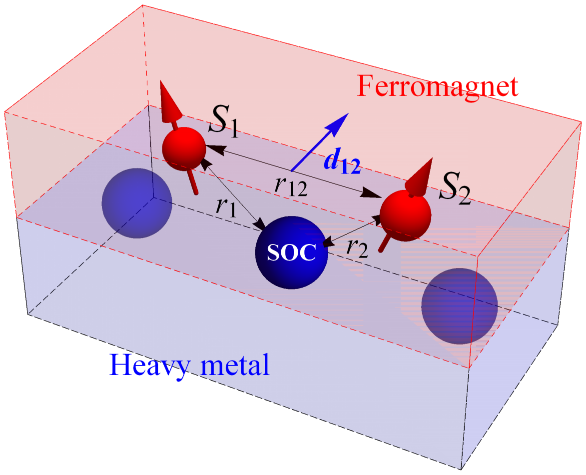

Figure 3.13: Sketch of the Dzyaloshinskii-Moriya interaction at the interface between heavy metal and ferromagnet. S_1 and S_2 represent two spins of the ferromagnetic layer, while SOC represents an atom of the HM with large spin-orbit coupling.

in a continuum approximation for ultrathin FM films, which reads like [33]

$$\begin{aligned} E_{\mathrm{DMI}} &= \int_V D\left[m_z(\nabla\cdot\mathbf{m}) - (\mathbf{m}\cdot\nabla)m_z\right]dV \\ &= D\left[\left(m_z\frac{\partial m_x}{\partial x} - m_x\frac{\partial m_z}{\partial x}\right) + \left(m_z\frac{\partial m_y}{\partial y} - m_y\frac{\partial m_z}{\partial y}\right)\right]dV\,, \end{aligned} \tag{3.45}$$

where the integral is over volume of the magnetic object. By calculating the variation $\delta E_{\mathrm{DMI}}(\delta\mathbf{m})$, it is possible to include the DMI into the LLG equation. By using again the fact that $\nabla\cdot(a\mathbf{b}) = a\nabla\cdot\mathbf{b} + \mathbf{b}\cdot\nabla a$ we obtain that

$$\begin{aligned} \delta E_{\mathrm{DMI}}(\delta\mathbf{m}) &= \int_V D\left[\delta m_z(\nabla\cdot\mathbf{m}) + m_z(\nabla\cdot\delta\mathbf{m}) - \delta\mathbf{m}\cdot\nabla m_z - \mathbf{m}\cdot\nabla\delta m_z\right]\,dV \\ &= \int_V 2D\left[\delta m_z(\nabla\cdot\mathbf{m}) - \nabla m_z\cdot\delta\mathbf{m}\right] + D\nabla\cdot(m_z\delta\mathbf{m} - \mathbf{m}\delta m_z)\,dV\,. \end{aligned} \tag{3.46}$$

Then, by transforming the volume integral into a surface integral it is possible to obtain

$$\begin{aligned}\delta E_{\mathrm{DMI}}(\delta\mathbf{m}) &= \int_V 2D\left[\delta m_z(\nabla\cdot\mathbf{m}) - \nabla m_z\cdot\delta\mathbf{m}\right]\,dV \\ &\quad + \oint_S D\left((\mathbf{m}\cdot\mathbf{u}_z)\delta\mathbf{m} - \mathbf{m}(\delta\mathbf{m}\cdot\mathbf{u}_z)\right)\cdot\mathbf{n}\,dS \\ &= \int_V \mu_0 M_s\mathbf{H}_{\mathrm{DMI}}\cdot\delta\mathbf{m}\,dV + \oint_S D\left((\mathbf{m}\cdot\mathbf{u}_z)\mathbf{n} - (\mathbf{m}\cdot\mathbf{n})\mathbf{u_z}\right)\cdot\delta\mathbf{m}\,dS \\ &= \int_V \mu_0 M_s\mathbf{H}_{\mathrm{DMI}}\cdot\delta\mathbf{m}\,dV + \oint_S D\left[\mathbf{m}\times(\mathbf{n}\times\mathbf{u}_z)\right]\cdot\delta\mathbf{m}\,dS \qquad (3.47)\end{aligned}$$

where **n** is the unitary vector, normal to the surface and

$$\begin{aligned}\mathbf{H}_{\mathrm{DMI}} &= \frac{2D}{\mu_0 M_s}\left[\nabla m_z - (\nabla\cdot\mathbf{m})\mathbf{u}_z\right] \\ &= \frac{2D}{\mu_0 M_s}\left[\frac{\partial m_z}{\partial x}\hat{\mathbf{x}} + \frac{\partial m_z}{\partial y}\hat{\mathbf{y}} - \left(\frac{\partial m_x}{\partial x} + \frac{\partial m_y}{\partial y}\right)\hat{\mathbf{z}}\right] \qquad (3.48)\end{aligned}$$

is the effective DMI field, which could have been also obtained by calculating $\delta E_{\mathrm{DM}}/\delta\mathbf{m}$ as indicated by Eq. (3.25). Nevertheless, the full variational calculus shows that DMI also affects the system boundary conditions. In fact, the surface integral (see Eq. (3.24) in Section 3.3), including the exchange contribution, now reads like

$$\oint_S \left\{2A\frac{\partial\mathbf{m}}{\partial n} + D\left[\mathbf{m}\times(\mathbf{n}\times\mathbf{u}_z)\right]\right\}\cdot\delta\mathbf{m}\,dS\,, \qquad (3.49)$$

which must be zero for an arbitrary variation of $\delta\mathbf{m}$. Hence, the new boundary conditions are given by

$$\frac{\partial\mathbf{m}}{\partial n} = \frac{D}{2A}\left[\mathbf{m}\times(\mathbf{u}_z\times\mathbf{n})\right]\,. \qquad (3.50)$$

By combining these results with Eq. (3.26), it is possible to see that the effect of DMI is the addition of the $\mathbf{H}_{\mathrm{DMI}}$ field to the previously defined effective field $\mathbf{H}_{\mathrm{eff}}$ and the modification of the boundary conditions according to Eq. (3.50).

Experimentally, several effects of the DMI have been observed in ultrathin multilayers, such as chiral domain walls [34], asymmetric bubble expansion [35, 36] or asymmetric spin waves propagations [37]. Furthermore, DMI can also favours new type of magnetization patterns such as Skyrmions [38] or helices.

3.6.3 Spin Hall effect

The spin Hall (SH) effect is a relativistic phenomenon in which a charge current is transformed into a transverse spin-current due to spin-orbit coupling [39, 40]. In ultrathin multilayers this effect can be exploited to inject a spin-current into the FM layer, which can eventually affect the magnetization dynamics through the spin transfer torque [41, 42, 43]. The SH mechanism is sketched in Fig. 3.14. In ultrathin films the

FM layer has a high resistivity due to its small thickness and, therefore, it is possible to inject electrical current mostly through the neighbouring layers. If the layers have a high spin-orbit coupling, electrons with different spins are scattered in opposite directions, leading to a spin-current perpendicular to the charge current. The spin-polarization of the spin-current will also be perpendicular to the charge current and the spin-current. For instance, the spin-current along the z direction in Fig. 3.14 is polarized along the y direction since the charge current is flowing along the x direction. More details about the microscopic origin of the SH effect and can be found in Ref. [40].

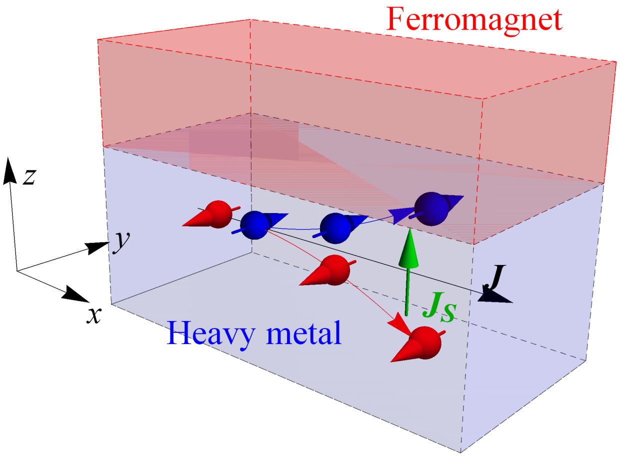

Figure 3.14: Sketch of the SH mechanism. Due to spin-orbit interactions, opposite spins are deflected in opposite directions leading to a spin-current J_S perpendicular to the charge current J.

The SH torque can be included into the LLG equation by adding the following term

$$\boldsymbol{\tau}_{SH} = \frac{|g|}{2} \frac{\mu_B J \theta_{SH}}{M_s |e| d} \left[\mathbf{m} \times (\mathbf{m} \times \boldsymbol{\sigma}) \right] , \tag{3.51}$$

where θ_{SH} is known as the SH angle, which represents the ratio between spin-current and charge current. In other words, θ_{SH} indicates how much of the charge currents is transformed into spin-current by the SH mechanism. Eq. (3.51) has the same form of Eq. (3.37), describing the Slonczewski STT, and indeed it represents the same mechanism (a torque due to a spin-current injected perpendicularly to the magnetic sample). The only differences are: (1) the amplitude of the spin-current, which now is expressed as $J\theta_{SH}$ instead of JP, and (2) the polarization of the spin-current $\boldsymbol{\sigma}$, which is now fixed by the SH mechanism. In particular $\boldsymbol{\sigma} = \hat{\mathbf{J}}_c \times \hat{\mathbf{J}}_s$, where $\hat{\mathbf{J}}_c$ indicates the direction of the charge current and $\hat{\mathbf{J}}_s$ is the direction of the spin-current. Referring to the system depicted in Fig. 3.14, $\hat{\mathbf{J}}_s = \mathbf{u}_z$ and $\hat{\mathbf{J}}_c = \mathbf{u}_x$, therefore $\boldsymbol{\sigma} = \mathbf{u}_y$. Analogously to the Slonczewski case, the SH torque in the LL formalism reads like

$$\boldsymbol{\tau}_{SH} = \frac{|g|}{2}\frac{\mu_B J\theta_{SH}}{M_s|e|d}\left[\mathbf{m}\times(\mathbf{m}\times\boldsymbol{\sigma}) - \mathbf{m}\times\boldsymbol{\sigma}\right] \, . \tag{3.52}$$

Since the spin polarization is fixed to the y direction, the SH torque is maximized when the magnetization points along the z or x direction, while it is null when the magnetization points along the y direction. For magnetic domain walls this means that the SH effect is maximum for Néel walls, whose magnetization points along the x direction, while is zero for Bloch walls, whose magnetization points along the y direction (see Section 3.9 for more details). Néel domain walls are additionally favoured by the DMI and in fact, the combination of DMI and SH effect has been shown to efficiently drive the domain walls in these systems [43]. Additionally, SH torque has been exploited for SH nano-oscillators [44] or SH induced magnetization switching [45].

3.7 Stochastic magnetization dynamics

The LLG equation, augmented with the STT contributions can describe the magnetization dynamics towards its equilibrium state. The equation is deterministic, meaning that, knowing the initial state and the applied torques, the magnetization dynamics and the final state are fully determined. However, at finite temperature, each magnetic moment fluctuates around its equilibrium position due to the thermal noise. Thermal fluctuations arise from the interaction between the magnetic moments and other microscopic degrees of freedom such as phonons or electrons, which also lead to the damping torque discussed in Sec. 3.4. Indeed, fluctuations and dissipation mechanisms are related by the fluctuation-dissipation theorem [46, 47]. Thermal noise can have an important effect on the magnetization dynamics and it has been included into the micromagnetic formalism by Brown [46]. He added a stochastic (Gaussian) magnetic field $\mathbf{H}_{\mathrm{th}}$ which has the following properties:

$$\langle H_{\mathrm{th},i}\rangle = 0 \, , \tag{3.53}$$

$$\langle H_{\mathrm{th}}(t,\mathbf{r})_i H_{\mathrm{th}}(t',\mathbf{r}')_j\rangle = 2D\ \delta_{ij}\delta(\mathbf{r}-\mathbf{r}')\delta(t-t') \, , \tag{3.54}$$

where the brackets indicates a statistical average and the i and j indexes indicate the Cartesian components of the field. Eq. (3.53) means that the mean value of the Gaussian noise is zero, as expected for thermal fluctuations. While Eq. (3.54) means that the amplitude of the fluctuations of each component of the random field are uncorrelated in time and space. An uncorrelated noise is usually called ”white” noise. Thermal fluctuations can be considered white up to frequency $\omega \sim k_B T/\hbar \sim 10$ THz [46] . Since the typical scale of magnetization dynamics is $1 - 10$ GHz (see Fig. 3.9), it is reasonable to consider the noise as white. Here D represents the amplitude of thermal fluctuations which has been calculated by a twofold approach: (1) with the fluctuation-dissipation theorem. (2) with the Fokker-Planck equation by imposing that the magnetization follows the Maxwell-Boltzmann distribution. Both approaches (see Appendix A) yields

$$D = \frac{\alpha k_B T}{(1+\alpha^2)\gamma_0 \mu_0 M_s \Delta V}\,, \tag{3.55}$$

where ΔV is the volume of the elementary cell. We recall that, in micromagnetics, ΔV cannot be arbitrary small since it must be large enough to contain a large number of magnetic moments. Below $\Delta V \sim 1$ nm^3 one should start to consider atomistic modelling [48] and the amplitude of the thermal noise changes, avoiding the divergence at $\Delta V \to 0$. The LLG equation, augmented with the stochastic field $\mathbf{H}_{\mathrm{th}}$ is also called LLG-Langevin equation. More generally, Langevin equations are dynamics equations which include stochastic terms. With the inclusion of thermal noise, the magnetization dynamics is stochastic (rather than deterministic) and observables like magnetization, energies, etc. have to be considered as averages of probability distributions.

3.8 The Landau-Lifshitz-Bloch equation

Thermal effects can be introduced as an additional random field in the LLG equation if the temperature is still well below the Curie temperature ($T \ll T_C$). In fact, in micromagnetics, as described in Sec. 3.4, the magnetization $\mathbf{M}(\mathbf{r})$ at each point represents an average over many microscopic magnetic moments and it is assumed that the time over which the magnetization of each cell reaches its equilibrium value M_s is much shorter than the typical time-scales of the LLG dynamics. Under this assumption, the magnetization can be written as $\mathbf{M} = M_s\mathbf{m}$, where M_s represents the magnetization modulus. However, this assumption breaks for T close to T_C where the dynamics of the magnetization modulus (longitudinal dynamics) slows down [49, 50] [2]. At the same time, the transverse relaxation becomes faster close to T_C [49] so that longitudinal and transverse relaxation times become comparable and it is no longer possible to neglect the longitudinal dynamics. Additionally, in experiments where the sample's temperature changes significantly, such as ultrafast optical switching [52] or heat assisted magnetic recording, the magnetization modulus M_s is no longer constant and it changes with the sample temperature. The LLG-Langevin equation seriously overestimates the Curie temperature [49] and it cannot reproduce the correct scaling of $M_s(T)$. This is because, by dividing the sample into elementary volumes ΔV, we impose a cut-off on high frequency (short wavelength) magnons which cannot be included into the modelling. More precisely, all magnons with $\lambda < 2\Delta x$ are not taken into account, where λ represents the magnon wavelength and Δx is the cell dimension along the x direction

---

[2] The increase of the longitudinal relaxation time close to T_C is a typical phenomenon of second order phase transition known as critical slowing down [51].

for instance. Hence, for high temperature, we cannot use the LLG equation and we need to find another formalism, which can include the longitudinal dynamics and the correct scaling of $M_s(T)$. A micromagnetic approach that can include these features is the Landau-Lifshitz-Bloch (LLB) equation, developed by Garanin [53] and tested against atomistic simulations [49] for the scaling of $M_s(T)$ and the longitudinal and transverse susceptibilities. The LLB equation reads like [53, 49]

$$\frac{d\mathbf{m}}{dt} = -\gamma_0(\mathbf{m}\times\mathbf{H}_{\text{eff}}) - \gamma_0\frac{\alpha_\perp}{m^2}(\mathbf{m}\times(\mathbf{m}\times\mathbf{H}_{\text{eff}})) + \gamma_0\frac{\alpha_\parallel}{m^2}(\mathbf{m}\cdot\mathbf{H}_{\text{eff}})\mathbf{m}\,, \tag{3.56}$$

where $\alpha_\perp$ and $\alpha_\parallel$ represent the perpendicular and longitudinal damping parameter respectively. Both damping parameters depend on temperature according to the following expressions [53, 49]:

$$\alpha_\perp = \alpha_0\left(1-\frac{T}{3T_C}\right)\,, \quad \alpha_\parallel = \alpha_0\left(\frac{2T}{3T_C}\right)\,, \tag{3.57}$$

where α_0 represents a microscopic damping parameter. The first two terms on the RHS of Eq. (3.56) are equivalent to the first two terms in the LLG equation (Eq. (3.33)), describing the precessional and transverse (dissipative) dynamics of the magnetization. The last term on the RHS of Eq. (3.56) (absent in the LLG formalism) describes the longitudinal relaxation dynamics and, in fact, it is parallel to $\mathbf{m}$ rather than perpendicular as the previous ones. Another difference of the LLB equation is that the modulus of the magnetization vector $m = |\mathbf{m}|$ depends on the temperature, $m = m(T)$, and it varies between $0 \leq m(T) \leq 1$, contrary to the LLG case where it is unitary ($m = 1$).

The effective field in the LLB equation is defined as

$$\mathbf{H}_{\text{eff}} = \frac{2A}{\mu_0 M_s m^2}\nabla^2\mathbf{m} + \mathbf{H}_{\text{an}} + \mathbf{H}_{\text{dmg}} + \mathbf{H}_{\text{ext}} + \begin{cases} \frac{1}{2\chi_\parallel}\left(1-\frac{m^2}{m_e^2}\right)\mathbf{m}, & T<T_C \\ -\frac{1}{\chi_\parallel}\left(1+\frac{3}{5}\frac{T_C m^2}{(T-T_C)}\right)\mathbf{m}, & T>T_C \end{cases}\,, \tag{3.58}$$

where the first term represents the exchange field (within the LLB formalism) [54, 50], while $\mathbf{H}_{\text{an}}$, $\mathbf{H}_{\text{dmg}}$ and $\mathbf{H}_{\text{ext}}$ are the anisotropy, demagnetizing and external field respectively. These fields are calculated as in the LLG formalism but taking into account that m and the material parameters (A, K_u etc.) depend on temperature. In this case M_s indicates the saturation magnetization at $T = 0$ (hence $\mathbf{M}(T) = M_s\mathbf{m}(T)$).

The last term is the "internal" exchange field and it does not appear in the LLG formalism. It represents the effect of the exchange interaction between the magnetic moments inside each elementary cell, which determines the value of $m(T)$. [3] If the modulus of the magnetization m is different from its equilibrium value $m_e(T)$, the internal

---

[3] As described in Sec. 2.4.2, the alignment of the magnetic moments inside each cell, and the corresponding value of $m(T)$, is determined by a competition between thermal agitation and exchange interaction which forces the spin alignment.

field will drive it towards its equilibrium value. The strength of the field is proportional to the longitudinal susceptibility $\tilde{\chi}_{\|}$, defined as $\tilde{\chi}_{\|} = \partial m_e / \partial H_{\text{ext}}$ in the limit $H_{\text{ext}} \to 0$, as introduced in Sec. 2.4.2. $m_e(T)$ and the corresponding susceptibility have to be introduced as parameters into the LLB equation and, typically, they are calculated by a mean-field approach (as the Weiss model) [50, 6, 7] or by atomistic simulations [55]. The results obtained by mean-field for $m_e(T)$ and $\tilde{\chi}_{\|}(T)$ are shown in Fig. 2.6.

Hence, apart from the precessional and transversal dynamics described in Section 3.4, the LLB equation takes into account also the longitudinal dynamics of the magnetization. These different dynamics are sketched in Fig. 3.15.

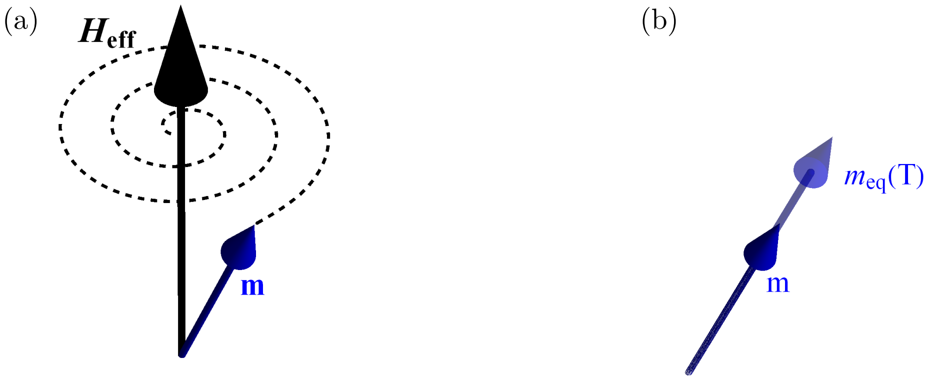

Figure 3.15: (a) Precessional and transversal dynamics. (b) Longitudinal dynamics.

The LLB equation and the internal exchange field were calculated by Garanin [53] by introducing thermal fluctuations into the the atomistic LLG equation for single spins and then using the Fokker-Planck equation to obtain the dynamics for the averaged magnetization (see Appendix B).

3.8.1 Revisiting the time-scales

The LLB equation includes the longitudinal magnetization dynamics: the relaxation of the magnetization modulus towards its equilibrium value $m_e(T)$. Fig. 3.9 of the previous section showed the typical time-scales of magnetization dynamics as described by the LLG equation. In particular, it includes the Larmor frequency (the spin precession around the effective field) and the transverse relaxation (the aligning of the spin towards the effective field). It is interesting to compare also with the longitudinal relaxation frequency ($f_{||}$), as shown in Fig. 3.16(a), which depicts the longitudinal, transverse and Larmor frequencies as function of the applied field, calculated at $T = 0.3T_C$ (room temperature for $T_C = 850$ K as in Permalloy). Analogously to the transverse frequency, the longitudinal frequency is calculated by assuming a small displacement along the magnetization direction. The effect of the applied field is neglected in the calculation since it has a negligible effect compared to the exchange field. The longitudinal frequency is much higher, $f_{||} \sim 1$ THz. This is expected since the internal exchange field is the strongest field acting on the magnetization. This is not surprising at room temperature and it simply justifies the use of LLG for $T \ll T_C$, where, indeed, longitudinal dynamics is neglected because it is assumed much faster than Larmor precession and transverse relaxation. On the other hand, Fig. 3.16(b) represents the transverse and longitudinal frequencies as function of temperature. Close to T_C the two frequencies become comparable, underlying the need of using the LLB formalism at these temperatures.

3.8.2 Spin transfer torque in the LLB equation

The spin transfer torque in the LLB equation was firstly introduced by Schieback et al. [56], neglecting terms of the second order in the damping parameter (α_0^2). This approach is motivated by the fact that it is not clear whether the spin transfer torque terms have to be added to Gilbert (LLG) or Landau-Lifshitz (LL) form of the equation of motion (see for instance Ref. [57, 58]) but, in the LLB, the two forms are equivalent neglecting terms of order α_0^2. In the LLG form the damping term is expressed in terms of the magnetization derivative, while in the LL form it is expressed in terms of the effective field. In the LLG case, the two approaches are equivalent due to the constraint on the magnetization modulus and the two forms can be recasted one into the other by simply rescaling the STT parameters. Note that, also in the absence of STT, the Gilbert and LL forms are exactly equivalent only neglecting terms of the second order in magnetic damping (typically small). However, for the LLB case, there are two main complications: (1) the LLB is derived originally in the LL form, with the transverse relaxation expressed in terms of the effective field, and it is not clear whether it can be transformed into the LLG form since above T_C second order terms can be significant due to their temperature dependence. (2) For the LLB, the Gilbert and LL forms of the STT are different since there are no constraint on the magnetization modulus. Nevertheless, the differences are of the second order in the damping parameter and, for $T < T_C$, where such terms can be neglected, the two approaches coincides upon a redefinition of the parameters. In the following, we shall transform the LLB equation with STT into its Gilbert form, showing the differences between the LL and Gilbert expressions. Finally, we show that the two different approaches are equals if we neglect terms of the second order in the damping

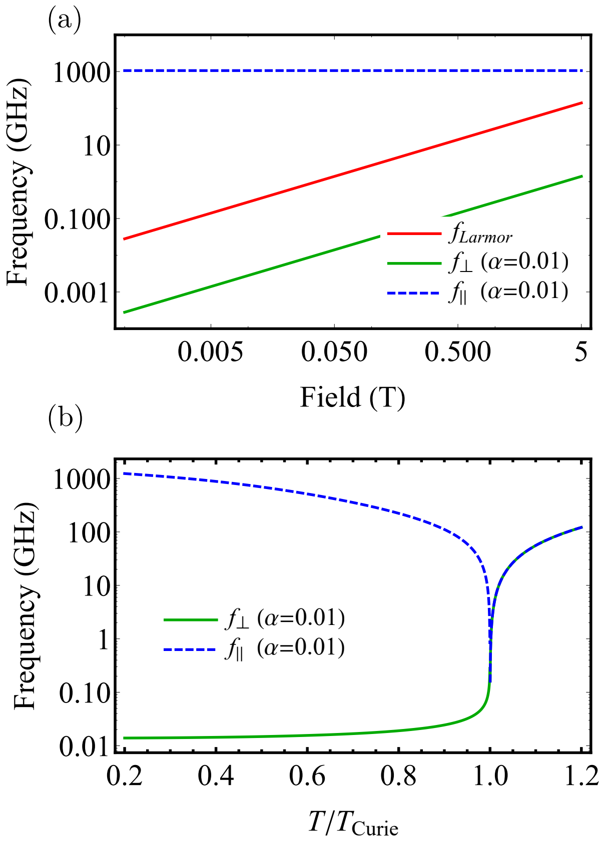

Figure 3.16: (a) Characteristic frequency of the magnetization dynamics as function of the applied field. Larmor frequency (f_{Larmor}), transverse ($f_\perp$) and longitudinal relaxation ($f_\parallel$). (b) Transverse and longitudinal frequency as function of temperature.

parameter. The LLB equation, augmented with the STT terms, reads like [56]

$$\begin{aligned} \frac{d\mathbf{m}}{dt} &= -\gamma_0(\mathbf{m}\times\mathbf{H}_{\text{eff}}) - \gamma_0\frac{\alpha_\perp}{m^2}(\mathbf{m}\times(\mathbf{m}\times\mathbf{H}_{\text{eff}})) + \gamma_0\frac{\alpha_\parallel}{m^2}(\mathbf{m}\cdot\mathbf{H}_{\text{eff}})\mathbf{m}\,, \\ & -u(\mathbf{J}\cdot\nabla)\mathbf{m} + \frac{u}{m}\xi_{LL}\mathbf{m}\times(\mathbf{J}\cdot\nabla)\mathbf{m}\,, \end{aligned} \tag{3.59}$$

where u stands for the same pre-factor already appearing in Section 3.5, namely

$$u = \frac{|g|}{2}\frac{\mu_B P}{|e|M_s(1+\xi^2)}\,. \tag{3.60}$$

The same expression, in the Gilbert version, reads like

$$\begin{aligned} \frac{d\mathbf{m}}{dt} &= -\gamma_0(\mathbf{m}\times\mathbf{H}_{\text{eff}}) - \frac{\alpha_\perp}{m^2}\left(\mathbf{m}\times\frac{d\mathbf{m}}{dt}\right) + \gamma_0\frac{\alpha_\parallel}{m^2}(\mathbf{m}\cdot\mathbf{H}_{\text{eff}})\mathbf{m}\,, \\ & -u(\mathbf{J}\cdot\nabla)\mathbf{m} + \frac{u}{m}\xi\mathbf{m}\times(\mathbf{J}\cdot\nabla)\mathbf{m}\,, \end{aligned} \tag{3.61}$$

which, transformed into the LL forms, gives

$$\begin{aligned}\frac{d\mathbf{m}}{dt} &= -\frac{\gamma_0}{1+\tilde{\alpha}_\perp^2}(\mathbf{m}\times\mathbf{H}_{\text{eff}}) - \frac{\gamma_0\tilde{\alpha}_\perp}{(1+\tilde{\alpha}_\perp^2)m}\left[\mathbf{m}\times(\mathbf{m}\times\mathbf{H}_{\text{eff}})\right] + \gamma_0\frac{\alpha_\parallel}{m^2}(\mathbf{m}\cdot\mathbf{H}_{\text{eff}})\mathbf{m}\,,\\ &\quad -\frac{1}{1+\tilde{\alpha}_\perp^2}\left[u(1+\tilde{\alpha}_\perp\xi)(\mathbf{J}\cdot\nabla)\mathbf{m} - \frac{u}{m}(\xi-\tilde{\alpha}_\perp)\mathbf{m}\times(\mathbf{J}\cdot\nabla)\mathbf{m}\right]\\ &\quad +\frac{1}{1+\tilde{\alpha}_\perp^2}\frac{u}{m^2}\tilde{\alpha}_\perp\left(\xi-\tilde{\alpha}_\perp\right)\left[\mathbf{m}\cdot(\mathbf{J}\cdot\nabla)\mathbf{m}\right]\mathbf{m}\,, \end{aligned} \tag{3.62}$$

where $\tilde{\alpha}_\perp = \alpha_\perp/m$. It is possible to check that, if we neglect terms of order $\tilde{\alpha}_\perp^2$ and $\tilde{\alpha}_\perp\xi$, which are typically small for $T < T_C$, Eq. (3.59) and Eq. (3.62) coincide upon the redefinition $\xi_{LL} = \xi - \tilde{\alpha}_\perp$. Note that, in the LLB, where there is no constraint on the magnetization modulus, the adiabatic STT presents a longitudinal term along the direction of $\mathbf{m}$.

A more rigorous approach to include the STT into the LLB formalism would be to start from the atomistic LLG equation augmented with STT and follow the same procedure of Garanin for the standard LLB (see Appendix B). Nevertheless, in Chapter 5, we will use the LLB equation augmented with STT both including and neglecting 2nd order terms. The results are consistent within the two approaches. However, in that case, this is also because the Joule heating contribution is dominant and second order terms of the STT play a minor role.

3.8.3 Stochastic LLB

The LLB equation includes the effect of temperature within the temperature dependence of the micromagnetic parameters. In this sense, the microscopic thermal fluctuations are already included (and averaged) into the LLB. Nevertheless, at high temperature, fluctuations of individual magnetization vectors (around their mean value) are important and thermal noise needs to be introduced explicitly. The stochastic LLB equation, introduced by Evans et al. [59], reads like

$$\begin{aligned}\frac{d\mathbf{m}}{dt} &= -\gamma_0(\mathbf{m}\times\mathbf{H}_{\text{eff}}) - \gamma_0\frac{\alpha_\perp}{m^2}\left[\mathbf{m}\times\left[\mathbf{m}\times(\mathbf{H}_{\text{eff}}+\mathbf{H}_{\text{th}}^\perp)\right]\right]\\ &\quad +\gamma_0\frac{\alpha_\parallel}{m^2}(\mathbf{m}\cdot\mathbf{H}_{\text{eff}})\mathbf{m} + \mathbf{H}_{\text{th}}^\parallel\,, \end{aligned} \tag{3.63}$$

where $\mathbf{H}_{\text{th}}^\perp$ and $\mathbf{H}_{\text{th}}^\parallel$ are random fields [4] with (white noise) properties:

$$\langle H_{\text{th,i}}^{\perp,\parallel}\rangle = 0\,, \tag{3.64}$$

$$\langle H_{\text{th}}^\perp(t,\mathbf{r})_i H_{\text{th}}^\perp(t',\mathbf{r}')_j\rangle = \frac{2k_BT(\alpha_\perp-\alpha_\parallel)}{\gamma_0\mu_0M_sV\alpha_\perp^2}\delta_{ij}\delta(\mathbf{r}-\mathbf{r}')\delta(t-t')\,, \tag{3.65}$$

$$\langle H_{\text{th}}^\parallel(t,\mathbf{r})_i H_{\text{th}}^\parallel(t',\mathbf{r}')_j\rangle = \frac{2k_BT\alpha_\parallel\gamma_0}{\mu_0M_sV}\delta_{ij}\delta(\mathbf{r}-\mathbf{r}')\delta(t-t')\,. \tag{3.66}$$

---

[4] In reality $\mathbf{H}_{\text{th}}^\parallel$ is not a field since it has units of (1/s). However we keep the notation for convenience.

The amplitude of the noise is calculated as described in Section 3.7 and Appendix A, that is, by calculating the Fokker-Planck equation corresponding to Eq. (3.63) and imposing the Maxwell-Boltzmann distribution as an equilibrium solution of the system.

As described in Appendix B, in order to obtain the LLB equation, one needs to add thermal fluctuations into the atomistic LLG equation and eventually calculate the average magnetization to finally get the LLB equation. Thus, one might wonder whether we are counting two times the same fluctuations. The answer is yes and no. As discussed in the previous sections, thermal fluctuations in the macroscopic LLG (or LLB) do not include magnons with wavelength smaller than $2\Delta x$, where Δx is the dimension of the elementary volume cell, which eventually becomes the dimension of the computational cell (see Chapter 4). On the other hand, when including thermal fluctuations into the atomistic LLG (which are eventually included into the temperature dependence of the micromagnetic parameters) we include all magnons. Thus, we are including the fluctuations two times. However, the main contribution to the temperature dependence of the micromagnetic parameters is given by high frequency magnons [14], which are not included into the thermal noise. Therefore, we could say that magnons with wavelength smaller than the cell size are included into the temperature dependence of the micromagnetic parameters, while magnons with wavelength larger than the cell size are included explicitly by thermal fluctuations. More advanced descriptions can avoid any overlapping by calculating the temperature dependence of the micromagnetic parameters directly from atomistic simulations of the elementary cell [55].

3.9 Magnetic domain wall

In the previous sections we have presented the different equations used to analyse the magnetization dynamics at low or high temperatures (LLG and LLB equations). Furthermore, the different contributions to the magnetization dynamics have been introduced: the effective field and the spin transfer torques. These equations are general and they can describe the dynamics of arbitrary magnetic patterns.

We shall now present some specific magnetic configurations which will be extensively analysed in this thesis: **magnetic domain walls (DWs)**. As anticipated in Section 3.1, a DW represents the boundary between two different magnetic domains. The DW structure depends primarily on the type of system that we are considering. In this thesis we will consider films (or nano-wires) as the one sketched in Fig. 3.11. Depending on the thickness of the FM layer and on the neighbouring layers, the magnetization lies along the plane of the film (in-plane systems) or perpendicularly to the film (out-of-plane systems), as sketched in Fig. 3.12(b) and (c). In-plane structures and out-of-plane structures have different types of DW.

3.9.1 Magnetic domain walls in in-plane magnetized strip

Part II of this thesis will be devoted to the study of DW motion in Permalloy (Py) nano-strips. Py is an alloy of Iron (Fe) and Nickel (Ni) where the magnetization lies in-plane, along the main axis of the nano-strip, since it has a negligible magneto-crystalline anisotropy and it is dominated by shape anisotropy. Typically, the width (w) of such nano-strips ranges in between 50nm $< w < 1$ μm, while the thickness (t) varies in between 5nm $< t <$ 30 nm.

In nano-strips with in-plane magnetization it is possible to observe two types of DW: transverse walls as the one sketched in Fig. 3.17(a), where the magnetization points along the y direction, and vortex walls as the one represented in Fig. 3.17(b), where the magnetization forms a vortex-like pattern. The boundaries of the transverse wall form an angle of 45° with the domains, since in this way $\nabla \cdot \mathbf{M} = 0$ and the magnetostatic energy is minimized. A system can have transverse wall or vortex wall, depending on its cross section. In fact, as the thickness and the width of the strip increase, the magnetostatic energy of a transverse wall increases and, at a certain point, the system prefers vortex wall, reducing magnetostatic energy but with a penalty in exchange energy. A typical phase diagram is shown in Fig. 3.18.

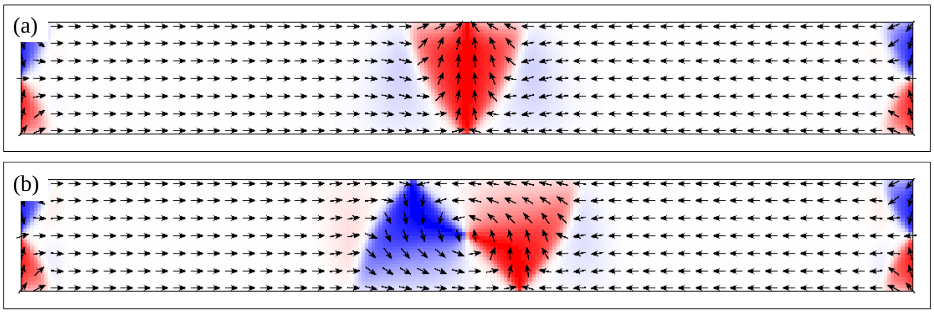

Figure 3.17: (a) Transverse wall. (b) Vortex wall.

3.9.2 Magnetic domain walls in out-of-plane magnetized strip

In part III of this thesis we will analyse the DW dynamics in out-of-plane magnetized systems as the one described in Section 3.6. Similarly to the case of in-plane samples, also in these systems there are two kind of DWs. Néel DWs, shown in Fig. 3.19(a), where the magnetization points along the x direction inside the DW, and Bloch DWs, shown in Fig. 3.19(b), where the magnetization points along the y direction inside the DW. From a magnetostatic point of view, Néel DWs do not generate surface charges since the magnetization is parallel to the surface at the strip edges. However, they generate volume charges since $\nabla \cdot \mathbf{M} \neq 0$. On the other hand, Bloch DWs do not generate volume charges since $\nabla \cdot \mathbf{M} = 0$ but they generate surface charges at the edges, where the magnetization is perpendicular to the surface. As a consequence, Néel or Bloch DWs are stabilized depending on the strip cross-section: stripes with larger widths have more volume charges, which increase the energy of Néel walls and favour Bloch walls. For typical ultrathin films, if the width is larger than 30-50 nm Bloch DWs are more stable

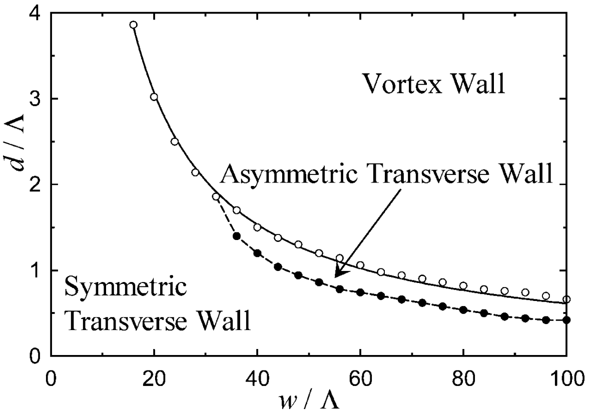

Figure 3.18: Domain wall phase diagram as function of the sample width (w) and thickness (d), normalized to the exchange length Λ. Figure taken from Ref. [60]. Vortex walls are favoured for large strip widths or thickness. Asymmetric transverse walls represent a particular kind of transverse walls slightly tilted along the x direction [60].

than Néel DWs. A characteristic phase diagram between Bloch and Néel walls can be found in Ref. [61].

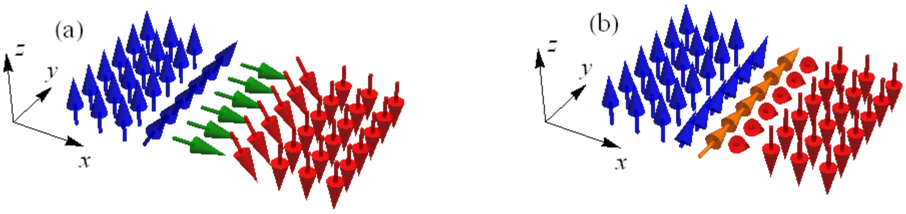

Figure 3.19: (a) Néel domain wall. (b) Bloch domain wall.

Chiral domain walls

However, the DMI, introduced in Section 3.6.2, can stabilize Néel DWs with fixed chirality even in strips where the demagnetizing energy would favour Bloch DWs. Fixed chirality means that the magnetization rotates always in the same directions when passing from up to down and from down to up domains. For instance, for a given DMI all the DWs between up and down domains will point along the positive x direction, while all the DWs between down and up domains will point oppositely along the negative

x direction. Conventionally we can call this chirality as right-handed chirality. If we invert the sign of the DMI all the DWs will switch their orientation and they will have left-handed chirality. [5] A sketch of DWs with fixed chirality is shown in Fig. 3.20. The sense of rotation between up-down domains and down-up domains is always fixed. In Section 3.9.3 we will give more insights into the different types of DWs in out-of-plane structures and we will show how the demagnetizing and DMI energies affect their static configuration.

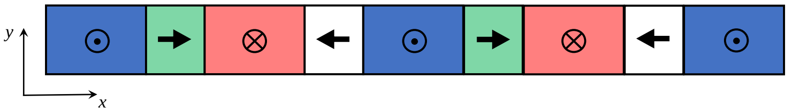

Figure 3.20: Sketch of DW chirality.

3.9.3 Collective Coordinate model and Domain Wall dynamics

In the context of DW motion, a useful tool is the Collective-Coordinates (CC) model, which rearrange the LLG equation in terms of the DW position q, internal angle φ and DW width Δ. This procedure implies an assumption on the magnetization profile, which is assumed to follow a one-dimensional DW solution. In developing the CC model, it is convenient to write the LLG Eq. (3.33) in spherical coordinates. As done in Section 3.2.2, we write the magnetization as $\mathbf{m} = (\sin\theta\cos\phi, \sin\theta\sin\phi, \cos\theta)$, where the angles θ and ϕ are defined in Fig. 3.5(a). In spherical coordinates, the LLG equations read like

$$\dot{\theta} + \alpha\sin\theta\dot{\phi} = -\frac{\gamma_0}{\mu_0 M_s \sin\theta}\frac{\delta\mathcal{E}}{\delta\phi}\,, \tag{3.67}$$

$$\alpha\dot{\theta} - \sin\theta\dot{\phi} = -\frac{\gamma_0}{\mu_0 M_s}\frac{\delta\mathcal{E}}{\delta\theta}\,, \tag{3.68}$$

---

[5] The convention to associate right-handed chirality to positive DMI ($D > 0$) and left-handed chirality to negative DMI ($D < 0$) is purely arbitrary.

where $\mathcal{E}$ is the energy density of the system, i.e., the integrand of Eq. (3.22). The different energy densities in polar coordinates can be expressed as

$$\begin{aligned}
\mathcal{E}_{\text{exch}} &= A(\nabla\mathbf{m})^2 = A\left[(\nabla\theta)^2 + \sin^2\theta(\nabla\phi)^2\right] , & (3.69)\\
\mathcal{E}_{\text{an}} &= K_u[1-(\mathbf{m}\cdot\hat{\mathbf{u}}_z)^2] = K_u\sin^2\theta\,, & (3.70)\\
\mathcal{E}_{\text{dmg}} &= -\frac{1}{2}\mu_0 M_s\mathbf{m}\cdot\mathbf{H}_{\text{dmg}} = -\frac{1}{2}\mu_0 M_s^2\mathbf{m}\cdot\bar{\bar{N}}\mathbf{m} & \\
&= -\frac{1}{2}\mu_0 M_s^2(N_x m_x^2 + N_y m_y^2 + N_z m_z^2) & \\
&= -\frac{1}{2}\mu_0 M_s^2[N_z + (N_x - N_z)\sin^2\theta + (N_y - N_x)\sin^2\theta\sin^2\phi]\,, & (3.71)\\
\mathcal{E}_{\text{DMI}} &= D\left[\cos\phi\frac{\partial\theta}{\partial x} + \sin\phi\frac{\partial\theta}{\partial y} + \sin\theta\cos\theta\left(\sin\phi\frac{\partial\phi}{\partial x} - \cos\phi\frac{\partial\phi}{\partial y}\right)\right] , & (3.72)\\
\mathcal{E}_{\text{a}} &= -\mu_0 M_s(H_x\sin\theta\cos\phi + H_y\sin\theta\sin\phi + H_z\cos\theta)\,. & (3.73)
\end{aligned}$$

In calculating these terms we have assumed a uniaxial anisotropy along the z direction and we have neglected the demagnetizing interaction between different spins. In fact, the CC model consider a local demagnetizing field, $\mathbf{H}_{\text{dmg}} = \bar{\bar{N}}\mathbf{m}$, where $\bar{\bar{N}}$ is the demagnetizing tensor which is assumed diagonal (see Section 3.2.3). The demagnetizing and magneto-crystalline anisotropies are usually combined in an effective anisotropy energy, which reads like

$$\mathcal{E}_{\text{dmg}} + \mathcal{E}_{\text{an}} = \overbrace{\left[K_u + \frac{1}{2}\mu_0 M_s^2(N_x - N_z)\right]}^{K_0}\sin^2\theta + \overbrace{\left[\frac{1}{2}\mu_0 M_s^2(N_y - N_x)\right]}^{K}\sin^2\theta\sin^2\phi\,, \tag{3.74}$$

where the constant term $(1/2)\mu_0 M_s^2 N_z$ has been neglected since it does not affects the system. The demagnetizing factors $N_{x,y,z}$ depend exclusively on the system geometry. To calculate their value, the CC model assumes a three domain model as sketched in Fig. 3.21. For an ultrathin films $N_z \sim 1$ and $N_z \gg N_x, N_y$. These latter factors are relevant only in the the DW (where the magnetization lays in-plane) and they can be calculated analytically for the central domain as function of the strip width (w), the DW width (Δ) and the strip thickness (t) [62]. The effective anisotropy K_0 is usually defined as $K_0 = K_u - (1/2)\mu_0 M_s^2$ (see Section 3.6.1). K is the DW shape anisotropy and, in the absence of DMI, it determines the stable DW configuration between Bloch or Néel, depending on the sign of $(N_y - N_x)$. If $N_y > N_x$, $K > 0$ and the DW shape anisotropy favours Néel walls, while if $N_y < N_x$, $K < 0$ and Bloch walls are favoured.

The magnetization profile of a DW in a system with out-of-plane magnetization, can be described by the following ansatz [13]

$$\begin{aligned}
\theta(x,t) &= 2\arctan\left\{\exp\left[Q\left(\frac{x-q(t)}{\Delta}\right)\right]\right\} , & (3.75)\\
\phi(x,t) &= \varphi(t)\,, & (3.76)
\end{aligned}$$

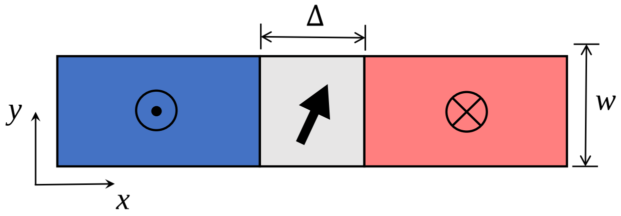

Figure 3.21: Three domains assumption to calculate the demagnetizing factors.

where q is the DW position, φ is the DW internal angle and Δ is the DW width, as sketched in Fig. 3.22(a). The parameter Q selects if the domain configuration is up-down ($Q = 1$) or down-up ($Q = -1$). Fig. 3.22 represents an up-down configuration. Eq. (3.75) and (3.76) depend only on the x coordinate along the nano-wire. In this sense, the CC model is a one-dimensional (1D) model since the variation of the magnetization along the z and y directions are neglected. [6] Fig. 3.22(b) shows the magnetization profile defined by Eq. (3.75) and (3.76) with $q = 0$, $\Delta = 5$ nm and $\varphi = \pi/2$. The DW width parameter is outlined in blue. The total extension of the DW is given by $\int \sin\theta dx = \pi\Delta$, which is outlined in red. By using this ansatz, we have that

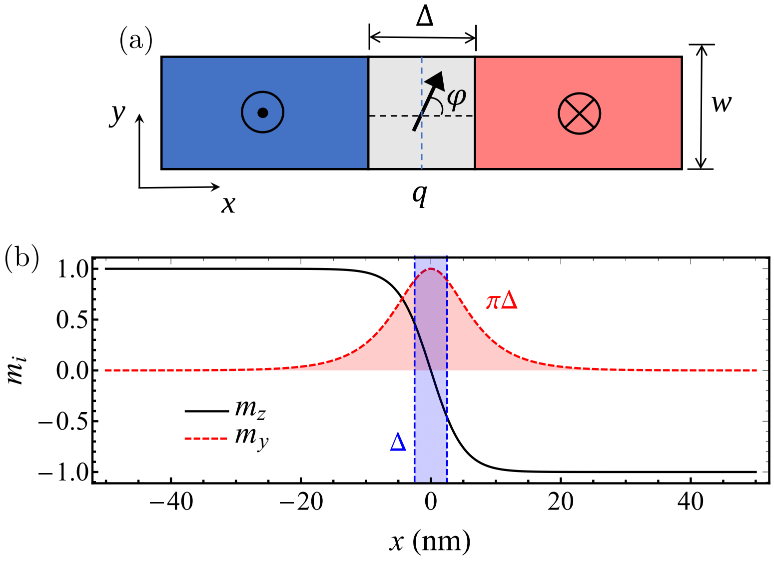

Figure 3.22: (a) Sketch of the collective coordinates related to the DW dynamics. The position q, the internal angle φ and the DW width Δ. (b) 1D model profile. $m_z = \cos\theta$ and $m_y = \sin\theta \sin\varphi$ with $\varphi = \pi/2$.

---

[6] The same profile can be used for a DW in in-plane systems by redefining the magnetization coordinates as $\mathbf{m} = (\cos\theta, \sin\theta\cos\phi, \sin\theta\sin\phi)$.

$$\begin{aligned}
\nabla\theta &= \frac{\partial\theta}{\partial x} = Q\frac{\sin\theta}{\Delta}\,, \qquad \nabla\phi = \nabla\varphi = 0\,, && (3.77)\\
\delta\theta &= -Q\left[\frac{\sin\theta}{\Delta}dq + \frac{\sin\theta(x-q)}{\Delta^2}\delta\Delta\right]\,, \qquad \delta\phi = \delta\varphi && (3.78)\\
\dot\theta &= -Q\left[\frac{\sin\theta}{\Delta}\dot q + \frac{\sin\theta(x-q)}{\Delta^2}\dot\Delta\right]\,, \qquad \dot\phi = \dot\varphi\,. && (3.79)
\end{aligned}$$

At the same time, the energy density of the system becomes

$$\begin{aligned}
\mathcal{E} &= A\left(\frac{\partial\theta}{\partial x}\right)^2 + K_0\sin^2\theta + K\sin^2\theta\sin^2\phi + D\cos\phi\left(\frac{\partial\theta}{\partial x}\right)\\
&\quad -\mu_0 M_s(H_x\sin\theta\cos\phi + H_y\sin\theta\sin\phi + H_z\cos\theta)\\
&= A\frac{\sin^2\theta}{\Delta^2} + K_0\sin^2\theta + K\sin^2\theta\sin^2\phi + QD\cos\phi\frac{\sin\theta}{\Delta}\\
&\quad -\mu_0 M_s(H_x\sin\theta\cos\phi + H_y\sin\theta\sin\phi + H_z\cos\theta)\,, && (3.80)
\end{aligned}$$

where we used the fact that $Q^2 = 1$. By integrating the energy density along the x direction, it is possible to obtain the DW surface energy density σ (J/m^2) in terms of the DW coordinates (q, φ, Δ), namely

$$\begin{aligned}
\sigma &= \int_{-\infty}^{\infty}\mathcal{E}dx\\
&= \frac{2A}{\Delta} + 2\Delta(K_0 + K\sin^2\varphi) + \pi QD\cos\varphi - \mu_0 M_s\pi\Delta(H_x\cos\varphi + H_y\sin\varphi)\\
&\quad -2Q\mu_0 M_s q H_z\,, && (3.81)
\end{aligned}$$

where we have used the fact that, according to Eq. (3.75)

$$\int_{-\infty}^{\infty}dx = \int_0^{\pi}\frac{\Delta}{\sin\theta}d\theta\,. \qquad (3.82)$$

Hence, the variation of the DW energy density, in terms of DW coordinates, reads like

$$\delta\sigma = \frac{\partial\sigma}{\partial q}\delta q + \frac{\partial\sigma}{\partial\varphi}\delta\varphi + \frac{\partial\sigma}{\partial\Delta}\delta\Delta\,, \qquad (3.83)$$

where

$$\begin{aligned}
\frac{\partial\sigma}{\partial q} &= -2Q\mu_0 M_s H_z\,, && (3.84)\\
\frac{\partial\sigma}{\partial\varphi} &= 4\Delta K\sin\varphi\cos\varphi - \pi QD\sin\varphi - \mu_0 M_s\pi\Delta(H_y\cos\varphi - H_x\sin\varphi)\,, && (3.85)\\
\frac{\partial\sigma}{\partial\Delta} &= -\frac{2A}{\Delta^2} + 2(K_0 + K\sin^2\varphi) - \mu_0 M_s\pi(H_x\cos\varphi + H_y\sin\varphi)\,. && (3.86)
\end{aligned}$$

At the same time, by using the LLG equations (3.67) and (3.68) we have that [63]

$$\begin{aligned}
\delta\mathcal{E} &= \frac{\partial\mathcal{E}}{\partial\theta}\delta\theta + \frac{\partial\mathcal{E}}{\partial\phi}\delta\phi \\
&= \frac{\mu_0 M_s}{\gamma_0}\left[(\sin\theta\dot{\phi} - \alpha\dot{\theta})\delta\theta - \sin\theta(\dot{\theta} + \alpha\sin\theta\dot{\phi})\delta\phi\right] \\
&= \frac{\mu_0 M_s}{\gamma_0}\left\{\left[\sin\theta\dot{\varphi} - \alpha Q\left(-\frac{\sin\theta}{\Delta}\dot{q} - \frac{\sin\theta(x-q)}{\Delta^2}\dot{\Delta}\right)\right] Q\left(-\frac{\sin\theta}{\Delta}\delta q - \frac{\sin\theta(x-q)}{\Delta^2}\delta\Delta\right)\right. \\
&\quad \left. - \sin\theta\left[Q\left(-\frac{\sin\theta}{\Delta}\dot{q} - \frac{\sin\theta(x-q)}{\Delta^2}\dot{\Delta}\right) + \alpha\sin\theta\dot{\varphi}\right]\delta\varphi\right\} \\
&= -\frac{\mu_0 M_s}{\gamma_0}\left(\frac{\sin^2\theta}{\Delta}Q\dot{\varphi} + \alpha\frac{\sin^2\theta}{\Delta^2}\dot{q} + \frac{\sin^2\theta(x-q)}{\Delta^3}\dot{\Delta}\right)\delta q \\
&\quad -\frac{\mu_0 M_s}{\gamma_0}\left(\frac{\sin^2\theta(x-q)}{\Delta^2}Q\dot{\varphi} + \alpha\frac{\sin^2\theta(x-q)}{\Delta^3}\dot{q} + \alpha\frac{\sin^2\theta(x-q)^2}{\Delta^4}\dot{\Delta}\right)\delta\Delta \\
&\quad +\frac{\mu_0 M_s}{\gamma_0}\left(\frac{\sin^2\theta}{\Delta}Q\dot{q} + \frac{\sin^2\theta(x-q)}{\Delta^2}Q\dot{\Delta} - \alpha\sin^2\theta\dot{\varphi}\right)\delta\varphi\,,
\end{aligned} \tag{3.87}$$

where we have used the relations (3.77), (3.78) and (3.79). Also in this case, we can obtain the variation of the energy in terms of the DW coordinates by integrating Eq. (3.87) along the x direction, obtaining [63]

$$\delta\sigma = -\frac{2\mu_0 M_s}{\gamma_0}\left(Q\dot{\varphi} + \alpha\frac{\dot{q}}{\Delta}\right)\delta q + \frac{2\mu_0 M_s}{\gamma_0}(Q\dot{q} - \Delta\alpha\dot{\varphi})\delta\varphi - \frac{2\mu_0\alpha M_s}{\gamma_0}\frac{\pi^2}{12}\frac{\dot{\Delta}}{\Delta}\delta\Delta\,, \tag{3.88}$$

where we have used the fact that (see also Appendix C)

$$\int_{-\infty}^{\infty}\sin^2\theta(x-q)dx = 0 \quad \text{and} \quad \int_{-\infty}^{\infty}\frac{\sin^2\theta}{\Delta^2}(x-q)^2 = \frac{\pi^2}{6}\,. \tag{3.89}$$

Finally, by comparing Eq. (3.83) and Eq. (3.88), we obtain [63]

$$\left(Q\dot{\varphi} + \alpha\frac{\dot{q}}{\Delta}\right) = \gamma_0 Q H_z\,, \tag{3.90}$$

$$\left(Q\frac{\dot{q}}{\Delta} - \alpha\dot{\varphi}\right) = \gamma_0\frac{2K}{\mu_0 M_s}\sin\varphi\cos\varphi - \frac{\pi}{2}\frac{QD}{\mu_0 M_s\Delta}\sin\varphi - \frac{\pi}{2}(H_y\cos\varphi - H_x\sin\varphi)\,, \tag{3.91}$$

$$\dot{\Delta} = \frac{12\gamma_0}{\mu_0 M_s\alpha\pi^2}\left[\frac{A}{\Delta} - \Delta(K_0 + K\sin^2\varphi) + \mu_0 M_s\Delta\frac{\pi}{2}(H_x\cos\varphi + H_y\sin\varphi)\right]\,, \tag{3.92}$$

which are obtained directly from the LLG equation using the ansatz (3.75) [63]. In order to separate $\dot{q}$ and $\dot{\varphi}$, Eq. (3.90) and (3.91) can be rearranged as

$$\dot{q} = \frac{\Delta\gamma_0}{1+\alpha^2}\left[\alpha Q H_z + Q H_K \frac{\sin 2\varphi}{2} - \frac{\pi}{2} H_{\mathrm{DMI}} \sin\varphi - Q\frac{\pi}{2}(H_y \cos\varphi - H_x \sin\varphi)\right], \tag{3.93}$$

$$\dot{\varphi} = \frac{\gamma_0}{1+\alpha^2}\left[H_z - \alpha\left(H_K \frac{\sin 2\varphi}{2} - Q\frac{\pi}{2} H_{\mathrm{DMI}} \sin\varphi - \frac{\pi}{2}(H_y \cos\varphi - H_x \sin\varphi)\right)\right]. \tag{3.94}$$

Eq. (3.93), (3.94) and (3.92) describe the dynamics of the DW coordinates (q, φ, Δ) as function of the applied field $\mathbf{H} = (H_x, H_y, H_z)$. Note that the accuracy of the results depends on the accuracy of the anstaz (3.75).

An alternative approach to derive the CC model equations is to use a Lagrangian approach, firstly introduced by Döring to obtain the LLG equation [64]. Within this approach the DW profile is directly introduced into the Lagrangian and the CC equations are directly derived by the Euler-Lagrange equations, considerably simplifying the mathematical derivation (see Appendix C).

3.9.4 Domain wall static configurations

Before looking at the DW dynamics, it is interesting to analyse the DW static configurations. The DW energy is given by

$$\sigma = \frac{2A}{\Delta} + 2\Delta(K_0 + K\sin^2\varphi) + \pi Q D\cos\varphi - \mu_0 M_s \pi\Delta(H_x\cos\varphi + H_y\sin\varphi). \tag{3.95}$$

For simplicity, we start by neglecting the effect of an external field ($H_{x,y} = 0$). Under such assumption, the DW energy becomes

$$\sigma = \frac{2A}{\Delta} + 2\Delta(K_0 + K\sin^2\varphi) + \pi Q D\cos\varphi. \tag{3.96}$$

The static DW configuration (φ_0, Δ_0) must satisfy the conditions

$$\frac{\partial\sigma}{\partial\Delta} = 0, \qquad \frac{\partial\sigma}{\partial\varphi} = 0, \tag{3.97}$$

which yield

$$\frac{\partial\sigma}{\partial\Delta} = -\frac{2A}{\Delta_0^2} + 2(K_0 + K\sin^2\varphi) = 0 \Rightarrow \Delta_0 = \sqrt{\frac{A}{K_0 + K\sin^2\varphi}}, \tag{3.98}$$

$$\begin{aligned}\frac{\partial\sigma}{\partial\varphi} &= \sin\varphi_0(4\Delta K\cos\varphi_0 - \pi Q D) = 0 \Rightarrow \\ &\Rightarrow \varphi_0 = \begin{cases} 0 & |\pi D| > |4\Delta K|, \quad QD < 0 \\ \pi & |\pi D| > |4\Delta K|, \quad QD > 0 \\ \arccos\left(\frac{\pi Q D}{4\Delta K}\right) & |\pi D| < |4\Delta K| \end{cases}.\end{aligned} \tag{3.99}$$

In Eq. (3.98) we can recognize the exchange length, introduced in Section 3.4.1. In fact, typically $K_0 \gg K$ and $\Delta_0 \sim \sqrt{A/K_0}$. In the absence of magneto-crystalline or surface anisotropy, the shape anisotropy can be estimated as $K_0 \sim (1/2)\mu_0 M_s^2$ and Δ_0 reduces to the exchange length for soft-samples (where magnetostatic interactions dominate over magntocrytalline anisotropy). On the other hand, if $K_u \gg (1/2)\mu_0 M_s^2$, $\Delta_0 \sim \sqrt{A/K_u}$. In this context, the meaning of the exchange length becomes more clear. It represents the DW width parameter which indicates the length-scale over which the magnetization changes between two domains. As it can be deduced from Eq. (3.96), the DW width is given by a competition between the exchange energy, which would like to have a wider DW, and the shape and magneto-crystalline anisotropies which would like to have a narrow DW.

Regarding the equilibrium angle φ_0, in the absence of DMI Eq. (3.99) would becomes $4\Delta K \cos\varphi_0 \sin\varphi_0$ and $\varphi_0 = n\pi$ or $\varphi_0 = n(\pi/2)$, with $n = 0, 1, ..,$ depending on the sign of $K = (1/2)\mu_0 M_s^2(N_y - N_x)$. Typically, for ultrathin films, $N_y < N_x$ and $K < 0$, which favours Bloch DWs with $\varphi_0 = n(\pi/2)$. On the other hand, DMI favours Néel DWs if $\pi D > 4\Delta K$. Note that the sign of the DMI and the domain configuration (Q) fix the DW chirality, as anticipated in Section 3.6.2. The equilibrium angle φ_0 as function of DMI parameter D is plotted in Fig. (3.23) for $Q = 1$.

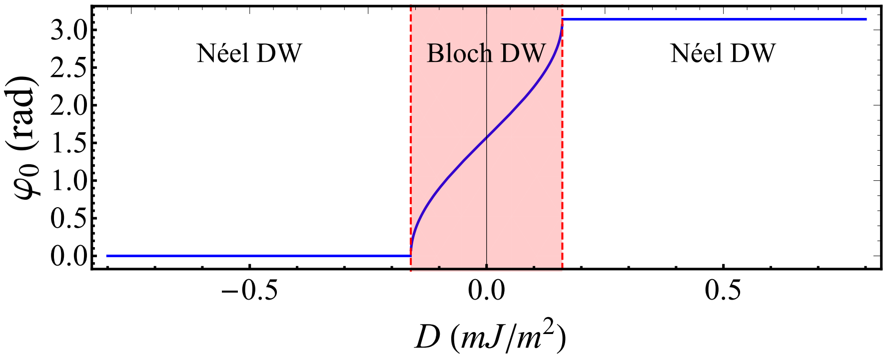

Figure 3.23: DW equilibrium angle φ_0 as function of the DMI constant D for $Q = 1$.

3.9.5 Field driven domain wall dynamics

After describing the DW static configurations, we analyse the DW dynamics. Henceforth we shall assume $Q = 1$. For simplicity, the DW width is considered as static ($\dot{\Delta} = 0$, $\Delta = \Delta_0 = \sqrt{A/K_0}$). By imposing the condition $\dot{\Delta} = 0$ in Eq. (3.92), we obtain $\Delta = \sqrt{A/(K_0 + K\sin^2\varphi)}$, as also calculated from Eq. (3.97). Hence, if the DW angle φ varies with time, also the DW width oscillates. However, since usually $K_0 \gg K$, the variation is negligible and the DW width can be considered as constant.

DWs can be moved by several means. The conventional way is by an external magnetic field along the direction of a neighbouring domain. As described in Section 3.2.4, the Zeeman energy, related to the external field, favours magnetic configurations parallel to the applied field. Hence, the domains aligned with the field will tend to expand while the domains opposite to the field will shrink. The DW will move accordingly. As described in the previous sections, the magnetization is driven by two kind of torques: the precessional torque, which leads to the spins precession along the effective field, and the dissipative torque (damping-like torque), which leads to the spins alignment along the effective field. Consider for instance an out-of-plane sample with a Néel DW, whose magnetization points along the positive x direction, as the one sketched in Fig. 3.19(a), and an external field along the positive z direction. The precession torque $(-\gamma_0 \mathbf{m}_{\mathrm{DW}} \times \mathbf{H}_z)$ points along the positive y direction leading to a DW rotation in the plane of the film. On the other hand, the dissipative torque $(-\gamma_0 \alpha \mathbf{m}_{\mathrm{DW}} \times (\mathbf{m}_{\mathrm{DW}} \times \mathbf{H}_z))$ points along the positive z direction, leading to DW motion and the expansion of the positive domain. Note indeed, that it is the damping-like torque that does not conserve the system energy and drive the system towards the energy minimum. The DW rotation further triggers the DW internal field, which includes shape H_K and DMI H_{DMI} fields, which both will try to restore the DW equilibrium configuration. Hence, DW motion is characterized by two kinds of motion: the DW precession and the DW translation.

All these effects are enclosed in Eq. (3.93) and (3.94), describing the dynamics of the DW position and internal angle. From Eq. (3.94), we can look for a stationary solution for the DW angle. By imposing $\dot{\varphi} = 0$, we obtain

$$\dot{\varphi} = 0 \Rightarrow H_z = \alpha(H_K \frac{\sin 2\varphi}{2} - \frac{\pi}{2} H_{\mathrm{DMI}} \sin\varphi)\,. \tag{3.100}$$

In the absence of DMI ($H_{\mathrm{DMI}} = 0$)

$$H_z = \alpha(H_K \frac{\sin 2\varphi}{2}) \Rightarrow \sin 2\varphi^* = \frac{2H_z}{\alpha H_K}\,, \tag{3.101}$$

where φ^* represents a dynamical equilibrium angle, which is the result of a compensation between the external field and the shape anisotropy field. As a consequence, the DW moves at constant velocity, given by

$$\dot{q} \quad = \quad \frac{\Delta\gamma_0}{\alpha} H_z\,. \tag{3.102}$$

However, there is a limit to this rigid motion since $\sin\varphi^* < 1$, which implies that

$$\left|\frac{2H_z}{\alpha H_K}\right| \leq 1 \Rightarrow |H_z| \leq \left|\frac{\alpha}{2} H_K\right|\,. \tag{3.103}$$

This limiting field is usually called Walker Breakdown (H_W). After H_W the precessional torque cannot be compensated by the internal field and the DW internal angle precesses constantly during the DW motion. Due to this precessional motion, the DW velocity drops drastically after the H_W.

On the other hand, in the limit $H_{\mathrm{DMI}} \gg H_K$, we obtain for the equilibrium angle

$$H_z = -\alpha \frac{\pi}{2} H_{\mathrm{DMI}} \sin\varphi \Rightarrow \sin\varphi^* = -\frac{2H_z}{\alpha\pi H_{\mathrm{DMI}}}, \tag{3.104}$$

and the DW velocity is still given by Eq. (3.102). Nevertheless, the Walker Breakdown is now given by

$$\left|\frac{2H_z}{\alpha\pi H_{\mathrm{DMI}}}\right| \leq 1 \Rightarrow |H_w| = \left|\alpha\frac{\pi}{2}H_{\mathrm{DMI}}\right|. \tag{3.105}$$

Since the DMI field (H_{DMI}) can be much larger than the shape anisotropy field (H_K), the DMI can lead to considerably faster DW motion by increasing the Walker Breakdown field. The field driven DW dynamics is plotted in Fig. 3.24. Fig. 3.24(a) shows the DW velocity as function of the applied field for $D = 0$ and $D = 0.5$ mJ/m^2. The presence of DMI significantly increases the Walker Breakdown and, consequently, the DW velocity. Fig. 3.24 (b) represents the DW internal angle displacement ($\Delta\varphi$), normalized to $\pi/2$. $\pi/2$ represents a limiting equilibrium angle in the presence of DMI. After $\pi/2$, the DW starts precessing. In the absence of DMI the limiting angle is $\varphi = \pi/4$. The limiting equilibrium angle is shown in the inset of Fig. 3.24(b).

3.9.6 Spin transfer torques and current driven domain wall dynamics

Another way to move DWs is by electrical currents due to the STT effect. As commented in Sec. 3.5, the STT is related to the exchange interaction between the conduction electrons and the local magnetization. The main advantage over field driven motion is that neighbouring DWs can be displaced in the same direction. In the following, we will add the STT contributions to the CC model equations.

Zhang-Li spin transfer torque

The LLG equation in spherical coordinates, augmented with the Zhang-Li STT contribution (see Section 3.5), reads like

$$\begin{aligned}
\dot{\theta} + \alpha\sin\theta\dot{\phi} &= -\frac{\gamma_0}{\mu_0 M_s \sin\theta}\frac{\delta\mathcal{E}}{\delta\phi} - u\left[(\mathbf{J}\cdot\nabla)\theta + \xi\sin\theta(\mathbf{J}\cdot\nabla)\varphi\right], && (3.106)\\
\alpha\dot{\theta} - \sin\theta\dot{\phi} &= -\frac{\gamma_0}{\mu_0 M_s}\frac{\delta\mathcal{E}}{\delta\theta} - u\left[\xi(\mathbf{J}\cdot\nabla)\theta - \sin\theta(\mathbf{J}\cdot\nabla)\varphi\right], && (3.107)
\end{aligned}$$

where

$$u = \frac{|g|}{2}\frac{\mu_B P}{|e| M_s (1+\xi^2)}, \tag{3.108}$$

and ξ is the non-adiabatic STT. By following the same procedure of the previous section (using the ansatz (3.75) and integrating along the x coordinate) we can obtain the CC

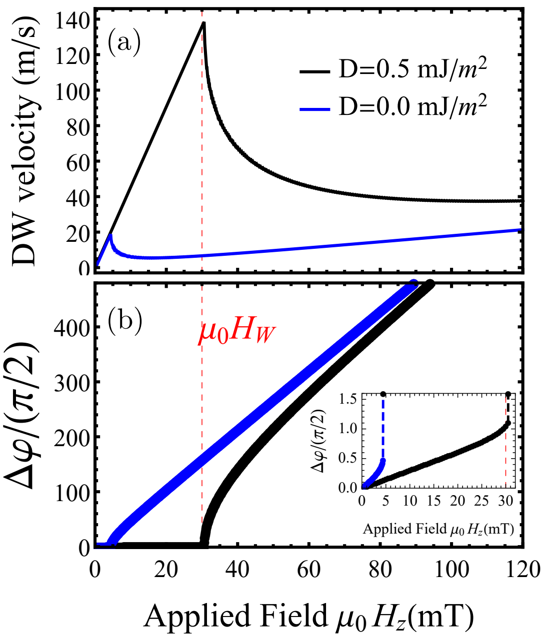

Figure 3.24: (a) DW velocity as function of the applied field for $D = 0$ and $D = 0.5\ \mathrm{mJ/m^2}$. (b) DW internal angle as function of the applied field for $D = 0$ and $D = 0.5\ \mathrm{mJ/m^2}$. As the applied field increases, the internal angle approaches a limiting equilibrium angle, $\varphi = \pi/2$ for $D = 0.5\ \mathrm{mJ/m^2}$ and $\varphi = \pi/4$ for $D = 0$, as shown in the inset. After H_W the DW starts precessing.

equations including the STT contributions, namely

$$\begin{aligned} \left(Q\dot{\varphi} + \alpha\frac{\dot{q}}{\Delta}\right) &= \gamma_0 Q H_z + \xi\frac{uJ_x}{\Delta}, \qquad (3.109) \\ \left(Q\frac{\dot{q}}{\Delta} - \alpha\dot{\varphi}\right) &= \gamma_0\frac{2K}{\mu_0 M_s}\sin\varphi\cos\varphi - \frac{\pi}{2}\frac{QD}{\mu_0 M_s \Delta}\sin\varphi - \frac{\pi}{2}(H_y\cos\varphi - H_x\sin\varphi) \\ &\quad + Q\frac{u}{\Delta}, \qquad (3.110) \end{aligned}$$

or, equivalently

$$\begin{aligned}
\dot{q} &= \frac{\Delta\gamma_0}{1+\alpha^2}\left[\alpha Q H_z + Q H_K \frac{\sin 2\varphi}{2} - \frac{\pi}{2} H_{\mathrm{DMI}} \sin\varphi - Q\frac{\pi}{2}(H_y \cos\varphi - H_x \sin\varphi)\right] \\
&\quad + \frac{1}{1+\alpha^2} u J_x (1+\xi\alpha)\,, \qquad (3.111) \\
\dot{\varphi} &= \frac{\gamma_0}{1+\alpha^2}\left[H_z - \alpha\left(H_K \frac{\sin 2\varphi}{2} - Q\frac{\pi}{2} H_{\mathrm{DMI}} \sin\varphi - \frac{\pi}{2}(H_y \cos\varphi - H_x \sin\varphi)\right)\right] \\
&\quad + \frac{Q}{1+\alpha^2}\frac{u J_x}{\Delta}(\alpha - \xi)\,. \qquad (3.112)
\end{aligned}$$

The DW dynamics as predicted by Eq. (3.111) and (3.112) is plotted in Fig. 3.25(a)-(b), as function of the current density and different non-adiabatic parameters. The polarization of the current is set to $P = 0.4$ and the domain configuration is $Q = 1$. For $\xi = 0$ the DW does not move until a critical current density J_C, which can be calculated analogously to the WB by imposing that $\dot{\varphi} = 0$. For $\xi = \alpha$ the STT contribution in Eq. (3.112) vanishes and the DW moves rigidly, independently on current density. For $\xi = 2\alpha$ the DW moves even at low current densities but it shows a WB behaviour at the critical current density J_C. Below J_C the DW moves rigidly also for $\xi = 0$ and $\xi = 2\alpha$. In these cases, analogously to the field driven dynamics, the internal equilibrium angle increases as the current approaches J_C (not visible in the scale of Fig. 3.25 (b)). Note that for positive currents ($J_x > 0$), the DW velocities are always negative, i.e., along the electrons flow. If $Q = -1$ the direction of the DW motion does not change as it only depends on the sign of the current.

Spin Hall effect

Following the same strategy, it is possible to add the Slonczewski-like STT. In the context of DW motion in ultrathin films, the Slonczewski-like STT is typically due to the spin Hall (SH) effect, as described in Section (3.6). Hence, it is convenient to add directly the SH contribution (note that the difference is simply in the pre-factor). The LLG equation in spherical coordinates, augmented with the SH term, reads like

$$\begin{aligned}
\dot{\theta} + \alpha \sin\theta\dot{\phi} &= -\frac{\gamma_0}{\mu_0 M_s \sin\theta}\frac{\delta\mathcal{E}}{\delta\phi} - cJ_x^{\mathrm{HM}} \cos\theta \sin\theta \sin\phi\,, \qquad (3.113) \\
\alpha\dot{\theta} - \sin\theta\dot{\phi} &= -\frac{\gamma_0}{\mu_0 M_s}\frac{\delta\mathcal{E}}{\delta\theta} - cJ_x^{\mathrm{HM}} \cos\phi\,, \qquad (3.114)
\end{aligned}$$

where we have considered that the spin-current polarization is $\boldsymbol{\sigma} = \hat{\mathbf{u}}_y$, as in the SH case. J_x^{HM} indicates the current density in the heavy metal under layer, which is responsible for the perpendicular spin-current (see Section 3.6). The pre-factor c is given by

$$c = \frac{|g|}{2}\frac{\mu_B \theta_{SH}}{M_s |e| d}\,. \qquad (3.115)$$

Also in this case, by following the same procedure and integrating along the x direction we obtain

$$\begin{aligned}
\left(Q\dot{\varphi}+\alpha\frac{\dot{q}}{\Delta}\right) &= \gamma_0 Q H_z+\xi\frac{uJ_x}{\Delta}+Q\frac{\pi}{2}cJ_x^{\mathrm{HM}}\cos\varphi\,, && (3.116)\\
\left(Q\frac{\dot{q}}{\Delta}-\alpha\dot{\varphi}\right) &= \gamma_0\frac{2K}{\mu_0 M_s}\sin\varphi\cos\varphi-\frac{\pi}{2}\frac{QD}{\mu_0 M_s\Delta}\sin\varphi-\frac{\pi}{2}(H_y\cos\varphi-H_x\sin\varphi)\\
&\quad +Q\frac{u}{\Delta}\,, && (3.117)
\end{aligned}$$

or, equivalently

$$\begin{aligned}
\dot{q} &= \frac{\Delta\gamma_0}{1+\alpha^2}\left[\alpha Q H_z+QH_K\frac{\sin 2\varphi}{2}-\frac{\pi}{2}H_{\mathrm{DMI}}\sin\varphi-Q\frac{\pi}{2}(H_y\cos\varphi-H_x\sin\varphi)\right]\\
&\quad +\frac{1}{1+\alpha^2}bJ_x(1+\xi\alpha)-\frac{\alpha}{1+\alpha^2}Q\Delta\frac{\pi}{2}cJ_x^{\mathrm{HM}}\cos\varphi\,, && (3.118)\\
\dot{\varphi} &= \frac{\gamma_0}{1+\alpha^2}\left[H_z-\alpha\left(H_K\frac{\sin 2\varphi}{2}-Q\frac{\pi}{2}H_{\mathrm{DMI}}\sin\varphi-\frac{\pi}{2}(H_y\cos\varphi-H_x\sin\varphi)\right)\right]\\
&\quad +\frac{Q}{1+\alpha^2}\frac{bJ_x}{\Delta}(\alpha-\xi)-\frac{1}{1+\alpha^2}\frac{\pi}{2}cJ_x^{\mathrm{HM}}\cos\varphi\,. && (3.119)
\end{aligned}$$

The DW dynamics, as predicted by Eq. (3.118) and (3.119) is plotted in Fig. 3.25 (c)-(d) for $Q=1$. Note that, the SH torque has no effect if $\varphi=n\pi/2$, since the DW is already aligned with the spin-polarization. Hence, the DW needs to be a Néel DW in order to be efficiently displaced by the SH effect. Depending on the current density, the DW reaches a new equilibrium state where the DW internal angle and velocity are given by

$$\varphi^*=\arctan\left(\frac{Q}{\alpha}\frac{H_{\mathrm{SH}}}{H_{\mathrm{DMI}}}\right)\qquad v_{\mathrm{DW}}=-\gamma_0\frac{\pi}{2}H_{\mathrm{DMI}}\sin\varphi^*\,, \tag{3.120}$$

where $H_{\mathrm{SH}}=cJ_x^{\mathrm{HM}}/\gamma_0$. As the equilibrium angle approaches $\pi/2$, the efficiency of the SH torque is reduced. Eventually, the DW approaches a limiting velocity v_d, which only depends on the DMI field [33], namely

$$v_d=-\gamma_0\Delta\frac{\pi}{2}H_{\mathrm{DMI}}\,. \tag{3.121}$$

Note that the velocity is positive (opposite to the electrons flow). In general, the sign of the velocity depends on the SH angle and the DMI.

Recent experiments [42, 65] suggested the presence of an additional field-like (FL) torque, generated by the SH effect or Rashba effect [66, 40] at the interface. This effect can be included phenomenologically into the LLG equation by an additional in-plane field along the y direction [67]. In fact, the torque that must be added to the LLG equation is $\boldsymbol{\tau}_{FL}=-\gamma_0\mathbf{m}\times\mathbf{H}_{FL}$ (as an additional external field), where $\mathbf{H}_{FL}=H_{FL}^0\hat{\boldsymbol{\sigma}}$ [66, 42, 67]. H_{FL}^0 and $\hat{\boldsymbol{\sigma}}$ are given by

$$H_{FL}^0=\frac{\alpha_R P}{\mu_0\mu_B M_s}\,,\qquad \hat{\boldsymbol{\sigma}}=\hat{\mathbf{u}}_z\times\hat{\mathbf{J}}_c\,, \tag{3.122}$$

where α_R quantifies the strength of the Rashba spin-orbit coupling [66, 67] and $\hat{\mathbf{J}}_c$ is the direction of the charge current. In our case, being $\hat{\mathbf{J}}_c = \hat{\mathbf{u}}_x$, $\hat{\boldsymbol{\sigma}} = \hat{\mathbf{u}}_y$. Therefore the FL torque can be included into the CC model equations by simply substituting [67]

$$H_y = \frac{\alpha_R P}{\mu_0 \mu_B M_s} \, . \tag{3.123}$$

The results of this section have been calculated using the material parameters summarized in Table 3.1. The thickness of the sample is 0.8nm.

A (J/m)	$\mathrm{M_s}$ (A/m)	$\mathrm{K_u}$ (J/m^3)	K (J/m^3)	α	D (J/m^2)	θ_{SH}
17×10^{-12}	1.03×10^{6}	1.3×10^{6}	2.3×10^{5}	0.2	0.5×10^{-3}	0.1

Table 3.1: Material parameters used in the CC model.

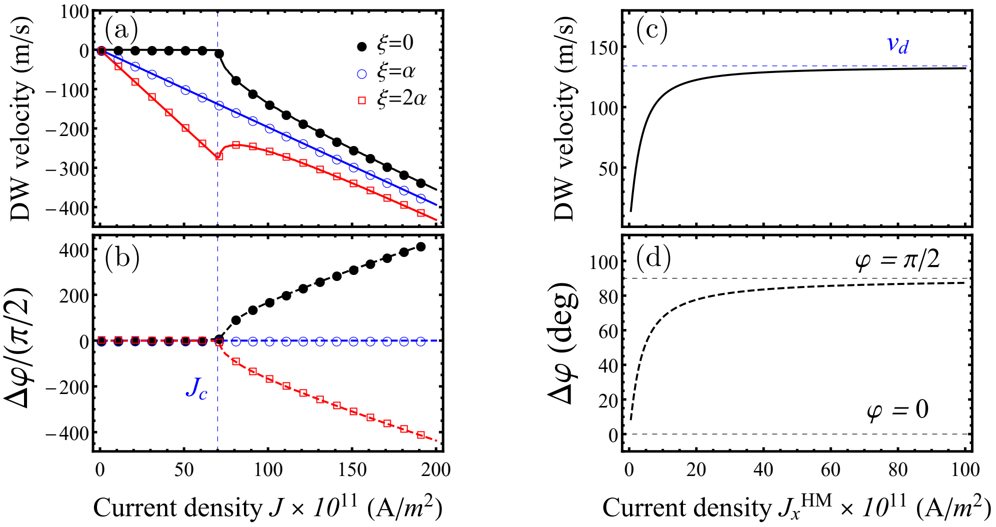

Figure 3.25: DW velocity (a) and internal angle (b) as function of current density for different non-adiabatic parameters, as predicted by Eq. (3.111) and (3.112). DW velocity (c) and internal angle (d) as function of current density (in the heavy metal), as predicted by Eq. (3.118) and (3.119). All data are for an up-down domain configuration ($Q = 1$).

To summarize, in this section we have analysed the DW dynamics by means of the CC model. We saw that DWs can be moved by external magnetic fields and by spin-currents. It is important to remember that the accuracy of the CC model, is intrinsically related to the DW profile (3.75). In real systems, the presence of disorder can lead to more complex DW structures which cannot be described by Eq. (3.75). The CC model can give significant insights about the average behaviour of the DW but full micromagnetic simulations remain essential to explore the global DW dynamics, without assuming a predetermined solution.

Chapter 4

Numerical aspects

This chapter presents the implementation of the micromagnetic code, used to solve numerically the Landau-Lifshitz-Gilbert and Landau-Lifshitz-Bloch equations. We will describe the implementation of the different torques and we will present conventional numerical methods used to solve differential equations. The code is designed to run on graphics processing units, which allow faster computations. Finally, the code will be tested against standard micromagnetic problems and compared to existing codes.

4.1 Micromagnetic code

Both the Landau-Lifshitz-Gilbert (LLG) and Landau-Lifshitz-Bloch (LLB) equations are non-linear and non-local (due to the long-range demagnetizing field) differential equations. Hence, an analytical solution is often impossible to achieve and one needs to solve the LLG and LLB numerically. In this chapter we present the numerical implementation of the LLB equation but the same approach is used for the LLG. Differences between the two implementations will be described when present.

The first step is the spacial discretization. Numerically, we cannot deal with a continuous function but we need to have a discrete set of elements. Hence, the continuous function $\mathbf{m}(\mathbf{r})$ is transformed into an array $\mathbf{m} = \{\mathbf{m}_1, \mathbf{m}_2, ..., \mathbf{m}_N\}$ by sample discretization. Each element corresponds to a certain spatial coordinate and N is the total number of elements. Numerical approaches can be classified into two main categories: **finite-difference** methods, where the system is discretized into a mesh of rectangular cells, or **finite-element** methods, where the system is discretized with elements of arbitrary shapes. Finite-difference methods have the advantages of easy-implementation and, in this case, an efficient evaluation of the demagnetizing field (see FFT method in Section 4.1). The main disadvantage is that a finite-difference meshing is not very accurate in the presence of curved surfaces, which can be better reproduced by a finite-element meshing. Our code uses a finite-difference approach. The discretization is shown in Fig. 4.1. For convenience, the array is organized in a 3-dimensional array with indexes $\{i, j, k\}$, which reflect the spacial coordinates $\{x, y, z\}$. Within this approach the total number of elements N is given by $N = N_x \times N_y \times N_z$, where $N_{x,y,z}$ represents the number of cells along each direction. $N_{x,y,z}$ are given by $N_{x,y,z} = L_{x,y,z}/\Delta_{x,y,z}$, where $L_{x,y,z}$ is the sample dimension along a certain direction and $\Delta_{x,y,z}$ is the corresponding cell dimension. $N_{x,y,z}$ must be integer numbers, meaning that the cell size must be a sub-multiple of the sample size.

$$\boldsymbol{\mu}_i \to \mathbf{m}(\mathbf{r}) \to \mathbf{m}_i$$

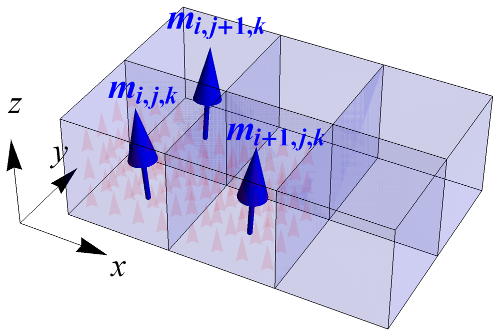

Figure 4.1: Finite-difference discretization scheme.

Furthermore, care needs to be taken in choosing the cell size in order to describe the magnetization dynamics with the required accuracy. In fact, the magnetization of each cell is described by a single vector and it represents an average value. Thus, we want the magnetization of the single cell to be uniform in order to not lose relevant information. A natural choice is the exchange length which describes the spacial length-scale at which the magnetization changes, as commented in Section 3.4. Thus the cell size has to satisfy the following condition:

$$\Delta_{x,y,z} \leq \mathrm{Min}\{l_{\mathrm{ex}}, l_{\mathrm{w}}\}\,, \tag{4.1}$$

where we recall that

$$l_{\mathrm{ex}} = \sqrt{\frac{2A}{\mu_0 M_s}}\,, \quad l_{\mathrm{w}} = \sqrt{\frac{A}{K_u}}\,, \tag{4.2}$$

or, in systems where shape and magneto-crystalline anisotropy are comparable

$$l_{\mathrm{ex}} = \sqrt{\frac{A}{K_0}}\,. \tag{4.3}$$

Below the exchange length the magnetization is uniform as we need.

Note that also the effective field is a function of space (since it is a function of the magnetization) and, therefore, it must be also discretized. This holds also for the STT contributions which are eventually added to the LLB and LLG equations.

Solvers

After discretization, the LLB equation (3.56) is transformed into a set of N differential equations. Namely

$$\frac{d\mathbf{m}_i}{dt} = -\gamma_0(\mathbf{m}_i \times \mathbf{H}_i^{\text{eff}}) - \gamma_0\frac{\alpha_\perp}{m_i^2}(\mathbf{m}_i \times (\mathbf{m}_i \times \mathbf{H}_i^{\text{eff}})) + \gamma_0\frac{\alpha_\parallel}{m_i^2}(\mathbf{m}_i \cdot \mathbf{H}_i^{\text{eff}})\mathbf{m}_i\,, \tag{4.4}$$

$$\tag{4.5}$$

where $i = 1, ..., N$. Here, for simplicity, we labelled the array elements with the sole index i. However, we recall that they are labelled with three indexes $\{i, j, k\}$ which reflect the spacial coordinates $\{x, y, z\}$, as shown in Fig. 4.1. The full notation will be used when necessary. There are different methods to solve numerically differential equations. Our code includes the Heun's method and the Runge-Kutta 4^{th} order method. The Heun's method is less accurate and requires a smaller time-step. However it has advantages when dealing with the stochastic LLB since it converges to the correct stochastic interpretation (see Appendix A). Numerical methods for stochastic differential equations (SDE) can converge to the Ito interpretation, to the Stratonovich interpretation or to none of them [47]. In general the convergence is weaker than the corresponding deterministic equation. The properties of the thermal noise were calculated by using the Stratonovich interpretation, both in the LLB and the LLG equations. Thus we want a numerical method that converges to this solutions. For the LLG equation both methods are good [47], but with the LLB equation only the Heun method gives the correct solution [59]. In the following, we shall describe the two methods in more details.

Heun's method - Consider a differential equation of the form

$$\frac{d\mathbf{y}}{dt} = f(t, \mathbf{y})\,, \qquad \mathbf{y}(0) = y_0\,, \tag{4.6}$$

where the second equation represents the initial condition. According to Heun's method, the value of the function $\mathbf{y}$ at the instant $t + \Delta t$, can be calculated as

$$\mathbf{y}(t + \Delta t) = \mathbf{y}(t) + \frac{\Delta t}{2}\left[f(t, \mathbf{y}(t)) + f(t + \Delta t, \tilde{\mathbf{y}}(t + \Delta t)\right]\,, \tag{4.7}$$

where

$$\tilde{\mathbf{y}}(t + \Delta t) = \mathbf{y}(t) + \Delta t f(t, \mathbf{y}(t))\,. \tag{4.8}$$

Δt is the time-step which represents an important parameter in numerical simulations. It is related to the time-scales described in Section 3.4.2 and, in particular, it needs to be smaller than the typical time-scales of the magnetization dynamics. However, a very small time-step would significantly slow down the simulations. On the contrary, a large time-step would allow fast simulations but it would give rise to a large error, which leads to divergences and numerical instabilities. In fact, numerical methods always entails a certain error in the solution, which depends on the time-step and the integration method.

There are two kind of errors in numerical simulations: a local error, which is the error of each iteration, and a global error, which is the cumulative error after a certain number of iterations. Clearly, the two errors are correlated. We want the global error to remain constant, otherwise, the solution will diverge after a certain number of steps. A simple empirical test is to test the solutions for different time-steps, checking that the result is independent on the time-step. This test ensures that the solution does not diverge, at least during the time-window of the simulation. In general, we want the largest possible time-step which ensures the numerical stability of the solution.

Runge-Kutta 4^{th} *order method-* The Runge-Kutta 4^{th} order method allows to calculate the solution of the differential Eq. (4.6) as

$$\mathbf{y}(t+\Delta t) = \mathbf{y}(t) + \frac{\Delta t}{6}(k_1 + 2k_2 + 2k_3 + k_4)\,, \tag{4.9}$$

where

$$\begin{aligned}
k_1 &= f(t,\mathbf{y})\,, && (4.10)\\
k_2 &= f\left(t + \frac{\Delta t}{2}, \mathbf{y}(t) + \frac{\Delta t}{2}k_1\right)\,, && (4.11)\\
k_3 &= f\left(t + \frac{\Delta t}{2}, \mathbf{y}(t) + \frac{\Delta t}{2}k_2\right)\,, && (4.12)\\
k_4 &= f\left(t + \Delta t, \mathbf{y}(t) + \Delta t k_3\right)\,. && (4.13)
\end{aligned}$$

For the LLB equation

$$\begin{aligned}
\mathbf{y} &\rightarrow \mathbf{m}_i\,, && (4.14)\\
f(t,\mathbf{y}) &\rightarrow -\gamma_0(\mathbf{m}_i \times \mathbf{H}_i^{\text{eff}}) - \gamma_0\frac{\alpha_\perp}{m_i^2}(\mathbf{m}_i \times (\mathbf{m}_i \times \mathbf{H}_i^{\text{eff}})) + \gamma_0\frac{\alpha_\parallel}{m_i^2}(\mathbf{m}_i \cdot \mathbf{H}_i^{\text{eff}})\mathbf{m}_i\,. && (4.15)
\end{aligned}$$

The numerical methods that we have described are applied to each magnetization vector $\mathbf{m}_i$. The code is written in C^{++} and CUDA. This latter is used to run the code on NVIDIA graphics processing units (GPUs).

Parallel programming

In sequential codes, operations on arrays such as $\mathbf{m} = \{\mathbf{m}_1, ..., \mathbf{m}_N\}$ would imply the use of *for* loops. The N differential equations, one for each element $\mathbf{m}_i$, would be solved **sequentially** one after the other. The same holds for the micromagnetic fields: each field $\mathbf{H}_i$, affecting the magnetization $\mathbf{m}_i$, would be calculated sequentially, one after the other. A typical function of the code would look like

```
void function(m, ....){
        for (int k=0;k<Nz;k++){
                for(j=0;j<Ny;j++){
                        for(i=0;i>Nx;i++){

                        m(i,j,k)= .... ;        }

                        }
                }
        }
```

The use of GPUs can increase the speed of micromagnetic simulations by **parallelizing** the operations. The micromagnetic fields, $\mathbf{H}_i$, and the differential equations for each element, $\mathbf{m}_i$, are calculated simultaneously, i.e., in parallel. CUDA is a specific programming language, which allows to perform operations on NVIDIA GPUs. GPUs, in fact, have a large number of (less powerful) cores which can run simultaneously. Typically each pixel of the screen is assigned to a core. The code still runs on the computer processing units, which allocate the memory on the GPU and calls *kernels* to perform operation on the GPUs. A *kernel* is a function that run on the GPUs and it has the form

```
__global__ void function(m, ...){
    int idx;
    idx=blockIdx.x*blockDim.x+threadIdx.x;

                        m[idx]= ....

                }
```

The suffix global means a function that is called by the host (the CPU) and it runs on the GPU. The *for* loops have disappeared. In their place there is the new index *idx*. Each element $\mathbf{m}_i$ and $\mathbf{H}_i$ is associated with a specific *thread*, which has index *idx*. Threads are organized in Blocks and they are lunched simultaneously, avoiding the need of for loops. A kernel is called from the host in the following way:

```
function<<<dimGrid, dimBlock>>>(m, ... )
```

where dimBlock specifies the dimension of a single Block, i.e., how many threads (elements) can be hosted, and dimGrid specifies the numbers of Blocks, which are organized in grid. More details about parallel programming can be found in Ref. [68]. The structure of the code is depicted in Fig. 4.2. In the following, we shall see how to implement numerically the different contribution to the effective field.

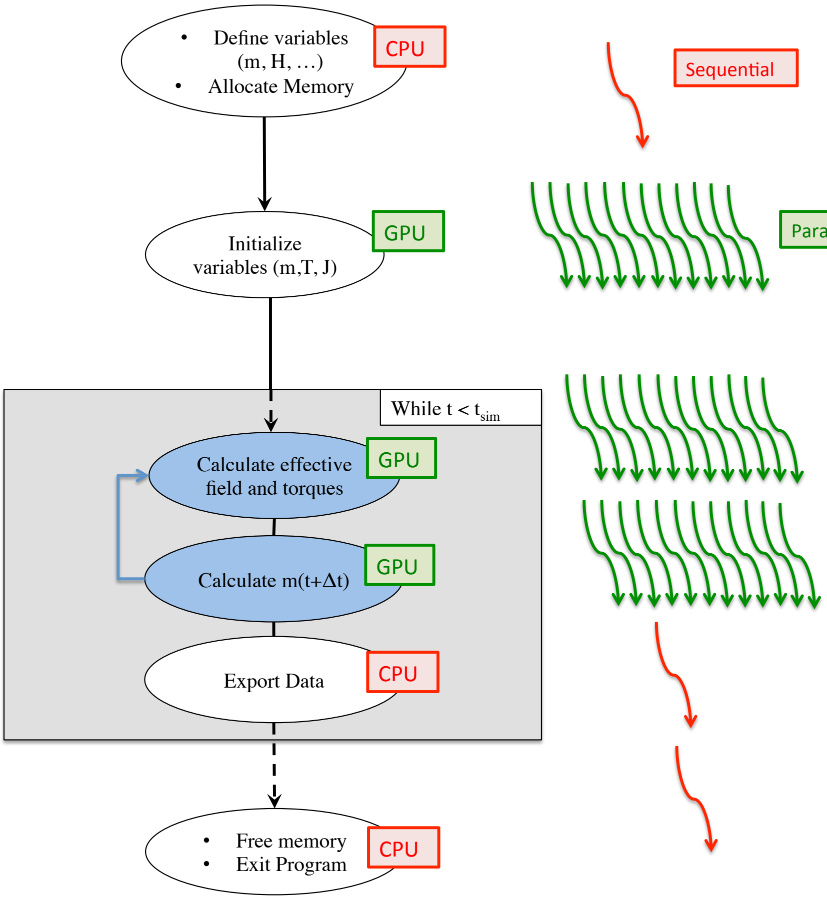

Figure 4.2: Code structure.

Exchange, DMI and STT

The exchange field in the LLB equation is given by

$$\mathbf{H}^{\mathrm{ex}} = \frac{2A(T)}{\mu_0 m_e^2(T) M_s} \nabla^2 \mathbf{m} \,. \tag{4.16}$$

Numerically, it can be calculated as

$$\mathbf{H}^{\mathrm{ex}}_{i,j,k} = \frac{2A_0}{\mu_0 M_s} \sum_{l,m,n} \frac{\mathbf{m}_{l,m,n} - \mathbf{m}_{i,j,k}}{\Delta^2_{l,m,n}} \,, \tag{4.17}$$

where the sum is over the nearest neighbours and Δ_l is the cell dimension along the l direction. Furthermore, we have used the fact that, in mean-field approximation, $A(T) = A_0 m_e^2$. With a different approximation, the exchange field presents an additional term proportional $\nabla A \cdot \nabla \mathbf{m}$. The DMI and STT contributions involve $\partial_i \mathbf{m}$, where $i = x, y, z$. Numerically, they can calculated as

$$\begin{aligned}
\partial_x \mathbf{m}_{i,j,k} &= \frac{\mathbf{m}_{i+1,j,k} - \mathbf{m}_{i-1,j,k}}{2\Delta x} \,, & (4.18)\\
\partial_y \mathbf{m}_{i,j,k} &= \frac{\mathbf{m}_{i,j+1,k} - \mathbf{m}_{i,j-1,k}}{2\Delta y} \,, & (4.19)\\
\partial_z \mathbf{m}_{i,j,k} &= \frac{\mathbf{m}_{i,j,k+1} - \mathbf{m}_{i,j,k-1}}{2\Delta z} \,. & (4.20)
\end{aligned}$$

By substituting the derivatives with their numerical counterparts in Eq. (3.62) and Eq. (3.48) we evaluate the STT and DMI contributions. An example of the original code, used to calculate the exchange field is shown in Appendix D.

Anisotropy, Internal exchange and external fields

The anisotropy, internal exchange and external fields are local, i.e, they do no involve interactions with other spins of the system. Thus, their evaluation is straightforward. The internal exchange field is given by

$$\mathbf{H}^{\mathrm{int}}_i = \frac{1}{2\chi_\parallel(T_i)}\left(1 - \frac{m_i^2}{m_e^2(T_i)}\right)\mathbf{m}_i \,. \tag{4.21}$$

The uniaxial anisotropy is calculated as

$$\mathbf{H}^{\mathrm{an}}_i = \frac{2K_u(T_i)}{\mu_0 M_s m_e(T_i)} (\hat{\mathbf{u}}_k \cdot \mathbf{m}_i)\hat{\mathbf{u}}_k \,, \tag{4.22}$$

where $\hat{\mathbf{u}}_k$ is the uniaxial anisotropy direction. The applied field in each cell is simply $\mathbf{H}^a_i$.

Demagnetizing field

The demagnetizing field is the most expensive field in terms of computational costs. This is because it involves the interaction of the single magnetization vector with all the others and with itself. The demagnetizing field can be calculated as

$$\mathbf{H}^M(\mathbf{r}) = -\frac{1}{4\pi}\int_V \nabla\cdot\mathbf{M}(\mathbf{r}')\frac{\mathbf{r}-\mathbf{r}'}{|\mathbf{r}-\mathbf{r}'|^3}d^3r' + \frac{1}{4\pi}\int_S \mathbf{n}\cdot\mathbf{M}(\mathbf{r}')\frac{\mathbf{r}-\mathbf{r}'}{|\mathbf{r}-\mathbf{r}'|^3}d\Sigma' \,, \tag{4.23}$$

which come from the gradient of Eq. (3.14). By discretizing the sample as described in the previous sections, Eq. (4.23) become

$$\begin{aligned}\mathbf{H}^M(\mathbf{r_i}) &= -\frac{1}{4\pi}\sum_j\int_{V_j} \nabla\cdot\mathbf{M}(\mathbf{r}'_\mathbf{j})\frac{\mathbf{r_i}-\mathbf{r_j}'}{|\mathbf{r_i}-\mathbf{r}'_\mathbf{j}|^3}d^3r'_j + \frac{1}{4\pi}\sum_j\int_{S_j} \mathbf{n}\cdot\mathbf{M}(\mathbf{r}'_\mathbf{j})\frac{\mathbf{r_i}-\mathbf{r_j}'}{|\mathbf{r_i}-\mathbf{r}'_\mathbf{j}|^3}d\Sigma'_j \,,\\ &= \frac{1}{4\pi}\sum_j\int_{S_j} \mathbf{n}\cdot\mathbf{M}(\mathbf{r}'_\mathbf{j})\frac{\mathbf{r_i}-\mathbf{r_j}'}{|\mathbf{r_i}-\mathbf{r}'_\mathbf{j}|^3}d\Sigma'_j \,, \end{aligned} \tag{4.24}$$

since the magnetization is assumed constant inside each micromagnetic cell and, therefore, the first term vanishes. $\mathbf{M}(\mathbf{r}_j)$ corresponds to the magnetization of cell j and, consistently with the formalism that we have introduced in this chapter, it can be written in a compact form as $\mathbf{M}(\mathbf{r}_j) = \mathbf{M}_j$. Analogously, $\mathbf{H}^M(\mathbf{r}_i) = \mathbf{H}_i^M$. Eq. (4.24) can be written as

$$\mathbf{H}_i^M = \sum_j N_{i-j}\mathbf{M}_j \,, \tag{4.25}$$

where N_{i-j} is 3×3 tensor, known as **demagnetizing tensor**, that depends only on the cell dimensions and the distance between the other cells. Explicitly,

$$N_j = \begin{bmatrix} N_{xx,j} & N_{xy,j} & N_{xz,j} \\ N_{yx,j} & N_{yy,j} & N_{yz,j} \\ N_{zx,j} & N_{zy,j} & N_{zz,j} \end{bmatrix} . \tag{4.26}$$

From the reciprocity theorem it follows that N_j must be symmetric and, therefore, it has only 6 independent components [69]. These coefficients are calculated analytically as described in Ref. [70, 69]. The direct evaluation of the demagnetizing field by Eq. (4.25) would require an operation count of $O(N^2)$, where N is the number of cells. Nevertheless, the number of operations can be reduced by using the fast Fourier transform (FFT). In fact, by Fourier transforming Eq. (4.25) we obtain

$$\tilde{\mathbf{H}}_k^M = \tilde{N}_k\tilde{\mathbf{M}}_k \,, \tag{4.27}$$

where the sum vanishes due to the properties of the FFT when applied to a convolution of functions as Eq. (4.25). In this way, the number of operations can be reduce to $O(N\log N)$, which is the operations needed for the FFT. Furthermore, the FFT method requires a padding of the magnetization [69], i.e, we need to add a number of zeros in each direction of the magnetization vector, equal to the size of the magnetization vector in that direction. The coefficients N_j and $\tilde{N}_k$ depend only on the geometry and they can be calculates only once in the code. The final demagnetizing field is obtained by finally transforming back $\tilde{\mathbf{H}}_k^M$. An example of the original code, used to calculate the demagnetizing field is shown in Appendix D.

Boundary conditions

The terms that involve $\partial_i \mathbf{m}$, require a specification of the boundary conditions, since they need the value of the magnetization vector outside of the boundary. In a system without DMI, the boundary conditions (3.28) can be implemented by setting the magnetization outside of the boundary equal to the magnetization at the boundary. For instance, along the x direction

$$\mathbf{m}(N_x+1,j,k) = \mathbf{m}(N_x,j,k)\,, \qquad \mathbf{m}(0,j,k) = \mathbf{m}(1,j,k)\,, \tag{4.28}$$

where the elements $\mathbf{m}(N_x+1,j,k)$ and $\mathbf{m}(0,j,k)$ are outside of the grid. In the presence of DMI, the boundary condition are transformed according to Eq. (3.50).

4.2 Code verification

The code has been tested against standard micromagnetic problems, proposed in Ref. [71]. In this section, we describe the Standard Problems 4 and 5 and we show the solution computed with our code. The solution is compared with the results obtained with MuMax [8] and OOMMF [72], common and well tested micromagnetic code. The test is performed with the LLB at $T = 0$, which is equal to LLG in this limit.

Standard Problem 4

The standard problem 4 consist of a field driven magnetization switching. The initial magnetization state, depicted in Fig. 4.3, is switched by applying an external field $\mu_0\mathbf{H} = (-24.6, 4.3, 0)$ mT. The sample dimension are $L = 500$nm, $d = 125$nm and thickness $t = 3$nm. The following material parameters are considered

A	$13 \times 10^{-12}\ J/m$
M_s	$8 \times 10^5\ A/m$
α	0.02

Table 4.1: Standard Problem 4 material parameters.

The system is discretized in cells of $\Delta x = \Delta y = 5$ nm and $\Delta z = 3$ nm. The time-step is set to $\Delta t = 100$fs. The average magnetization components, $\langle m_x \rangle$, $\langle m_y \rangle$ and $\langle m_z \rangle$, as function of time, are shown in Fig. 4.4 (a), (b) and (c) respectively. The calculations performed with our code, labelled as *code*, present a very good agreement with the results of OOMMF and MuMax.

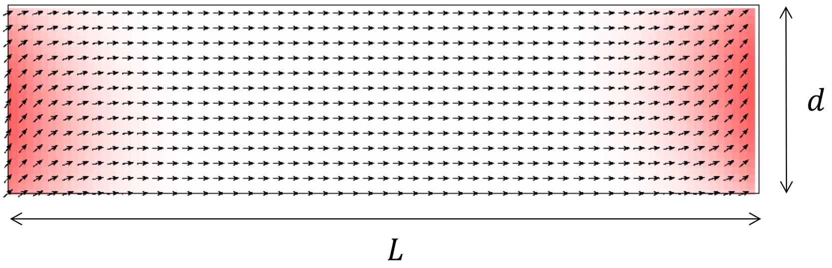

Figure 4.3: Standard Problem 4 initial State. Color scale as in Fig. 3.1.

Standard Problem 5

The standard problem 5 is meant for checking the correct implementation of the (Zhang-Li) STT. The initial state is a magnetic vortex , shown in Fig. 4.5, which is excited by the application of current. The system dimension are $L = 100\text{nm}$ and thickness $t = 10\text{nm}$. The system is discretized in cell of dimensions $\Delta x = \Delta y = \Delta z = 5$ nm. The same material parameters as in standard problem 4 are considered. The polarization of the current is set to $P = 0.4$.
The vortex core, whose coordinate are proportional to the components $\langle m_x \rangle$ and $\langle m_y \rangle$, moves in almost circular orbits before reaching a new equilibrium position. The orbits depend on the amplitude of the current, included in the pre-factor u, and the non-adiabatic parameter ξ. The standard problem 5 requires the evaluation of the vortex orbits for the following combination of u and ξ:

u=53.35 m/s	$\xi = 0$
u=53.17 m/s	$\xi = 0.05$
u=53.0 m/s	$\xi = 0.1$
u=50.0m/s	$\xi = 0.5$

Table 4.2: Standard Problem 5 STT parameters.

The different trajectories are shown and compared to MuMax in Fig. 4.6. Also in this case, the agreement is very good.

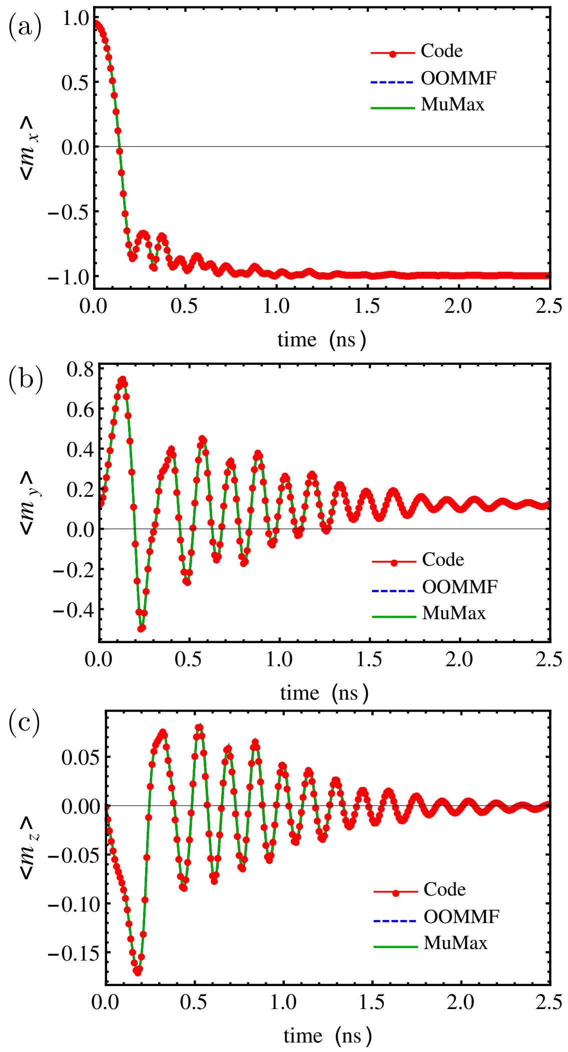

Figure 4.4: Average magnetization (a) $\langle m_x \rangle$, (b) $\langle m_y \rangle$ and (c) $\langle m_z \rangle$ as function of time.

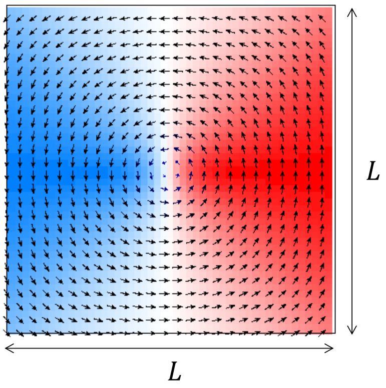

Figure 4.5: Standard Problem 5. Initial State. Color scale as in Fig. 3.1.

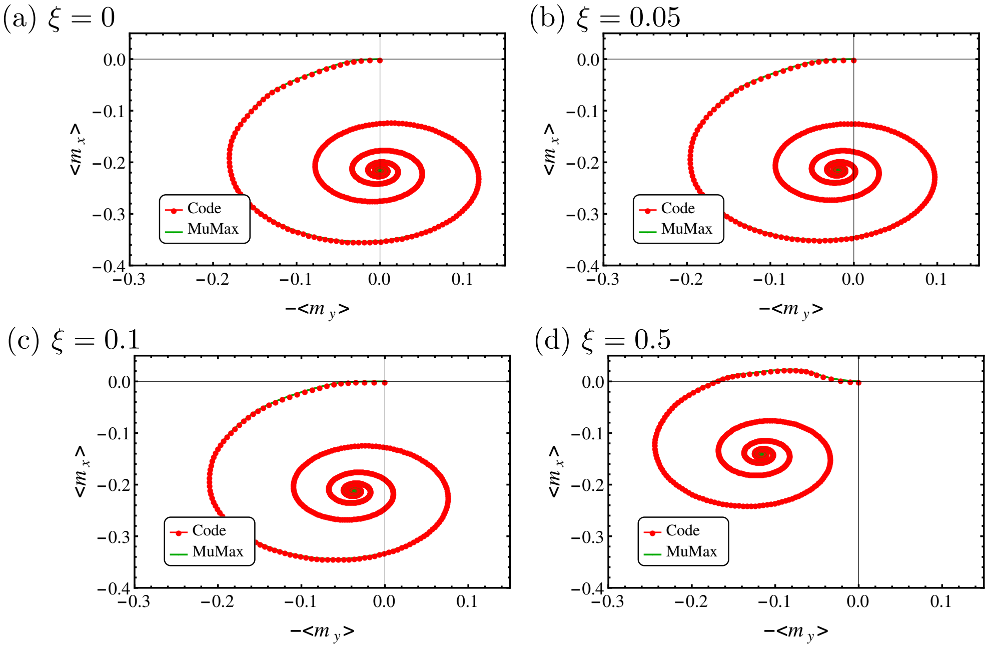
(a) $\xi = 0$

(b) $\xi = 0.05$

(c) $\xi = 0.1$

(d) $\xi = 0.5$

Figure 4.6: Vortex core trajectories, $\{-\langle m_y\rangle, \langle m_x\rangle\}$, for different combinations of u and ξ as indicated in the label and in Table 4.2

Thermal noise test

The implementation of the thermal noise is tested as described in Ref. [59], where the stochastic LLB was introduced. As commented in Section 3.8, the amplitude of the stochastic fields is set by imposing that the probability distribution of the magnetization follows the Maxwell-Boltzmann (MB) distribution. In the micromagnetic code, we introduce the thermal fields $\mathbf{H}_{\text{th}}^{\perp,\parallel}$ given by

$$\mathbf{H}_{\text{th},i}^{\perp} = \boldsymbol{\eta}_i \sqrt{\frac{2(\alpha_\perp - \alpha_\parallel) k_B T}{\gamma_0 \mu_0 M_s \alpha_\perp^2 \Delta V \Delta t}}\,, \quad \mathbf{H}_{\text{th},i}^{\parallel} = \boldsymbol{\omega}_i \sqrt{\frac{2\gamma_0 \alpha_\parallel k_B T}{\mu_0 M_s \Delta V \Delta t}}\,, \tag{4.29}$$

where $\boldsymbol{\eta}_i$ and $\boldsymbol{\omega}_i$ $(i = 1, .., N)$ are Gaussian distributed random vectors with zero mean and unitary standard deviation. The random vectors must be re-generated at each time step and they ensure they white noise feature of the thermal fluctuations. ΔV is the volume of the computational cell and Δt is the time-step. The amplitude of the fields is calculated from the stastistical properties described in Section 3.8.3. Similarly, the thermal field $\mathbf{H}_{\text{th}}$ of the LLG equation is

$$\mathbf{H}_{\text{th},i} = \boldsymbol{\eta}_i \sqrt{\frac{2\alpha k_B T}{\gamma_0 \mu_0 M_s \Delta V \Delta t}}\,. \tag{4.30}$$

The system consider in Ref. [59] is a single cell subject to thermal agitation. If the implementation is correct, the orientation of the magnetization vector has to follow the MB distribution

$$P_0(\mathbf{m}) = f_0 \exp\left[-F(\mathbf{m})/k_B T\right]\,, \tag{4.31}$$

where f_0 is a normalizing constant. In the absence of anisotropies and external field, the free energy F is given by [53, 59]

$$\frac{F}{M_s V} = \frac{1}{8\xi_\parallel(T)} \left(\frac{m^2 - m_e^2}{m_e^2}\right)\,, \tag{4.32}$$

where V indicates the volume of the computational cell. This energy corresponds to the energy of the internal exchange field of the LLB equation [53]. As in Ref. [59], we calculate the magnetization modulus $|\mathbf{m}|$ each $\Delta t = 1$ps, for a total simulation time of $t = 10$ ns. The probability of finding the system with a certain $|\mathbf{m}|$ should follow the distribution $P(|\mathbf{m}|) = c|\mathbf{m}|P_0(\mathbf{m})$, where c is a normalizing constant. Contrary to Ref. [59], we use the same parameter as in the previous standard problems since they corresponds to the typical systems studied in this thesis. The Curie temperature is set to $T_C = 850$ K. The Probability Density Function (PDF) obtained for $|\mathbf{m}|$ is shown in Fig. 4.7 for different temperatures, together with the distribution $P(|\mathbf{m}|)$. The results follow the correct distribution as expected.

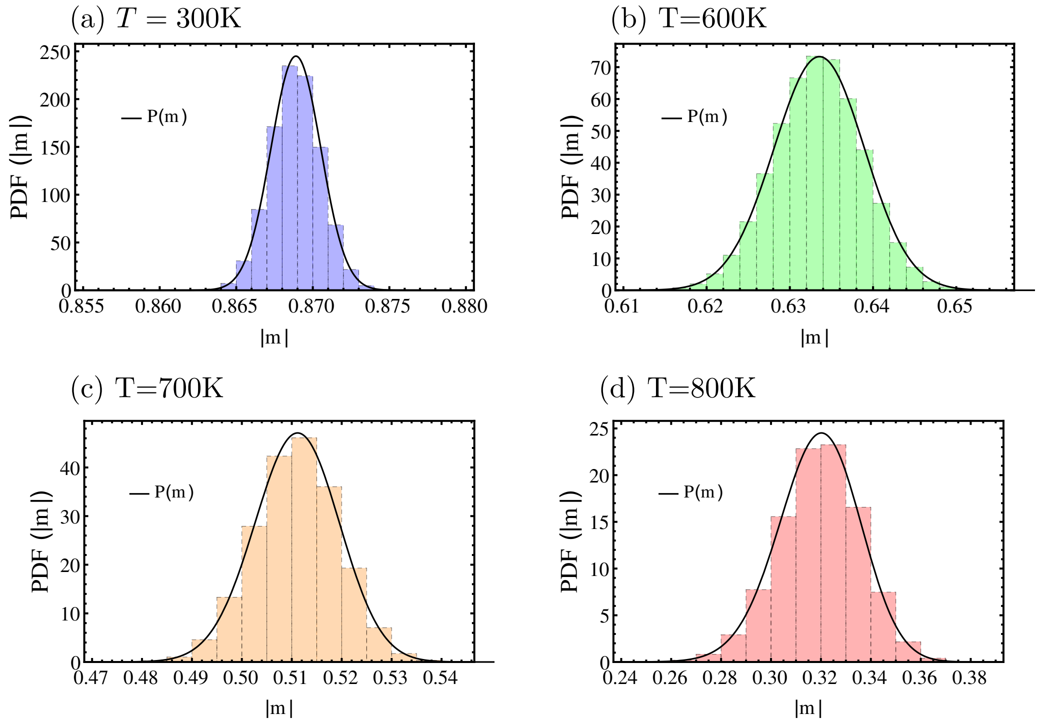
(a) $T = 300$K (b) T=600K (c) T=700K (d) T=800K

Figure 4.7: Probability Density Function (PDF) of the magnetization modulus $|m|$ for different temperatures.

4.3 Heat equation

An additional feature of our micromagnetic code is the possibility to solve simultaneously the LLB/LLG equation together with the heat equation, which describes the temperature evolution of the sample. The heat equation is given by [73]

$$\frac{\partial T_i}{\partial t} = \frac{k}{\rho C}\nabla T_i + \frac{Q_i}{\rho C}\,, \tag{4.33}$$

where k is the thermal conductivity, ρ is the density and C is the specific heat capacity of the sample. Q is a heating term which can be Joule heating or laser heating. Also the heat equation is solved for each cell. Within the LLG approach the temperature and the magnetization are coupled through the thermal noise, while within the LLB approach they are additionally coupled through the temperature dependence of the micromagnetic parameters. An important contribution to the temperature evolution is given by the substrate, which absorbs the heat of the sample. This is implemented effectively into the heat equation by adding the following term [74]

$$-\frac{T - T_{\text{sub}}}{\tau}\,, \tag{4.34}$$

where T_{sub} represents the substrate temperature and τ the rate at which the heat is absorbed. This implementation is tested again COMSOL simulations [75] and it shows a good agreement as depicted in Fig. 4.8. The results depicted in Fig. 4.8 correspond to the temperature evolution of a Py strip, which will be further analysed in Chapter 7. Fig. 4.8(a) depicts the temperature evolution of the strip as a consequence of a current pulse of $t_p = 4$ns and $J = 3 \times 10^{12}$ A/m^2, while Fig. 4.8(b) represents the temperature profile along the strip at $t = 4$ns. The central increase is due to the presence of a notch as will be further detailed in Chapter 7.

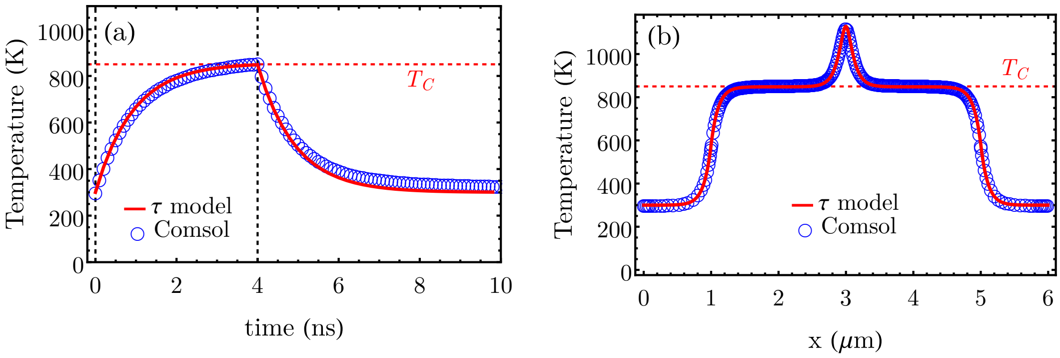

Figure 4.8: (a) Temperature evolution of a Py strip as a consequence of a current pulse of $t = 4$ns and $J = 3 \times 10^{12}$ A/m^2. (b) Temperature profile along the strip at $t = 4$ns. The central increase is due to the presence of a notch.

Part II

Influence of Joule heating and temperature gradients on domain wall dynamics

Chapter 5

Introduction

Magnetic domain walls (DWs) can be efficiently displaced by spin-polarized currents thanks to the so-called spin transfer torque (STT). Due to the exchange interaction between the conduction electrons and the local magnetization, an electrical current, flowing through a ferromagnet, gets spin-polarized and, at the same time, affects the local magnetization. This mechanism has attracted a considerable attention due to its potential for the realization of new logic [3] and memory devices [2]. In particular the current-induced DW motion on Py nanostrip has been extensively studied during the last decade. Several experiments showed that electrical currents can displace DWs along the direction of the electron flow [76, 77, 78] and/or assist the field-driven DW depinning from patterned constrictions [79]. An extended review about current-induced DW dynamics can be consulted in Ref. [80]. These observations are usually interpreted in terms of the adiabatic and non-adiabatic STTs that a spin polarized current exerts on non-uniform magnetic patterns.

However, it is well known that, apart from the STTs, an electric current also generates heating as due to the Joule effect and several works indicated that its effect can be significant [81, 82]. This is particularly relevant in systems with notches or curved geometries, where non-uniform current densities can generate additional thermal gradients along the sample, which are hardly detectable in experiments. Hence, on the one hand, it is important to evaluate the effect of Joule heating in order to properly evaluate the STT contribution. On the other hand, one might wonder if it is possible to use Joule heating to efficiently control magnetic DWs. Indeed, heat is already used to help the magnetization switching in heat assisted magnetic recording (HAMR) devices, where the sample is heated in order to reduce the energy barrier between two magnetic states. Furthermore, recent experiments have shown that laser pulses alone can promote ultra-fast switching of the magnetization in several systems [83, 84, 52]. Despite an ongoing debate regarding the mechanisms responsible for this effect, heat was shown to be an essential ingredient in these processes [85, 86]. All these observation led to the emergence of a new branch of research known as spin-caloritronics, which aims to study the interplay between charge, spin and heat.

In the context of the DW motion, recent theoretical predictions [87, 88, 54, 89] and few experiments [90, 91, 92] have indicated that thermal gradients can actually drive DWs. From a technological point of view, DW motion by thermal gradient is interesting for several reasons. Firstly, thermally induced motion can be excited in several systems (ferromagnets, ferrimagnets, antiferromagnets, insulators or conductors). Secondly, DW motion by thermal currents has very small dissipation since thermally excited spin-current are carried by magnons, which do not involve any electrons displacement. Additionally, this effect could represent an efficient way to recycle the heat generated in electronic circuits. From a theoretical point of view it is known that the thermally induced DW motion is due to at least two effects: (1) the so-called entropic torque which drives the DW towards the hotter region of the sample due to minimization (maximization) of its free energy (entropy), and (2) the magnonic STT which drives the DW towards the hot or the cold region depending on the interaction between the DW and the thermally excited magnons. However, the interplay between entropic torque and magnonic STT is still under debate and theoretical efforts are limited to ideal cases with linear thermal gradients.

Here, we firstly evaluate the effect of Joule heating on current-induced DW dynamics by means of a novel micromagnetic framework, which allows to solve the heat transport and the magnetization dynamics simultaneously.

In Chapter 6 we analyse the effect of Joule heating on DW dynamics in curved Py nanostrips, as experimentally investigated in Ref. [91]. We show that, depending on the patterning methods, thermal gradients can arise during the current pulse and they can significantly affect the DW dynamics, consistently with the experimental observations [91]. In this study the heat Eq. (4.33) is coupled to the conventional LLG Eq. (3.33). This chapter is adapted from Ref. [5].

In Chapter 7 we analyse the effect of Joule heating on current-induced DW depinning. The system is chosen to reproduce the experimental setup described in Ref. [78], where a significant increase of the strip temperature was observed. In this case, the heat Eq. (4.33) is coupled to the LLB equation, which allows to describe the magnetization dynamics even close to the Curie temperature. We show that, due to the notch, non-uniform Joule heating can lead to a local destruction of the ferromagnetic order, which eventually helps the depinning. Furthermore, symmetric phase diagrams (pinning-depinning) with respect to the current-polarity, as the ones observed in the experiment [78], can be obtained only by including the Joule heating contribution. This chapter is adapted from Ref. [6].

Finally, in Chapter 8, we analyse the DW motion by localized temperature gradients as the ones generated by non-uniform Joule heating or by laser pulses. The different contributions to thermally induced DW motion (entropic torque and magnonic STT) are isolated and compared. A third driving force, due to a thermally induced dipolar field, is found and described. Thermally induced DW motion is finally analysed in realistic strips by introducing edge roughness. We show that entropic torque dominates over the magnonic STT, which would drive the DW towards the cold region due to the prevalence of low frequency magnons. This chapter is adapted from Ref. [7].

As commented, the results presented in this part are adapted from Ref. [5, 6, 7] by the author. For this reason Chapter 6, 7 and 8 are self-consistent and they can be read separately. For the same reason, several concepts are repeated among these chapters, especially in the introductory parts and when describing the simulation methods and the equations.

Chapter 6

Domain wall dynamics along curved strips under current pulses: the influence of Joule heating

The current-induced domain wall dynamics along curved ferromagnetic strips is studied by coupling the magnetization dynamics to the heat transport. Permalloy strips with uniform and non-uniform cross section are evaluated taking into account the influence of the electrical contacts used to inject the current pulses and the substrate on top of which the ferromagnetic strip is sited. Micromagnetic simulations indicate that the geometry and the non-ferromagnetic materials in the system play a significant role in current-induced domain wall dynamics. Due to the natural pinning, domain walls are hardly affected by the spin-transfer torques when placed in uniform cross section strips under current pulses with reduced magnitude. On the contrary, the current-induced domain wall displacement is significantly different in strips with non-uniform cross section, where thermal gradients emerge as due to the Joule heating. It is found that these thermal gradients can assist or act against the pure spin-transfer torques, in agreement with recent experimental observations.[1]

6.1 Introduction

Since the theoretical prediction by Berger [19] and Slonzewski [20], and due to its potential for the development of logic and recording devices [2, 3], the study of the current-induced domain wall motion (CIDWM) along ferromagnetic strips is a subject of intense

---

[1] Adapted from V.Raposo, S.Moretti, M.A. Hernandez and E. Martinez, Appl. Phys. Lett. 108, 042405 (2016)

fundamental and technological interest. The current driven DW motion along Permalloy (Py) ferromagnetic strips has been extensively analyzed during the last decade. Experiments have evidenced that the injection of an electrical current through the strip can drive domain walls (DWs) in the direction of the electron flow [76, 77, 78] and/or assist the field-driven depinning from a patterned constriction [79]. DW transformations [93], and even nucleation of multiple walls [81] have been also observed. An extended review, including the most relevant literature of the topic, can be consulted in [80] and references therein.

These observations are usually interpreted in terms of the adiabatic and non-adiabatic spin-transfer torques (STTs) that a spin polarized current exerts on the spatially-dependent magnetic texture of the DW [27, 28]. However, as indicated by the high disparity between the material parameters governing the STTs as deduced from experiments of similar Py samples [80], the underlying mechanisms are still not well understood. Up to now, the micromagnetic simulations (μM) and the one-dimensional model (1DM) adopted to explain the experimental measurements usually assume that the current density is uniformly flowing through the strip [27, 28, 94]. This constitutes an oversimplification when the strip cross section is non-uniform, and especially when the current is forced to pass through constrictions.

Apart from the STTs, it is well known that an electric current also generates heating as due to the Joule effect. Although several works indicate that Joule heating is significant [81, 82], its influence on the CIDWM have been theoretically studied only qualitatively, by assuming that it results in an increase of the global temperature of the sample [95]. These approaches neglect the multilayer structure underneath the Py strip as well as the electrical contacts used to inject the current. However, the presence of these non-ferromagnetic materials could promote the appearance of non-uniform temperature patterns over the sample, which has been shown to play a significant role in the heat transport as excited by the current injection [96, 91, 73, 82].

Indeed, recent observations by Torrejon et al. [91] indicate that both the contacts and the substrate strongly influence the CIDWM. In their analysis [91], two vortex DWs sited in a curved Ta/Py/Pt multilayer on top of a SiO_2/Si substrate are displaced differently under the same current pulses, and the probability of CIDWM was found much higher when the STT drives the DW towards the center of the strip. These results were explained in terms of a simple 1DM as due to an effective thermodynamics force [97], which is proportional to the local thermal gradient arising from the heat transport over the entire system. However, a full micromagnetic analysis is still missing.

Apart from the STTs and thermodynamics forces, it is also well know that vortex DWs experience some inertia [98]. Under a current pulse, the vortex core is shifted along the transversal direction, and once the current is switched off, the DW continues propagating due to the gyrotropic vortex-core motion. The relaxation time of this DW automotion is comparable to the cooling time of the strip, and therefore, it also influences the CIDWM observations due to the STTs and thermal gradients. Although the adopted 1DM could provide a qualitative description of the vortex DW dynamics, full μM simulations would be needed to provide a more realistic description.

Moreover, in order to isolate the influence of the thermal gradients on the CIDWM, inertia effects should be avoided, as otherwise they strongly mask the pure thermodynamic phenomenon. Therefore, an investigation of the CIDWM under both STT and heat transport in systems with negligible inertia is still lacking and very timely.

Here we report a micromagnetic study of the CIDWM taking into account the spatial and temporal dependence of current pulses injected along curved Py strips. Both the electrical contacts used to inject the current pulses and the vertical stack in which the Py is sandwiched are considered to describe the current driven magnetization dynamics coupled to the heat transport self-consistently. The considered samples, although have a similar in-plane shape as the ones experimentally studied in Ref. [91], were intentionally chosen here to have a different cross section which, instead of vortex configuration, favor transverse DW configurations even after the current injection. Two different curved samples are intended to depict uniform and non-uniform cross section, and consequently, resulting in uniform and non-uniform current and temperature profiles.

Our results point out that all these heat flow effects, as linked to the ferromagnetic strip geometry and its environment, play a significant role on the CIDWM, and therefore, they need to be taken into account in order to provide a proper description of the experimental observations.

6.2 Results and Discussion

Evaluated samples here were intentionally chosen to favour transverse DW configurations with negligible inertia, and they are depicted in Fig. 6.1(a)-(b). Two Au contacts at the ends of the lateral pads are used to inject current pulses along a 10nm-thick Py strip, which is on top of a SiO_2/Si substrate (see top inset in Fig. 6.1). This substrate is an extended film where a 500nm-thick Si layer is isolated from the Py by means of a 40nm-thick SiO_2/Si layer. The central part of the Py strip extends over 12 μm along the x-axis.

Two different curved geometries are considered. The first one has uniform cross section (UCS), with a fixed width of 300 nm between pads, and it was generated by firstly drawing the rectangular 300nmx10nm cross section in contact with the left pad, and after that, by extruding it along the x-axis following a sinusoidal shape, as shown in Fig. 6.1(c). The second Py strip was generated by firstly drawing the wave-like curve for the bottom edge of the strip, and then translating it over 300nm along the transversal direction (y-axis), as shown in Fig. 6.1(d). Therefore, its transverse cross section is non-uniform. In what follows, these two samples will be referred as uniform-cross section (UCS) and non-uniform cross section (NUCS) respectively. The current is injected in the Py strips from the Au contacts.

6.2.1 Electro-thermal characterization

Similarly to previous analysis [96, 91, 73, 82], the electro-thermal characterization of the system was performed by using the commercial software COMSOL [75] including not

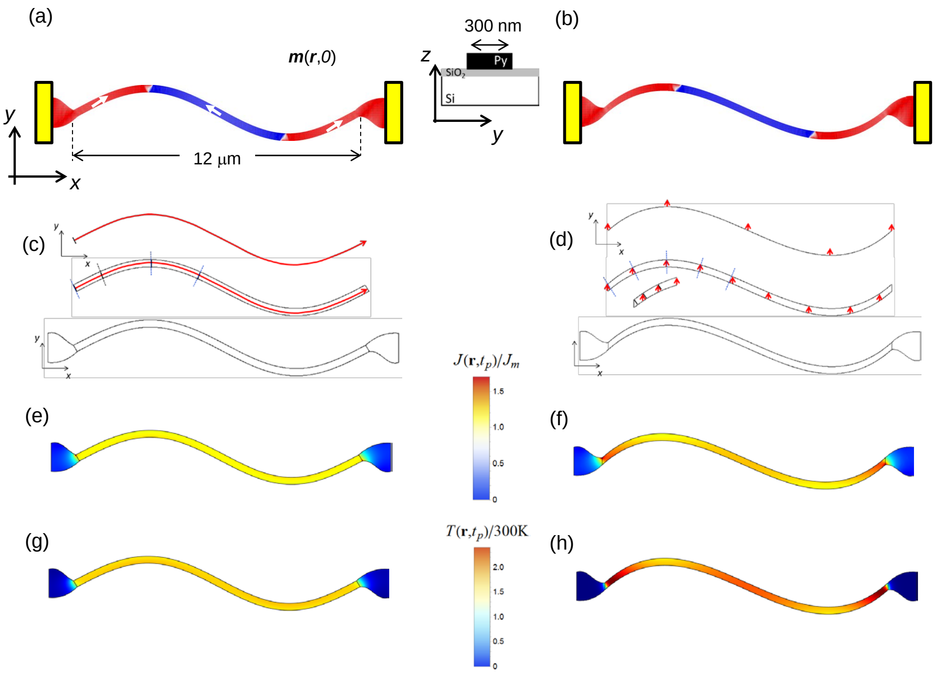

Figure 6.1: Geometry generation of the samples with uniform cross section (a) and non-uniform cross section (b). Geometry of the analyzed samples for uniform cross section (left column) and non-uniform cross section strips (right column). (c)-(d) Initial DW configurations at rest. (e)-(f) current distribution $\mathbf{J}(\mathbf{r},t)/J_m$ normalized to the uniform cross section value ($J_m = 2$ TA/m^2). (g)-(h) Temperature profile $T(\mathbf{r},t)$ under a current pulse of $J_m = 2$ TA/m^2 at $t = t_p = 4$ ns. The central inset between (a) and (b) shows the vertical composition the stack.

only the Py strips, but also the Au contacts and SiO$_2$/Si substrate. This tool allows us to solve the Laplace Eq. for the electrostatic potential coupled to the heat Eq. describing the induced heat transport. However, importing the COMSOL data during the micromagnetic simulations would significantly slow down the simulation. Therefore, we use a phenomenological term in order to take into account the substrate and we solve the heat Eq. within the micromagnetic code. The validity of this approach is tested against full COMSOL simulations. The electrical current density, on the other hand, is calculated with COMSOL and imported only once into the micromagnetic code. The normalized current density distribution $\mathbf{J}(\mathbf{r},t)/J_m$, with J_m being the value of current density where the strip cross section is 300nmx10nm, is shown in Fig. 6.1 (e) and (f) for each sample respectively, which clearly indicate the uniform and non-uniform distribution as due to the in-plane geometry.

The current flows firstly through the wide pads with low density, and then it adapts to the constrained curved shape of the Py strip being tangential to its edges as imposed by the null conductivity of the surrounding media.

The local temperature $T(\mathbf{r},t)$ is determined by solving the heat Eq.

$$\frac{\partial T(\mathbf{r},t)}{\partial t} = \frac{k}{\rho C}\nabla^2 T(\mathbf{r},t) + \frac{J^2(\mathbf{r},t)}{\sigma\rho C} - \frac{T(\mathbf{r},t)-T_{\text{ref}}}{\tau}\,, \tag{6.1}$$

where ρ is the density, C is the heat capacity, and k is the thermal conductivity of each material forming the system. The first term on the rhs of Eq. (6.1) represents the heat diffusion and it tries to homogenize the temperature over a short scale. The second term describes the heat source as due to the Joule heating. The last term in (6.1) is a phenomenological Newton-like term describing the heat flow between the Py and its environment, which includes the surrounding air, the Au electrical contacts and the SiO_2/Si substrate. T_{ref} is the reference temperature of the environment and τ the characteristic time describing the rate at which the heat is transferred. It was confirmed that using this phenomenological Newton-like term with $T_{\text{ref}} = 300\text{K}$ and $\tau = 1$ ns, the space and temporal evolution of the local temperature $T(\mathbf{r},t)$ calculated by COMSOL is accurately described by Eq. (6.1) for the Py strip. The thermal parameters of Py are: $\rho_{\text{Py}} = 8.7\times10^3$ Kg/m^3, $C_{\text{Py}} = 0.43$ J/(gK) and $k_{\text{Py}} = 46.4\ W/(Km)$. As the SiO_2/Si substrate is a very good electrical isolator, the electrical conductivity (σ) is assumed to be only different from zero in the Py: $\sigma_{\text{Py}} = 4\times10^6(\Omega m)^{-1}$. The parameters describing the thermal properties of the SiO/Si substrate are: $\rho_{\text{Si}} = 2.329\times10^3$ Kg/m^3, $C_{\text{Si}} = 0.7J/(gK)$, and $k_{\text{Si}} = 130\ W/(Km)$. The 40nm-thick SiO_2 layer has a very low thermal conductivity ($k_{\text{SiO}} = 4.2\times10^{-2}\ W/(Km)$) and, as pointed by a recent study by Ramos et al. [96], it is assumed to generate a thermal resistance [99, 96] between the Py and the Si layers of $TR_{\text{SiO}} = 2.2\times10^{-8}$ m^{2}K/W. Due to the high thermal conductivity of the Au, these electrical contacts are considered as sinks for the heat, and therefore their temperature is fixed to room temperature ($T_{\text{Au}} = 300$ K).

Due to the non-uniform current density distribution $\mathbf{J}(\mathbf{r},t)$, and also determined by the Au contacts and the SiO_2/Si substrate, the temperature distribution $T(\mathbf{r},t)$ during and after the current pulse is space dependent over the Py strip. The temperature profiles $T(\mathbf{r},t)$ at the end of a current pulse of length $t_p = 4$ns and $J_m = 2$ TA/m^2 are depicted in Fig. 6.1 (g)-(h) for both UCS and NUCS samples. As it is clearly shown, the non-uniform density current $\mathbf{J}(\mathbf{r},t)$ generates non-uniform temperature profiles in the strip with NUCS, which depicts hot and cold points, and consequently, thermal gradients emerge along the strip (Fig. 6.1(h)). On the contrary, the temperature, although higher than in the ferromagnetic pads, is almost uniform along the strip with uniform cross section (Fig. 6.1(g)). In order to provide further details related to the time-dependent profiles, the space and temporal evolution of the temperature over the Py strip is shown in Fig. 6.2. COMSOL results are obtained by solving the heat Eq. (6.1) without the Newton-like term but taking into account the full 3D system, which includes the Py strip, the Au contacts and the SiO/Si substrate. The results computed from the heat Eq. (6.1) are also included for comparison. The remarkable agreement between them certifies the validity of the adopted approach to study the current-induced DW dynamics coupled to the heat transport.

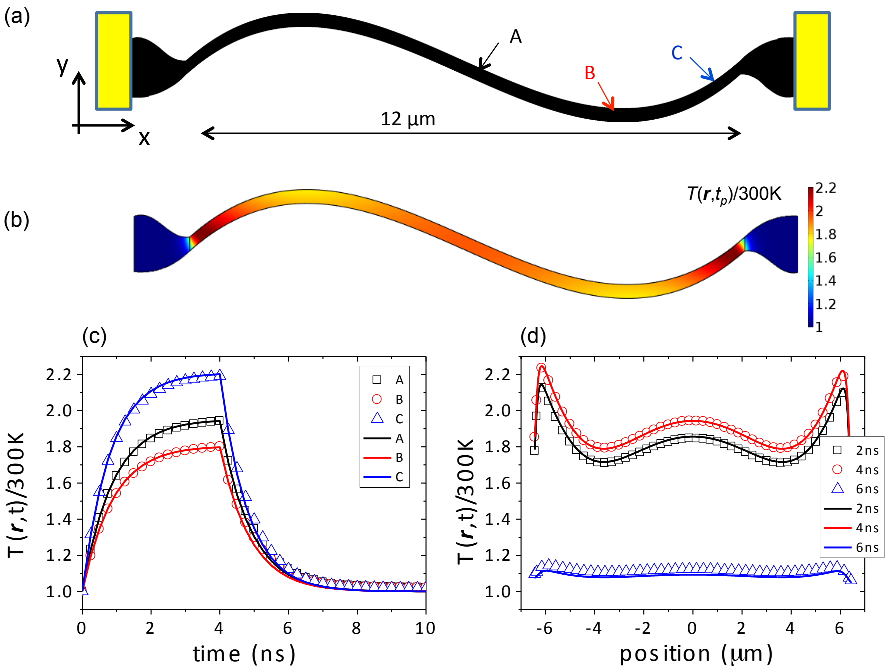

Figure 6.2: Temporal evolution of the temperature along the NUCS strip under a current pulse with $J_m = 2\ \mathrm{TA/m^2}$ and $t_p = 4$ ns. (a) Sketch of the strip and labels (A,B,C) of representative positions. (b) Temperature distribution $T(\mathbf{r}, t)$ along the strip at $t = 4$ns. (c) $T(\mathbf{r}, t)$ as a function of time at three representative positions along the strip (A, B, and C are marked in (a)). (d) $T(\mathbf{r}, t)$ along the central line of the strip for different instants during and after the current pulse. Full symbols corresponds to COMSOL predictions computed by solving the Laplace Eq. and the heat Eq. with the full system, which includes the Py strip, the Au contacts and the $\mathrm{SiO_2/Si}$ substrate. Lines were computed by solving the heat Eq. (6.1) for the Py strip. In this case, the additional Newton-like term accounts for the presence of the Au contacts and the substrate from phenomenological point of view.

6.2.2 Coupled magneto-heat dynamics

Having described the electric and thermal problems, our goal here is to evaluate the influence of the uniform and non-uniform current $\mathbf{J}(\mathbf{r}, t)$ and temperature $T(\mathbf{r}, t)$ profiles on the CIDWM. To this end, the CIDWM is numerically studied here in a self-consistent manner by coupling the Landau-Lifshitz-Gilbert Eq. augmented by the STTs [79, 78] to the heat flow. The LLG Eq. augmented by the STTs is [28, 94]

$$\begin{aligned}\frac{\partial \mathbf{m}}{\partial t} &= -\frac{\gamma_0}{1+\alpha^2}\left[\mathbf{m}\times(\mathbf{H}_{\text{eff}}+\mathbf{H}_{\text{th}})\right]-\frac{\gamma_0\alpha}{1+\alpha^2}\left\{\mathbf{m}\times\left[\mathbf{m}\times(\mathbf{H}_{\text{eff}}+\mathbf{H}_{\text{th}})\right]\right\}\\ &\quad +\frac{u}{1+\alpha^2}(1+\xi\alpha)\mathbf{m}\times(\mathbf{m}\times(\mathbf{J}\cdot\nabla)\mathbf{m})+\frac{u}{1+\alpha^2}(\xi-\alpha)\mathbf{m}\times(\mathbf{J}\cdot\nabla)\mathbf{m}\,,\end{aligned} \tag{6.2}$$

where γ_0 is the gyromagnetic ratio, α is the Gilbert damping and $\mathbf{m}=\mathbf{m}(\mathbf{r})/M_s$ is the local magnetization normalized to the saturation magnetization M_s. The effective field $\mathbf{H}_{\text{eff}}$ includes the exchange and magnetostatic interactions [94]. The 3rd and 4th terms are adiabatic and non-adiabatic STTs, with $u=\mu_B P/(|e|M_s(1+\xi^2))$, where μ_B is the Bohr magneton, e is the electric charge, P is the spin polarization factor and ξ is the non-adiabatic parameter. $\mathbf{J}=\mathbf{J}(\mathbf{r},t)$ is the current density current along the strip, which was obtained from the preliminary electro-thermic characterization. Thermal fluctuations are taken into account through a stochastic thermal field $\mathbf{H}_{\text{th}}$, which has white noise properties with the correlator [94, 46, 47]

$$\langle H_{\text{th}}(\mathbf{r},t)_i H_{\text{th}}(\mathbf{r}',t')_j\rangle=\frac{2\alpha k_B T}{\gamma_0\mu_0 M_s V}\delta_{ij}\delta(\mathbf{r}-\mathbf{r}')\delta(t-t'), \tag{6.3}$$

where k_B is the Boltzmann constant, μ_0 the vacuum permeability and V the volume of the computational cell.

Therefore, the CIDWM is micromagnetically evaluated here by solving both (6.2) and (6.1) in coupled manner by means of a 4th-order Runge-Kutta scheme with a time step of $\Delta t = 0.5$ ps, with $\mathbf{J}(\mathbf{r},t)$ as computed by COMSOL as the only external input. Typical magnetic Py parameters were considered: M_s=8.6×10^5 A/m, exchange constant $A=1.3\times10^{-11}$ J/m, $\alpha=0.02$, $P=0.4$, $\xi=0.04$. The Py strips were discretized using a finite-differences scheme with cells of $\Delta x=\Delta y=5$ nm in side, and thickness equal to the one of the Py layer ($\Delta z=10$ nm). Several preliminary tests were performed to certify the numerical validity of the presented results for smaller cell sizes and time steps.

Similarly to the experimental study [91], the initial magnetic configuration was obtained by firstly saturating the magnetization along the transverse y-axis, and then relaxing the magnetic state in the absence of excitation. The resulting state consists of two transverse DWs as shown in Fig. 6.1(a) and (b). The head-to-head Left DW is close to the top of the left bend, whereas the tail-to-tail one stays around the corresponding bend at the right branch. Starting from these states, current pulses with fixed length of $t_p = 4$ ns are injected between the contacts. In order to preserve the local temperature below the Curie temperature, the maximum current amplitude is varied up to $J_m = 3$ TA/m^2. As a reference test, we firstly studied the magnetization dynamics

	Uniform cross section (UCS)		Non-Unifrom cross section (NUCS)	
$B_{\text{dep}}^{\text{Left}}$ (mT)	-1.175	+0.925	-0.825	+1.2
$B_{\text{dep}}^{\text{Right}}$ (mT)	+0.975	-1.1	+1.2	-0.825
$J_{\text{dep}}^{\text{Left}}$ (TA/m^2)	-6.75	-7.25	-8.25	-5.25
$J_{\text{dep}}^{\text{Right}}$ (TA/m^2)	+6.75	+6.75	+5.25	+8.25

Table 6.1: Depinning fields and currents for right and left DWs.

in the absence of Joule heating, which is the conventional approach adopted to the describe CIDWM under STTs. In this case the temperature of the Py strip is uniform, and therefore, only the Eq. (6.2) is solved. However, the explicit space dependence of $\mathbf{J}(\mathbf{r}, t)$, as given in Fig. 6.1 (e)-(f), is taken into account to evaluate the STTs. At $T = 0$ no net displacement was observed for any of the DWs even for $J_m = 3$ TA/m^2. The reason behind is the local pinning that each DW experiences as due to the unavoidable edge roughness. At uniform room temperature ($T = 300$K), ten different stochastic realizations were evaluated to obtain statistically meaningful results. Neither in this case, were any of the two DWs significantly moved from their initial position along the UCS and NUCS strips. Therefore, due to the local pinning, the current $\mathbf{J}(\mathbf{r}, t)$ is not strong enough to promote a significant displacement in the absence of thermal gradients.

Pinning potential

Before analysing the effect of Joule heating, it is important to study the pinning potential of the two DWs, since a different pinning potential could influence their displacement under the same driving force. In general, due to the curved geometry, and in particular in the non-uniform cross section strip, the evaluation of the local pinning at the initial location of each wall is not straightforward, as discussed hereafter. As the pinning is due to geometric effects, the local depinning that each DW experiences at its initial position was studied at zero temperature. This deterministic characterization of the local pinning was firstly done by applying static longitudinal positive and negative fields, along the x-axis. Note that the Left DW is a Head-to-Head DW whereas the Right DW is a Tail-to-Tail DW. The Left (Right) DW is pushed towards the left by a negative (positive) field. Due to the slightly different curvature radius at the initial DW locations, the local depinning field is different for each DW for both uniform cross section (UCS) and non-uniform cross section (NUCS) strips. The values of the depinning field to the left ($B_{\text{dep}}^{\text{Left}}$) and to the right ($B_{\text{dep}}^{\text{Right}}$) are given in Table 6.1 for each DW and for each UCS and NUCS strips. For instance, in the case of the NUCS strip, negative longitudinal field of -0.825mT is required to depinning both DWs towards the strip center, whereas a positive field of 1.2mT is required to promote the DW depinning towards to the left and right pads respectively. We have also computed the depinning currents ($J_{\text{dep}}^{\text{Left}}$ and $J_{\text{dep}}^{\text{Right}}$), which are defined as the minimum static current needed to promote the DW propagation to the left and to the right side respectively. Note that the STT pushes both DW in the direction of the electron flow (J is positive when the electrons flow from left to right). The results are also collected in the table. This pinning characterization also indicates the asymmetry of the local pinning potential for both UCS and NUCS samples and Left and Right DWs. In the particular case of the NUCS, the Left DW is depinned to the right with a minimum 5.25 TA/m^2, whereas the right DW needs 8 TA/m^2 to be depinned in the same direction. Although the current in the NUCS strip is non-uniform, these values indicate the asymmetry of the local pinning potential. Nonetheless, both current densities would lead to a temperature increase well above the Curie temperature and, in fact, they are both well above our threshold current $J_m = 3\text{TA/m}^2$.

Influence of Joule heating

In order to describe the influence of Joule heating on the CIDWM under current pulses, the analysis was performed by solving Eqs. (6.2)-(6.1), where not only the space distribution of the current $\mathbf{J}(\mathbf{r},t)$, but also the resulting temperature distribution $T(\mathbf{r},t)$ are taken into account. Typical transients micromagnetic snapshots are shown in Fig. 6.3 for a current pulse with $J_m = 3$ TA/m^2 and $t_p = 4$ ns. For the UCS strip (Fig. 6.3(a)) none of the two DWs is significantly shifted for their initial position. However, when the strip cross section is non-uniform (Fig. 6.3 (b)) the Left DW is noticeable displaced ($\Delta X_L \approx 700$ nm) whereas the Right one is hardly affected ($\Delta X_R \approx 50$ nm).

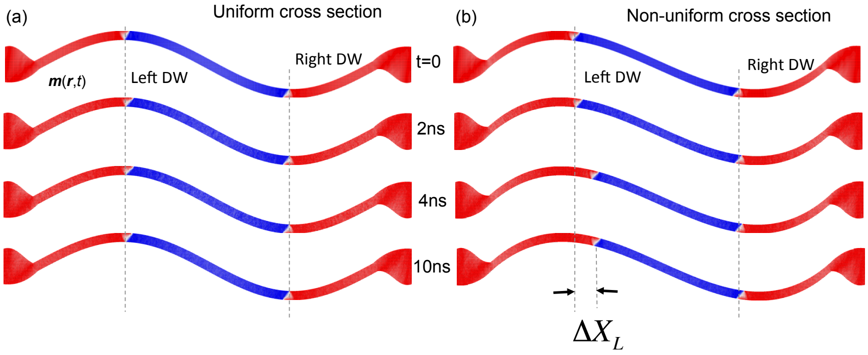

Figure 6.3: Typical micromagnetic snapshots at different instants under a current pulse with $J_m = 3$ TA/m^2 and $t_p = 4$ns for the uniform cross section (a), and non-uniform cross section (b) strips. The space and temporal evolution of the density current $\mathbf{J}(\mathbf{r},t)$ and the temperature $T(\mathbf{r},t)$ are taken into account.

The total displacement of the DWs as a function of J_m is shown in Fig. 6.4 (a) and (b) for both UCS and NUCS cases. Filled symbols correspond to the Joule heating study, by considering both the space and temporal dependence of $\mathbf{J}(\mathbf{r},t)$ and $T(\mathbf{r},t)$. Open symbols correspond to the case where the space and temporal dependence of $\mathbf{J}(\mathbf{r},t)$ is taken into account, but assuming that temperature remains uniform and equal to $T = 300$ K (no Joule heating). In both cases, the displacements of the Left (ΔX_L) and the Right (ΔX_R) walls were averaged over 10 stochastic realizations after 10ns, which is large enough to be sure that the DWs have stopped after the pulse ($t_p = 4$ ns). Indeed, the displacements were found quite similar to the ones achieved at the end of the pulse (4ns), indicating the absence of significant inertia effects.

As it was already pointed out, the net DW displacement for the UCS case remains below 100 nm for the maximum density current evaluated. On the other hand, when both $\mathbf{J}(\mathbf{r}, t)$ and $T(\mathbf{r}, t)$ are taken into account for the NUCS strip, the Left DW is remarkable shifted from its initial position as compared to the Right DW, which remains very close to its starting point.

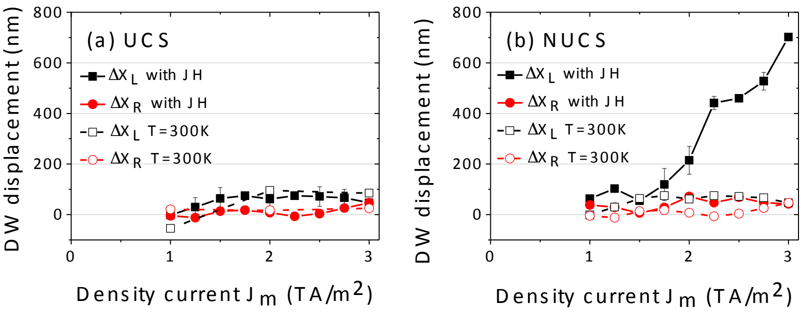

Figure 6.4: Total DW displacement ΔX_i as a function of density current J_m for pulses with $t_p = 4$ns along the uniform cross section UCS (a) and along the non-uniform cross section NUCS (b) for both Left (ΔX_L) and Right (ΔX_R) DWs. The result correspond to the mean values averaged over 10 stochastic realizations at 10ns. JH (Joule Heating) are results considering both the current $\mathbf{J}(\mathbf{r}, t)$ and the temperature $T(\mathbf{r}, t)$ distributions, whereas T=300K-results were obtained by assuming that the temperature is uniform over the sample.

As the critical depinning currents needed to depin both DWs are larger by a factor of two than the maximum amplitude of the injected pulses, there may be an additional ingredient supporting the larger displacement of the Left DW.

It has been theoretically suggested [54, 88] and experimentally confirmed [91, 90] that a DW can be driven by thermal gradient, from low to high temperature regions ($\nabla T > 0$), and this is precisely what our micromagnetic simulations are indicating. Indeed, as the central part of the NUCS strip is hotter than the initial positions of the walls, there is a thermal gradient supporting the current-induced motion of the Left DW towards the center of the strip, and at the same time, acting against it on the Right DW.

One-dimensional model

In order to qualitatively confirm this interpretation, the CIDWM was also analysed in the framework of the 1DM [18,20], which was extended here to study the dynamics of the two DWs coupled to the heat transport by considering the non-uniformities of the current pulse. In this 1DM, an effective thermal field, proportional to the local thermal gradient along the strip [97], is assumed to generate a local driving force on the DWs, $H_i(x,t) \propto \nabla T_i(x,t)$. The temporal evolution of the DW position ($X_L(x,t)$ and $X_R(x,t)$) and internal angle ($\phi_L(x,t)$ and $\phi_R(x,t)$) of each DW are computed from the following Eqs. [91]

$$\frac{\partial X_i(x,t)}{\partial t} = \frac{\Delta}{1+\alpha^2}\left[\gamma_0 \alpha H_i(x,t) - \gamma_0 H_K \frac{\sin 2\phi_i}{2} + (1+\xi\alpha)\frac{\mu_B P}{e M_s} J(x,t)\right], \tag{6.4}$$

$$\frac{\partial \phi_i(x,t)}{\partial t} = \frac{1}{1+\alpha^2}\left[\gamma_0 H_i(x,t) + \alpha\gamma_0 H_K \frac{\sin 2\phi_i}{2} + (\xi-\alpha)\frac{\mu_B P}{e M_s \Delta} J(x,t)\right], \tag{6.5}$$

where Δ is the DW width, H_K the shape anisotropy field and the index $i : L, R$ represents the Left and Right walls respectively. The field $H_i(x,t)$ is the thermodynamic field on the position of each wall pointing in the direction of the local thermal gradient $\nabla T_i(x,t)$ [91]

$$H_i(x,t) = \frac{\sigma_0}{2\mu_0 M_s (T_C - T_{ref})} \nabla T_i(x,t)\,, \tag{6.6}$$

where σ_0 is the energy of the walls per surface unit, and T_C the Curie temperature. The local temperature needed to compute $H_i(x,t)$ is obtained by solving the heat Eq. 6.1 by assuming that the current is flowing along the x-axis and it only depends on x ($\mathbf{J} = J(x,t)\hat{\mathbf{u}}_x$). Therefore, and for the sake of simplicity Eqs. (6.4) and (6.5) are numerically solved as coupled to the heat Eq. (6.1) by considering a straight strip with 12 μm in length (Note that the total length of the curved strips is larger than this value). All parameters in (6.4) - (6.5) are the same as in the full micromagnetic study, and $\Delta = 25$ nm, $\sigma_0 = 0.05$ J/m^2 and $H_K = 139261$ A/m were adopted to reproduce the micromagnetic results of the DW at rest and the Walker breakdown ($B_W = 1.75$ mT). The normalized current density profile $J(x,t)/J_m$ considered in this 1DM analysis is the one computed by COMSOL by averaging over the strip width for the non-uniform cross section sample. This profile is shown in Fig. 6.5(a) by open symbols, and it can be fitted to the following analytical expression

$$\frac{J(x,t)}{J_m} = A - B\exp\left[-\frac{(x-x_{0L})^2}{L^2}\right] - B\exp\left[-\frac{(x-x_{0R})^2}{L^2}\right], \tag{6.7}$$

with $A = 2.14$, $B = 1.06$, $L = 4.77$ μm, and $x_{0L} = -4$ μm, $x_0 R = +4$ μm. From this current profile $J(x,t)$, the space and temporal evolution of the temperature $T(x,t)$ along the straight strip is computed by solving Eq. (6.1) with the same inputs as for the full micromagnetic study described above and in the main text. The results for the local temperature at different instants of time along the strip under a current pulse with $J_m = 2$ TA/m^2 and $t_p = 4$ ns are shown in Fig. 6.5(b). These profiles, which accurately reproduce those obtained by COMSOL, clearly show the presence of the hot and cold points corresponding to positions with high and low density currents, and consequently, the appearance of thermal gradients along the strip. The temporal evolution of the temperature at two representative points is depicted in Fig. 6.5(c), which is also in good agreement with COMSOL and micromagnetic results described above. From $t = 0$, the temperature increases exponentially and it saturates to a terminal value before the current pulse is switched off at $t_p = 4$ ns. After that, the temperature relaxes to the room temperature with the same characteristic time $\tau = 1$ns. Starting from the initial positions $X_L(0) = -2.5$ μm and $X_R(0) = +2.5$ μm for the Left and the Right DWs respectively, their displacement ($\Delta X_i = X_i(10ns) - X_i(0)$) are analyzed in framework of the 1DM for the same current pulses as done in the full micromagnetic case. These 1DM predictions are shown in Fig. 6.5(d), and they are in good qualitative agreement with the full micromagnetic observations of Fig. 6.4(b). There is not quantitative agreement in the displacements but this is expected as neither the local pinning nor the curved shape of the strip are taken into account in the 1DM. Indeed, although the current profile is the one obtained from the curved strip, the thermal gradients in this 1DM study are larger due to the different length of the strip (12 μm for the 1DM description of the straight strip, which is smaller than the real length of the curved strip). Nevertheless, the same trends are clearly pointing out the main ingredients responsible for the observations. Indeed, the left wall is moved over larger distances as compared to the right wall, which remains close to its initial position for the evaluated pulses. These results can be understood by taking into account not only the STTs on each wall but also the effective thermal field proportional to the local thermal gradient at their starting positions, indicated by arrows in Fig. 6.5(a)-(b). The magnitude of the STT is exactly the same for the two walls, as $J(x, 0)$ does. However, the thermodynamic effective field $H_i(x, t)$ is different: while $\nabla T_L(x, t) > 0$ supports the STT pointing along the $x > 0$ for the Left DW, $\nabla T_R(x, t) < 0$ acts against the STT for the Right wall, and this explains the different displacements under the same current pulses.

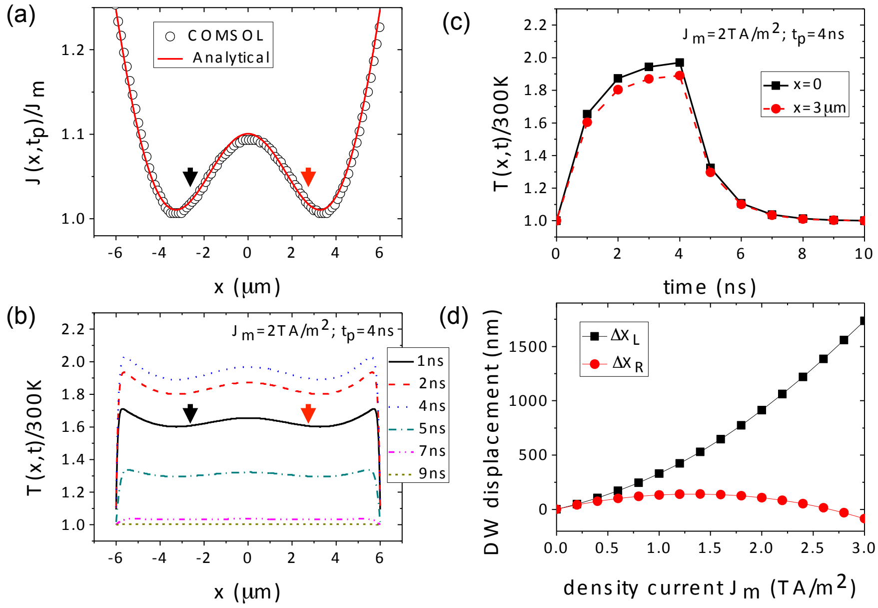

Figure 6.5: 1DM analysis of the CIDWM under non-uniform current pulses. (a) Density current profile $J(x,t)/J_m$ as computed by COMSOL (open symbols) and analytic fit (solid line) as described in the text. (b) $T(x,t)$ as a function of x for different instants during a current pulse with $J_m = 2\ \mathrm{TA/m^2}$ and $t_p = 4$ ns. (c) $T(x,t)$ as a function of time at two different positions along the strip. (d) Total DW displacement ΔX_i as a function of density current J_m for pulses with $t_p = 4$ ns along a straight strip with non-uniform density current as computed from the 1DM. The initial positions of the Left and Right DWs with respect to the strip center ($x = 0$) are $X_L(0) = -2.5\ \mu$m and $X_R(0) = +2.5\ \mu$m respectively.

6.3 Conclusions

To summarize, the current-induced motion along the curved Py strips with uniform and non-uniform cross sections has been analysed by micromagnetic simulations coupled to the heat transport considering the electrical contacts to inject the current pulses along with the conventionally used SiO_2/Si substrate underneath.

In the case of strips with UCS, the temperature increases from the contacts to the center of the strip over a very small typical distance < 100nm, but except from these lateral parts, the temperature of the strip remains uniform. Consequently, two DWs very far from these contacts are not affected by thermal gradients when driven by the spin-transfer torque. On the contrary, the DW dynamics is completely different along strips with non-uniform cross section, where the current becomes non uniform and therefore, it results in the appearance of thermal gradients along the strip. In this case, a thermodynamics force proportional to the local thermal gradient is found to enhance or reduce the DW displacement induced by the STT as depending on both its magnitude and direction. Our micromagnetic study, confirms that the cross section of the strip plays a significant role in the current-induced domain wall, and although performed for a different geometry intended to avoid inertia effects, also supports recent experimental observations and interpretations by Torrejon et al. [91].

The developed framework here would be useful for further studies providing meaningful descriptions of the current-induced DW depinning from notches, where high density currents are expected to generate substantial Joule heating, and therefore resulting in different estimations of the STT parameters. It also opens the door to the study of the thermal excitation of magnons in controlled manner by means of Joule heating, along with the investigation of the torque they exert on magnetic textures at the nanoscale. Apart from its fundamental interest, the control of the Joule heating could also be relevant for future technological applications.

Chapter 7

Influence of Joule heating on current-induced domain wall depinning

The domain wall depinning from a notch in a Permalloy nanostrip on top of a SiO_2/Si substrate is studied theoretically under application of static magnetic fields and the injection of short current pulses. The influence of Joule heating on current-induced domain wall depinning is explored self-consistently by coupling the magnetization dynamics in the ferromagnetic strip to the heat transport throughout the system. Our results indicate that Joule heating plays a remarkable role in these processes, resulting in a reduction in the critical depinning field and/or in a temporary destruction of the ferromagnetic order for typically injected current pulses. In agreement with experimental observations, similar pinning-depinning phase diagrams can be deduced for both current polarities when the Joule heating is taken into account. These observations, which are incompatible with the sole contribution of spin transfer torques, provide a deeper understanding of the physics underlying these processes and establish the real scope of the spin transfer torque. They are also relevant for technological applications based on current-induced domain-wall motion along soft strips. [1]

7.1 Introduction

Magnetic domain walls (DWs) in patterned nanostrips have attracted a considerable attention due to their application in field- and current-induced DW logic[3] and memory devices [2]. Key to the successful operation of these memory devices is the controllable motion of DWs between pinning sites using current pulses which, contrary to the field-driven case, will coherently drive neighboring walls in the same direction

---

[1] Adapted from S. Moretti, V. Raposo and E. Martinez, J. Appl. Phys. 119, 213902 (2016)

through the nanostrip. Experiments have shown that the injection of an electrical current through a soft Permalloy (Py) strip can drive domain walls in the direction of the electron flow [76, 77, 78] and/or assist the field-driven depinning from a patterned constriction[79]. DW transformations[100], and even the nucleation of multiple walls [81] have also been observed under injection of current pulses. These observations are usually interpreted in terms of the spin-transfer torque (STT) mechanism, as predicted by Berger and Slonczewski[19, 20]. Since the electrical current becomes spin-polarized in the magnetic direction of the ferromagnet, the polarization of the spin flips when a DW is encountered. Because of angular momentum conservation, this change in angular momentum of the conduction electrons leads to a reaction torque on the DW called adiabatic STT, and the DW is pushed in the direction of the electron flow. In addition to this torque, a second, non adiabatic STT was suggested[27, 26, 28, 101] to explain the discrepancies with the experimental results. The common interpretation is that the spin polarization of the electric current cannot follow the local magnetization within the DW, and a misalignment between the current and the DW magnetization occurs, which acts as an additional field-like torque on the DW. This torque is parametrized by the so-called non adiabatic parameter ξ. However, the physical origin, as well as the magnitude of this non adiabatic STT contribution, remains controversial to this day[80]. The debate is reinforced by the high disparity of the estimated STT parameters, spin polarization P and nonadiabaticity ξ, as deduced from experiments on similar Py samples (see [80] and references therein). Therefore, a complete understanding of these observations is lacking, and further theoretical and numerical efforts are still needed.

A typical design for measuring the STT parameters consists of analysing the depinning of a DW initially trapped at a notch. In the absence of current, the DW can be expelled from the notch under a sufficiently large magnetic field. Since the non-adiabatic contribution enters in the magnetization dynamics equation as an effective magnetic field[27, 26, 28, 101, 80, 102, 103], the STT parameters (P and ξ) can be inferred by measuring the reduction or the enhancement of the required field as a function of the injected current. The experimental results of critical depinning current as a function of the applied field are usually described in terms of standard micromagnetic and/or simple $1D$ models, which describe the DW dynamics governed by the Landau-Lifshitz-Gilbert (LLG) equation including the adiabatic and nonadiabatic STTs. However, these conventional approaches assume that the current density is flowing uniformly along the strip[102, 104, 105]. This constitutes an oversimplification when the strip cross section is non-uniform, and especially when the current is forced to pass through constrictions.

Apart from the STTs, it is well known that an electric current also generates Joule heating. Although several experimental works have indicated that its effect can be significant [79, 81, 82, 95, 106, 107, 108], its influence on DW depinning has not yet been assessed. Reductions in the DW propagation field [108] or in the switching field [106] have been experimentally observed in Py samples and ascribed to Joule heating. Furthermore, numerical studies[73, 91, 96] of the heat transport in these systems have shown that non-uniform temperature profiles can appear during the current pulse and that, depending on the current and the substrate, the local temperature can be close to or even above the

Curie temperature (T_C). Although thermal fluctuations at uniform room temperature have been studied numerically with the stochastic version of the Landau-Lifshitz-Gilbert equation[102, 94, 103], this Langevin approach is restricted to uniform temperatures well below the Curie threshold, and therefore it fails to describe the current-assisted DW depinning in systems where the temperature varies significantly. Here we develop a micromagnetic framework that couples both the electric and the heat transport to the magnetization dynamics self-consistently. Within this formalism, the magnetization dynamics is described by the Landau-Lifshitz-Bloch (LLB) equation[53, 49, 55, 50, 54, 56, 59], which allows us to properly describe the current-assisted DW depinning for temperatures close to or even above T_C.

As an archetypal experiment, the developed formalism is used here to numerically evaluate the phase diagram for current-assisted DW depinning studied experimentally by Hayashi et al.[79]. This experiment was performed on a 6μm-long Py nanostrip on top of a SiO$_2$/Si substrate. The Py strip has a 300nm × 10nm cross section and contains a triangular notch with a depth of $\approx$ 100nm. Four different initial magnetic DW configurations pinned at the notch were observed, depending on the nucleation process: vortex or transverse DWs, pinned at the center or at the left side of the notch (see Fig. 2 in[79] for a detailed description of the nucleation process). After nucleation and pinning of DWs, 4ns current pulses with both polarities ($J > 0$ and $J < 0$) of different amplitudes were applied through two gold contacts placed at a distance of 4μm from each other under bias static fields $\mathbf{H}_B = H_B\mathbf{u}_x$ along the longitudinal x-axis. A sketch of the system is shown in Fig. 7.1(a). After each current pulse, the presence or absence of the DW between the contacts was detected by resistance measurements, and the probability of current-assisted DW depinning was obtained as a function of the external field. The critical depinning current was defined as the one at which depinning probability exceeds 50%. As expected, in the absence of current pulses ($J = 0$), the DWs initially trapped at the center of the notch were symmetrically depinned by positive ($H_B > 0$) and negative ($H_B < 0$) fields with the same magnitude. By contrast, the DWs pinned at the left side of the notch are more easily depinned by negative fields than by positive fields, simply because of the asymmetric pinning potential[79]. However, in the presence of current pulses ($J \neq 0$), two noticeable results can be observed in the measured depinning diagrams shown in Fig. 3 of Ref.[79]. First, DW depinning is not achieved in the absence of an applied field, and therefore, the evaluated currents alone do not exert a significant force on the DWs. Second, regardless of the initial magnetic configuration, all phase diagrams show a marginal dependence on the current polarity, i.e. positive ($J > 0$) and negative ($J < 0$) currents produce roughly the same phase diagram. These observations are not fully compatible with pure STT contributions[26, 28], which push the DW in opposite directions, depending on current polarity. By contrast, they suggest that the experimental results could be compatible with Joule heating (JH), which does not depend on the current polarity. In fact, Hayashi et al. [79, 109] estimated an averaged temperature of about $\approx$ 780K during the injection of the pulses with $J \approx 3 \times 10^8$A/cm^2. These temperatures are close to the Curie temperature of Py ($T_C \approx$ 850K[81]), underscoring the need to consider the effects of Joule heating.

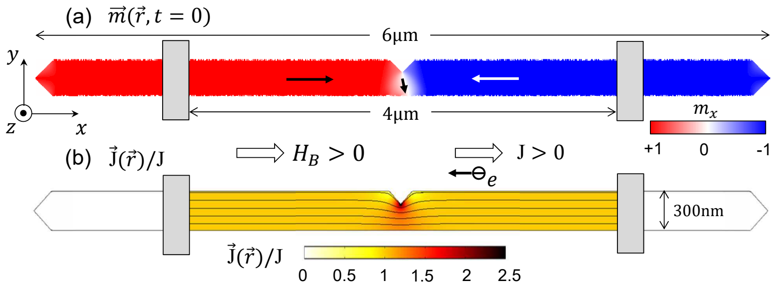

Figure 7.1: (a) Geometry of the Py strip and initial magnetization state, $\mathbf{m}(\mathbf{r}, t = 0)$. (b) Spatial distribution of the current density $\mathbf{J}(\mathbf{r}, t)$ during the current pulse $0 \leq t \leq 4\text{ns}$. Lines represent schematically the local direction of the current density while the color represents its local module normalized to the value at points distant from the notch (J), where the current density is uniform across the strip width and points along the x-axis.

In this paper, we analyse the current-assisted DW depinning from a notch under static fields and short current pulses, with emphasis on elucidating the effect of Joule heating. The paper is organized as follows. The conventional micromagnetic formalism based on the LLG equation and neglecting Joule heating is presented in Sec. 7.2.1, which also includes its predictions and stresses its limitations to explain the experimental observations. In Sec. 7.2.2 we describe the heat dynamics by means of electro-thermal simulations of the entire sample. A phenomenological model describing the heat transport is also presented and validated to further describe the heat transport coupled to the magnetization dynamics in the Py strip. The model developed for the heat transport is then coupled to the magnetization dynamics given by the LLB Eq. in Sec. 7.2.3, and the predictions for the DW depinning results are presented and compared with the experimental measurements. Sec. 7.2.3 presents a brief discussion of the results while the main conclusions of our study and their implications are summarized in Sec. 7.3.

7.2 Results and Discussion

7.2.1 Standard LLG model

In what follows, we focus our attention on the case of a transverse DW initially pinned in the center of the notch as shown in Fig. 7.1(a). Although the geometry and the dimensions of the Py strip were selected here to mimic the experimental samples studied by Hayashi et al.[79], the exact geometry and dimensions of the notch may slightly differ. In the present study, a 100nm-depth and 200nm-wide triangular notch is assumed. In addition to the notch, realistic conditions were considered by taking into account roughness [102] at the edges, with a characteristic size $\approx$ 5nm. In order to show the limitations of neglecting Joule heating, we first report the results obtained by standard micromagnetic simulations, where the magnetization dynamics at uniform and finite temperature $T \ll T_C$ is described by the Landau-Lifshitz-Gilbert (LLG) equation augmented by adiabatic and non-adiabatic STTs [26, 102]

$$\begin{aligned}\frac{\partial \mathbf{m}}{\partial t} &= -\frac{\gamma_0}{1+\alpha^2}\left[\mathbf{m}\times(\mathbf{H}_{\text{eff}}+\mathbf{H}_{\text{th}})\right] - \frac{\gamma_0\alpha}{1+\alpha^2}\left\{\mathbf{m}\times\left[\mathbf{m}\times(\mathbf{H}_{\text{eff}}+\mathbf{H}_{\text{th}})\right]\right\} \\ &\quad + \frac{u}{1+\alpha^2}(1+\xi\alpha)\mathbf{m}\times(\mathbf{m}\times(\mathbf{J}\cdot\nabla)\mathbf{m}) + \frac{u}{1+\alpha^2}(\xi-\alpha)\mathbf{m}\times(\mathbf{J}\cdot\nabla)\mathbf{m}\,,\end{aligned} \tag{7.1}$$

where $\mathbf{m}(\mathbf{r},t) = \mathbf{M}(\mathbf{r},t)/M_s$ is the normalized magnetization and $\mathbf{H}_{\text{eff}}(\mathbf{r},t)$ is the effective field, which includes the standard micromagnetic contributions [94, 110]. γ_0 is the gyromagnetic ratio and α is the Gilbert damping. $\mathbf{J}(\mathbf{r},t)$ is the current density and $u = \mu_B P^0/(M_s^0|e|(1+\xi^2))$, where μ_B is the Bohr magneton and e the elementary charge. P^0 and M_s^0 are the current polarization and the saturation magnetization at zero temperature while ξ represents the dimensionless non-adiabatic parameter [26, 28, 101]. Thermal fluctuations at uniform and constant room temperature $T = 300$K are taken into account through a stochastic thermal field $\mathbf{H}_{\text{th}}$, which has white noise properties with the correlator [94, 46, 47]

$$\langle H_{\text{th}}(\mathbf{r},t)_i H_{\text{th}}(\mathbf{r}',t')_j\rangle = \frac{2\alpha k_B T}{\gamma_0\mu_0 M_s V}\delta_{ij}\delta(\mathbf{r}-\mathbf{r}')\delta(t-t'), \tag{7.2}$$

where k_B is the Boltzmann constant, μ_0 the vacuum permeability and V the volume of the computational cell. Starting from the initial state depicted in Fig. 7.1(a), 4ns current pulses together with a bias field $\mathbf{H}_B = H_B\mathbf{u}_x$ are applied and the magnetization dynamics is studied by solving numerically Eq. (7.1) using a 4th-order Runge-Kutta scheme. $\mathbf{J}(\mathbf{r},t)$ was previously calculated by COMSOL[75] (see Fig. 7.1(b)) and included in Eq. (7.1). Typical Py parameters were considered: $M_s \equiv M_s^0 = 8.6\times10^5$ A/m^2, $A^0 = 1.3\times10^{-11}$ J/m (exchange constant at zero temperature), $\alpha = 0.02$, $P^0 = 0.4$ and $\xi = 0.04$ [80]. The micromagnetic results described below were obtained by using a computational time step of $\Delta t = 0.1$ps, and it was checked in several tested cases that a reduced time step of $\Delta t = 0.05$ps did not modify the obtained results. The Py strip is spatially discretized using cubic computational cells $\Delta x = \Delta y = \Delta z = 5$nm. In order to obtain the depinning probability at $T = 300$K, 10 stochastic realizations were evaluated. Under these conditions, we computed the critical DW depinning current J_d as a function of the bias field. As in Ref. [79], J_d is defined as the minimum current density needed to depin the DW with a probability higher than 50%. Henceforth, we shall use J to indicate the modulus of the current density at points distant from the notch, where $\mathbf{J}$ is uniform across the strip width and it points along the longitudinal direction ($\mathbf{u}_J = \mathbf{u}_x$). Note that, due to the notch, $|\mathbf{J}|$ is higher below the notch and has a y component (Fig. 7.1(b)). The DW was considered as depinned when it was expelled outside the gold contacts (Fig. 7.1), as would be obtained with magneto-resistance measurements[79].

The results are shown in Fig. 7.2(a) and 7.2(b) for negative and positive currents respectively. In the absence of current ($J = 0$), the depinning fields are $H_d^{\mp} = -75/+70$ Oe; i.e., slightly higher than the experimental ones [79] ($H_d^{\mp} = -54/+54$ Oe), meaning a slightly different notch. From the results collected in Fig. 7.2, two noticeable differences with the experimental observations (see Fig. 3(a) in [79]) can be found: On the one hand, the amplitude of the depinning currents J_d is around 5 times larger than the ones measured experimentally. On the other hand, the experimental depinning diagrams depicted in Fig. 3(a) of Ref. [79] are almost independent of the current polarity, i.e., positive and negative currents produce roughly the same reduction on the depinning field. However, and in agreement with the STT contribution that pushes the DW in opposite directions, here we found an evident asymmetric depinning diagram with respect to the current polarity. For instance, under negative current pulses ($J < 0$ with the electron flowing along the positive x direction, Fig. 7.2(a)), we found more depinning events for $H_B > 0$, where the STT and the bias field push the DW in the same direction. If we reverse the current ($J > 0$, Fig. 7.2(b)) we have more depinning events for $H_B < 0$. This asymmetric behaviour is due to the balance between the two driving forces: for $J < 0$, for instance, the STT pushes the DW always to the right, coherently with positive bias fields ($H_B > 0$) and opposite to negative bias fields. If we reverse the current, the situation is reversed and the STT favours negative bias fields, which push the DW to the left. We checked that it was not possible to reproduce the experimental phase diagram for any of the combinations of the STT parameters ($0 \leq P^0 \leq 1$ and $0 \leq \xi \leq 5\alpha$): an increase in ξ decreases the depinning current but increases the asymmetry with the current polarity. Also, an increase of P^0 up to unrealistic values ($P^0 = 1$) can decrease the depinning current but does not lead to the experimentally observed symmetry. These results indicate that conventional micromagnetic simulations are inadequate to reproduce the experimental results in these systems. As mentioned, Hayashi et al. [79] already estimated an average temperature between the contacts of about $T_{av} \approx 780$K during the injection of the pulses with $J \approx 3 \times 10^8$A/cm^2. These temperatures, being close to the Curie temperature of Py ($T_C \approx 850$K), suggest that a more realistic description, that takes into account Joule heating effects, needs to be adopted in order to correctly describe the current-assisted DW depinning in these systems.

7.2.2 Heat dynamics

In order to evaluate the relevance of Joule heating effects on the current-assisted DW depinning, a preliminary analysis of heat transport is required. The temperature evolution of the sample is governed by the heat equation

$$\frac{\partial T(\mathbf{r},t)}{\partial t} = \frac{k}{\rho C}\nabla^2 T(\mathbf{r},t) + \frac{Q(\mathbf{r},t)}{\rho C}\,, \tag{7.3}$$

where k is the thermal conductivity, ρ the density, and C the specific heat capacity of the material. $T = T(\mathbf{r},t)$ represents the temperature and Q the heat source. For Joule heating $Q(\mathbf{r},t) = \mathbf{J}(\mathbf{r},t)^2/\sigma$, where $\mathbf{J}(\mathbf{r},t)$ is the current density and σ is the electrical conductivity. Analytical solutions of Eq. (7.3) have been obtained under the

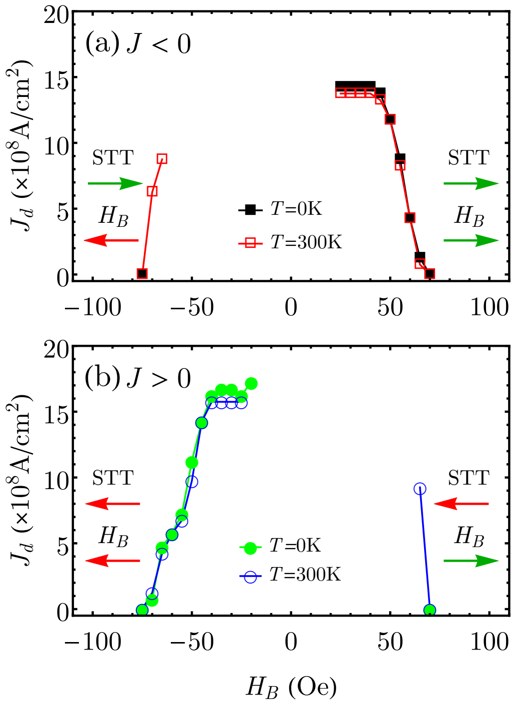

Figure 7.2: Depinning current (J_d) as a function of the bias field (H_B) obtained with the standard LLG equation in the absence of Joule heating for (a) negative and (b) positive current pulses. Results are shown for 0 and constant room temperature. STT (H_B) pushes the DW in the direction of the arrows. Errors bars, corresponding to the adopted current step, are smaller than the plot markers.

assumption of uniform temperature and semi-infinite substrate [111, 112]. Here, due to the non-uniform source and the finite substrate thickness, we solved Eq. (7.3) for the full system (Py/SiO$_2$/Si) by COMSOL simulations. Typical Py parameters [73] were considered: $\rho_{Py} = 8.7 \times 10^3$ Kg/m^3, $C_{Py} = 0.43$ J/(gK), $k_{Py} = 46.4$ W/(Km), $\sigma_{Py} = 4 \times 10^6$ $(\Omega\text{m})^{-1}$. For the Si substrate, nominal parameters were also assumed: $\rho_{\text{Si}} = 2.329 \times 10^3$ Kg/m^3, $C_{\text{Si}} = 0.7$ J/(gK) and $k_{\text{Si}} = 130$ W/(Km). The presence of a thin native SiO$_2$ interlayer [109] was also taken into account. Consistent with a previous analysis[96], this interlayer imposes a thermal resistance[99] between the Py strip and Si substrate (Ref. [75]). Here a thermal resistance of 2.2×10^{-8}m^{2}K/W was adopted to reproduce the experimental results[79]. Owing to the high thermal conductivity of Au, the electrical contacts are considered to be sinks for the heat, and therefore their temperature is fixed to room temperature. The electrical conductivity is assumed to be different from zero only in the Py and in the Au contacts.

As an example, the temperature of the Py strip is shown for a 4ns current pulse with a magnitude of $J = 3 \times 10^8$A/cm^2. COMSOL predictions are shown by blue dots in Fig.

7.3. The temporal evolution of the Py temperature, averaged over the region between the Au contacts (T_{av}^{Th}), is shown in Fig. 7.3(a). Upon application of the current pulse, T_{av}^{Th} increases monotonously (see Fig. 7.3(a) for $0 < t < 4$ns), and it relaxes again to room temperature once the current pulse is switched off (see Fig. 7.3(a) for $t > 4$ns). The temperature profile ($T(\mathbf{r}, t)$) along the middle line of the Py strip ($y = 150$nm), at the end of the pulse ($t = 4$ns), is shown in Fig. 7.3(b). The temperature profile indicates that the temperature is not uniform along the Py strip, with remarkable variations around the notch, where the current density is larger (see Fig. 7.1(b)).

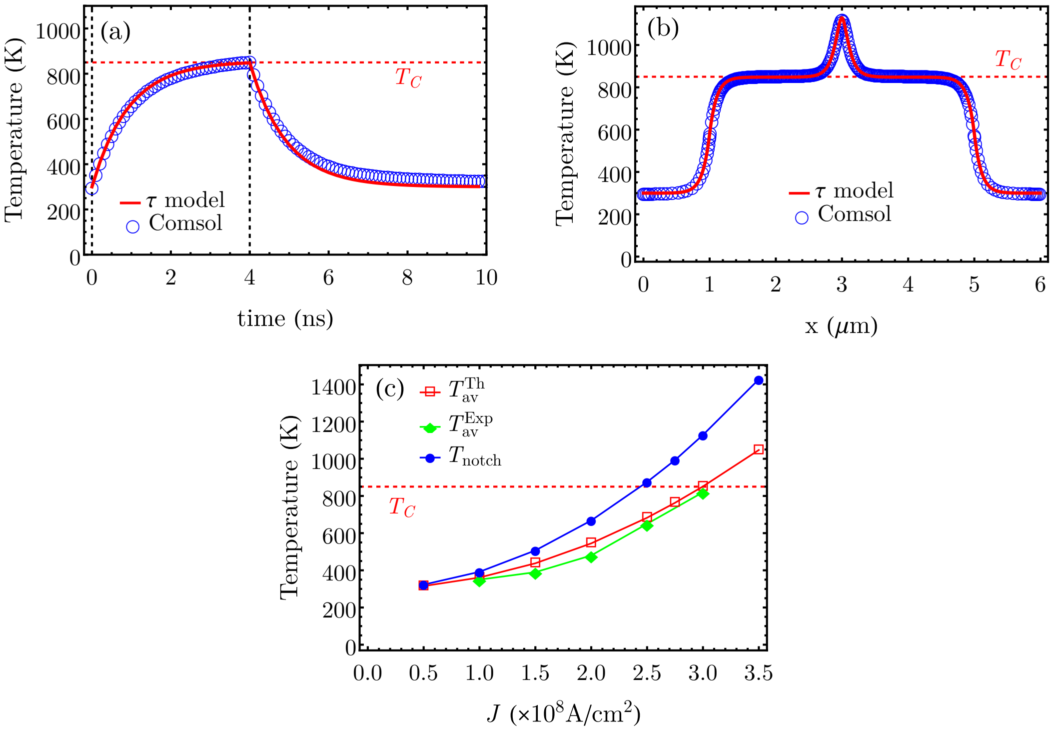

Figure 7.3: (a) Temporal evolution of the averaged temperature ($T_{av}^{Th}(t)$) in the Py strip for $J = 3 \times 10^8 \mathrm{A/cm}^2$. The average was computed between the two contacts used to inject the current pulse. (b) Temperature profile ($T(x, y = 150\mathrm{nm})$ vs x) in the middle of the strip ($y = 150$nm) at $t = 4$ns for the same current $J = 3 \times 10^8 \mathrm{A/cm}^2$. (c) Average temperature (T_{av}^{Th}) at the end the pulse ($t = 4$ns) as a function of the applied current density J. The experimental data (T_{av}^{Exp}) were extracted from Ref. [79]. The theoretically computed local temperature at the notch location (T_{notch}) is also shown.

Since the inclusion of the substrate into the micromagnetic code would be prohibitive from a computational point of view [2], we adopted a phenomenological model of the heat

---

[2] An alternative could be importing the temperature distribution obtained by COMSOL at each time-

transport by adding an additional term into Eq. (7.3), which now reads[74]

$$\frac{\partial T(\mathbf{r},t)}{\partial t} = \frac{k}{\rho C}\nabla^2 T(\mathbf{r},t) + \frac{Q(\mathbf{r},t)}{\rho C} - \frac{T(\mathbf{r},t) - T_0}{\tau} \tag{7.4}$$

where the last term in Eq. (7.4) takes into account the cooling of the wire through the substrate and the surrounding ambient. The parameter τ represents the characteristic time at which the heat flows from the strip to the substrate and it was fixed to $\tau = 0.9$ns in order to have, for all the currents and at the end of the 4 ns pulse, the same averaged temperature as estimated experimentally in Ref. [79] (T_{av}^{Exp}), and also obtained by the COMSOL simulations described above. Unlike Eq. (7.3), the phenomenological heat Eq. (7.4) is only solved for the Py strip, and therefore, it can be implemented to evaluate the heat transport and the magnetization dynamic simultaneously. In order to validate this phenomenological model, its predictions are depicted in Fig. 7.3(a) and (b) by solid red lines. Both the temporal evolution (Fig. 7.3(a)) and the local temperature profile (Fig. 7.3(b)) are in remarkable agreement with COMSOL results, which allows us to easily couple the heat transport to the magnetization dynamics in our micromagnetic code.

Fig. 7.3(c) shows the Py temperature as a function of J. The calculated average temperature (T_{av}^{Th}) is in agreement with the experimental values (T_{av}^{Exp}) of Ref. [79]. Note that for large current pulses ($J \geq 2.5 \times 10^8 \mathrm{A/cm^2}$), even if the average temperature T_{av} remains below the Curie point, the local temperature at the notch (T_{notch}) reaches values above T_C (Fig. 7.3(c)), leading to a local destruction of the ferromagnetic order. In agreement with previous analysis [73] we found that the temperature dynamics strongly depends on the substrate. In particular, in our case it depends on the thickness of the small SiO_2 inter-layer. This can explain the comparable increases in temperature observed in similar Py samples for much lower current densities [106, 107, 108]. In some of those systems for instance, the SiO_2 insulating layer was much thicker (≈ 100 nm) [107, 108] or the substrate was different [106, 108] leading to a less efficient heat absorption and a higher increase in temperature.

7.2.3 Influence of Joule heating

In Sec. 7.2.1 we showed that the analysis of the current-assisted DW depinning in the framework of the conventional micromagnetic model, which includes the STTs but neglects Joule heating phenomena, is not sufficient to explain several features observed in the experiment[79]. In particular, the model overestimates the magnitude of the critical depinning currents as compared to those observed in the experiment. Moreover, the lack of symmetry with respect to the current polarity in the depinning phase diagrams predicted by this oversimplified model is not consistent with the experimentally observed

---

step. However, also this process would significantly slow down the simulations since the copy of data from and to the GPU's memory requires a considerable time and it would need to be repeated many times ($\approx 10^5$ times). Considering the remarkable agreement with the phenomenological model, this operation is not needed.

symmetry. Additionally, both the experimental measurements of the average temperature and the theoretical analysis performed in Sec. 7.2.2, indicate that Joule heating needs to be taken into account in order to provide a more realistic description of these systems. Therefore, the magnetization dynamics must be studied as being coupled to the heat transport excited by the current pulses.

Since the sample reaches temperatures near or even above T_C we can not use the LLG equation, valid for $T \ll T_C$. A natural choice is the Landau-Lifshitz-Bloch (LLB) equation [53], which can describe the magnetization dynamics for a wide range of temperatures, even above T_C [49, 55]. It has been used to describe ultrafast demagnetization processes [50] as well as DW motion by thermal gradients[54]. Here we extend its application to the analysis of the JH effect in current-assisted DW depinning. The STT contributions were included in the LLB Eq. [59] by Schieback et al. [56]. The LLB equation describing the magnetization dynamics under STT reads as [3]

$$\begin{aligned}
\frac{d\mathbf{m}}{dt} = & -\frac{\gamma_0}{1+\tilde{\alpha}_\perp^2}(\mathbf{m}\times\mathbf{H}_{\text{eff}}) - \frac{\gamma_0\tilde{\alpha}_\perp}{(1+\tilde{\alpha}_\perp^2)m}\left\{\mathbf{m}\times\left[\mathbf{m}\times(\mathbf{H}_{\text{eff}}+\mathbf{H}_{\text{th}}^{\perp})\right]\right\} \\
& +\gamma_0\frac{\alpha_\parallel}{m^2}(\mathbf{m}\cdot\mathbf{H}_{\text{eff}})\mathbf{m}+\mathbf{H}_{\text{th}}^{\parallel} \\
& -\frac{1}{1+\tilde{\alpha}_\perp^2}\left[u(1+\tilde{\alpha}_\perp\xi)(\mathbf{J}\cdot\nabla)\mathbf{m}-\frac{u}{m}(\xi-\tilde{\alpha}_\perp)\mathbf{m}\times(\mathbf{J}\cdot\nabla)\mathbf{m}\right] \\
& +\frac{1}{1+\tilde{\alpha}_\perp^2}\frac{u}{m^2}\tilde{\alpha}_\perp\left(\xi-\tilde{\alpha}_\perp\right)\left[\mathbf{m}\cdot(\mathbf{J}\cdot\nabla)\mathbf{m}\right]\mathbf{m}\,, \qquad (7.5)
\end{aligned}$$

where $\tilde{\alpha_\perp} = \alpha_\perp/m$. Apart from the conventional precessional and damping terms (first and second term on the RHS of Eq. 7.5) the LLB equation includes an additional longitudinal relaxation term (third term on the RHS of Eq. 7.5) which describes the relaxation of the modulus of **m** towards its equilibrium value $m_e(T)$. $m_e(T)$ represents the normalized equilibrium magnetization at each temperature, which we calculated by using the Brillouin function for 1/2 spins, namely [11][4]

$$m_e = \tanh\left[\frac{\mu_0\mu_{\text{Py}}}{k_B T}H_B + \frac{T_C}{T}m_e\right]\,, \qquad (7.6)$$

where μ_{Py} represents the Py atomic magnetic moment and H_B the external field. We assumed $\mu_{\text{Py}} = \mu_B$ according to previous calculations [113]. A characteristic feature of the LLB is precisely that, contrary to the LLG, **m** is not unitary but its modulus varies depending on the temperature. Note that, this longitudinal relaxation is neglected within the LLG formalism since, at $T = 300K$, it is much faster than the transverse relaxation.

---

[3] Eq. (7.5) is different from the LLB equation used in Ref. [6] due to the presence of an additional term in the STT and the damping term $1+\tilde{\alpha_\perp}^2$. Eq. (7.5) is the correct one since we realized that there was an error in Ref. [6]. However, the differences are only of the second order in the damping parameter and we checked that the results are not affected.

[4] The effect of H_B has been neglected in the calculation since its contribution is negligible for the magnitude of the maximum applied field ($H_B^{max} \approx 10$mT).

However it becomes particularly important at T close to T_C where longitudinal and transverse relaxation times are comparable. $\alpha_\perp$ and $\alpha_\parallel$ are the transverse and the longitudinal damping parameters respectively. They depend on the temperature as [53, 49, 55] $\alpha_\perp = \alpha_0(1 - T/(3T_C))$ and $\alpha_\parallel = 2\alpha_0 T/(3T_C)$ for $T < T_C$, while $\alpha_\perp = \alpha_\parallel = 2\lambda T/(3T_C)$ for $T > T_C$. α_0 represents a microscopic damping parameter. In the limiting case of zero temperature $\alpha_\perp$ reduces to the conventional Gilbert damping with $\alpha \equiv \alpha_0$ and $\alpha_\parallel = 0$. The effective field $\mathbf{H}_{\text{eff}}$ is given by [53, 49, 55]

$$\mathbf{H}_{\text{eff}} = \mathbf{H}_{\text{exch}} + \mathbf{H}_B + \mathbf{H}_{\text{dmg}} + + \begin{cases} \frac{1}{2\chi_\parallel}\left(1 - \frac{m^2}{m_e^2}\right)\mathbf{m}, & T < T_C \\ -\frac{1}{\chi_\parallel}\left(1 + \frac{3}{5}\frac{T_C m^2}{(T-T_C)}\right)\mathbf{m}, & T > T_C \end{cases}, \tag{7.7}$$

where $\mathbf{H}_B$, $\mathbf{H}_{\text{dmg}}$ are the external bias field and the demagnetizing field respectively. $\chi_\parallel$ is the longitudinal susceptibility, defined as [49, 55]

$$\chi_\parallel = \left.\frac{\partial m_e}{\partial H_B}\right]_{H_B \to 0} = \left.\frac{\frac{\mu_0\mu_B}{k_B T}B'(x)}{1 - \frac{T_C}{T}B'(x)}\right]_{x=\frac{T_C}{T}m_e}, \tag{7.8}$$

being $x = \frac{\mu_0\mu_B}{k_B T}H_B + \frac{T_C}{T}m_e$ and $B'(x) = \frac{\partial \tanh x}{\partial x}$. $m_e(T)$ and $\chi_\parallel(T)$ are shown in Fig. 7.4 [5].

The exchange field $\mathbf{H}_{\text{exch}}$ is given by [55, 56, 54]

$$\mathbf{H}_{exch} = \frac{2A(T)}{m_e^2 M_s^0}\nabla^2\mathbf{m}, \tag{7.9}$$

where $A(T)$ is the temperature-dependent exchange constant. Here we follow the same assumption adopted in Ref. [50, 114], where $A(T)$ scales with T as $A(T) = A^0 m_e^2(T)$. M_s^0 and A^0 represent the saturation magnetization and the exchange constant at $T = 0$ respectively. The stochastic fields $\mathbf{H}_{\text{th}}^{\perp,\parallel}$ take into account longitudinal and transverse fluctuations of the magnetization. They are considered to have white noise properties with the following correlators [59]

$$\begin{aligned} \langle H_{\text{th}}^{\perp}(\mathbf{r},t)_i H_{\text{th}}^{\perp}(\mathbf{r}',t)_j\rangle &= \frac{2k_B T(\alpha_\perp - \alpha_\parallel)}{\gamma_0\mu_0 M_s^0 V \alpha_\perp^2}\delta_{ij}\delta(\mathbf{r}-\mathbf{r}')\delta(t-t'), \\ \langle H_{\text{th}}^{\parallel}(\mathbf{r},t)_i H_{\text{th}}^{\parallel}(\mathbf{r}',t)_j\rangle &= \frac{2\gamma_0 k_B T\alpha_\parallel}{\mu_0 M_s^0 V}\delta_{ij}\delta(\mathbf{r}-\mathbf{r}')\delta(t-t'). \end{aligned} \tag{7.10}$$

The last three terms in Eq. (7.5) describe the STT as introduced by Schieback et al. [56][6]. The temperature dependence of the current polarization is assumed to be [56] $P = P^0 m_e(T)$. Eqs. (7.4) and (7.5) are simultaneously solved by Heun's method for a 4ns

---

[5] At $T = T_C$ the susceptibility has a critical point and it is not defined. This point is avoided in the numerical simulations

[6] Terms of the second order in damping ($\tilde{\alpha}_\perp^2$, $\tilde{\alpha}_\perp\xi$,...), appearing in Eq. (7.5), have been neglected in Ref. [56].

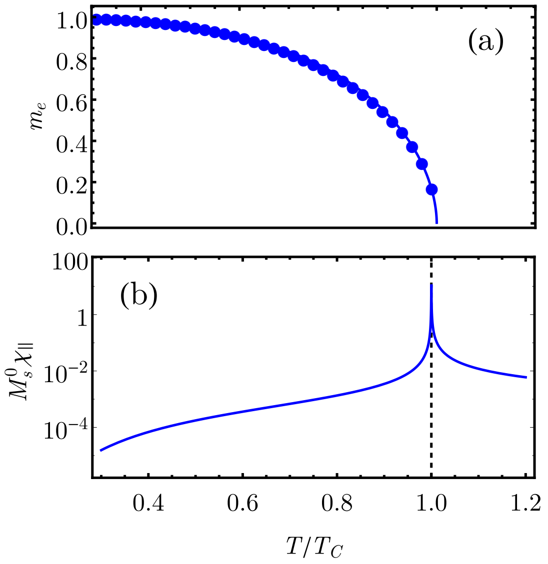

Figure 7.4: (a) Normalized equilibrium magnetization $m_e(T)$ and (b) longitudinal susceptibility $\chi_{||}(T)$ multiplied by M_s^0 (in order to be dimensionless) as function of temperature. Dots in (a) represent a numerical solution of Eq. (7.6). The line is a fit of the solution.

current pulse over a total simulation time of 10ns. Note that within this magneto-thermal framework, the magnetization dynamics, Eq. (7.5), is coupled to the temperature dynamics, Eq. (7.4), both through the thermal fields and the temperature dependence of the magnetic parameters.

New phase diagram

The new depinning diagrams are shown in Fig. 7.5. The depinning currents are now in quantitative agreement with the experimental measurements (see Fig. 3(a) in Ref. [79]). Moreover, the symmetry with respect to the current polarity of the phase diagram is also reproduced. Indeed, the depinning currents are almost independent of the current polarity ($J > 0$ or $J < 0$). These observations can be explained by the pivotal role of Joule heating, which has no dependence on the current direction. The main effects of the temperature rise are the increase in thermal fluctuations, the decrease in the depinning field, and the local destruction of the ferromagnetic order for high currents. While the first two effects, together with the applied field and STT, are responsible for the depinning at $J < 2.5 \times 10^8$ A/cm^2, the last effect drives the depinning for $J \geq 2.75 \times 10^8$ A/cm^2.

The scale at the right hand side of Fig. 7.5 shows the average temperature T_{av}^{Th} between the contacts for each current pulse at 4ns. The local temperature can deviate from this average, and, depending on J, it can reach higher values around the notch, where the current is larger (Fig. 7.3(b)). Accordingly, the mechanism by which the DW is depinned depends on the magnitude of the current injected.

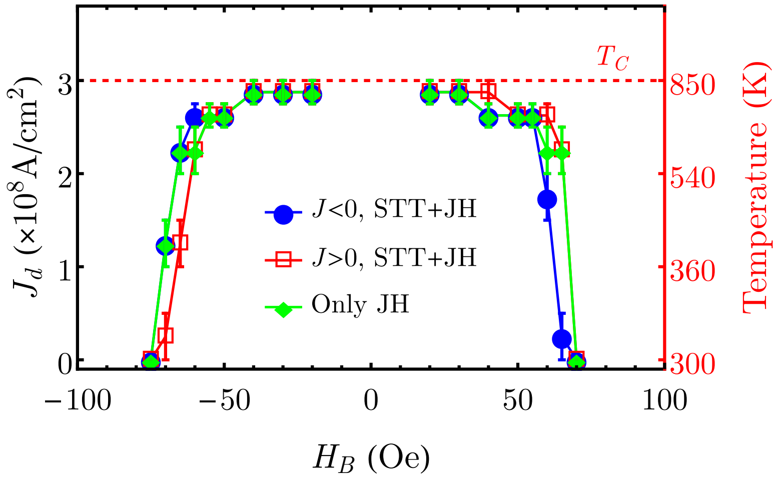

Figure 7.5: Depinning current (J_d) vs bias field (H_B) obtained with the LLB Eq. (7.5) including Joule heating (7.4). Results including the STTs are shown for positive (open red squares), and negative (full blue circle) currents. Green diamonds correspond to the results obtained in the absence of STTs ($P^0 = 0$). The scale (non linear) at the right-hand side shows the average temperature T_{av} between the contacts for each current at 4ns.

Depinning processes

Fig. 7.6(a)-(c) represent the temperature and magnetic patterns for $J = -2 \times 10^8$ A/cm^2, $J = -2.75 \times 10^8$ A/cm^2 and $J = -3 \times 10^8$ A/cm^2 respectively, with different bias fields, at $t = 2$, 4 and 6 ns. It is possible to see the different dynamics depending on the current (temperature) and fields.

For $J = -2 \times 10^8$ A/cm^2 (Fig. 7.6(a)) the DW is depinned only when STT and bias field act coherently (see Fig. 7.6 (a) for $t = 4$ and 6 ns). The temperature of the strip remains below the Curie temperature ($T_{av} \approx 600$K) and the effect of JH is limited.

On the other hand, for $|J| = 2.75 \times 10^8$ A/cm^2 (Fig. 7.6(b)), the average temperature between the contacts is $T_{av} \approx 740$ K $< T_C$ while the local temperature below the notch is larger than the Curie threshold ($T_{notch} \approx 980$ K $> T_C$). In this case, the ferromagnetic order is destroyed around the notch position, as shown in Fig. 7.7(b) at $t = 4$nm. After the pulse, the DW is re-nucleated below the notch but it adopts a different internal structure. The new structure can either be a displaced transverse (or vortex) wall or a meta-stable state which then collapses into a transverse or vortex wall. An example of this after-effect configuration is shown in the transient magnetization states of Fig. 7.7 at $t = 6$ns and $t = 9$ns. Note the meta-stable state shown in Fig. 7.7(b). The new

DW is found to have a lower depinning field and it is eventually depinned from the notch. We found a new critical depinning field for the re-nucleated DW of about 45 Oe. This decrease in the depinning field can be attributed to the new DW structure and the complex re-nucleation process (note that the re-nucleation takes place under the effect of the bias field and can involve transitions from meta-stable states).

Finally, during the injection of a current pulse of $|J| = 3 \times 10^8$ A/cm^2, the temperature between the contacts (not only under the notch) reaches T_C, and therefore the ferromagnetic order is temporarily destroyed between them (see Fig. 7.6 (c)). Once the current pulse is switched off ($t > 4$ns), the ferromagnetic order is recovered as $T(\mathbf{r}, t)$ relaxes back to uniform room temperature, as described in Fig. 7.3(a). Finally, a new DW is re-nucleated outside the notch. This re-nucleation process is influenced by the shape anisotropy and the static applied field. The ferromagnetic order is not destroyed outside the region between the contacts because no current has flowed there. These outside regions preserve a quasi-uniform magnetization pointing in opposite directions along the x-axis and, as a consequence, a DW is forced to be re-nucleated between the contacts for $t > 4$ns. Note that once the DW is out of the notch, it also undergoes a local pinning due to the edge roughness, which generates a minimum DW propagation field along the strip of $H_p \approx 15$ Oe. Therefore, depending on the applied field, the re-nucleated DW can finally be expelled from the contact area, resulting in a depinning event. The absence of points for $|H_B| < 20$ Oe is precisely due to this propagation field. In agreement with the experimental results, no DW depinning is achieved in the absence of external field. The emergence of multiple-domains states, as consequence of re-nucleation due to Joule heating above T_C, was also observed experimentally in other studies on Py strips [107, 108]. Here due to the reduced dimensions and the sides effect, we mainly observe one re-nucleated DW.

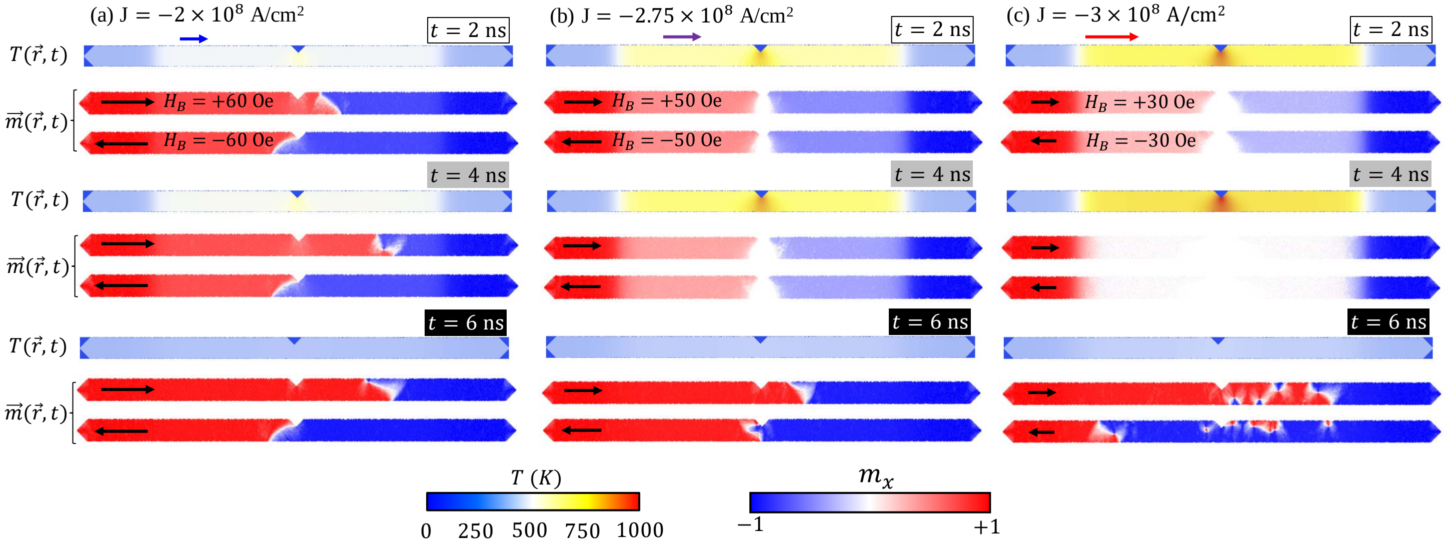

Figure 7.6: (a) Magnetization and temperature dynamics for $J = -2 \times 10^8$ A/cm^2. (b) Magnetization and temperature dynamics for $J = -2.75 \times 10^8$ A/cm^2. (c) Magnetization and temperature dynamics for $J = -3 \times 10^8$ A/cm^2. Static images represent the temperature and magnetization patterns for the corresponding current and fields at $t = 2$, 4 and 6 ns.

Since these results clearly indicate a remarkable influence of Joule heating in current-assisted DW depinning, it is interesting to evaluate the magnetization dynamics coupled to the heat transport in the absence of STTs ($P^0 = 0$). This case is depicted by green diamonds in Fig. 7.5. These latter results are very close to those observed in the presence of STTs (blue circles and red squares in Fig. 7.5). Consequently, they suggest that STTs do not play a dominant role for $|J| > 2.5 \times 10^8$ A/cm^2. By contrast, for such large currents, Joule heating and the applied field are the main agents responsible for the DW depinning events. For lower currents ($|J| < 2.5 \times 10^8$ A/cm^2), where DW depinning is mainly achieved because of the applied field, the contribution of the STTs is also small, as can be deduced by considering the similarity of the results with and without STTs in Fig. 7.5.

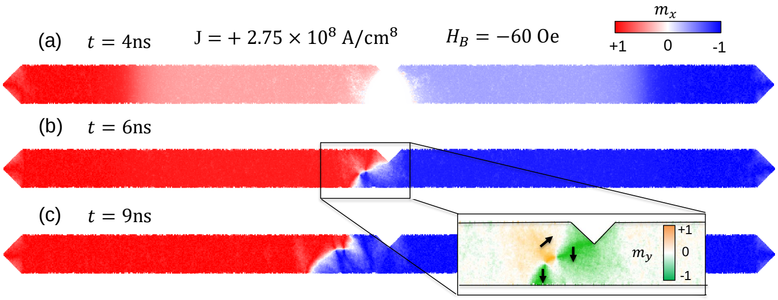

Figure 7.7: Snapshots of the magnetization for $H_B = -60$ Oe and $J = 2.75 \times 10^8$ A/cm^2 at $t = 4$ns, 6ns and 9ns. The detail in (b) represents a meta-stable state formed after re-nucleation.

Discussion

Before concluding, it is interesting to inspect the different effects of the temperature rise. As previously commented, temperature is coupled to the magnetization dynamics through the thermal fields and the temperature dependence of the magnetic parameters. However, by simulating the DW depinning without thermal fields (Eq. 7.10) we found that thermal fluctuations effect is negligible. Indeed we obtained almost the same depinning diagram even without the random thermal fields. The main actor is therefore the temperature dependence of the micromagnetic parameters, which is indeed responsible for the destruction of the ferromagnetic order and the previously described depinning events at high currents. However, even at $T < T_C$, temperature can significantly affect the depinning field. By performing purely field driven depinning simulations at constant **uniform** temperature, we found that the depinning field changes with T as $H_d(T) \approx H_d^0 m_e(T)$, where H_d^0 is the depinning field at $T = 0$. This means that temperature is actually decreasing the pinning barrier. Such behaviour is due to exchange and magnetostatic energies which scale as $m_e(T)^2$ and give rise to the pinning barrier. Since the Zeeman energy scales as $m_e(T)$, the resulting depinning field (defined as the field at which the Zeeman energy is equal to the energy barrier) scales as $m_e(T)$. Note that this behaviour is true for a system at constant and uniform temperature but, in our case, time- and space-dependent temperature patterns can lead to further pinning and the behaviour of the depinning field might be more complicated. The analysis performed at constant uniform temperature simply help us to understand one of the possible effect of the temperature rise.

Experimental observations (in uniform Py strips) of decreases in the DW propagation field [108] or in the switching field [106] due to Joule heating, can be explained by the same mechanism, as already anticipated in Ref. [106, 108]. Note also that even if temperature effects can be divided into these two contributions (thermal noise and temperature dependence of the micromagnetic parameters) at a micromagnetic level, from a more fundamental and microscopic point of view, all of them are related to thermal agitation of single spins. Finally, although it is not the main objective of the present study, it is interesting to comment about one of the main results of Hayashi et al. [79] which is the independence of the critical depinning current on the DW type (transverse or vortex) at low fields (high currents). Our analysis, although performed only on one DW type, points out, in agreement with the conclusion of Ref. [79], that such independence might be due to thermal effects which overcome the STTs and are indeed independent on the DW type.

7.3 Conclusions

The current-assisted DW depinning from a notch in a Permalloy strip on top of a Silicon substrate has been evaluated under static fields and short current pulses. The non-uniform spatial distribution of the current due to the notch results in significant non-uniform temperature profiles through the sample. Owing to Joule heating, the temperature can reach values close to or even above the Curie point for commonly injected currents in typical experiments. Although significant Joule heating have been observed in experimental studies, its effect has been overlooked in the theoretical descriptions.

Here, we have developed a formalism to properly describe the magnetization dynamics coupled to the heat transport. In particular, the depinning diagrams of the critical depinning current as a function of the applied field were experimentally found to be insensitive to the current polarity in the system under study, an observation which is not compatible with the sole contribution of the spin transfer torques. Our analysis demonstrates that indeed Joule heating is crucial to reproduce these experimental observations [79]. In agreement with previous studies [73, 96], the temperature evolution of the strip strongly depends on the current amplitude and the substrate. Below the notch, temperature is much higher than the average value. The rise in temperature leads to an increase in thermal agitation and in a reduction of the depinning field. Moreover, under typically injected current pulses, Joule heating can lead to a local destruction of the ferromagnetic order during which the DW is destroyed and then re-nucleated with a different internal structure (vortex, transverse or a meta-stable state) and a lower depinning field.

Our findings suggest that previous estimations of STT parameters based on depinning experiments, performed by fitting the experimental data with conventional micromagnetic and/or 1D models at constant and uniform temperature, must be carefully considered in systems where Joule heating is relevant. In addition, the formalism introduced here can be used to study the interplay between STT and thermal gradients in systems where the temperature changes dynamically.

Chapter 8

Domain wall motion by localized temperature gradients

Magnetic domain wall (DW) motion induced by a localized Gaussian temperature profile is studied in a Permalloy nanostrip within the framework of the stochastic Landau-Lifshitz-Bloch equation. The different contributions to thermally induced DW motion, entropic torque and magnonic spin transfer torque, are isolated and compared. The analysis of magnonic spin transfer torque includes a description of thermally excited magnons in the sample. A third driving force due to a thermally induced dipolar field is found and described. Finally, thermally induced DW motion is studied under realistic conditions by taking into account the edge roughness. The results give quantitative insights into the different mechanisms responsible for domain wall motion in temperature gradients and allow for comparison with experimental results. [1]

8.1 Introduction

Controlling magnetic domain walls (DW) in ferromagnetic (FM) and antiferromagnetic (AFM) nanostructures has recently attracted a considerable interest due to its potential for new logic [3] and memory devices [2] and for the very rich physics involved. In fact, DWs can be moved by several means such as external magnetic fields [115], spin polarized currents [20, 19, 42, 43] or spin waves [116, 117, 118, 119]. A new interesting option is the motion of DW by thermal gradients (TG), which was recently observed in few experiments on ferromagnetic (FM) conductors [90, 91], semiconductors [114] and insulators [92]. Spin caloritronics [120] is a new emerging subfield of Spintronics which aims to understand such complex interaction between heat, charge and spin transport. One of the interesting features of thermally induced DW motion is its applicability to

---

[1] Adapted from S. Moretti, V. Raposo, E. Martinez and L. Lopez-Diaz, Phys. Rev. B 95, 064419 (2017)

FM insulators and AFM [121]. Furthermore, since it does not imply charge transport and related Joule heating, it would avoid energy dissipation in FM conductors or it might represent a solution for harvesting the heat dissipated in electronic circuits. [120, 122]

From a theoretical point of view, it is known that thermally induced DW motion has at least two main causes: (1) the so-called entropic torque (ET) [88, 89, 87], which drives the DW towards the hot region due to maximization (minimization) of Entropy (Free Energy); (2) the magnonic spin transfer torque (μSTT) [54, 118, 87], due to the interaction between thermal magnons, propagating from the hot to the cold region, and the DW. While the entropic torque always drives the DW towards the hotter region [88, 89, 87, 5] (the DW energy is always lower where the temperature is higher), the μSTT can drive the DW either towards the hot or the cold part depending on the magnons behavior [117]: if magnons are transmitted through the DW, then angular momentum transfer leads to DW motion towards the hot part (opposite to the direction of magnon propagation), as predicted in Refs. [87, 54, 118]. On the other hand, if magnons are reflected, linear momentum transfer leads to DW motion towards the cold part (the same direction as magnon propagation) as shown in Refs. [123, 124, 116]. Moreover, magnon reflection or transmission depends on many factors such as the DW width, Dzyaloshinskii-Moriya interaction (DMI) [124] and magnon frequency (wavelength) [117]. Recently, Kim et al. [125] pointed out another possible mechanism of thermally induced DW motion based on Brownian thermophoresis, which predicts a DW drifting towards the colder region in a thermal gradient.

As we have briefly described, the picture is rather complex and the main responsible for DW motion in a thermal gradient might depend on the system under investigation. Although numerical studies [88] suggest that the ET is much stronger than μSTT, a detailed comparison is still lacking. Furthermore, previous analyses focused on linear thermal gradients [88, 54] where both effects are simultaneously present. However, ET and μSTT have different interaction ranges: the ET is intrinsically *local* (i.e., the DW needs to be inside the TG in order to *feel* the energy gradient and move), while the μSTT depends on the magnon propagation length [126], which can be larger than the TG extension. Therefore, the dominant effect (μSTT or ET) might depend on the distance from the TG and the comparison between different contributions at different distances remains to be evaluated. Moreover, previous theoretical analysis were performed on perfect samples without considering the effect of pinning, which is essential for comparison with experimental observations.

In this work we study, by means of micromagnetic simulations, the DW motion induced by a *localized* Gaussian temperature profile (as would be given by a laser spot) placed at different distances from the DW in a Permalloy nanostrip as sketched in Fig. 8.1. We separate magnonic and entropic contributions and we reveal the main responsible for DW motion at each distance. We point out the existence of a third driving force due to a thermally induced dipolar field generated by the laser spot. Such force was ignored before since most theoretical studies were neglecting long-range dipolar interaction. [54, 88, 87] Finally, by including edge roughness, we analyse the thermally induced DW motion under realistic conditions. The article is structured as follows:

Sec. 8.2 describes the numerical methods and the system under investigation. The main observations are outlined in Sec. 8.3 while the different driving mechanism are explained in more details in Sec. 8.3.1 (Entropic torque), 8.3.2 (Thermally induced dipolar field) and 8.3.3 (Magnonic spin transfer torque). Finally, the results for a realistic strip are shown in Sec. 8.3.4 and the main conclusions are summarized in Sec. 8.4.

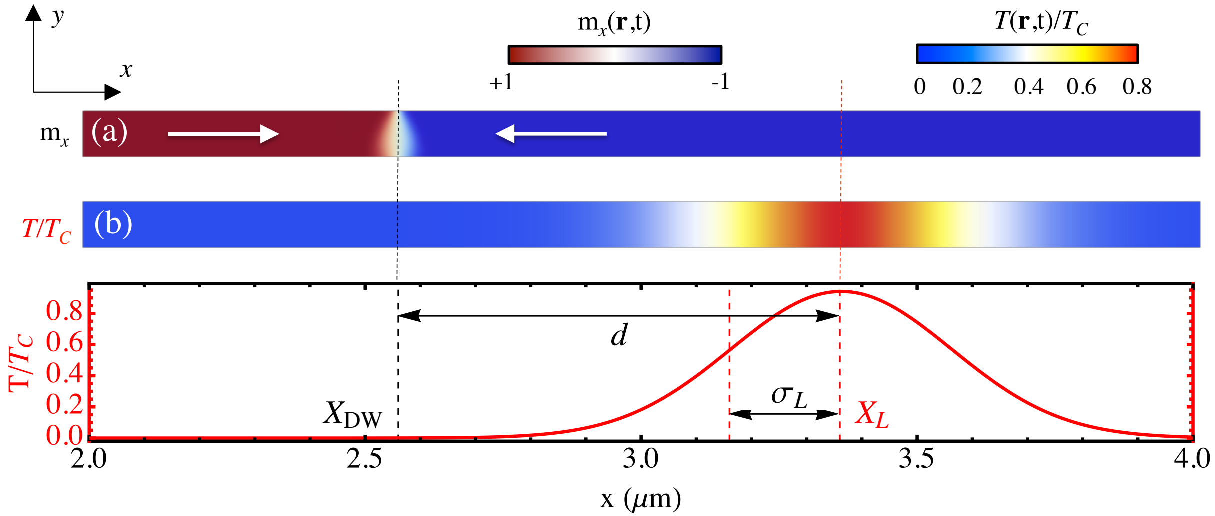

Figure 8.1: (a) Initial magnetization state. (b) Temperature profile along the strip T/T_C, with reference to the laser position X_L, the distance d from the DW and the laser width σ_L.

8.2 Methods

Magnetization dynamics is analysed in a Permalloy nanostrip of length $L_x = 5.12\mu$m and cross section $S = (80 \times 10)$nm^2 with a head-to-head transverse DW (TW) placed and relaxed in its center ($X_{DW} = 2.56\mu$m). The initial magnetic configuration and reference frame are shown in Fig. 8.1(a). Magnetization lies in-plane along the x direction and the TW is stable for these dimensions. Magnetic evolution is studied by means of the stochastic Landau-Lifshitz-Bloch (LLB) equation: [53, 49, 55, 59, 6]

$$\begin{aligned}\frac{d\mathbf{m}}{dt} &= -\gamma_0(\mathbf{m}\times\mathbf{H}_{\mathrm{eff}}) + \frac{\gamma_0\alpha_{\parallel}}{m^2}(\mathbf{m}\cdot\mathbf{H}_{\mathrm{eff}})\mathbf{m} \\ &\quad -\frac{\gamma_0\alpha_{\perp}}{m^2}\left\{\mathbf{m}\times\left[\mathbf{m}\times(\mathbf{H}_{\mathrm{eff}}+\mathbf{H}_{\mathrm{th}}^{\perp})\right]\right\} + \mathbf{H}_{\mathrm{th}}^{\parallel}\,, \end{aligned} \tag{8.1}$$

where γ_0 is the gyromagnetic ratio. $\alpha_\perp = \alpha_0[1 - T/(3T_C)]$ and $\alpha_\parallel = \alpha_0(2T/3T_C)$ are the transverse and longitudinal damping parameters respectively, where α_0 is a microscopic damping parameter coupling the spins to the lattice, and T_C indicates the Curie temperature. $\mathbf{m}(\mathbf{r}) = \boldsymbol{M}(\mathbf{r})/M_0$ represents the normalized magnetization vector, with M_0 being the saturation magnetization at zero temperature. $\mathbf{H}_{\mathrm{eff}}$ is the effective magnetic field given by

$$\mathbf{H}_{\mathrm{eff}} = \frac{2A(T)}{\mu_0 M_0 m_e^2}\nabla^2\mathbf{m} + \mathbf{H}_{\mathrm{dmg}} + \begin{cases} \frac{1}{2\tilde{\chi}_{\parallel}}\left(1-\frac{m^2}{m_e^2}\right)\mathbf{m}, & T < T_C \\ -\frac{1}{\tilde{\chi}_{\parallel}}\left(1+\frac{3}{5}\frac{T_C m^2}{(T-T_C)}\right)\mathbf{m}, & T > T_C \end{cases} . \tag{8.2}$$

The first term on the right-hand side (RHS) is the exchange field [88, 54] ($A(T)$ is the temperature dependent exchange stiffness, μ_0 is the vacuum permeability, and m_e is the equilibrium magnetization modulus). $\mathbf{H}_{\mathrm{dmg}}$ is the demagnetizing field, while the last term represents the longitudinal exchange field, which drives the modulus of $\mathbf{m}$ towards its equilibrium value at each temperature, $m_e(T)$. $\tilde{\chi}_\parallel$ is the longitudinal susceptibility defined as $\tilde{\chi}_\parallel = (\partial m_e/\partial H_a)_{H_a\to 0}$, with H_a being the external field. The choice of LLB is preferred over the conventional Landau-Lifshitz-Gilbert (LLG) equation since it allows to describe magnetization dynamics for temperatures even close to T_C. Furthermore, it naturally includes the ET within the temperature dependence of the micromagnetic parameters $\mathbf{m}(T)$ and $A(T)$ [88]. In fact, in the LLB, $\mathbf{m}$ is not restricted to unity and its value depends on the temperature, as well as the values of $\tilde{\chi}_\parallel$, $\alpha_\perp$ and $\alpha_\parallel$. However, the ET only depends on $\mathbf{m}(T)$ and $A(T)$, since they directly affect the DW energy, while the other parameters ($\tilde{\chi}_\parallel$, $\alpha_\perp$, $\alpha_\parallel$) affect the dynamics.

The function $m_e(T)$ needs to be introduced as an input into the model and, within the mean-field approximation (MFA) and in the classic limit, it is given by the Langevin function: [11, 50] $m_e = \coth(x) - 1/x$, with $x = \mu_0\mu_{\mathrm{Py}}H_a/(k_B T) + 3T_C m_e/T$, where μ_{Py} is the Py magnetic moment and k_B the Boltzmann constant. The second term represents the Weiss molecular field expressed in term of T_C. For the calculation we considered $H_a \to 0$ since there is no applied field. The obtained m_e and $\tilde{\chi}_\parallel$ are shown in Fig. 8.2. Within the MFA the temperature dependence of the exchange stiffness is given by $A(T) = A_0 m_e(T)^2$, [50, 114, 6] where A_0 is the exchange stiffness at $T = 0$. The dynamics of the magnetization modulus (the *longitudinal* dynamics) is described by the second term on the RHS of Eq. (8.1), proportional to $\alpha_{\|}$ and it is governed by the longitudinal exchange field in Eq. (8.2), proportional to $\tilde{\chi}_{\|}$. Such dynamics becomes important at $T \approx T_C$ when longitudinal and transverse relaxation times are comparable.

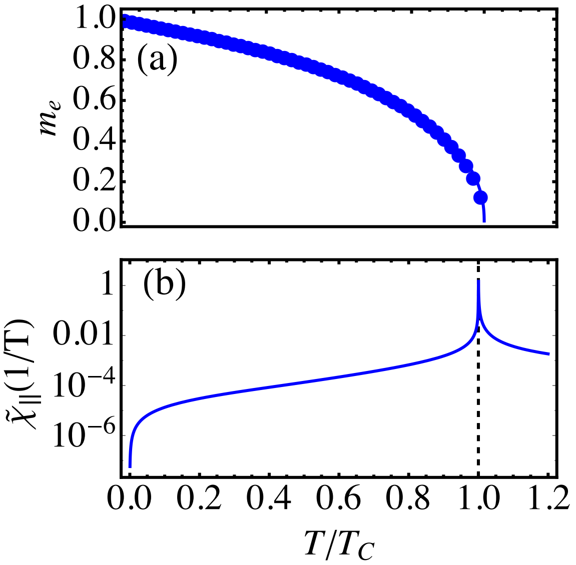

Figure 8.2: (a) Equilibrium magnetization $m_e(T)$ obtained with the Langevin function [11]. Dots correspond to numerical results while the solid line is a fit of the numerical solution. (b) Longitudinal susceptibility $\tilde{\chi}_{\|} = (\partial m_e/\partial H_a)_{H_a \to 0}$.

$\mathbf{H}_{\text{th}}^{\perp}$ and $\mathbf{H}_{\text{th}}^{\|}$ are transverse and longitudinal stochastic fields, which introduce thermal fluctuations - and therefore excite thermal magnons - into the system. They have white noise properties with correlators given by [59]

$$\begin{aligned} \left\langle H_{\text{th}}^{\perp}(\boldsymbol{r},t)_i H_{\text{th}}^{\perp}(\boldsymbol{r'},t')_j \right\rangle &= \frac{2k_B T(\alpha_{\perp} - \alpha_{\|})}{\gamma_0 \mu_0 M_s^0 V \alpha_{\perp}^2} \delta_{ij} \delta(\boldsymbol{r} - \boldsymbol{r'}) \delta(t - t') \,, \\ \left\langle H_{\text{th}}^{\|}(\boldsymbol{r},t)_i H_{\text{th}}^{\|}(\boldsymbol{r'},t')_j \right\rangle &= \frac{2\gamma_0 k_B T \alpha_{\|}}{\mu_0 M_s^0 V} \delta_{ij} \delta(\boldsymbol{r} - \boldsymbol{r'}) \delta(t - t') \,, \end{aligned} \tag{8.3}$$

which are obtained by imposing the Maxwell-Boltzmann distribution as the solution of the Fokker-Planck equation calculated from the stochastic LLB [59]. Note that a cut-off on the magnon wavelength is imposed by discretizing the sample in cubic cells (as commonly done in finite-difference solvers); that is, magnons with wavelength smaller than $2\Delta x$ cannot be included in the thermal noise, where Δx is the cell size. Within the LLB formalism, their contribution is still included in the temperature dependence of the micromagnetic parameters $m_e(T)$ and $A(T)$, but any flux of such small wavelength magnons, from one cell to another, is neglected. This means that our analysis of the magnonic STT is restricted to thermal magnons with $\lambda > 2\Delta x$. For this reason we chose cells of dimensions $2.5 \times 5 \times 10$nm in order to include a higher flux of magnons along the x direction. In Sec. 8.3.3 we will see that these magnons have a very small propagation length ($L_p \sim 80$nm, see Eq. 8.15) and therefore they can be ignored when they are excited far from the DW position. Inside the TG, where they could reach the DW, their contribution is ignored and this constitutes a limitation of our model. At the end of Sec. 8.3.3 we will briefly discuss the possible effects of such small wavelength magnons.

In summary, the ET is naturally included into the model by the temperature dependence of $\mathbf{m}(T)$ and $A(T)$ while magnons are excited by the stochastic fields. At a given temperature we would have both effects simultaneously. To isolate the effect of the ET we simply perform simulations without thermal field and we label these kind of simulations as *Entropic*. To isolate the effect of magnons we perform simulations by keeping $\mathbf{m}(T)$ and $A(T)$ constant at their $T = 0$ values and we label these kind of simulations as *Magnonic*. Simulations with the full stochastic LLB (Eq. (8.1)) are labelled as *Full*. The *Magnonic* simulations correspond to what one would observe within the LLG framework for $T \ll T_C$, assuming that $m_e(T)$ and $A(T)$ do not change with temperature. Indeed we checked that for $T_L = 200, 400$K (where the LLG framework can be applied) the *Magnonic* results correspond with the results of the conventional LLG.

Eq. (8.1) is solved by finite difference method with a customized software. [6, 5] We use the mentioned cell size ($2.5 \times 5 \times 10$ nm) and a time step of 0.1ps testing that smaller time steps produce equal results. Typical Py parameters are considered: $A_0 = 1.3 \times 10^{-11}$J/m, $M_0 = 8.6 \times 10^5$ A/m, $\alpha_0 = 0.02$ and $T_C = 850$K. The strip temperature is given by a Gaussian profile:

$$T(x) = T_0 + T_L \exp\left[-\frac{(x - X_L)^2}{2\sigma_L^2}\right] , \tag{8.4}$$

where $T_0 = 0$ and T_L is the laser temperature. X_L is the laser spot position, and σ_L is the Gaussian profile width. For our study we chose $\sigma_L = 200$nm, which would correspond to a laser waist of $\sqrt{2}\sigma_L \approx 280$ nm, reasonable for typical lasers. [90] We performed simulations placing the laser spot at different distances from the DW ($d = X_L - X_{DW}$). Distances correspond to integer multiples of σ_L i.e. $d = X_L - X_{DW} = N\sigma_L$ with $N = 1, 2, ..., 10$. Simulations are performed for 4 different laser temperature $T_L = 200, 400, 600$ and $800K$. The temperature profile is plotted in Fig. 8.1(b) for $T_L = 800K$. Five different stochastic realizations are considered when thermal fluctuations are taken into account (*Magnonic* and *Full* simulations). The gradient extension from X_L is approximatively equal to $3\sigma_L$. In other words $\nabla T(X_{\mathrm{DW}}) \approx 0$ if $d > 3\sigma_L$. In fact, $\nabla T(3\sigma_L) \approx 0.1$K/nm and the estimated entropic field (see Sec. 8.3.1) is $\mu_0 H_E \approx 0.06$ mT. Furthermore, $T = 0$K is imposed for $d > 4.5\sigma_L$ so that $\nabla T(X_{\mathrm{DW}}) = \mu_0 H_E = 0$ if $d > 4.5\sigma_L$. We simulate an infinite strip by removing the magnetic charges appearing at both sides of the computational region [94]. The simulation time window is varied depending on d

and the DW velocity, with a maximum simulation time of $t_{max} = 500$ns.

8.3 Results and Discussion

Fig. 8.3 shows the normalized DW displacement ($\Delta x/d$) as function of time for the *Entropic* , *Magnonic* and *Full* cases, calculated with $T_L = 800K$, for three different distances as labelled on top of each column: $d = 2\sigma_L$ (Fig. 8.3(a)-(c)) , $d = 4\sigma_L$(Fig. 8.3(d)-(f)) and $d = 6\sigma_L$ 8.3(g)-(i)). The displacement is normalized to the laser distance d and therefore $\Delta x/d = 1$ indicates that the DW has reached the laser spot.

For $d = 2\sigma_L$ the DW moves towards the laser spot both for *Magnonic* (Fig. 8.3(b)) and *Entropic* (Fig. 8.3(a)) cases (and therefore obviously in the *Full* (Fig. 8.3(c)) case). The DW is inside the TG ($\nabla T(X_{\mathrm{DW}}) \neq 0$) and its motion can be attributed mostly to the ET. [88, 89, 87] In the *Magnonic* case the motion could be given by a magnons stream passing adiabatically through the DW, but also by the effect of an averaged ET. Note that thermal magnons, apart from the μSTT, also introduce an averaged ET [87, 5]: where the temperature is higher, the *averaged* M_s (over more cells) is lower (as in the *Entropic* case) due to higher thermal fluctuation. More precisely, we recall that also the temperature dependence of $\mathbf{m}$ and A is given by averaged high frequency magnons which cannot be included in the thermal fluctuations due to the spatial discretization. This averaged ET is, however, a small contribution compared to the one given by high frequency magnons as can be seen by the time scale in Fig. 8.3(a) and (b).

For $d = 4\sigma_L$ the DW moves towards the hotter region in the *Entropic* case (Fig. 8.3(d)) and towards the colder region in the *Magnonic* case (Fig. 8.3(e)). The latter could be attributed to μSTT (Sec. 8.3.3) while the first effect is unexpected since at $d = 4\sigma_L$, $\nabla T(X_{\mathrm{DW}}) \approx 0$ and the ET should have no effect (we recall that the gradient extension is approximatively $3\sigma_L$). This is even more visible in the $d = 6\sigma_L$ case where, although it is certain that $\nabla T(X_{\mathrm{DW}}) = 0$, the DW moves towards the hotter region (Fig. 8.3(g)). Note that the DW moves with different velocities when it is outside ($x > X_L - 3\sigma_L$) or inside ($x < X_L - 3\sigma_L$) the TG. We conclude that there must be another long-range driving force - not related to magnons - that drives the DW in this case. As we will discuss in Sec. 8.3.2, this force is given by a thermally induced dipolar field. In the *Magnonic* case (Fig. 8.3(h)) the DW does not move, compatibly with μSTT if we assume that magnons are already damped for such distance ($d = 6\sigma_L = 1.2$ μm). Indeed we estimated a magnon propagation length of 330 nm ($\ll 1.2\mu$m) for our sample (Sec. 8.3.3). Different laser temperatures ($T_L = 200, 400, 600K$) produce qualitatively similar behaviors for all the distances. Furthermore, for all cases the *Full* simulations are very similar to the *Entropic* simulations suggesting that the ET dominates over the μSTT. [2]

---

[2] To be sure that the results are not numerical artefacts we performed simulations for the symmetric cases $d = -2\sigma_L, -4\sigma_L, -6\sigma_L$ obtaining equal results.

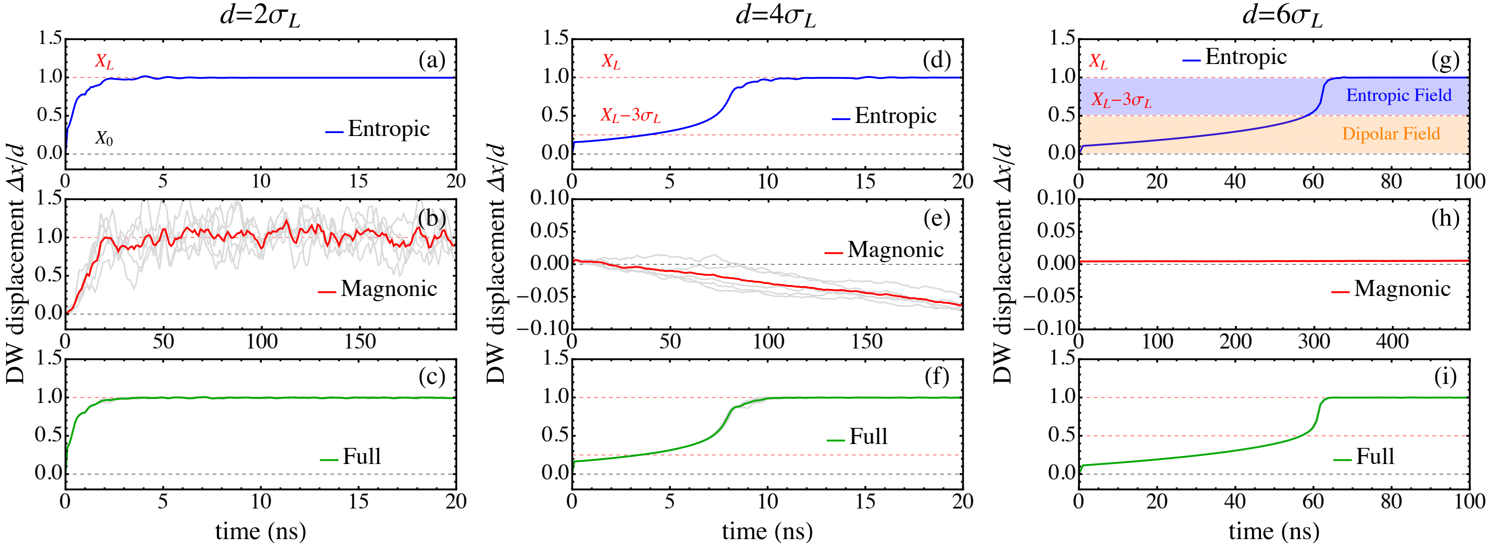

Figure 8.3: DW displacement as function of time for $d = 2\sigma_L$ (a,b,c), $d = 4\sigma_L$ (d,e,f) and $d = 6\sigma_L$ (g,h,i), for the *Entropic*, *Magnonic* and *Full* cases as labelled in each plots. Displacement Δx is normalized to d: a displacement of 1 means that the DW has reached the center of the laser spot. X_L indicates the laser position, X_0 the DW position and $X_L - 3\sigma_L$ the extension of the TG i.e. the region where $\nabla T(x) \neq 0$.

Fig 8.4(a) shows the averaged DW velocity [3] as function of laser distance. As mentioned, the ET dominates the DW dynamics and in fact *Entropic* and *Full* velocities almost coincide. The averaged velocity decreases with distance but it is different from 0 even for the maximum distance we analysed ($d = 10\sigma_L = 2$ μm) meaning that, with enough time $t > t_{max}$, the DW would reach the laser spot since the velocities are always positive (towards the hot part). On the other hand, *Magnonic* simulations give rise to positive velocity for $d = 2, 3\sigma_L$ due to an averaged ET, negative velocities (towards the cold part) for $d = 4, 5\sigma_L$ and almost null velocities for $d \geq 6\sigma_L$. In all the cases, the velocities due to μSTT are much smaller than the *Entropic* velocities, in agreement with previous predictions [88]. Details of the averaged magnons velocities are shown in the inset of Fig. 8.4(a).

Fig. 8.4(b) displays the average *Full* velocity as function of laser distance for 4 different laser temperatures: at $d = 2, 3\sigma_L$ the maximum DW velocity is observed for $T_L = 400$K due to the Walker breakdown (WB) threshold at $T_L = 600$K, predicted also for thermal induced DW motion [88]: Below 600K the entropic field (Sec. 8.3.1) is compensated by the DW shape anisotropy and the DW moves rigidly without changing its internal structure. For $T_L > 600K$ the DW anisotropy cannot compensate the entropic field and the DW precesses, changing its internal structure and resulting in a slower velocity. On the other hand, for $d \geq 4\sigma_L$ the maximum temperature coincides with maximum velocity since the thermally induced dipolar field is below the WB and the DW moves faster while outside the TG. In what follows we will analyse each contribution separately.

---

[3] If the DW reaches the laser spot, the averaged velocity is obtained as d/t_L where t_L is the time needed to reach the spot. If the DW does not reach the laser spot, then the velocity is obtained as d/t_{max}, where t_{max} is the maximum simulation time.

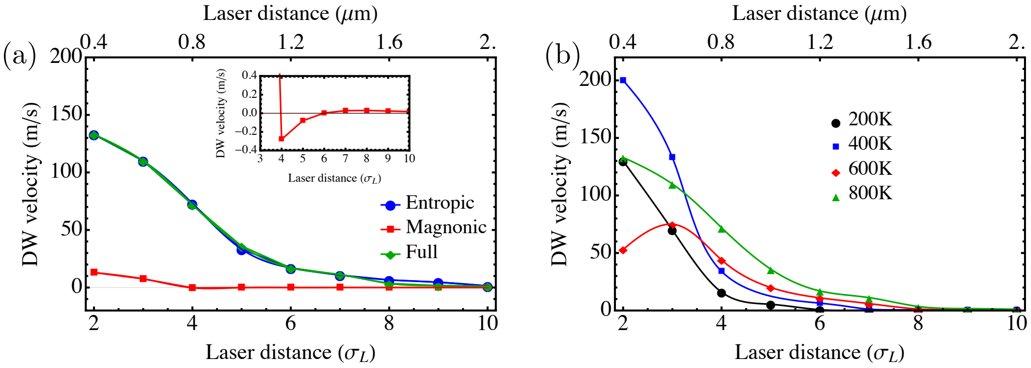

Figure 8.4: (a) DW average velocity as function of laser distance, for the *Entropic* (Blue dots), *Magnonic* (Red squares) and *Full* cases (Green diamonds) respectively. The inset shows a detail of the *Magnonic* case from $d = 4\sigma_L$ to show the negative small velocities, not visible in comparison with the *Entropic* velocities. (b) DW average *Full* velocities for different temperatures. At $d = 2\sigma_L$ the maximum velocity is observed at $T = 400$K due to the WB threshold at $T \geq 600$K.

8.3.1 Entropic field

The ET originates from the fact the the DW free energy ($\Delta F(T)$) decreases with temperature and, as a consequence, the DW moves towards the hotter region in order to minimize its free energy. [54, 88, 89] It is called *Entropic* since DW entropy increases with temperature and leads to the overall decrease of the free energy [127, 89, 88], $\Delta F = \Delta U - T\Delta S$, with ΔU being the DW internal energy [127, 88] and ΔS being the DW entropy [127, 88]. In the thermodynamic picture of LLB, entropy is included in the temperature dependent DW free energy density [127, 88, 60]

$$\epsilon_{\mathrm{DW}}(T) = 4\sqrt{A(T)(K_0(T) + K_S(T)\sin^2\phi)}\,, \tag{8.5}$$

where $K_0(T)$ and K_S are effective anisotropy constants, and ϕ is the internal DW angle. In the case of Permalloy, the anisotropies are both of magnetostatic origin (shape anisotropies) and they are given by

$$\begin{aligned} K_0(T) &= \frac{1}{2}\mu_0 M_0^2 (N_y - N_x) m(T)^2\,, \\ K_S(T) &= \frac{1}{2}\mu_0 M_0^2 (N_z - N_y) m(T)^2\,, \end{aligned} \tag{8.6}$$

being $N_{x,y,z}$ the demagnetizing factors. As in MFA also $A(T)$ decreases with T as $m(T)^2$, $\epsilon_{\mathrm{DW}}(T)$ decreases as

$$\epsilon_{\mathrm{DW}}(T) = 4\sqrt{A_0(K_0^0 + K_S^0\sin^2\phi)}m(T)^2\,, \tag{8.7}$$

where K_0^0 and K_S^0 are the shape anisotropies at $T = 0$. Therefore, the temperature gradient introduces a DW energy gradient, which leads to the equivalent field (the so-called *Entropic* field)

$$\begin{aligned}\mu_0\mathbf{H}_E &= -\frac{1}{2m_eM_0}\nabla\epsilon_{\mathrm{DW}} = -\frac{1}{2m_eM_0}\frac{\partial\epsilon_{\mathrm{DW}}}{\partial T}\frac{\partial T}{\partial x}\hat{x} \\ &= -\frac{4A_0}{M_0\Delta_0}\frac{\partial m}{\partial T}\frac{\partial T}{\partial x}\hat{x}\,, \end{aligned} \tag{8.8}$$

where we have assumed that the gradient is only along the $\hat{x}$ direction and we have used the fact that

$$\frac{\partial\epsilon_{\mathrm{DW}}(T)}{\partial T} = 2m\epsilon_{\mathrm{DW}}^0\frac{\partial m}{\partial T} = \frac{8mA_0}{\Delta_0}\frac{\partial m}{\partial T}\,. \tag{8.9}$$

$\Delta_0 = \sqrt{A_0/(K_0 + K_S^0\sin^2\phi)}$ and ϵ_{DW}^0 are the DW width and energy at $T = 0$ respectively. In Ref. [88] Schlickeiser et al. proposed an analytical expression for $\mu_0\mathbf{H}_E^*$ by solving the LLB equation in the 1D approximation. Within the MFA their expression is indeed equivalent to Eq. (8.8). In fact,

$$\begin{aligned}\mu_0\mathbf{H}_E^* &= -\frac{2}{\Delta(T)M_0}\frac{\partial A(T)}{\partial T}\frac{\partial T}{\partial x}\hat{x} \\ &\overset{\mathrm{MFA}}{=} -\frac{4A_0}{\Delta_0M_s}\frac{\partial m}{\partial T}\frac{\partial T}{\partial x}\hat{x}\,. \end{aligned} \tag{8.10}$$

Fig. 8.5(a) shows the strip temperature profile for $T_L = 800$K and $X_L = 3.16\mu$m. Fig. 8.5(b) depicts the corresponding DW energy profile $\epsilon_{\mathrm{DW}}[T(x)]$ (Eq. (8.7)) and Fig. 8.5(c) the resulting entropic field $\mu_0H_E(x)$ (Eq. (8.8)). The entropic field always pushes the DW towards the center of the laser spot where $\mu_0H_E = 0$ since $\nabla T = 0$. Note that indeed, the ET is *local* because it depends on $\nabla T(x)$: if $\nabla T(x) = 0$ then $\mu_0H_E(x) = 0$. The maximum field is approximatively at $d = 1\sigma_L$, where ∇T is maximum.

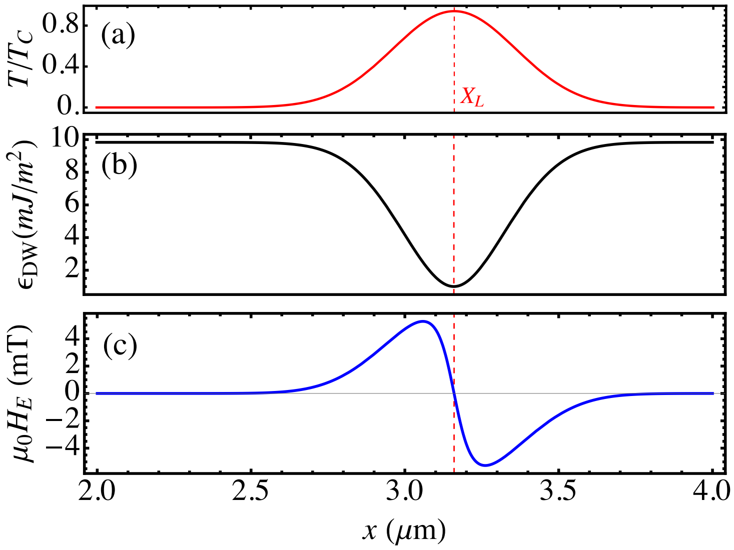

Figure 8.5: (a) Temperature profile $T(x)$ for $X_L = 3.16\mu\mathrm{m}$ and $T_L = 800$K. (b) Corresponding DW energy profile $\epsilon_{DW}(T(x))$ as given by Eq. (8.7) and (c) the resulting Entropic field as predicted by Eq. (8.8).

8.3.2 Thermally induced dipolar field

Since in the *Entropic* simulations the DW moves even when $\nabla T(X_{\rm DW}) = 0$, there must be another force responsible for its motion at large distances. A natural candidate is the demagnetizing field which is a long-range interaction. Indeed, a thermally induced dipolar field (TIDF) was found to be the responsible for the DW motion at large distances. Fig. 8.6(a) displays the TIDF ($H_{\rm dip}$) of a uniform magnetized strip with the laser spot. Strip magnetization is saturated along x ($m_x = -1$) and the TIDF is calculated by subtracting the demagnetizing field of the strip without the laser spot from the demagnetizing field of the same uniform strip with the laser spot (in this way we can isolate the effect of the laser). The field has a minimum at X_L and positive tails outside the thermal gradient (Fig. 8.6(a),(c)). The laser temperature is set to the minimum value $T_L = 200$K. The TIDF is due to the volume charges $\rho_M = -\nabla \cdot \mathbf{M}$, shown in Fig. 8.6(b), which arise from the variation of magnetization modulus. Positive and negative charges, on the left and right side of X_L respectively, sum their effect in the center giving rise to the minimum value of the TIDF (maximum in modulus) while they compete each other outside the laser spot giving rise to the decaying behavior.

A comparison between the TIDF and the entropic field is shown in Fig. 8.6(c). As expected, beyond $2\sigma_L$ the TIDF is much larger than the entropic field that rapidly decays to 0 outside the TG. $\mu_0 H_E$ decays as $\nabla T \propto (x - X_L)e^{-|x-x_L|^2/(2\sigma_L^2)}$ as expected, while the TIDF decays as $1/x^3$ as expected for a dipolar field (Fig. 8.6(c)). Before $2\sigma_L$ the comparison has no meaning since the TIDF is calculated for a uniform magnetization and it would change once the DW approaches the laser center.

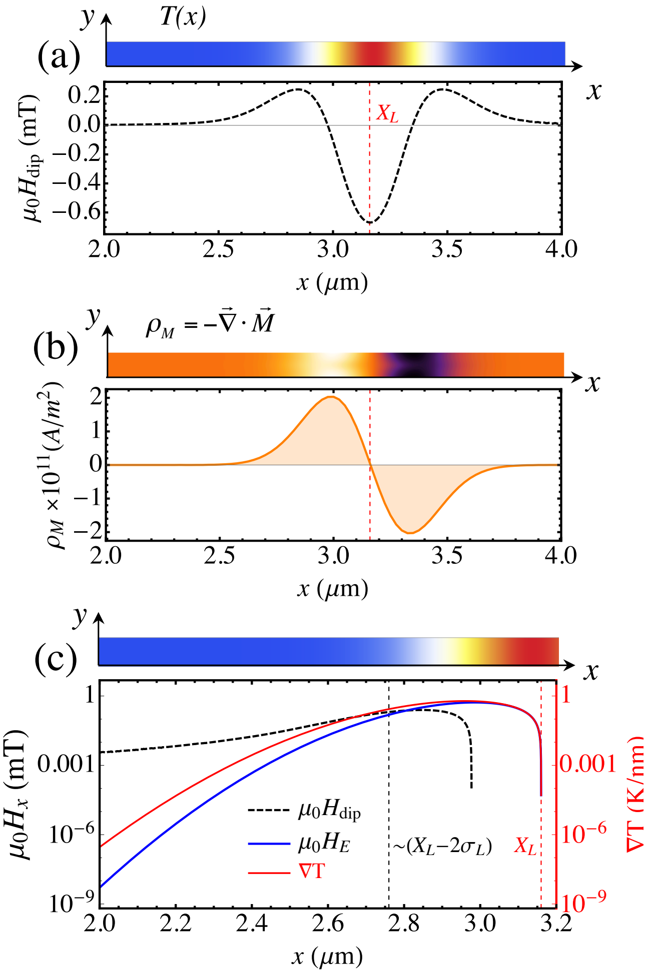

Figure 8.6: (a) Thermally induced dipolar field and (b) volume charges $\rho_M = -\nabla \cdot \mathbf{M}$ for $X_L = 3.16\mu\text{m}$ and $T_L = 200\text{K}$. (c) Comparison between the entropic and demagnetizing field. Beyond $2\sigma_L$ from the laser spot, the demagnetizing field dominates.

To further check our explanation, a 1D model was implemented following Ref. [88]. The model originally includes the ET while the TIDF was added by fitting the micromagnetic TIDF (Fig. 8.6(a)). The field is set different from zero only if $d > 2\sigma_L$ since it has no meaning for closer distances as previously commented. The 1D model equations governing the DW internal angle ϕ and DW position q read like:

$$\begin{aligned}\dot{\phi} &= \gamma_0\left[\left(H_{\text{dip}} - \frac{4A_0}{\mu_0 M_0 \Delta_0}\frac{\partial m}{\partial x}\right) - \alpha_\perp \frac{K_S^0}{\mu_0 M_0}\sin(2\phi)\right], \\ m\frac{\dot{q}}{\Delta_0} &= \gamma_0\left[\alpha_\perp\left(H_{\text{dip}} + \frac{4A_0}{\mu_0 M_0 \Delta_0}\frac{\partial m}{\partial x}\right) + \frac{K_S^0}{\mu_0 M_0}\sin(2\phi)\right].\end{aligned} \tag{8.11}$$

The second term on the RHS of Eq. (8.11) is the entropic field as derived in Eq. (8.8) while the first term is the TIDF. Both fields depend on the DW position q. The results of the 1D model calculations are plotted in Fig. 8.7. For $d = 2\sigma_L$ (Fig. 8.7(a)) the model gives equal results with or without TIDF, as expected (the TIDF is null in this case) and the agreement with simulations is good. For $d = 4\sigma_L$ the model without TIDF (purple dashed line) predicts no DW motion, as expected from the ET since the DW is outside the temperature gradient. On the other hand, the model with the TIDF (black dotted line) predicts DW motion and shows a better agreement with simulations confirming our hypothesis.

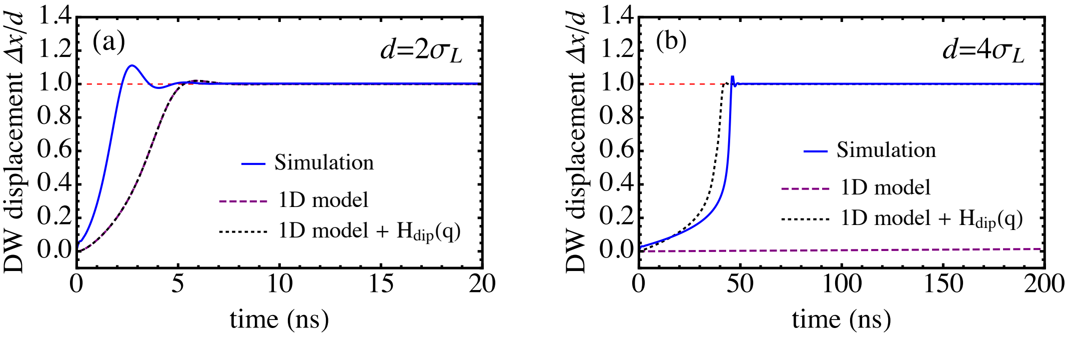

Figure 8.7: DW displacement as function of time as predicted by the 1D model with or without the demagnetizing field for $d = 2\sigma_L$ (a) and $d = 4\sigma_L$ (b). The model without demagnetizing field does not predict any motion for $d \geq 4\sigma_L$.

By using the 1D model it is also possible to estimate the WB thermal gradient:

$$\nabla T_W = \frac{\Delta_0 \alpha_\perp K_S^0}{4A_0(\partial m/\partial T)}. \tag{8.12}$$

Due to the presence of $\partial m/\partial T$ the WB also depends on the absolute temperature T which affects $\partial m/\partial T$ [88]. The WB as function of temperature is plotted in Fig. 8.8.

The blue points represent the maximum value of $\nabla T(x)$ (being a Gaussian profile, ∇T is not constant) applied in the simulations for different laser temperatures. The crossing of the WB occurs at $T \approx 660K$, in reasonable agreement with our observation ($T = 600K$, Fig. 8.4(b)). The small difference could be given by the effect of the TIDF or by the uncertainty on the 1D parameters (K_S^0,Δ_0).[4]

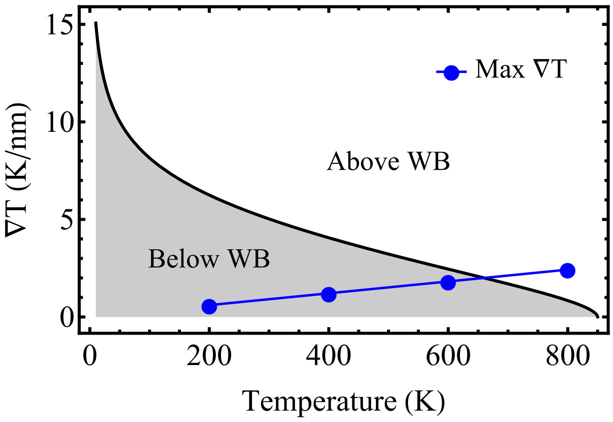

Figure 8.8: WB thermal gradient as function of temperature (Eq. (8.12)). For a Gaussian profile, as the one applied in our simulations, ∇T is not constant, the blue points represent the maximum value of ∇T for each temperature which occurs approximatively at $1\sigma_L$ from the laser spot center.

Magnetostatic effects on thermally induced DW motion were already discussed by Berger [128] . Despite the common magnetostatic origin, the TIDF shown here presents some differences: In Ref. [128] the thermal gradient affects the magnetostatic energy of the domains (much more relevant in bulk samples such as the ones analysed by Berger), whereas here, it is the Gaussian temperature profile by itself that generates new magnestostatic volume charges which give rise to the TIDF.

8.3.3 Magnonic spin transfer torque

Magnons can drive the DW either towards the hot or the cold part depending on their interaction with the DW: they drive the DW towards the cold part if they are reflected by the DW [116, 117, 123] due to linear momentum transfer, while they drive the DW towards the hot part if they pass through the DW due to angular momentum transfer [118, 117, 87]. As already mentioned, we observe DW motion towards the hot part for $d = 2, 3\sigma_L$ (Fig. 8.3(b)), DW motion towards the cold part for $d = 4, 5\sigma_L$ (Fig. 8.3(e), inset of Fig. 8.4(a)) and no DW motion for $d \geq 6\sigma_L$ (Fig. 8.3(h), inset of Fig. 8.4(a)). At $d = 2, 3\sigma_L$ the motion is probably due to an averaged ET (as commented in Sec. 8.3)

---

[4] Δ_0 is calculated by fitting the static Bloch profile obtaining $\Delta_0 = 30$ nm. K_S^0 is obtained by calculating the static DW widths (Δ_1,Δ_2) and energies (ϵ_1,ϵ_2) for in-plane and out-of-plane DW ($\phi_1 = 0$, $\phi_2 = \pi/2$) and using the relation $K_S^0 = (1 + ab)/a$ (Ref. [60]), with $a = (\Delta_1/\Delta_2)^2$ and $b = (\epsilon_1/\epsilon_2)^2$, obtaining $K_S^0 \approx 2.9 \times 10^5$ J/m^3

and it is not possible to isolate the effect of magnons. For $d \geq 6\sigma_L$ the magnons are already damped and therefore they do not interact with the DW. In fact, by fitting the magnon accumulation [126] $\delta m_y(x,t) = m_y(x,t) - m_y(x,0)$, we estimate a magnon propagation length $L_p = 330$nm (Fig. 8.9(a)). This means that at $d = 4, 5\sigma_L$ (200 nm and 400 nm respectively from the end of the laser spot) the DW is within the magnon propagation length, while at $d = 6\sigma_L$ the DW is at $\approx 2L_p$, where magnons are clearly damped. Therefore, at $d = 4, 5\sigma_L$, where $\nabla T(X_{DW}) \approx 0$ the motion towards the cold part should be given by the μSTT. To better understand such behavior, thermally excited magnons were analysed by means of 2-Dimensional Fast Fourier Transform (FFT) in the middle of the strip ($y_0 = 40nm$) i.e. by calculating the FFT power [116]

$$\tilde{m_y}(\omega, k_x) = \mathcal{F}_{\text{2D}}\left[m_y(x, y_0, t) - m_y(x, y_0, 0)\right] , \tag{8.13}$$

where the FFT is calculated with respect to $\{x, t\}$. Fig. 8.9(b) shows the normalized magnons frequency spectrum ($\sum_{k_x} \tilde{m_y}(\omega, k_x)$) at the laser spot (LS) (region 1: $X_L \pm$ 330nm) and right before the LS (region 2: $(X_L - 5\sigma_L) \pm 330$nm). At the LS (black dots) magnons have a wide range of frequency while before the laser spot (green line) only low frequency magnons have propagated, in agreement with previous observation [126]. The cut-off at $f_0 \approx 9$GHz is due to lateral width confinement [116]. Therefore, the average magnon propagation length, previously calculated (Fig. 8.9(a)), is mainly related to low frequency magnons. This is a relevant observation since the magnons frequency strongly affects magnons transmission or reflection at the DW [117]. In particular, low frequency magnons are likely to be reflected [117, 116] and would produce motion towards the cold part. To further understand the interaction between magnons and the DW, the DW dynamics excited by monochromatic spin waves (SW) was analysed in the same Py strip. SW were locally excited by a transverse sinusoidal field $\mathbf{H}_a(x) = H_0 \sin(2\pi f)\hat{y}$ at a distance of 100nm from the DW (Fig. 8.10(a)). The excitation region has dimensions $10 \times 80 \times 10$ nm and $\mu_0 H_0$ is set to 10mT. The DW dynamics by different frequencies is shown in Fig. 8.10(b), while the spin wave propagation length as function of frequency is depicted in Fig. 8.10(c). Consistently with previous analysis [116, 119] the DW moves towards the cold part (in this case cold means away from the antenna position i.e. in the same direction as magnons propagation) for low frequency, $f = 18, 25$ GHz, while no motion towards the hot direction is observed within the maximum applied frequency, $f_{\max} = 100$ GHz (Fig. 8.10 (b)). Moreover, the monochromatic analysis allows to study the frequency dependent magnon propagation length, and indeed it confirms that magnon propagation length decays with the magnons frequency (Fig. 8.10(c)). Note that the propagation length of low frequency magnons is in good agreement with our calculation for thermal magnons ($L_p = 330$ nm). Furthermore, following Ref. [126], the frequency dependent propagation length $L_p(\omega)$ can be estimated as $1/(\alpha_\perp \omega)\partial\omega/\partial k$ and $\partial\omega/\partial$ k can be calculated from the spin waves dispersion relation in our system [129]

$$\omega = \omega_0 + l_{ex}^2 \omega_M k^2 , \tag{8.14}$$

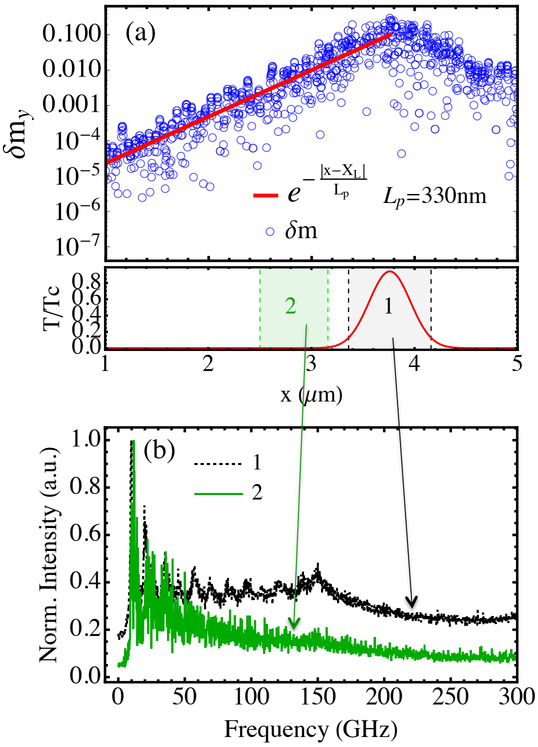

Figure 8.9: (a) Magnon accumulation as defined in Ref. [126] ($\delta m_y(x,t) = m_y(x,t) - m_y(x,0)$) for $X_L = 3.76\mu\text{m}$. The time t at which the magnons accumulations is calculated is $t = 10\text{ns}$, long enough so that magnons have propagated along the strip and they have reached an equilibrium state. Magnons decays exponentially as shown by the fit with $e^{-|x-X_L|/L_p}$, where $L_p = 330\text{nm}$ is the magnon propagation length. (b) FFT intensity as function of magnons frequency in region 1: $X_L \pm 330\text{nm}$ (below the laser spot, black dots) and region 2: $(X_L - 5\sigma_L) \pm 330\text{nm}$ (outside the laser spot, green line).

where l_{ex} is the exchange length and $\omega_M = \gamma_0 M_0 m_e(T)$. The cut-off frequency $\omega_0 = 2\pi f_0$ is taken from simulations. We finally obtain

$$L_p(\omega) = \frac{1}{\alpha_\perp \omega}\frac{\partial \omega}{\partial k} = \frac{2l_{\text{ex}}}{\alpha_\perp}\frac{(\omega_M(\omega - \omega_0))^{1/2}}{\omega}\,. \tag{8.15}$$

Eq. 8.15 is also plotted in Fig. 8.10(c) showing a good agreement with the simulation results. At high frequency, where $l_{ex}^2 \omega_M k^2 \gg \omega_0$, Eq. 8.15 simply reduces to $L_p \cong \lambda/(\pi\alpha)$, where λ is the magnon wavelength.[126]

In the laser spot case, an additional proof of magnons reflection is given by the FFT power in a region $X_0 \pm 330$ nm, where X_0 is chosen in order to remain outside both the TG and the DW as sketched in Fig. 8.11. The FFT is performed with (Fig. 8.11 (b)) or without (Fig. 8.11(a)) the DW. The left bright branches correspond to magnons

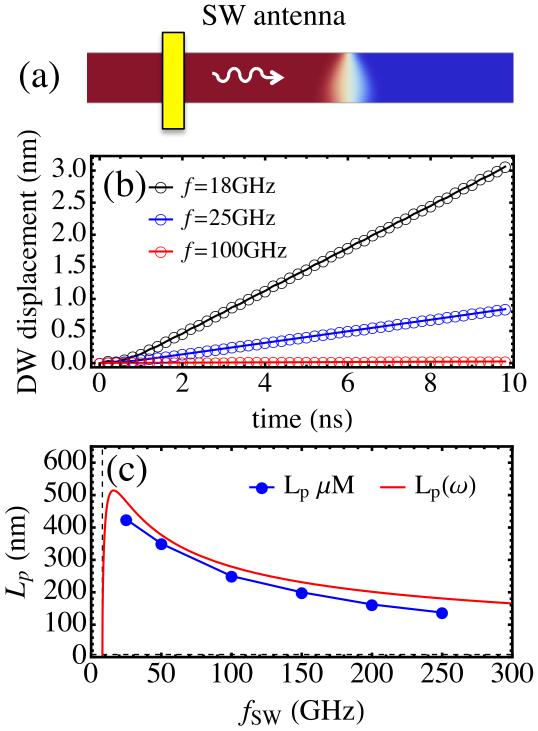

Figure 8.10: (a) Schematic representation of the monochromatic spin waves simulations. (b) DW displacement as function of time for different frequencies. The maximum displacement is obtained for the lowest frequency ($f = 18$ GHz). (c) SW propagation length as function of SW frequency.

propagating from right to left, moving away from the laser spot, as expected. In the FFT with the DW (Fig. 8.11(b)) a small branch appears on the right side, which corresponds to magnons propagating from left to right, towards the laser spot, as a consequence of reflection by the DW [116].

Therefore we conclude that the DW motion towards the cold part is due to low frequency magnons, excited by the laser, which have larger propagation length and are reflected by the DW. The result is different from that predicted by Kim and Tserkovnyak [87], where DW was supposed to move towards the hotter region due to magnons transmission through the DW. The difference is probably due to the different magnon wavelength: in Ref. [87] the authors assumed that the thermal magnon wavelength is much shorter than the DW width, focusing on magnon transmission and the adiabatic STT. In our case, low-frequency (large-wavelength) modes dominate outside the TG due to their larger propagation length and they are mainly reflected by the DW. From Eq. 8.14 we can also estimate the wavelength of the reflected magnons. The frequency range of the reflected branch in Fig. 8.11(b) is approximatively $f_0 < f < 20$GHz which corresponds to a wavelength range $50 < \lambda < 400$nm, larger than or comparable to the DW width parameter

$\Delta_0 = 30$nm. Inside the TG ($d = 2\sigma_L$) the motion is towards the hotter region, consistent with the result of Kim and Tserkovnyak. [87] In the *Full* simulations the DW moves towards the hot part for $d = 4, 5\sigma_L$ meaning that the dipolar field is stronger than the μSTT in this system.

As commented in Sec. 8.2, our analysis of the magnonic STT neglects magnons with $\lambda < 5$nm. Due to their small propagation length ($L_p \sim 80$nm) they can have an effect only at $d = 2, 3\sigma_L$, when the DW is inside the TG. Since their wavelength is much smaller than the DW width, they are expected to pass adiabatically through the DW, moving it towards the hotter region as the ET. This would lead to higher velocities for the *Magnonic* case at $d = 2, 3\sigma_L$, however, their contribution is expected to be small since their propagation length is comparable to the full DW width ($\pi\Delta_0 \sim 90$nm) and therefore, angular momentum transfer is strongly reduced.

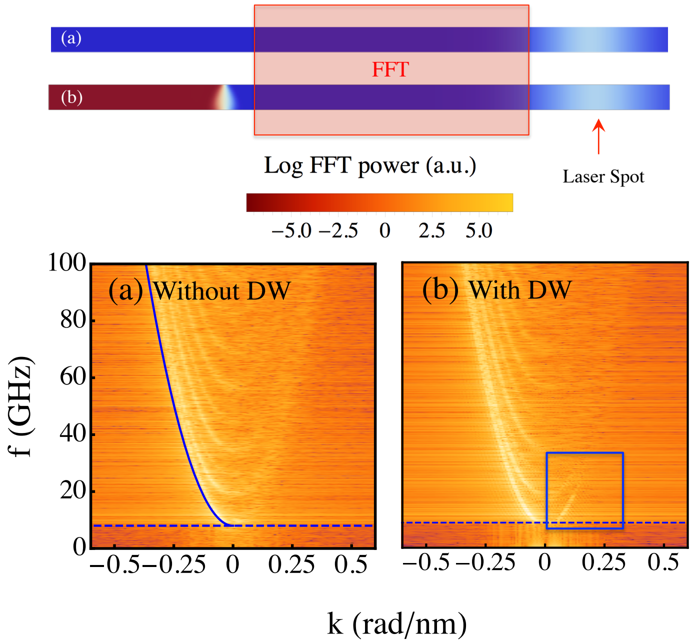

Figure 8.11: Log FFT intensity as function of frequency f and wave vector k calculated at $X_0 \pm 330$nm with (b) or without (a) the DW. The plot shows typical SW dispersion curves. The left branches correspond to magnons propagating from right to left (away from the laser spot), while right branches correspond to magnons propagating from left to right (towards the laser spot). A small right branch at low frequency can be observed in the case with DW (b), which corresponds to magnons reflected by the DW. Blue dashed line indicates the cut-off at $f \approx 9$GHz, while the blue solid line in (a) corresponds to Eq. 8.14, which shows a good agreement with the FFT intensity.

8.3.4 Realistic sample

Our previous results, as well as former theoretical investigations [88, 87, 123], were obtained for a perfect strip where even a small driving force was able to move the DW. However, it is well known that defects or inhomogeneities give rise to DW pinning and a finite propagation field ($H_p \neq 0$) below which the DW remains pinned. We have also analysed DW motion by TG under realistic conditions to see in which case the TG is strong enough to depin the DW. The introduction of edge roughness with a characteristic size of 2.5 nm gives rise to a DW propagation field of $\mu_0 H_p = (3.5 \pm 0.5)$mT. Also in this case the sample temperature follows Eq. (8.4) but the strip temperature T_0 is set $T_0 = 300$K as it would be in conventional experiments. Considering the same ΔT of the previous analysis and in order to remain below T_C we can only apply $\Delta T = 400$K and $\Delta T = 200$K. As shown in Fig. 8.12 , the DW moves towards the laser spot only if it is close enough to the laser spot ($d \leq 2\sigma_L$) and only if $\Delta T = 400$K. Therefore, under realistic conditions, long-range dipolar field and μSTT are not strong enough to move the DW as they are likely hindered below the propagation field in typical experiments. This observation is indeed in agreement with recent experimental observation [90] where the DW motion towards the (close) laser spot was succesfully explained by the sole effect of ET [90].

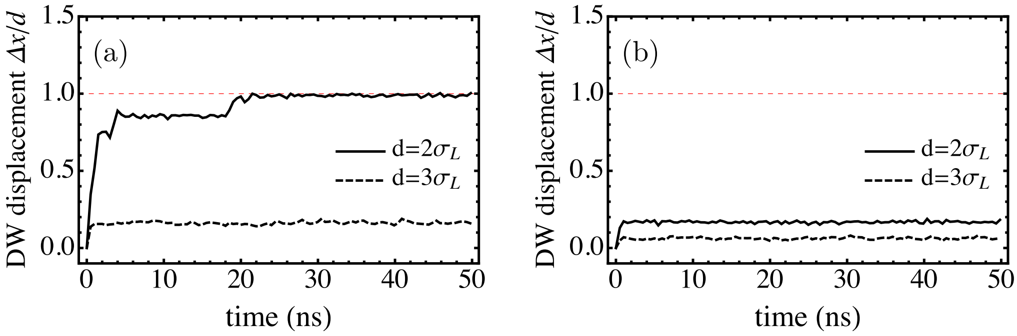

Figure 8.12: DW displacement as funciton of time for $\Delta T = 400$K (a) and $\Delta T = 200$ K (b), for $d = 2\sigma_L$ (full black line) and $d = 3\sigma_L$ (black dashed line). The DW reaches the laser spot (red dashed line at $\Delta x/d = 1$) only for $\Delta T = 400$K at $d = 2\sigma_L$.

8.4 Conclusions

DW motion by Gaussian temperature profiles was analysed in a Py strip under perfect and realistic conditions. Apart from the already known entropic and magnonic contributions, a third driving force was observed due to a thermally induced dipolar field. Such force drives the DW towards the hotter region. An expression for the entropic field was derived in terms of the DW energy and compared with previous expressions showing equal results. The entropic torque pushes the DW towards the hot part and dominates the DW dynamic when the DW is within the TG, while the dipolar field dominates when the DW is outside the TG. In fact, the μSTT drives the DW towards the cold part due to the prevalence of low frequency magnons, which propagate over larger distances ($L_p \approx 330$nm) and are reflected by the DW in the studied sample. Finally, under realistic conditions, the entropic torque is strong enough to move the DW only if the laser spot is closer than $2\sigma_L$ and $\Delta T \geq 400$K. These conclusions can be generalized to other in-plane samples, but we cannot rule out that, in systems with low damping the magnonic STT could overcome the thermally induced dipolar field outside the TG. These results give important insights into the different mechanism responsible for DW motion under thermal gradients and allows for comparison with experimental results in these systems.

Chapter 9

Conclusions and future perspectives

To summarize, the effects of Joule heating and localized temperature gradients on DW dynamics were analysed by means of a novel micromagnetic framework which couples heat and magnetization dynamics self-consistently. A phenomenological Newton-like term in the heat equation can account for the substrate, which absorbs a considerable amount of the heat and would be difficult to include in the micromagnetic software. The accuracy of this phenomenological term was tested against full (sample and substrate) COMSOL simulations showing a remarkable agreement. Furthermore, we showed that curved geometries and patterned constrictions can generate temperature gradients along the sample, which can have significant effects on the DW dynamics. In particular, if the temperature increase remains below the Curie temperature, the DW is generally displaced towards the hotter region, while, if the overall temperature increase is close to the Curie temperature, we can incur local destruction of the ferromagnetic order which may help the DW depinning under external applied fields. Finally, the main driving forces responsible for the thermally induced DW motion were isolated and compared: the entropic torque, due to the minimization of the DW energy. The magnonic STT, due to the interaction between the DW and thermally excited magnons and the thermally induced dipolar field. The entropic torque is identified as the leading contribution and, in realistic condition, it can drive the DW towards the hotter region only if the DW is close to the thermal gradient. A pure, thermally induced DW motion, was also recently observed experimentally [130].

Many questions and interesting new directions are still open. The magnonic STT, for instance, strongly depends on the magnons transmission or reflection from the DW and it is not clear why certain magnons frequencies are transmitted while other are reflected. Moreover, a complete understanding of the interaction between magnons and DWs is still lacking. Non-linear effects and resonances with the DW internal oscillations modes are also interesting aspects that require further investigations. Furthermore, it is reasonable to assume that the transmission and reflection will also depends on sample dimensions, leaving plenty of room for the study and the optimization of magnonic circuits which exploit DWs as active components [131, 132]. Besides, our study was focused on in-plane magnetized systems and it could be interesting to extend it to ultrathin films [4] with out-of-plane magnetization. In fact, in these latter systems, heat could have a larger effect due to the smaller Curie temperature of ultrathin films (for instance a 1 nm thick Cobalt layer has a Curie temperature of 500 K). Hence, a smaller increase in temperature can have bigger effects. Lastly, the novel micromagnetic framework could be extended to analyse ultrafast switching or heat assisted switching where heat and temperature dynamics play an important role.

Part III

Modelling of domain wall motion in ultrathin systems

Chapter 10

Introduction

In the previous part, domain wall (DW) motion was analysed along in-plane magnetized samples, where the electrical current flows mainly through the ferromagnetic layer and DWs are displaced by the Zhang-Li spin-transfer torque (STT). However, recent advances in material deposition introduced the possibility of creating ultrathin ferromagnetic (FM) layers with a thickness of few angstroms, where the magnetization is out-of-plane. An example of typical ultrathin system is shown in Fig. 3.11. At this scale, the interfacial interactions with the neighbouring layers play a relevant role and they can affect many properties of the sample. For instance, the out-of-plane magnetization is due to the presence of a perpendicular magnetic anisotropy (PMA) which originates from the spin-orbit interaction between the FM layer and the neighbouring layers. Furthermore, in samples with broken inversion symmetry where top and bottom layers are different, chiral DWs can be stabilized by the Dzyaloshinskii-Moriya interaction (DMI) (see Section 3.6.2). A recent review about interfacial effects in magnetism can be consulted in Ref. [4].

An efficient way to displace DWs in ultrathin films is by exploiting the spin Hall (SH) effect. In fact, due to the large resistivity of the FM layer, the electrical current flows mainly through the conducting neighbouring layers and, due to the SH effect, a spin-current is generated perpendicularly to the electron flows and injected into the FM layer. Eventually, the spin-current exerts a torque on the FM layer as a consequence of the Slonczewsky-like STT (see Section 3.5 and 3.6).

These systems present several advantages over in-plane magnetized samples. For instance, DWs in out-of-plane samples are smaller and they can be packed with higher density, leading to a larger capacity for memory devices [133]. Furthermore, several experiments [134, 43] suggested that the current-induced DW motion requires lower current densities with respect to the conventional Zhang-Li STT in in-plane samples.

Nonetheless, these systems present also some issues and, in particular, disorder can have a strong impact on DW motion. More generally, the role of disorder in ultrathin systems is still under debate and poorly understood [4]. For in-plane systems edge roughness was the main source of disorder while thickness fluctuations and defects can be assumed as the main source of disorder in ultrathin films. Experiments on field-driven

DW motion have shown that DWs in ultrathin films move as a one-dimensional elastic interface in a two-dimensional pinning potential [135, 136] and (under certain conditions) they are expected to follow the so-called creep law

$$v = v_0 \exp\left[-\eta(\mu_0 H_z)^{-1/4}\right] , \tag{10.1}$$

where η is scaling constant which depends on the pinning potential and on the DW energy. More precisely, the creep theory predicts that, at $T = 0$ the DW does not move until a critical depinning field (H_{dep}). However, for $T > 0$, thermal fluctuations lead to a finite DW velocity even if $H_z < H_{\mathrm{dep}}$. Eq. (10.1) holds for $H_z \ll H_{\mathrm{dep}}$, while intermediate regimes can be observed if $H_z \approx H_{\mathrm{dep}}$ [137, 138]. The predictions of the creep theory are shown in Fig. 10.1 for $T = 0$ and $T = 300$K. The LLG predictions for a perfect sample are labelled as *Perfect* in Fig. 10.1. The $T = 0$ prediction can be obtained also by introducing disorder into the LLG equation, for instance by introducing grains with randomly distributed parameters, which mimic the disorder. However, the $T = 300$K prediction present more complications: firstly, the implementation of a realistic disorder is not straightforward and secondly, the DW velocities predicted under the creep regime are considerably small ($\sim 0.01 - 0.1$ m/s) and one would need to simulate very long times in order to allow the DW to pass through different pinning sites as in typical experiments. Nonetheless, if the DW moves with enough velocity, as in intermediate regimes between creep and flow (the so-called depinning regime) [137, 138] micromagnetic simulations can successfully reproduce the experimental behaviour.

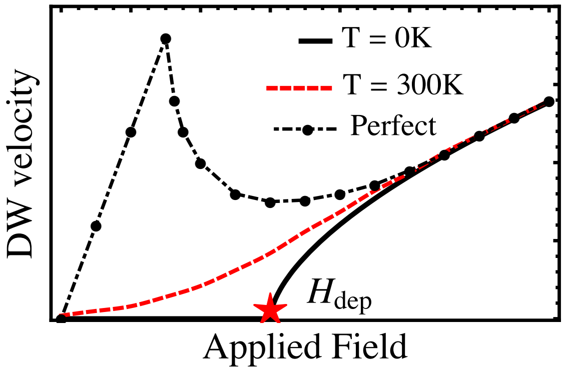

Figure 10.1: DW velocity *vs* applied field as predicted by the LLG equation in a perfect system and by the *creep* law at $T = 0$ and $T = 300$K.

In this part, field and current driven DW motion in ultrathin films is analysed by analytical models and micromagnetic simulations. In Chapter 11, the field and current driven DW motion in Pt/Co/Pt$_{\mathrm{x}}$Au$_{1-\mathrm{x}}$ samples is analysed by micromagnetic simulations and 1D model. The experimental data for the DW velocity as function of the applied field are reproduced in order to obtain the damping parameter and the disorder model. On a second step, by using the parameters obtained in the field driven analysis, the DW motion by SH torque is analysed for different SH angles. A particular attention is devoted to the role of disorder which is shown to significantly affect both the field and current driven DW dynamics. This work was performed in collaboration with an experimental group from the University of Leeds.

In the last part, Chapter 12, the depinning field as function of the damping parameter is analysed by micromagnetic simulations. Contrary to conventional approximations, which assume that the depinning field is independent on damping, we show that it strongly decreases for small damping parameters. This behaviour is explained by a 1D model and it is related to the DW internal dynamics and the finite size of the pinning barrier. All these results illustrate the procedure and the main issues related to the modelling of DW motion in ultrathin films. At the same time, they provide useful insights about the role of disorder in these systems. Chapter 11 reports unpublished results while Chapter 12 is adapted from Ref. [9]. As in the previous part, each chapter is written independently and it can be read separately. For the same reason, several concepts are repeated among the chapters, especially in the introductory part and when describing the simulations methods.

Chapter 11

Modelling of domain wall motion in $\mathrm{Pt/Co/Pt_xAu_{1-x}}$

Domain wall motion in ultrathin multilayers of $\mathrm{Pt/Co/Pt_xAu_{1-x}}$ is analysed by means of micromagnetic simulations. The domain wall velocity as function of the applied field is measured experimentally in these systems by bubble expansion. Our work is focused on reproducing the domain wall velocity in order to extract the damping parameter (α) from the micromagnetic simulations. On a second step, the current induced domain wall motion, due to the spin Hall torque from the neighbouring layers, is analysed for different spin Hall angles. This latter analysis will allow to extract the spin Hall angle from the current driven measurements. The modification of the top layer, going from $\mathrm{Pt/Co/Au}$ to $\mathrm{Pt/Co/Pt}$ and a mixed alloy $\mathrm{Pt/Co/Pt_{50}Au_{50}}$ changes the films properties and tunes the efficiency of the spin Hall torque. In our study, a particular emphasis is given to the role of disorder which is found to have a significant effect both on the field driven and current driven domain wall motion. [1]

11.1 Introduction

Magnetic domain walls (DWs) in ultrathin systems can be efficiently displaced by electrical currents. Typical ultrathin films consist of multilayers made of Heavy Metal (HM)/Ferromagnet (FM)/HM or metal oxides such as Pt/Co/Pt or $\mathrm{Pt/Co/AlO_x}$, where the FM has a thickness of typically few nanometers. Due to the small thickness of the FM layer, the neighbouring layers have an important effect on the sample properties. For instance, due to spin-orbit interaction with the neighbouring layers, these systems present perpendicular magnetic anisotropy (PMA) and, in samples with broken inversion symmetry, the Dzyalonshinsky-Moriya Interaction (DMI) favours Néel DW with fixed chirality (see Section 3.6). The current-induced DW motion is also due to the spin

---

[1] Collaboration with K. Shahbazi, A. Hrabec and C.H. Marrows from University of Leeds.

Hall effect from the neighbouring layers. In fact, due to high resistivity of the thin FM layer [139], the electrical current flows mainly through the HM layers where the spin Hall effect gives rise to a spin-current perpendicular to the electron flow. The spin-current is eventually injected into the FM where it drives the DWs by means of the Slonczewski-like STT (see Section 3.6). Since the current is polarized along the y direction (see Fig. 3.14), the DW needs to have a Néel configuration in order to maximize the effect of the Slonczewski-like torque. As a consequence, the cooperation of DMI and SH effect is able to effectively drive DWs [43, 134].

As anticipated, these systems present advantages with respect to in-plane samples, where the current flows through the FM layer and the DWs are displaced by the Zhang-Li STT. In particular, DWs in PMA systems are smaller and they can be packed with a larger density, leading to a larger capacity for memory devices [133]. Furthermore, SH driven DWs require smaller current densities ($\approx 10^{11}$ A/m^2) [43] with respect to Zhang-Li driven DWs ($\approx 10^{12}$ A/m^2) [78].

Nonetheless, also these systems present issues and, in particular, DWs are strongly affected by disorder [63]. For instance, field-driven DWs are shown to present a plateau in the DW velocity, which cannot be explained by the usual flow regime [140, 63, 141]. Only for very high fields, it is possible to recover the flow regime, which holds for perfect samples. For small fields, the DW moves according to the creep law [135], which describes the motion of an elastic interface across random pinning sites.

More generally, the effect of disorder on DW dynamics in these kind of systems is still under debate and poorly understood. For instance, it has been shown to significantly affect Skyrmions trajectories [142] or to induce the formation of vertical Bloch lines (VBL) inside the DWs [140]. From the modelling point of view, a critical issue is the choice of the disorder model. Typically, disorder is introduced by changing certain micromagnetic parameters like the saturation magnetization M_s or the uniaxial anisotropy K_u, which are assumed to follow a normal distribution around their mean value. However, one can choose to change one or more parameters and this can have different effects on the magnetization dynamics. For instance, Voto et al. [141] showed that a fluctuation of the local anisotropy axis leads to a shift in the DW velocity even in the flow regime, which is not observed by simply changing the modulus of the uniaxial anisotropy K_u.

Here, we reproduce the experimental results of DW velocity as function of the applied field, measured in three samples consisting of Pt/Co/Pt, Pt/Co/Pt$_{50}$Au$_{50}$ and Pt/Co/Au. The composition of the top layer is varied in order to change the material properties and tune the DMI and the SH efficiencies. We adopt a disorder model which mimic a thickness fluctuation across the sample, as it can be generated during the growth process. From these simulations we extract the damping parameter, which is the only free parameter together with the disorder parameters. On a second step, by using the damping parameter and the disorder model obtained from the field driven analysis, we study the SH driven DW motion for different SH angles. This latter description will allow the measurement of the SH angle from current driven experimental data. Disorder is shown to significantly affect both the field driven and current driven DW motion. The determination of the damping parameter and the disorder model from separate analyses is essential in order to have a consistent description of field and current driven motion. In fact, typical analyses are focused only on the current driven results, which are fitted by using both damping and SH angle as free parameters.

11.2 Methods

11.2.1 Experimental measurements [2]

The trilayers of Pt(3 nm)/Co/$\mathrm{Pt_xAu_{1-x}}$(3 nm), where x varies between 0 and 1, were prepared by sputtering at high temperatures as described in Ref. [143]. The seed Pt layer was sputtered directly on a C-plane sapphire substrate at 500° C followed by the Co sputtering at 100° C. The $\mathrm{Pt_xAu_{1-x}}$ layer was grown by co-sputtering from Pt and Au targets at 100° C in a way that the sputtering powers were adjusted to keep the rate $1A/s$. The quality of these layers was confirmed by the x-ray diffraction technique. All the films show a square hysteresis loop as a function of perpendicular magnetic field confirming the out-of-plane character of the Cobalt. The uniaxial anisotropy K_u and magnetization M_s were measured by vibrating sample magnetometry (SQUID-VSM). The temperature dependent magnetization data can be fitted with Bloch law $M_s = 1 - cT^{3/2}$ from which the extracted exchange stiffness is $A = 17 \pm 1$ pJ/m. The DMI constant is measured by measuring the DW velocity as function of the in-plane field H_x, as described in Ref. [35, 36] (see also Fig. 11.1). Bubble domains are expanded by means of a small out-of-plane field which is kept constant. Data for the DW velocity as function of the in-plane field, together with the DMI measurements are shown in Fig. 11.1. The thickness of the samples is also measured by using Transmission Electrons Microscopy (TEM) techniques. The samples growth and the measurements were performed by collaborators from the University of Leeds (UK). The samples parameters are summarized in Table 11.1.

Sample	t (nm)	$M_s \times 10^5$ (A/m)	$K_u \times 10^5$ (J/m^3)	D (mJ/m^2)
Pt/Co/Pt	1.19 ± 0.9	6.8 ± 0.7	5.3 ± 1.0	0
Pt/Co/PtAu	1.29 ± 0.9	6.1 ± 0.7	4.8 ± 0.9	0.25 ± 0.05
Pt/Co/Au	1.08 ± 0.9	6.8 ± 0.8	7.1 ± 1.1	0.76 ± 0.11

Table 11.1: Measured parameters for the three sample Pt/Co/Pt, Pt/Co/PtAu and Pt/Co/Au.

11.2.2 Micromagnetic simulations

For the micromagnetic simulations we consider a rectangular sample of dimension $(1024 \times 512 \times t)$ nm^3, where t is the Co thickness. We use periodic boundary conditions along the y direction, in order to simulate an extended thin film. In the experimental measurements the domains are bubble domains and the DWs are circular rather than straight lines (see

---

[2] From A.Hrabec, K. Shahbazi and C.H. Marrows, unpublished.

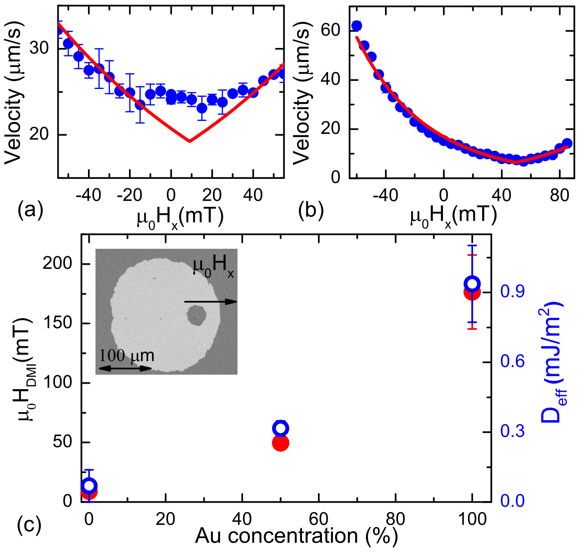

Figure 11.1: DW velocity as a function of in-plane magnetic field $\mu_0 H_x$ in case of Pt (a) and $\mathrm{Pt}_{50}\mathrm{Au}_{50}$ (b) capping layers for a fixed value of the out-of-plane field. (c) Effective DMI field $\mu_0 H_{\mathrm{DMI}}$ and effective DMI constant D as a function of Au concentration x in Pt/Co(6A)/Au films. An example of Kerr image of the bubble expansion is shown in inset. Figure from A. Hrabec, K. Shahbazi and C.H. Marrows, unpublished.

the inset in Fig. 11.1). However, for bubbles with radius $r \gg 10$ μm (see Appendix E), the DW behaves as a straight line since the surface tension is negligible. On the other hand, we will incur in an error if we try to reproduce the results by simulating smaller bubble expansions. In fact, for smaller bubbles the surface tension is relevant and it wants to collapse the bubble domain, reducing the efficiency of the out-of-plane field (see Appendix E). Magnetization dynamics is analysed by means of the LLG equation [11]:

$$\frac{d\mathbf{m}}{dt} = -\frac{\gamma_0}{1+\alpha^2}\left[\mathbf{m} \times (\mathbf{H}_{\mathrm{eff}} + \mathbf{H}_{\mathrm{th}})\right] - \frac{\gamma_0 \alpha}{1+\alpha^2}\left\{\mathbf{m} \times \left[\mathbf{m} \times (\mathbf{H}_{\mathrm{eff}} + \mathbf{H}_{\mathrm{th}})\right]\right\} , \tag{11.1}$$

where $\mathbf{m}(\mathbf{r}, t) = \mathbf{M}(\mathbf{r}, t)/M_s$ is the normalized magnetization vector, with M_s being the saturation magnetization. γ_0 is the gyromagnetic ratio and α is the Gilbert damping. $\mathbf{H}_{\mathrm{eff}} = \mathbf{H}_{\mathrm{exch}} + \mathbf{H}_{\mathrm{DMI}} + \mathbf{H}_{\mathrm{an}} + \mathbf{H}_{\mathrm{dmg}} + H_z \hat{\mathbf{u}}_z$ is the effective field, including the exchange, DMI, uniaxial anisotropy, demagnetizing and external field contributions [11] respectively. Thermal fluctuations at uniform and constant room temperature $T = 300$K are taken into account through a stochastic thermal field $\mathbf{H}_{\mathrm{th}}$, which has white noise properties with the correlator [94, 46, 47]

$$\langle H_{\mathrm{th}}(\mathbf{r},t)_i H_{\mathrm{th}}(\mathbf{r}',t')_j\rangle = \frac{2\alpha k_B T}{\gamma_0\mu_0 M_s V}\delta_{ij}\delta(\mathbf{r}-\mathbf{r}')\delta(t-t'), \tag{11.2}$$

where k_B is the Boltzmann constant, μ_0 the vacuum permeability and V the volume of the computational cell. Disorder is taken into account by dividing the sample into grains by Voronoi tessellation [8, 144], as shown in Fig. 11.2(a). In each grain the micromagnetic parameters $\{M_s, D_c, K_u\}$ change in a correlated way in order to mimic a normally distributed thickness [145]:

$$t_G = N(t,\delta) \rightarrow \begin{cases} M_G &= (M_s t_G)/t \\ K_G &= (K_u t)/t_G \\ D_G &= (D_c t)/t_G \end{cases}, \tag{11.3}$$

where the subscript G stands for grain, t is the average thickness of the Co layer and δ is the standard deviation of the thickness normal distribution. The sample is discretized in cells of dimensions $(2\times 2\times t)$nm^3, smaller than the exchange length $l_{ex}\sim 5$nm. Different grain sizes (GS) and thickness fluctuations are tested in order to reproduce the experimental results. A DW is placed and relaxed at the center of the sample as depicted in Fig. 11.2(b). Eq. (11.1) is solved by the finite difference solver MuMax 3.9.3 [8].

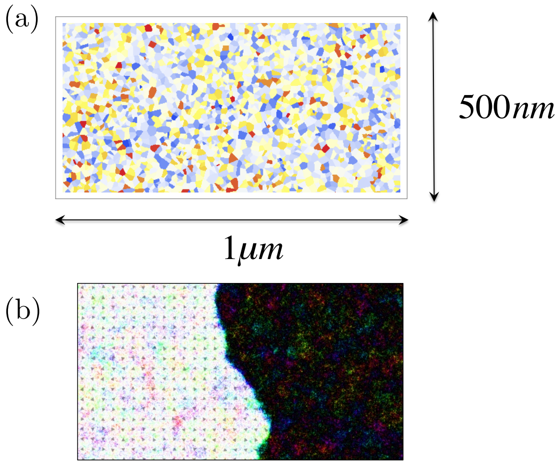

Figure 11.2: (a) A typical grains pattern. (b)DW initial configuration.

11.3 Results and discussion

11.3.1 Field driven DW motion

The best fitting parameters are summarized in Table 11.2 together with the measured depinning field B_{dep}.

Sample	B_{dep} (mT)	GS (nm)	δ	α
Pt/Co/Pt	32 ± 1	15	8%	0.2 ± 0.05
Pt/Co/PtAu	56 ± 1	15	16%	0.4 ± 0.05
Pt/Co/Au	75 ± 1	15	15%	0.4 ± 0.05

Table 11.2: Depinning field and fitting parameters.

The larger depinning field is reflected in a larger value of the thickness fluctuation for the PtAu and Au top layers. This can be explained by considering that the Co/Au interface is rougher than the Pt/Co interface since gold atoms poorly interact with the Co atoms. Nonetheless, also the damping parameter is larger for the Au and PtAu top layer and this can also affect the depinning field (see Chapter 12). The larger damping parameter of Pt/Co/Au and Pt/Co/PtAu suggests a larger spin-pumping effect [18] for the Co/Au interface but further checks are needed in order to confirm this hypothesis. The results obtained for the field driven DW dynamics are shown in Fig. 11.3 for the three samples. The agreement, especially for the Pt/Co/PtAu and the Pt/Co/Au samples, is remarkably good. The black solid lines in each plot represent the prediction of the 1D model in the absence of disorder for the obtained damping parameter. The 1D model is in agreement with the experimental results only for the Pt/Co/Pt sample in the region where $B_z \gg B_{\text{dep}}$. On the contrary, for the Au and the PtAu top layers, both the micromagnetic simulations and the experimental results deviate from the 1D model predictions (Fig. 11.3(a)-(b)). This result is important since a common method to extrapolate the damping parameter is to fit the DW velocity vs applied field curve with the 1D model equations

$$v_{\text{DW}} = \frac{\gamma_0 \Delta_{\text{DW}}}{\alpha} H_z \,, \quad v_{DW} = \frac{\alpha \gamma_0 \Delta_{\text{DW}}}{1+\alpha} H_z \,, \tag{11.4}$$

valid for $H_z < H_{\text{WB}}$ and $H_z \gg H_{\text{WB}}$ respectively, where H_{WB} indicate the Walker Breakdown field. Our results indicate that if we are too close to the depinning field, full micromagnetic simulations are needed in order to extract the damping parameter.

11.3.2 Current driven

By using the same disorder and damping parameters, we analyse the DW motion induced by the SH torque. The LLG equation augmented with the SH torque is given by (see

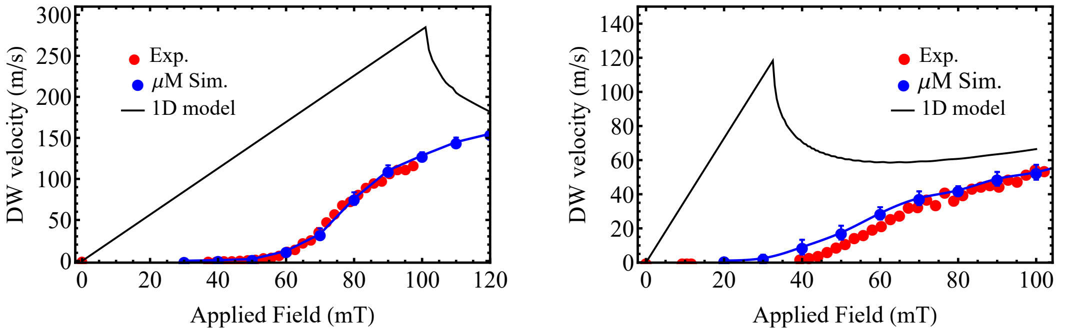

(a) Pt/Co/Au

(b) Pt/Co/PtAu

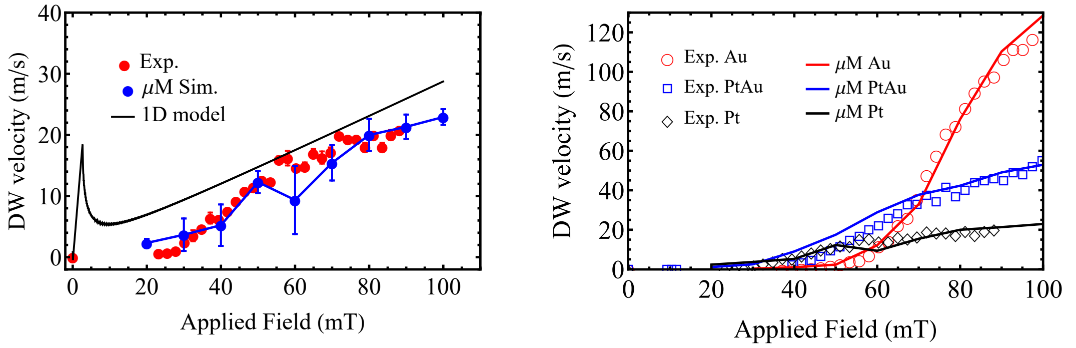

(c) Pt/Co/Pt

(c)

Figure 11.3: DW velocity as function of the applied field for (a) Pt/Co/Au, (b) Pt/Co/PtAu and (c) Pt/Co/Pt. Red dots correspond to experimental data and blue dots correspond to μM simulations. The black full line indicates the one-dimensional model prediction in the absence of disorder. (d) DW velocity as function of the applied, experimental data (dots) vs μM results (lines) for the three samples.

also Section 3.6)

$$\begin{aligned}\frac{d\mathbf{m}}{dt} &= -\frac{\gamma_0}{1+\alpha^2}\left[\mathbf{m}\times\left(\mathbf{H}_{\text{eff}}+\mathbf{H}_{\text{th}}\right)\right]-\frac{\gamma_0\alpha}{1+\alpha^2}\left\{\mathbf{m}\times\left[\mathbf{m}\times\left(\mathbf{H}_{\text{eff}}+\mathbf{H}_{\text{th}}\right)\right]\right\}\\ &\quad+\frac{\mu_B J\theta_{\text{SH}}}{|e|M_s(1+\alpha^2)t}\left[\mathbf{m}\times\left(\mathbf{m}\times\hat{\mathbf{u}}_y\right)+\alpha\left(\mathbf{m}\times\hat{\mathbf{u}}_y\right)\right]\,, \qquad (11.5)\end{aligned}$$

where μ_B is the Bohr magneton, J is the current density flowing through the HM, e is the electron charge and θ_{SH} is the SH angle. The only free parameter is now the SH angle. The current driven results are shown in Fig. 11.4 for the Pt/Co/Au and the Pt/Co/PtAu samples. The SH torque has no effect on the Pt/Co/Pt sample since the wall is Bloch and, additionally, the two spin-currents from the top and bottom Pt layers compensate each others (the top and bottom layer have the same thickness and the same resistivity). The DMI constant of the Pt/Co/Au and Pt/Co/PtAu is enough to stabilize

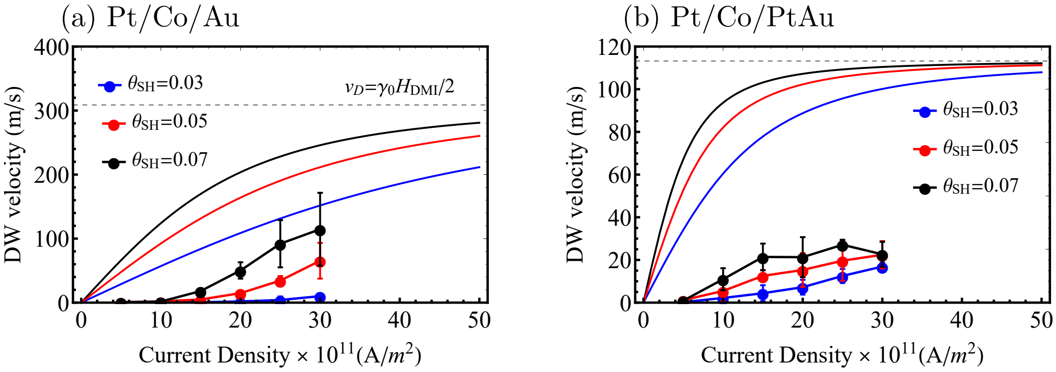

Figure 11.4: (a) DW velocity as function of the current density for (a) Pt/Co/Au and for (b) Pt/Co/PtAu. The solid lines indicate the prediction of the 1D model in the absence of disorder for the corresponding SH angle.

perfect Néel walls in these samples and, therefore, the SH torque is maximized. Indeed, the solid lines represent the prediction of the 1D model for perfect Néel walls. The DMI fixes the saturation velocity as discussed in Section 3.9.3. However, disorder considerably reduces the efficiency of the SH torque and the DW velocity. This is because disorder affects the DW internal configuration which deviates from a perfect Néel configuration and, therefore, the efficiency of the SH torque is reduced. Furthermore, these results will allow the measurements of the SH angle by comparing the experimental data of the DW velocity with the micromagnetic simulations. Also in this case our results suggest that full micromagnetic simulations are needed in order to reproduce the DW dynamics.

11.4 Conclusions

To summarize, the field and current driven DW dynamics in Pt/Co/Pt$_x$Au$_{1-x}$ samples is analysed by full micromagnetic simulations. The field driven results are compared with the experimental measurements in order to extract the disorder and damping parameters. With this input, the current driven dynamics is analysed for different SH angles. Both the field and current driven analysis are compared with the prediction of the 1D model for perfect samples. Our results indicate that disorder has a significant and non-trivial influence on the DW dynamics. We have shown that full micromagnetic simulations are needed if one wants to obtain the damping parameter from the field driven measurements, while the 1D model gives the correct results only if $H_z \gg H_{\mathrm{dep}}$. In the current driven analysis, disorder strongly reduces the efficiency of the SH torque by affecting the DW internal configuration. These analyses illustrate the procedure and the main issues related to the modelling of DW motion in ultrathin films and, furthermore, they provide significant insights into the role of disorder in DW dynamics in ultrathin films. The micromagnetic results can be further used to extract the SH angle from the current driven measurements.

Chapter 12

Dynamical depinning of chiral domain walls

The domain wall depinning field represents the minimum magnetic field needed to move a domain wall, typically pinned by samples' disorder or patterned constrictions. Conventionally, such field is considered independent on the Gilbert damping since it is assumed to be the field at which the Zeeman energy equals the pinning energy barrier (both damping independent). Here, we analyse numerically the domain wall depinning field as function of the Gilbert damping in a system with perpendicular magnetic anisotropy and Dzyaloshinskii-Moriya interaction. Contrary to expectations, we find that the depinning field depends on the Gilbert damping and that it strongly decreases for small damping parameters. We explain this dependence with a simple one-dimensional model and we show that the reduction of the depinning field is related to the finite size of the pinning barriers and to the domain wall internal dynamics, connected to the Dzyaloshinskii-Moriya interaction and the shape anisotropy. [1]

12.1 Introduction

Magnetic domain wall (DW) motion along ferromagnetic (FM) nanostructures has been the subject of intense research over the last decade owing to its potential for new promising technological applications [3, 2] and for the very rich physics involved. A considerable effort is now focused on DW dynamics in systems with perpendicular magnetic anisotropy (PMA) which present narrower DWs and a better scalability. Typical PMA systems consist of ultrathin multi-layers of heavy metal/FM/metal oxide (or heavy metal), such as Pt/Co/Pt [135, 138] or Pt/Co/AlOx [41, 42, 146], where the FM layer has a thickness of typically $0.6-1$ nm. In these systems, PMA arises mainly from interfacial interactions between the FM layer and the neighbouring layers (see Ref. [4] and

---

[1] Adapted from S. Moretti, M. Voto and E. Martinez, Phys. Rev. B 96, 054433 (2017)

references therein). Another important interfacial effect is the Dzyaloshinskii-Moriya interaction (DMI) [32, 33], present in systems with broken inversion symmetry such as Pt/Co/AlOx. This effect gives rise to an internal in-plane field that fixes the DW chirality (the magnetization rotates always in the same direction when passing from up to down and from down to up domains) and it can lead to a considerably faster domain wall motion [33] and to new magnetic patterns such as Skyrmions [38] or helices [147]. Normally, DWs are pinned by samples' intrinsic disorder and a minimum propagation field is needed in order to overcome such pinning energy barrier and move the DW. Such field is the DW depinning field (H_{dep}) and it represents an important parameter from a technological point of view since a low depinning field implies less energy required to move the DW and, therefore, a energetically cheaper device.

From a theoretical point of view, DW motion can be described by the Landau-Lifshitz-Gilbert (LLG) equation [11] which predicts, for a perfect sample without disorder, the velocity *vs* field curve depicted in Fig. 10.1 and labelled as *Perfect*. In a disordered system, experiments have shown that a DW moves as a general one-dimensional (1D) elastic interface in a two-dimensional disordered medium [135, 138] and that it follows a theoretical velocity *vs* driving force curve, predicted for such interfaces [148, 149] (also shown in Fig. 10.1 for $T = 0$ and $T = 300$K). Moreover, this behaviour can be reproduced by including disorder in the LLG equation [94, 141, 63]. At zero temperature ($T = 0$) the DW does not move as long as the applied field is lower than H_{dep}, while, at $T \neq 0$, thermal activation leads to DW motion even if $H < H_{\text{dep}}$ (the so called *creep* regime). For high fields ($H >> H_{\text{dep}}$) the DW moves as predicted by the LLG equation in a perfect system. Within the creep theory, the DW is considered as a simple elastic interface and all its internal dynamics are neglected. Conventionally, H_{dep} is considered independent of the Gilbert damping because it is assumed to be the field at which the Zeeman energy equals the pinning energy barrier [136, 150] (both damping independent). Such assumption, consistently with the creep theory, neglects any effects related to the internal DW dynamics such as DW spins precession or vertical Bloch lines (VBL) formation [140]. The damping parameter, for its part, represents another important parameter, which controls the energy dissipation and affects the DW velocity and Walker Breakdown [60]. It can be modified by doping the sample [151] or by a proper interface choice as a consequence of spin-pumping mechanism [18]. Modifications of the DW depinning field related to changes in the damping parameter were already observed in in-plane systems [151, 152] and attributed to a non-rigid DW motion [151, 152]. Oscillations of the DW depinning field due to the internal DW dynamics were also experimentally observed in in-plane similar systems [153]. Additional dynamical effects in soft samples, such as DW boosts in current induced motion, were numerically predicted and explained in terms of DW internal dynamics and DW transformations [154, 155].

Here, we numerically analyse the DW depinning field in a system with PMA and DMI as function of the Gilbert damping. We observe a reduction of H_{dep} for low damping and we explain this behaviour by adopting a simple 1D model. We show that the effect is due to the finite size of pinning barriers and to the DW internal dynamics, related to the DMI and shape anisotropy fields. This article is structured as follows: in Section 12.2 we present the simulations method, the disorder implementation and the H_{dep} calculations. The main results are outlined and discussed in Section 12.3, where we also present the 1D model. Finally, the main conclusions of our work are summarized in Section 12.4.

12.2 Micromagnetic simulations

We consider a sample of dimensions $(1024 \times 1024 \times 0.6)$ nm^3 with periodic boundary conditions along the y direction, in order to simulate an extended thin film. Magnetization dynamics is analysed by means of the LLG equation [11]:

$$\frac{d\mathbf{m}}{dt} = -\frac{\gamma_0}{1+\alpha^2}\left(\mathbf{m} \times \mathbf{H}_{\text{eff}}\right) - \frac{\gamma_0 \alpha}{1+\alpha^2}\left[\mathbf{m} \times \left(\mathbf{m} \times \mathbf{H}_{\text{eff}}\right)\right] \,, \tag{12.1}$$

where $\mathbf{m}(\mathbf{r},t) = \mathbf{M}(\mathbf{r},t)/M_s$ is the normalized magnetization vector, with M_s being the saturation magnetization. γ_0 is the gyromagnetic ratio and α is the Gilbert damping. $\mathbf{H}_{\text{eff}} = \mathbf{H}_{\text{exch}} + \mathbf{H}_{\text{DMI}} + \mathbf{H}_{\text{an}} + \mathbf{H}_{\text{dmg}} + H_z \hat{\mathbf{u}}_z$ is the effective field, including the exchange, DMI, uniaxial anisotropy, demagnetizing and external field contributions [11] respectively. Typical PMA samples parameters are considered: $A = 17 \times 10^{-12}$ J/m, $M_s = 1.03 \times 10^6$ A/m, $K_u = 1.3 \times 10^6$ J/m^3 and $D = 0.9$ mJ/m^2, where A is the exchange constant, D is the DMI constant and K_u is the uniaxial anisotropy constant. Disorder is taken into account by dividing the sample into grains by Voronoi tessellation [8, 144], as shown in Fig. 12.1(a). In each grain the micromagnetic parameters $\{M_s, D_c, K_u\}$ change in a correlated way in order to mimic a normally distributed thickness [145]:

$$t_G = N(t_0, \delta) \rightarrow \left\{ \begin{array}{lcl} M_G & = & (M_s t_G)/t_0 \\ K_G & = & (K_u t_0)/t_G \\ D_G & = & (D_c t_0)/t_G \end{array} \right. \,, \tag{12.2}$$

where the subscript G stands for grain, t_0 is the average thickness ($t_0 = 0.6$nm) and δ is the standard deviation of the thickness normal distribution. The sample is discretized in cells of dimensions $(2 \times 2 \times 0.6)$nm^3, smaller than the exchange length $l_{ex} \sim 5$nm. Grain size is GS=15 nm, reasonable for these materials, while the thickness fluctuation is $\delta = 7\%$. Eq. (12.1) is solved by the finite difference solver MuMax 3.9.3 [8].

A DW is placed and relaxed at the center of the sample as depicted in Fig. 12.1(b). H_{dep} is calculated by applying a sequence of fields and running the simulation, for each field, until the DW is expelled from the sample, or until the system has reached an equilibrium state (i.e. the DW remains pinned): $\tau_{\max} < \epsilon(\alpha)$. $\tau_{\max}$ indicates the maximum torque, which rapidly decreases when the system is at equilibrium. It only depends on the system parameters and damping. For each value of α, we choose a specific threshold, $\epsilon(\alpha)$, in order to be sure that we reached an equilibrium state (see Appendix F for more details). The simulations are repeated for 20 different disorder realizations. Within this approach, H_{dep} corresponds to the minimum field needed to let the DW propagate freely through the whole sample. In order to avoid boundaries effects, the threshold for complete depinning is set to $\langle m_z \rangle > 0.8$, where $\langle m_z \rangle$ is averaged over all the realizations, i.e. $\langle m_z \rangle = \sum_{i=1}^{N} \langle m_z \rangle_i / N$, where $N = 20$ is the number of realizations. We checked that, in our case, this definition of H_{dep} coincides with taking $H_{\text{dep}} = \text{Max}\{H^i_{\text{dep}}\}$, with H^i_{dep} being the depinning field of the single realization. In other words, H_{dep} corresponds to the minimum field needed to depin the DW from any possible pinning site considered in the 20 realizations [2].

Following this strategy, the DW depinning field is numerically computed with two different approaches:
(1) by *Static* simulations, which neglect any precessional dynamics by solving

$$\frac{d\mathbf{m}}{dt} = -\frac{\gamma_0 \alpha}{1+\alpha^2} \left[\mathbf{m} \times (\mathbf{m} \times \mathbf{H}_{\text{eff}}) \right] . \tag{12.3}$$

This is commonly done when one looks for a minimum of the system energy and it corresponds to the picture in which H_{dep} simply depends on the balance between Zeeman and pinning energies.[3]
(2) by *Dynamic* simulations, which include precessional dynamics by solving the full Eq. (12.1). This latter method corresponds to the most realistic case. Another way to estimate the depinning field is to calculate the DW velocity *vs* field curve at $T = 0$ and look for minimum field at which the DW velocity is different from zero. For these simulations we use a moving computational region and we run the simulations for $t =$ 80ns (checking that longer simulations do not change the DW velocity, meaning that we reached a stationary state). This second setup requires more time and the calculations are repeated for only 3 disorder realizations.

Using these methods, the depinning field H_{dep} is calculated for different damping parameters α.

12.3 Results and discussion

12.3.1 Granular system

Our first result is shown in Fig. 12.2(a)-(b), which depicts the final average magnetization $\langle m_z \rangle$ as function of the applied field for different damping parameters. In the *Static* simulations (Fig. 12.2(a)) H_{dep} does not depend on damping, so that a static depinning field can be defined. Conversely, in the *Dynamic* simulations (Fig. 12.2(b)), H_{dep} decreases for low damping parameters. The depinning field is indicated by a star in each plot and the static depinning field is labelled as H_s. The same result is obtained by calculating H_{dep} from the DW velocity *vs* applied field plot, shown in Fig. 12.2(c). The stars in Fig. 12.2(c) correspond to the depinning fields calculated in the previous

---

[2] This definition is preferred over the average of H^i_{dep} since it is more independent on the sample size. In fact, by increasing the sample dimension along the x direction, we increase the probability of finding the highest possible pinning site in the single realization and the average of H^i_{dep} will tend to the maximum.

[3] This is solved by the *Relax* solver of MuMax with the assumption $\alpha/(1+\alpha^2) = 1$.

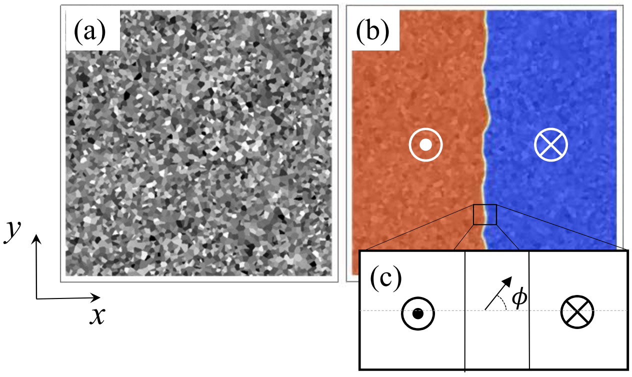

Figure 12.1: (a) Grains structure obtained by Voronoi tassellation. (b) Initial DW state. (c) Sketch of the internal DW angle ϕ.

simulations and they are in good agreement with the values predicted by the velocity *vs* field curve. The dynamical depinning field $\mu_0 H_d$, normalized to the static depinning field $\mu_0 H_s = (87 \pm 1)$mT, with μ_0 being the vacuum permeability, is shown in Fig. 12.2(d) as function of the damping parameter α. H_d saturates for high damping (in this case $\alpha \geq 0.5$) while it decreases for low damping until $H_d/H_s \sim 0.4$ at $\alpha = 0.02$. This reduction must be related to the precessional term, neglected in the static simulations. The same behaviour is observed with different grain sizes (GS=5 and 30 nm) and with a different disorder model, consisting of a simple variation of the K_u modulus in different grains. This means that the effect is not related to the grains size or to the particular disorder model we used.

Additionally, Fig. 12.3 represents the DW energy [4] as function of DW position and damping parameter for $\mu_0 H_z = 70$ mT. At high damping, the average DW energy density converges to $\sigma_\infty \sim 10$ mJ/m^2, in good agreement with the analytical value $\sigma_0 = 4\sqrt{AK_0} - \pi D = 10.4$ mJ/m^2, where K_0 is the effective anisotropy $K_0 = K_u - \mu_0 M_s^2/2$. On the contrary, for low damping, the DW energy increases up to $\sigma(0.02) \sim 14$ mJ/m^2. This increase, related to DW precessional dynamics, reduces the effective energy barrier and helps the DW to overcome the pinning barriers. Fig. 12.3(c) shows the total energy of the system (including Zeeman). As expected [156], the energy decreases as the DW moves.

---

[4] The DW energy is calculated as the energy of the system with the DW minus the energy of the system without the DW (uniform state). The profile is obtained by moving the DW with an external applied field and then subtracting the Zeeman energy.

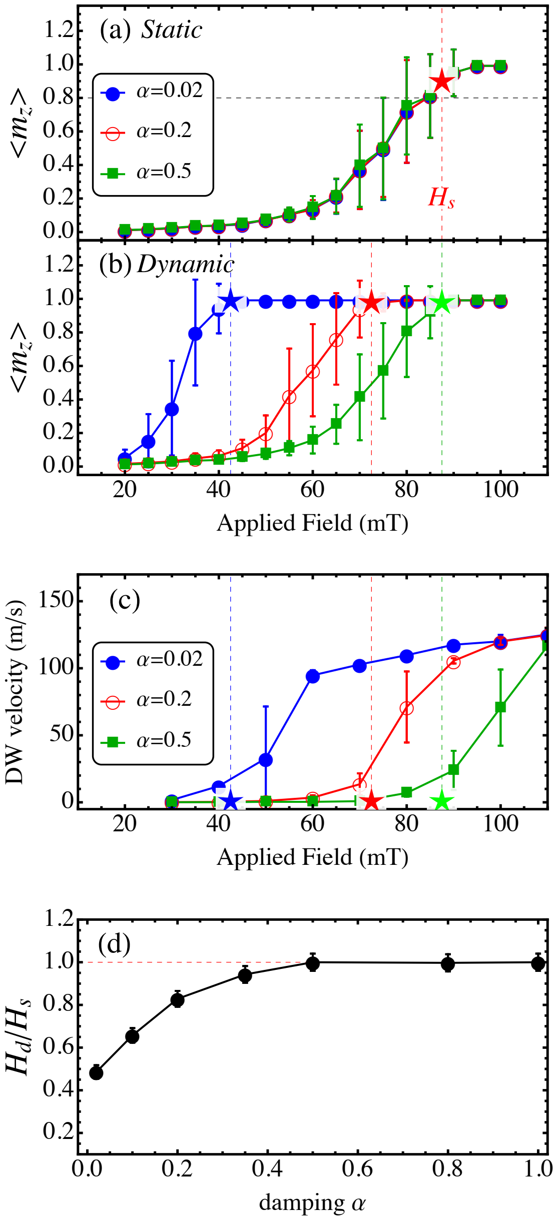

Figure 12.2: Average $\langle m_z \rangle$ as function of applied field for different damping parameters for the (a)*Static* simulations and (b)*Dynamic* simulations. (c) DW velocity vs applied field for different damping. (d) Dynamical depinning field, normalized to H_s, as function of damping.

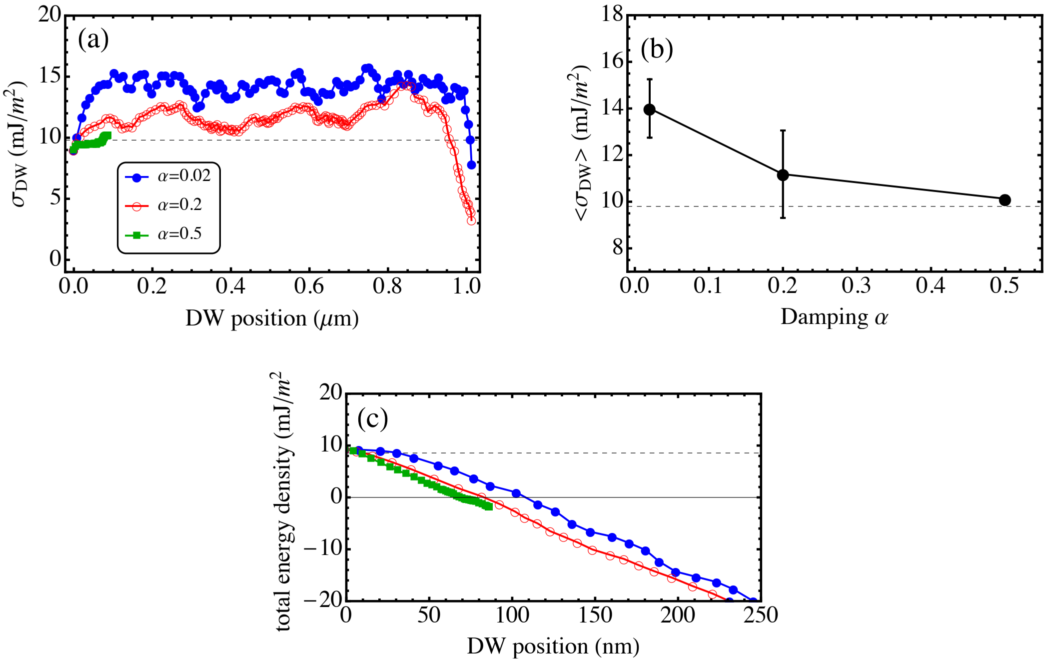

Figure 12.3: (a) DW energy density as function of DW position for different damping. The final drop corresponds to the expulsion of the DW. (b) Average DW density as funciton of damping. Dashed line represents the analytical value $\sigma_\infty \sim 10\ \mathrm{mJ/m^2}$. (c) Total energy density of the system as function of DW position for different damping parameters.

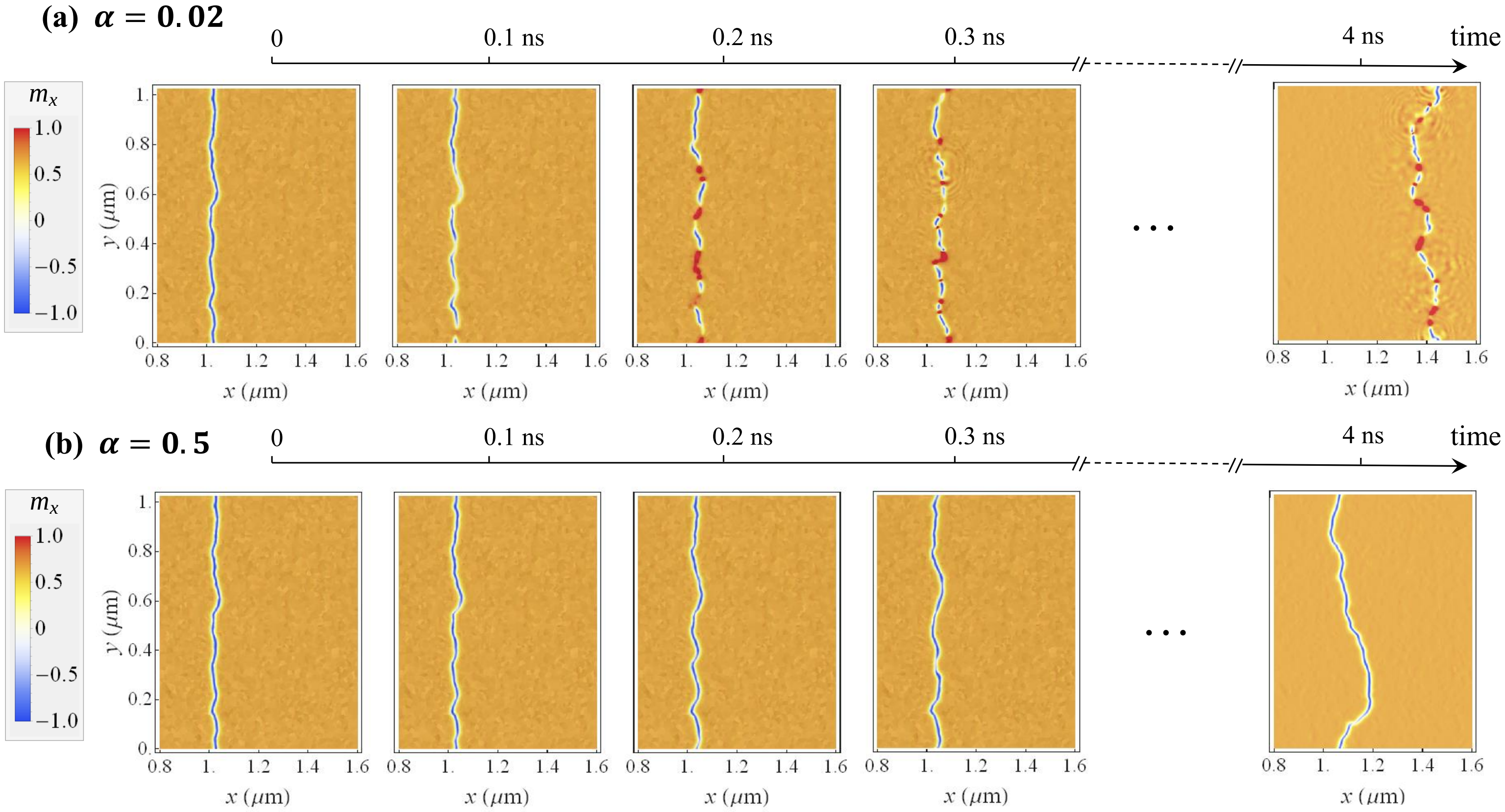

Figure 12.4: (a) Snapshots of the magnetization dynamics at subsequent instants under $\mu_0 H_z = 70\mathrm{mT}$, for two different damping: (a) $\alpha = 0.02$ and (b) $\alpha = 0.5$. The grains pattern, and therefore the energy barrier, is the same for both cases. In order to let the DW move across more pinning sites, these simulations were performed on a larger sample with $L_x = 2048$ nm.

Finally, Fig. 12.4 shows the DW motion as function of time for $\alpha = 0.02$ and $\alpha = 0.5$, along the same grain pattern (and therefore along the same pinning barriers). The applied field is $\mu_0 H_z = 70$mT, which satisfies $H_d(0.02) < H_z < H_d(0.5)$. The initial DW configuration is the same but, for $\alpha = 0.02$, VBL start to nucleate and the DW motion is much more turbulent. At $t = 4$ ns the DW has reached an equilibrium position for $\alpha = 0.5$, while it has passed through the (same) pinning barriers for $\alpha = 0.02$. Thus, one might think that the reduction of the depinning field could be related to the presence of VBL and their complex dynamics [140]. Further insights about this mechanism are given by analysing the DW depinning at a single energy barrier as described in the next subsection.

12.3.2 Single barrier

In order to understand how the DW precessional dynamics reduces H_{dep}, we micromagnetically analysed the DW depinning from a single barrier as sketched in Fig. 12.5. We considered a strip of dimensions $(1024 \times 256 \times 0.6)\text{nm}^3$ and we divided the strip into two regions, R_1 and R_2, which are assumed to have a thickness of $t_1 = 0.58$ and $t_2 = 0.62$ nm respectively. Their parameters vary accordingly (see Sec. 12.2), generating the DW energy barrier ($\delta\sigma$) shown in Fig. 12.5(b). A DW is placed and relaxed just before the barrier. The finite size of the DW ($\pi\Delta_{\text{DW}} \sim 15$ nm, with Δ_{DW} being the DW width parameter) smooths the abrupt energy step and, in fact, the energy profile can be successfully fitted by using the Bloch profile [60]

$$\begin{aligned}\sigma_{\text{DW}} &= \sigma_0 + \\ &+ \left(\frac{\delta\sigma}{2}\right)\left\{1+\cos\left(2\arctan\left[\exp\left(\frac{x_0-x}{\Delta_{\text{DW}}}\right)\right]\right)\right\}\,,\end{aligned} \tag{12.4}$$

where $x_0 = 20$ nm is the step position, while σ_0 and σ_1 are the DW energies at the left and right side of the barrier as represented in Fig. 12.5(b). This means that the pinning energy barrier has a spatial extension which is comparable to the DW width. By performing the same static and dynamic simulations, we obtain a static depinning field of $\mu_0 H_s = 120$ mT and, when decreasing the damping parameter, we observe the same reduction of the depinning field as in the granular system (see Fig. 12.5(c)). In this case the DW behaves like a rigid object whose spins precess coherently and no VBL nucleation is observed. Hence, the H_{dep} reduction does not depend directly on the presence of VBL but on the more general mechanism of spins' precession already present in this simplified case.

Nevertheless, an important characteristic of these single barrier simulations is that the barrier is localized and it has a finite size which is of the order of the DW width. Note that the same holds for the granular system: despite a more complex barrier structure, the dimension of the single barrier between two grains has the size of the DW width.

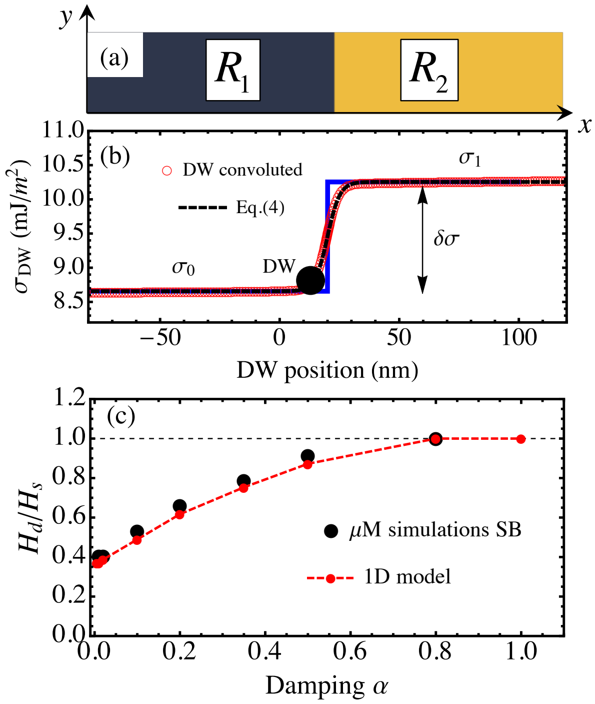

Figure 12.5: (a) Sketch of the two regions implemented for the single barrier (SB) micromagnetic simulations. (b) DW energy as function of DW position along the strip. Blue solid line represents the analytical value, red points the DW convoluted energy (due to the finite size of the DW) while black dashed line a fit using Eq. 12.4. (c) Dynamical depinning field, normalized to the static depinning field, for the single barrier simulations as function of damping, obtained from full micromagnetic simulations and the 1D model.

Thus, in order to understand the interplay between the DW precessional dynamics and the finite size of the barrier, we considered a 1D collective-coordinate model with a localized barrier. The 1D model equations, describing the dynamics of the DW position q and the internal angle ϕ (sketched in Fig. 12.1(c)), are given by [94]

$$\begin{aligned}(1+\alpha^2)\dot{\phi} &= \gamma_0[(H_z+H_p(q)) \\ &\quad -\alpha\underbrace{\left(H_K\frac{\sin 2\phi}{2}-\frac{\pi}{2}H_{\rm DMI}\sin\phi\right)}_{H_{\rm int}(\phi)}], \qquad (12.5)\end{aligned}$$

$$\begin{aligned}(1+\alpha^2)\frac{\dot{q}}{\Delta_{\rm DW}} &= \gamma_0\left[\alpha(H_z+H_p(q))\right. \\ &\quad \left.+\left(H_K\frac{\sin 2\phi}{2}-\frac{\pi}{2}H_{\rm DMI}\sin\phi\right)\right], \qquad (12.6)\end{aligned}$$

where $H_K = M_s N_x$ is the shape anisotropy field, favouring Bloch walls, with $N_x = t_0 \log 2/(\pi\Delta_{DW})$ [62] being the DW demagnetizing factor along the x axis. $H_{\mathrm{DMI}} = D/(\mu_0 M_s \Delta_{DW})$ is the DMI field. $H_{\mathrm{int}}(\phi)$ represents the internal DW field, which includes DMI and shape anisotropy. H_{int} favours Bloch ($\phi = \pm\pi/2$) or Néel wall ($\phi = 0$ or $\phi = \pi$) depending on the relative strength of H_K and H_{DMI}. In our system, the DMI dominates over shape anisotropy since $\mu_0 H_{\mathrm{DMI}} \sim 170$ mT while $\mu_0 H_K \sim 30$ mT. Hence, the DW equilibrium angle is $\phi = \pi$ ($\phi = 0$ or $\phi = \pi$ additionally depends on the sign of the DMI). $H_p(q)$ is the DW pinning field, obtained from the DW energy profile (Eq. (12.4)) as follows: the maximum pinning field is taken from the static simulations while the shape of the barrier is taken as the normalized DW energy gradient,

$$\begin{aligned} H_p(q) = H_s \left(\frac{\partial \sigma_{\mathrm{DW}}(x)}{\partial x}\right)_N = \\ = 2H_s \frac{\exp\left(\frac{x_0-q}{\Delta_{DW}}\right)\sin\left[2\arctan\left(\exp\left(\frac{x_0-q}{\Delta_{DW}}\right)\right)\right]}{1+\exp\left(\frac{2(x_0-q)}{\Delta_{DW}}\right)} \, . \end{aligned} \tag{12.7}$$

This choice might sound unusual and needs to be justified. In fact, having the DW energy profile, the depinning field could be simply calculated as [150]

$$H_{\mathrm{p}} = \frac{1}{2\mu_0 M_s}\frac{\partial \sigma(x)}{\partial x} \, . \tag{12.8}$$

This expression is derived by imposing that the derivative of the total DW energy $E(x) = -2\mu_0 M_s H_z x + \sigma(x)$ (Zeeman + internal energy) must always be negative. However, in our case also $M_s(x)$ depends on the DW position and the results obtained with Eq. (12.8) is different from the depinning field measured in the static single barrier micromagnetic simulations. For this reason we use Eq. (12.7) which keep the correct barrier shape and it presents the correct static value of the depinning field.
Finally, we recall that equivalent results are obtained by using a simple Gaussian shape for the pinning field, meaning that the key point is the localized shape of the barrier, rather than its exact form.

The corresponding pinning field is plotted in Fig. 12.6(a). The results for the dynamical H_{dep}, obtained with this modified 1D model, are plotted in Fig. 12.5(c) and they show a remarkable agreement with the single barrier micromagnetic simulations. This indicates that the main factors responsible for the reduction of H_{dep} are already included in this simple 1D model. Therefore, additional insights might come from analysing the DW dynamics within this 1D model. Fig. 12.6(b) and (c) represents the DW internal angle ϕ and the DW position q as function of time for different damping. The plots are calculated with $\mu_0 H_z = 55$ mT which satisfies $H_{\mathrm{dep}}(0.02) < H_z < H_{\mathrm{dep}}(0.1) < H_{\mathrm{dep}}(0.5)$. As shown in Fig. 12.6(b) and (c), below the depinning field ($\alpha = 0.1$, $\alpha = 0.5$), both the internal angle and the DW position oscillate before reaching the same final equilibrium state. However, the amplitude of these oscillations (the maximum displacement) depends on the damping parameter. Fig. 12.6(d) shows the final equilibrium position as function of the applied field for different damping. The equilibrium position is the same for all damping and it coincides with the position at which $H_z = H_p(q)$, as expected . Conversely, the maximum displacement, shown in Fig. 12.6(e), strongly increases for low damping parameters. For applied field slightly smaller than the depinning field, the DW reaches the boundary of the pinning barrier, meaning that a further increase of the field is enough to have a maximum displacement higher than the barrier size and depin the DW. In other words, the decrease of the depinning field, observed in the single barrier simulations, is due to DW oscillations that depend on α and that can be larger than the barrier size, leading to DW depinning for lower field. The DW dynamics and the depinning mechanism are further clarified in Fig. 12.6(f) and Fig. 12.6(g). Fig. 12.6(f) represents the DW coordinates $\{q, \phi\}$ for $\mu_0 H_z = 55$ mT and different damping. Before reaching the common equilibrium state, the DW moves in orbits (in the $\{q, \phi\}$ space) whose radius depends on the damping parameter. For $\alpha = 0.5$ (black line) the DW rapidly collapse into the final equilibrium state. Conversely, for $\alpha = 0.1$ (red open circles), the DW orbits around the equilibrium state before reaching it. If the radius of the orbit is larger than the barrier size the DW gets depinned, as in the case of $\alpha = 0.02$ (blue full circles). This mechanism is also represented in Fig. 12.6(g), where the DW orbits are placed in the energy landscape. The energy is calculated as $\sigma(q, \phi) = \sigma_{\mathrm{DW}}(q, \phi) - 2\mu_0 M_s H_z q$, where σ_{DW} is given by Eq. (12.4). Fig. 12.6(g) shows that the equilibrium state corresponds to the new minimum of the energy landscape. Furthermore, it confirms that the applied field is below the static depinning field, at which the pinning barrier would have been completely lifted. Nevertheless, while reaching the equilibrium state, the DW moves inside the energy potential and, if the radius of the orbit is larger than the barrier size, the DW can overcome the pinning barrier, as shown for $\alpha = 0.02$ in Fig. 12.6(g).

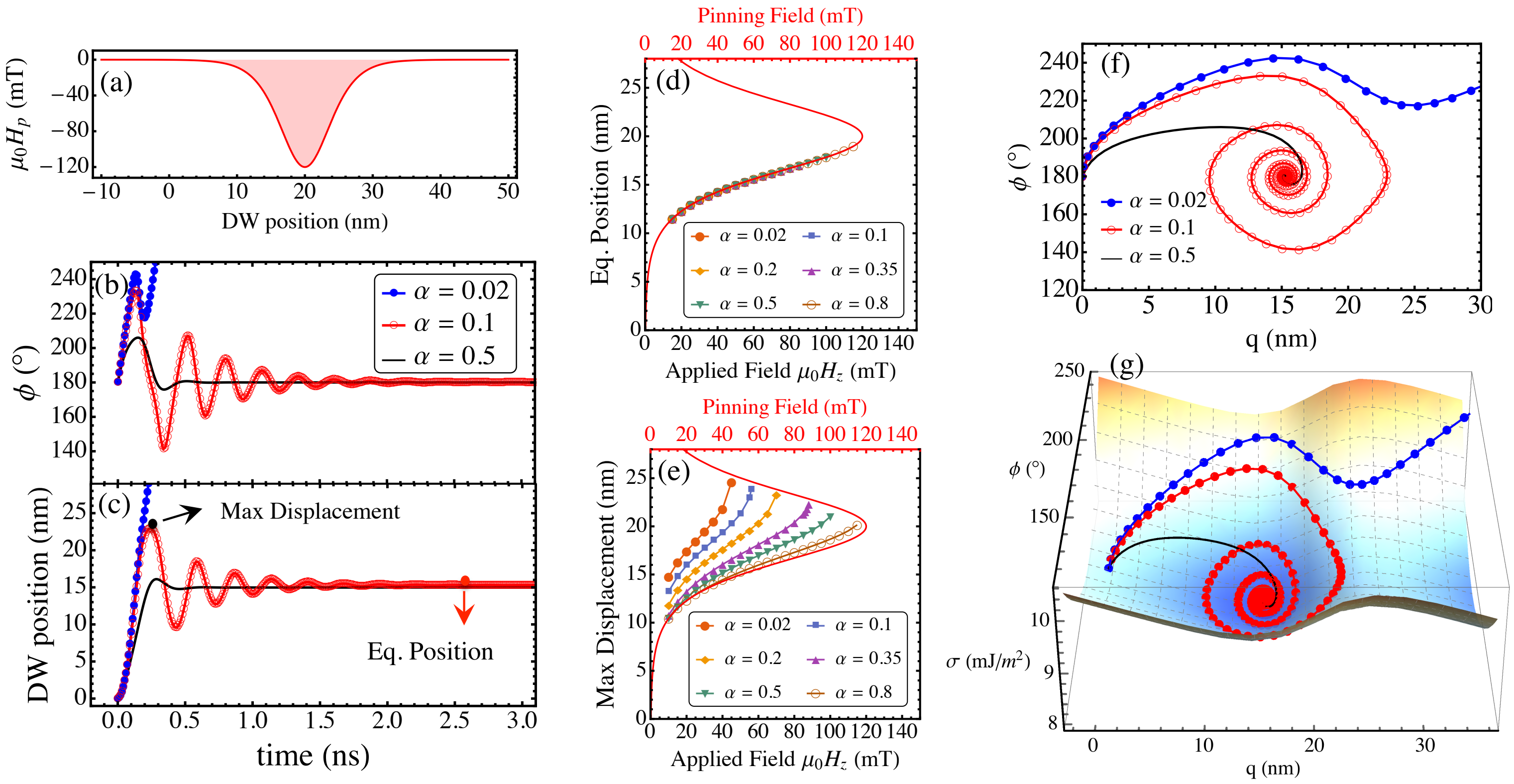

Figure 12.6: (a) Pinning field obtained from Eq. (12.7) as function of DW position. DW position internal angle ϕ as function of time for different damping parameter and $\mu_0 H_z = 55$ mT. (c) DW position q as function of time for different damping and $\mu_0 H_z = 55$ mT. (d) Equilibrium position as function of applied field for different damping. (e) Maximum DW displacement as function of the applied field for different damping. (f) DW coordinates $\{q, \phi\}$ for $\mu_0 H_z = 55$ mT and different damping. (g) DW coordinates $\{q, \phi\}$ inside the energy landscape: $\sigma = \sigma_{\mathrm{DW}}(q, \phi) - 2\mu_0 M_s H_z q$.

At this point we need to understand why the amplitude of the DW oscillations depends on damping. By solving Eq. (12.5) and Eq.(12.6) for the equilibrium state ($\dot{q}=0$, $\dot{\phi}=0$) we obtain

$$\begin{aligned} \dot{q}=0 \Rightarrow |H_p(q)| &= H_z + \frac{H_{\text{int}}(\phi)}{\alpha} \\ &\approx H_z - \frac{\pi}{2}\frac{H_{\text{DMI}}}{\alpha}\sin\phi\,, \qquad (12.9) \\ \dot{\phi}=0 \Rightarrow |H_p(q)| &= H_z - \alpha H_{\text{int}}(\phi) \\ &\approx H_z + \alpha\frac{\pi}{2}H_{\text{DMI}}\sin\phi\,, \qquad (12.10) \end{aligned}$$

since $\mu_0 H_{\text{DMI}} \gg \mu_0 H_K$ and, therefore, $H_{\text{int}} \approx -(\pi/2)H_{\text{DMI}}\sin\phi$. These equations have a single common solution which corresponds to $|H_p(q)| = H_z$ and $\phi = \phi_0 = \pi$ (at which $H_{\text{int}}(\pi) = 0$). However, at $t = 0$, the DW starts precessing under the effect of the applied field and, if $\phi \neq \pi$ when $|H_p(q)| = H_z$, the DW does not stop at the final equilibrium position but it continues its motion, as imposed by Eq. (12.9) and (12.10). In other words, the DW oscillations in Fig. 12.6(b) are given by oscillations of the DW internal angle ϕ, around its equilibrium value $\phi_0 = \pi$. These oscillations lead to a modification of the DW equilibrium position due to the DW internal field ($H_{\text{int}}(\phi)$), which exerts an additional torque on the DW in order to restore the equilibrium angle. As previously commented, if the amplitude of these oscillations is large enough, the DW gets depinned. From Eq. (12.9) we see that the new equilibrium position (and therefore the amplitude of the oscillations) depends on the DMI field, the value of the DW angle ϕ and the damping parameter.

In particular, damping has a twofold influence on this dynamics: one the one hand, it appears directly in Eq. (12.9), dividing the internal field, meaning that for the same deviation of ϕ from equilibrium, we have a stronger internal field for smaller damping. On the other hand, the second influence of damping is on the DW internal angle: once the DW angle has deviated from equilibrium, the restoring torque due to DMI is proportional to the damping parameter (see Eq. (12.10)). Hence, a lower damping leads to lower restoring torque and a larger deviation of ϕ from equilibrium. The maximum deviation of ϕ from equilibrium ($\delta\phi = \phi_{\text{max}} - \phi_0$) is plotted in Fig. 12.7(b) as function of damping for $\mu_0 H_z = 40$ mT. As expected, a lower damping leads to a larger deviation $\delta\phi$.

In this latter section, the DW was set at rest close to the barrier and, therefore, the initial DW velocity is zero. Nevertheless, one might wonder what happens when the DW reaches the barrier with a finite velocity. We simulated this case by placing the DW at an initial distance $d_1 = 200$ nm from the barrier. The results are shown in Fig. 12.8. Also for this configuration we performed static and dynamic simulations, neglecting or including the DW precessional dynamics respectively. The d_0 case corresponds to the DW at rest, relaxed just before the barrier and extensively analysed in the main text. The depinning field for the d_1 case is further reduced at small damping, reaching $H_d/H_s \sim 0.08$ ($H_d = 9$ mT and $H_s = 120$ mT) at $\alpha = 0.02$. Nevertheless, the depinning field remains constant in the static simulations independently on the velocity at which the DW hits the barrier. This suggests that, rather than related to the DW velocity,

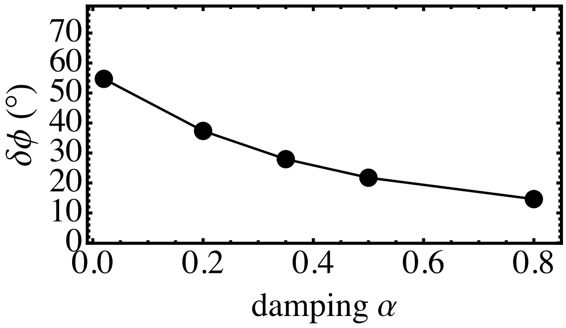

Figure 12.7: Maximum deviation of ϕ from its equilibrium position as function of damping.

the reduction is again related to the DW precession. When the DW starts from d_1 it reaches the barrier precessing, hence with a higher displacement from its equilibrium angle, which eventually leads to a larger effect of the internal field.

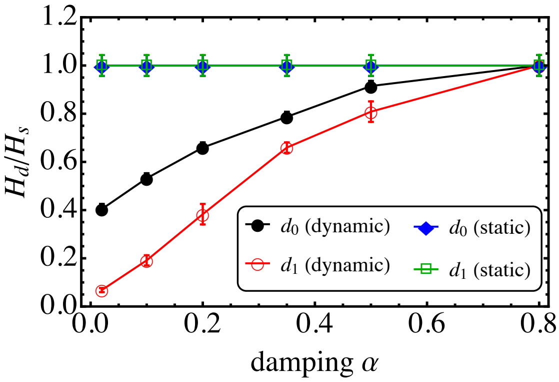

Figure 12.8: Dynamical depinning field as function of damping for static and dynamic simulations for the d_0 and d_1 cases.

12.3.3 Different DMI and pinning barriers

Finally, by using the 1D model it is possible to explore the dependence of H_{dep} on the pinning potential amplitude H_s (related to the disorder strength) and on the DMI constant D. The depinning field as function of damping for different values of H_s is plotted in Fig. 12.9(a). The reduction of H_{dep} is enhanced for larger values of H_s (strong disorder). This is consistent with our explanation, since for strong disorder we need to apply larger fields that lead to larger oscillations of ϕ.

Fig. 12.9(b) represents the dynamical H_{dep} as function of damping for $\mu_0 H_s = 120$ mT and different DMI constants (expressed in term of the critical DMI constant $D_c =$

$4\sqrt{AK_0}/\pi = 3.9$ mJ/m^2)[5]. In this case, the reduction of H_{dep} is enhanced for low DMI, until $D = 0.05D_c$, but a negligible reduction is observed for $D = 0$. This non-monotonic behaviour can be explained by looking at the dependence of $\delta\phi$ and H_{int} on the DMI constant.

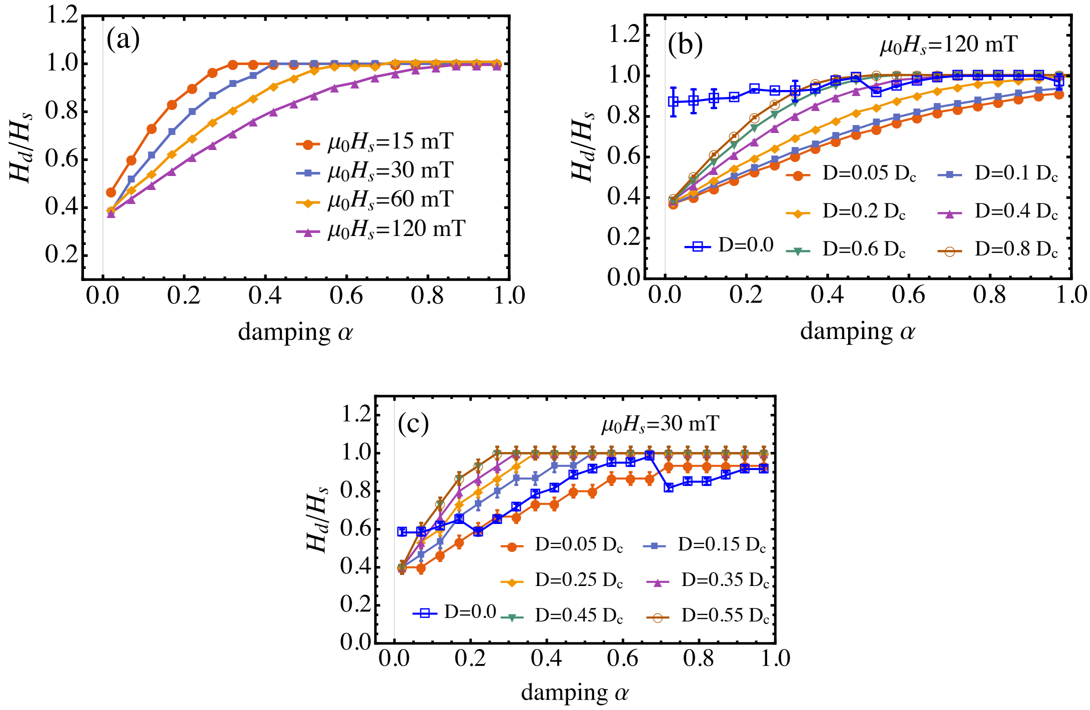

Figure 12.9: (a) Dynamical H_{dep} as function of damping for different H_s (disorder strength). (b) Dynamical H_{dep} as function of damping for different DMI constant and $\mu_0 H_s = 120$ mT. (c) Dynamical H_{dep} as function of damping for different DMI constant and $\mu_0 H_s = 30$ mT.

Fig. 12.10(a) shows the maximum fluctuation $\delta\phi$ as function of DMI for $\mu_0 H_z = 30$ mT. $\delta\phi$ increases for low DMI and it has a maximum at $\pi H_{\text{DMI}} = H_K$, which in our case corresponds to $D = 0.014D_c$. The increase of $\delta\phi$ for small values of D is due to the smaller restoring torque in Eq. (12.10). This holds until $\pi H_{\text{DMI}} = H_K$, where shape anisotropy and DMI are comparable and they both affect the DW equilibrium configuration. As a consequence, the reduction of H_{dep} is enhanced by decreasing D until $D \sim 0.014D_c$, while it is reduced if $0 < D < 0.014D_c$. Another contribution is given by the amplitude of the internal field, H_{int}. Fig. 12.10(b) depicts $\mu_0 H_{\text{int}}$ as function of $\delta\phi$ and D. The maximum $\delta\phi$, obtained at $\mu_0 H_z = 30$ mT, is additionally marked in the plot. The internal field decreases with the DMI but this reduction is compensated by an increase in $\delta\phi$, which leads to an overall increase of $\mu_0 H_{\text{int}}$, as discussed in the

---

[5] For $D > D_c$, DW have negative energies and the systems spontaneously breaks into non-uniform spin textures.

previous part. However, at very low DMI, the internal field is dominated by shape anisotropy and, independently on the DW angle displacement, it is too small to have an effect on the depinning mechanism. Note, however, that the amplitude of H_{int} should be compared with the amplitude of the pinning barrier H_s. Fig. 12.9(b) is calculated with $\mu_0 H_s = 120$ mT and the internal field, given by shape anisotropy ($H_K/2 \sim 15$ mT), has indeed a negligible effect. However, larger effects are observed, in the case $D = 0$, for smaller H_s, with reduction of H_{dep} up to $H_d/H_s \sim 0.6$, as shown in Fig. 12.9(c), which is calculated with $\mu_0 H_s = 30$ mT. In other words, the reduction of the depinning field depends on the ratio between the pinning barrier and the internal DW field.

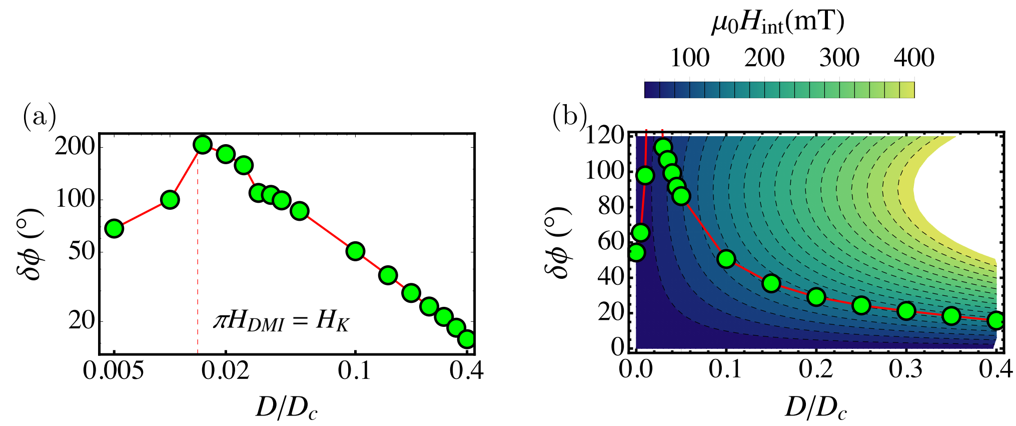

Figure 12.10: (a) Max DW angle fluctuation $\delta\phi = \phi_{\text{max}} - \phi_{\text{eq}}$ as function of DMI for $\mu_0 H_z = 30$ mT. (b) Internal DW field $\mu_0 H_{\text{int}}$ as function of DMI and $\delta\phi$. The green points correspond the max fluctuation plotted in (a). Note that the scale is logarithmic in (a).

Finally, it is interesting to see what happens for weaker disorder and different DMI in the system with grains. Fig. 12.11 shows the dynamical H_{dep}, for different pinning potential and different DMI, obtained in the granular system. The results are in good agreement with what predicted by the 1D model for different disorder strengths. However, we observe a smaller dependence on the DMI parameter. This is due to two reasons: (1) in the system with grains the static pinning barrier is $\mu_0 H_s = 87$ mT and the dependence of the depinning field with DMI is smaller for smaller barriers, as shown in Fig. 12.9(c). (2) The DW motion in the granular system presents the formation of VBL which might also contribute to the reduction of the depinning field. The mechanism is the same: a VBL is a non-equilibrium configuration for the DW (as a deviation of ϕ from equilibrium) that generates additional torques on the DW, which contribute to the DW depinning.

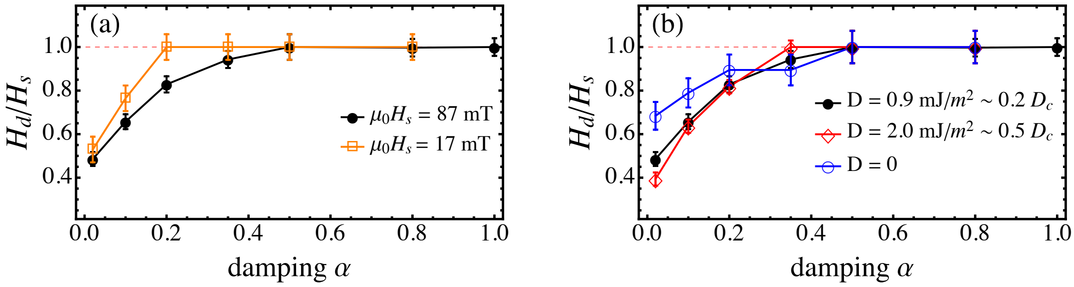

Figure 12.11: (a) Dynamical H_{dep} as function of damping for different H_s (disorder strength). (b) Dynamical H_{dep} as function of damping for different DMI constants.

12.4 Conclusions

To summarize, we have analysed the DW depinning field in a PMA sample with DMI and we found that H_{dep} decreases with the damping parameter with reductions up to 50%. This decrease is related to the DW internal dynamics and the finite size of the barrier. Due to DW precession, the DW internal angle (ϕ) deviates from equilibrium and triggers the internal DW field (DMI and shape anisotropy) which tries to restore the equilibrium angle. At the same time, the internal field pushes the DW above its equilibrium position within the energy barrier. This mechanism leads to DW oscillations and, if the amplitude of the oscillations is larger than the barrier size, the DW gets depinned for a lower field. Deviations of ϕ from equilibrium and DW oscillations are both damping dependent and they are enhanced at low damping.

In the system with grains the mechanism is the same but deviations from the internal DW equilibrium include the formation of VBL with more complex dynamics. The effect is enhanced for low DMI (providing that $\pi H_{\text{DMI}} > H_{\text{K}}$) and for stronger disorder since we need to apply larger external fields, which lead to larger DW oscillations. These results are relevant both from a technological and theoretical point of view, since they firstly suggest that a low damping parameter can lead to a lower H_{dep}. Furthermore, they show that micromagnetic calculations of the depinning field, neglecting the DW precessional dynamics can provide only an upper limit for H_{dep}, which could actually be lower due to the DW precessional dynamics.

Chapter 13

Conclusions and future perspectives

To conclude, several aspects of DW dynamics in ultrathin films have been analysed analytically and numerically by means of the micromagnetic software MuMax [8].

We analysed the field and current driven DW dynamics in $\mathrm{Pt/Co/Pt_xAu_{1-x}}$ samples. The fitting of the field driven data allowed an estimation of the damping parameter, while the fitting of the current driven data will allow a measurement of the SH angle. Furthermore, our results indicate a strong effect of disorder both in the field and current driven dynamics. In particular, for the field driven motion, disorder imposes limitation on the use of the 1D model to analyse the experimental data. Regarding the current driven dynamics, the efficiency of the SH mechanism is strongly reduced by disorder.

Lastly, we analysed the dependence of the depinning field on the damping parameters, showing, for the first time, that the depinning field can strongly decrease for small damping parameters. This reduction was eventually explained in terms of the finite size of the pinning barrier (comparable to the DW width) and the DW internal dynamics, related to the DMI and shape anisotropy. These results are compatible with the experimental trend [137] which indicates smaller depinning fields in systems with smaller damping [1].

Several interesting research directions are still open. Different disorder models, for instance, can be investigated and compared with the experimental results. More generally, the role of disorder needs to be further clarified both for DW and Skyrmion motion. Furthermore, the analysis of topologically protected patterns such as Skyrmion can provide useful insights into the dynamics of these exotic states of matter. From a micromagnetic point of view, several challenges are still open, for instance the inclusion of chiral [157] and non-local damping [158] or the effect of proximity induced magnetism. The field-like

---

[1] In general, there is no experiment directly confirming that a smaller damping leads to a smaller depinning field in PMA samples. However, experiments indicate that samples with smaller damping have a smaller depinning field [137]. This is usually interpreted in terms of the strength of the pinning potential which also plays a role. Our study suggests an additional ingredient that is in agreement with this trend.

torque, possibly due to SH or Rashba effect from the neighbouring layers [40] has been neglected in this study but recent experimental results [65] suggest that its contribution can be relevant and it remains to be evaluated. In general, the challenge of achieving fast and low current DW (Skyrmion) motion in these systems is still open, together with improvements of the existing DW based device concepts.

Part IV

Conclusions

Final Conclusions

To conclude, in this thesis we have analysed two aspects related to DW motion in ferromagnetic nanostructures.

In the first part (Part I) we investigated the effect of Joule heating and thermal gradients on DW motion along in-plane magnetized samples. The study was performed by means of a novel micromagnetic framework which couples heat transport and magnetization dynamics self-consistently. We showed that the presence of curved geometries (Chapter 6) or notches (Chapter 7) can give rise to thermal gradients along the sample, which can significantly affect the DW dynamics. For instance, for large current densities, we can incur a local destruction of the ferromagnetic order (below the notch) that can eventually help the DW depinning process. In Chapter 8 we analysed the main mechanisms related to thermally induced DW motion. We showed that, in the presence of a thermal gradient, the DW is mainly displaced towards the hotter region of the ferromagnetic strip due to the dominance of the entropic torque over the magnonic STT. This latter, due to the interaction between the DW and the thermally excited magnons, would drive the DW towards the colder region due to the prevalence of low frequency magnons, which are mainly reflected by the DW. A third driving force, due to a thermally induced dipolar field was also found and described. Future research directions include, for instance, the study of the interaction between magnons and DWs, both in in-plane and out-of-plane samples, which is not yet fully understood. Furthermore, DW motion by thermal gradients could be extended to ultrathin films with out-of-plane magnetization, where thermal effect could be enhanced due to the smaller Curie temperature. Another promising research direction, both from a technological and fundamental point of view, is laser induced ultrafast switching where the magnetization is switched by laser pulses and heat was shown to be an essential ingredient. More specific conclusions can be found in Chapter 9, at the end of Part I.

In Part III we analysed the field and current driven DW dynamics in ultrathin films with PMA and DMI. This part involved a collaboration with an experimental group at the University of Leeds. Indeed, Chapter 11 was devoted to the modelling of the DW motion in Pt/Co/$\mathrm{Pt_xAu_{1-x}}$ samples, where field and current driven DW velocities were measured experimentally. The fitting of the field-driven data allowed an estimation of the damping parameter, while the current driven analysis will allow the measurement of the SH angle (work in progress). Particular emphasis was devoted to the role of disorder in these kinds of system. More specifically, we showed that disorder considerably affects both the field and current driven DW dynamics. Finally, in Chapter 12, we analysed the damping dependence of the depinning field. We showed, for the first time, that a low damping parameter can lead to a small depinning field, contrary to common theoretical approaches and consistently with the experimental trend. Finally, we showed that the reduction of the depinning field is caused by the internal DW dynamics, related to shape anisotropy and DMI fields, and the finite size of the pinning barrier. In this context, further research directions are mainly related to the improvement of the micromagnetic model (chiral and non-local damping, spin pumping etc.), the analysis of topologically protected patterns such as Skyrmions and the achievement of fast and low-current DW (Skyrmions) motion. A more detailed conclusion can be found in Chapter 13, at the end Part II.

Our results provide significant insights into different mechanisms related to DW motion in ferromagnetic nanostructures. As introduced in Chapter 1, research in Spintronics and magnetism has potential for important applications in the information and communication technology sector. Faster and energetically cheaper devices could have an impact on the global energy production and, consequently, on carbon emission and climate change. Furthermore, spintronics devices could represent an alternative for CMOS based technology which is reaching its limit in scalability.

Nonetheless, I would like to end this thesis with a quote from a Nature Nanotechnology editorial [159], describing a more fundamental driving force for research, which includes the seek for technological improvement, fundamental knowledge and, in summary, beauty:

> ”What made Galileo point his telescope to the sky, Lavoisier develop new techniques to investigate matter, and Einstein spend sleepless nights wondering about the ultimate law of the Universe? Curiosity, yes, and a sense of beauty. Humans are a curious bunch. Babies taste everything within their grasp, teenagers feel the compulsion to undergo experiences, and scientists want to study things for the first time. **It is this feeling each one of us experiences when we are not satisfied about something — to know more, to improve, to fix — that creates new knowledge. This condition of general dissatisfaction, the result of a continual tension between our limits and our desires, acts as a powerful driving force for all that we do.** From our vantage point as human beings, limited in space, time and capabilities we can fully appreciate the imponderable beauty of the Universe. We feel its vastness can fulfil all our desires, and we are drawn in; but it’s an illusion for we will never be able to comprehend what this all means. Yet, just a glimpse of that beauty is all we seek, a drop of water for thirsty lips. And hence we investigate, ask questions, strive to find things out.” [159]

Bibliography

[1] S. O. Demokritov, V. E. Demidov, O. Dzyapko, G. A. Melkov, A. A. Serga, B. Hillebrands, and A. N. Slavin, Nature **443**, 430 (2006).

[2] S. S. P. Parkin, M. Hayashi, and L. Thomas, Science **320**, 190 (2008).

[3] D. Allwood, Science **309**, 1688 (2005).

[4] F. Hellman, A. Hoffmann, Y. Tserkovnyak, G. S. Beach, E. E. Fullerton, C. Leighton, A. H. MacDonald, D. C. Ralph, D. A. Arena, H. A. Dürr, P. Fischer, J. Grollier, J. P. Heremans, T. Jungwirth, A. V. Kimel, B. Koopmans, I. N. Krivorotov, S. J. May, A. K. Petford-Long, J. M. Rondinelli, N. Samarth, I. K. Schuller, A. N. Slavin, M. D. Stiles, O. Tchernyshyov, A. Thiaville, and B. L. Zink, Reviews of Modern Physics **89**, 025006 (2017).

[5] V. Raposo, S. Moretti, M. A. Hernandez, and E. Martinez, Applied Physics Letters **108**, 042405 (2016).

[6] S. Moretti, V. Raposo, and E. Martinez, Journal of Applied Physics **119**, 213902 (2016).

[7] S. Moretti, V. Raposo, E. Martinez, and L. Lopez-diaz, Physical Review B **95**, 064419 (2017).

[8] A. Vansteenkiste, J. Leliaert, M. Dvornik, M. Helsen, F. Garcia-Sanchez, and B. Van Waeyenberge, AIP Advances **4**, 107133 (2014).

[9] S. Moretti, M. Voto, and E. Martinez, Physical Review B **96**, 054433 (2017).

[10] S. Blundell, *Magnetism in Condensed Matter* (Oxford University Press, Oxford, 2003).

[11] G. Bertotti, *Hysteresis in Magnetism* (Academic Press, Cambridge, Massachusetts, 1998).

[12] J. D. Jackson, *Classical Electrodynamics* (John Wiley & Sons, New York, 1999).

[13] A. Aharoni, *Introduction to the theory of ferromagnetism* (Oxford University Press, New York, 1996).

[14] C. Kittel, *Introduction to Solid State Physics* (John Wiley & Sons, New York, 2005).

[15] A. Hubert and R. Schäfer, *Magnetic Domains* (Springer, Berlin, 1998).

[16] W. F. Brown, *Micromagnetics* (John Wiley & Sons, New York, 1963).

[17] E. Barati, M. Cinal, D. M. Edwards, and A. Umerski, Physical Review B **90**, 014420 (2014).

[18] Y. Tserkovnyak, A. Brataas, and G. E. W. Bauer, Physical Review Letters **88**, 117601 (2002).

[19] L. Berger, Journal of Applied Physics **55**, 1954 (1984).

[20] J. Slonczewski, Journal of Magnetism and Magnetic Materials **159**, L1 (1996).

[21] M. D. Stiles and J. Miltat, "Spin-Transfer Torque and Dynamics," in *Spin Dynamics in Confined Magnetic Structures III*, edited by B. Hillebrands and A. Thiaville (Springer Berlin Heidelberg, Berlin, Heidelberg, 2006) pp. 225–308.

[22] D. Ralph and M. Stiles, Journal of Magnetism and Magnetic Materials **320**, 1190 (2008).

[23] J.-V. Kim, in *Solid State Physics*, Vol. 63 (2012) pp. 217–294.

[24] J. Akerman, Science **308**, 508 (2005).

[25] A. V. Khvalkovskiy, D. Apalkov, S. Watts, R. Chepulskii, R. S. Beach, A. Ong, X. Tang, A. Driskill-Smith, W. H. Butler, P. B. Visscher, D. Lottis, E. Chen, V. Nikitin, and M. Krounbi, Journal of Physics D: Applied Physics **46**, 074001 (2013).

[26] S. Zhang and Z. Li, Physical Review Letters **93**, 127204 (2004).

[27] G. Tatara and H. Kohno, Physical Review Letters **92**, 086601 (2004).

[28] A. Thiaville, Y. Nakatani, J. Miltat, and Y. Suzuki, Europhysics Letters (EPL) **69**, 990 (2005).

[29] I. Dzyaloshinsky, Soviet Physics JETP **5**, 1259 (1957).

[30] T. Moriya, Physical Review **120**, 91 (1960).

[31] A. Fert and P. M. Levy, Physical Review Letters **44**, 1538 (1980).

[32] A. Crépieux and C. Lacroix, Journal of Magnetism and Magnetic Materials **182**, 341 (1998).

[33] A. Thiaville, S. Rohart, É. Jué, V. Cros, and A. Fert, EPL (Europhysics Letters) **100**, 57002 (2012).

[34] M. J. Benitez, A. Hrabec, A. P. Mihai, T. a. Moore, G. Burnell, D. McGrouther, C. H. Marrows, and S. McVitie, Nature Communications **6**, 8957 (2015).

[35] S.-G. Je, D.-H. Kim, S.-C. Yoo, B.-C. Min, K.-J. Lee, and S.-B. Choe, Physical Review B **88**, 214401 (2013).

[36] A. Hrabec, N. A. Porter, A. Wells, M. J. Benitez, G. Burnell, S. McVitie, D. McGrouther, T. A. Moore, and C. H. Marrows, Physical Review B **90**, 020402 (2014).

[37] K. Di, V. L. Zhang, H. S. Lim, S. C. Ng, M. H. Kuok, X. Qiu, and H. Yang, Applied Physics Letters **106**, 052403 (2015).

[38] S. Rohart and A. Thiaville, Physical Review B **88**, 184422 (2013).

[39] J. Hirsch, Phys. Rev. Lett. **83**, 1834 (1999).

[40] J. Sinova, S. O. Valenzuela, J. Wunderlich, C. H. Back, and T. Jungwirth, Reviews of Modern Physics **87**, 1213 (2015).

[41] T. A. Moore, I. M. Miron, G. Gaudin, G. Serret, S. Auffret, B. Rodmacq, A. Schuhl, S. Pizzini, J. Vogel, and M. Bonfim, Applied Physics Letters **93**, 262504 (2008).

[42] I. M. Miron, T. Moore, H. Szambolics, L. D. Buda-Prejbeanu, S. Auffret, B. Rodmacq, S. Pizzini, J. Vogel, M. Bonfim, A. Schuhl, and G. Gaudin, Nature materials **10**, 419 (2011).

[43] S. Emori, U. Bauer, S.-M. Ahn, E. Martinez, and G. S. D. Beach, Nature Materials **12**, 611 (2013).

[44] V. E. Demidov, S. Urazhdin, A. Zholud, a. V. Sadovnikov, and S. O. Demokritov, Applied Physics Letters **105**, 172410 (2014).

[45] K. Garello, C. O. Avci, I. M. Miron, M. Baumgartner, A. Ghosh, S. Auffret, O. Boulle, G. Gaudin, and P. Gambardella, Applied Physics Letters **105**, 212402 (2014).

[46] W. F. Brown, Physical Review **130**, 1677 (1963).

[47] J. L. Garcia-Palacios and F. J. Lazaro, Physical Review B **58**, 14937 (1998).

[48] R. F. L. Evans, W. J. Fan, P. Chureemart, T. A. Ostler, M. O. A. Ellis, and R. W. Chantrell, Journal of Physics: Condensed Matter **26**, 103202 (2014).

[49] O. Chubykalo-Fesenko, U. Nowak, R. W. Chantrell, and D. Garanin, Physical Review B **74**, 094436 (2006).

[50] U. Atxitia, O. Chubykalo-Fesenko, N. Kazantseva, D. Hinzke, U. Nowak, and R. W. Chantrell, Applied Physics Letters **91**, 232507 (2007).

[51] K. Chen and D. P. Landau, Physical Review B **49**, 3266 (1994).

[52] G. P. Zhang, T. Latta, Z. Babyak, Y. H. Bai, and T. F. George, Modern Physics Letters B **30**, 16300052 (2016).

[53] D. A. Garanin, Physical Review B **55**, 3050 (1997).

[54] D. Hinzke and U. Nowak, Physical Review Letters **107**, 027205 (2011).

[55] N. Kazantseva, D. Hinzke, U. Nowak, R. W. Chantrell, U. Atxitia, and O. Chubykalo-Fesenko, Physical Review B **77**, 184428 (2008).

[56] C. Schieback, D. Hinzke, M. Kläui, U. Nowak, and P. Nielaba, Physical Review B **80**, 214403 (2009).

[57] M. D. Stiles, W. M. Saslow, M. J. Donahue, and A. Zangwill, Physical Review B **75**, 214423 (2007).

[58] N. Smith, Physical Review B **78**, 216401 (2008).

[59] R. F. L. Evans, D. Hinzke, U. Atxitia, U. Nowak, R. W. Chantrell, and O. Chubykalo-Fesenko, Physical Review B **85**, 014433 (2012).

[60] A. Thiaville and Y. Nakatani, "Domain-Wall Dynamics in Nanowiresand Nanostrips," in *Spin Dynamics in Confined Magnetic Structures III*, edited by B. Hillebrands and A. Thiaville (Springer Berlin Heidelberg, Berlin, Heidelberg, 2006) pp. 161–205.

[61] E. Martinez, L. Torres, and L. Lopez-Diaz, Physical Review B **83**, 174444 (2011).

[62] S. Tarasenko, A. Stankiewicz, V. Tarasenko, and J. Ferré, Journal of Magnetism and Magnetic Materials **189**, 19 (1998).

[63] M. Voto, L. Lopez-Diaz, L. Torres, and S. Moretti, Physical Review B **94**, 174438 (2016).

[64] V. W. Doring, Z. Naturforschg **3a**, 373 (1948).

[65] M. Baumgartner, K. Garello, J. Mendil, C. O. Avci, E. Grimaldi, C. Murer, J. Feng, M. Gabureac, C. Stamm, Y. Acremann, S. Finizio, S. Wintz, J. Raabe, and P. Gambardella, Nature Nanotechnology **12**, 980 (2017).

[66] A. Manchon and S. Zhang, Physical Review B **78**, 212405 (2008).

[67] E. Martinez, G. Finocchio, L. Torres, and L. Lopez-Diaz, AIP Advances **3**, 072109 (2013).

[68] C. Zeller, CUDA Basics **NVIDIA Cor** (2011).

[69] J. E. Miltat and M. J. Donahue, in *Handbook of Magnetism and Advanced Magnetic Materials* (John Wiley & Sons, Chichester, UK, 2007).

[70] A. J. Newell, W. Williams, and D. J. Dunlop, Journal of Geophysical Research **98**, 9551 (1993).

[71] D. G. Porter and M. J. Donahue, http://www.ctcms.nist.gov/~rdm/mumag.org.html .

[72] M. J. Donahue, D. G. Porter, and Z. Yu, OOMMF: Object Oriented MicroMagnetic Framework .

[73] H. Fangohr, D. S. Chernyshenko, M. Franchin, T. Fischbacher, and G. Meier, Physical Review B **84**, 054437 (2011).

[74] N. Perez and L. Lopez-Diaz, Physical Review B **92**, 014408 (2015).

[75] COMSOL Inc., www.comsol.com (2017).

[76] A. Yamaguchi, T. Ono, S. Nasu, K. Miyake, K. Mibu, and T. Shinjo, Physical Review Letters **92**, 077205 (2004).

[77] G. S. D. Beach, C. Knutson, C. Nistor, M. Tsoi, and J. L. Erskine, Physical Review Letters **97**, 057203 (2006).

[78] M. Hayashi, L. Thomas, C. Rettner, R. Moriya, Y. B. Bazaliy, and S. Parkin, Physical Review Letters **98**, 1 (2007).

[79] M. Hayashi, L. Thomas, C. Rettner, R. Moriya, X. Jiang, and S. S. P. Parkin, Physical Review Letters **97**, 207205 (2006).

[80] O. Boulle, G. Malinowski, and M. Kläui, Materials Science and Engineering: R: Reports **72**, 159 (2011).

[81] A. Yamaguchi, S. Nasu, H. Tanigawa, T. Ono, K. Miyake, K. Mibu, and T. Shinjo, Applied Physics Letters **86**, 012511 (2005).

[82] J. Curiale, A. Lemaitre, T. Niazi, G. Faini, V. Jeudy, a. Lemaître, T. Niazi, G. Faini, and V. Jeudy, Journal of Applied Physics **112**, 103922 (2012).

[83] C. D. Stanciu, F. Hansteen, A. V. Kimel, A. Kirilyuk, A. Tsukamoto, A. Itoh, and T. Rasing, Physical Review Letters **99**, 047601 (2007).

[84] E. Beaurepaire, J.-C. Merle, A. Daunois, and J.-Y. Bigot, Physical Review Letters **76**, 4250 (1996).

[85] T. Ostler, J. Barker, R. Evans, R. Chantrell, U. Atxitia, O. Chubykalo-Fesenko, S. El Moussaoui, L. Le Guyader, E. Mengotti, L. Heyderman, F. Nolting, A. Tsukamoto, A. Itoh, D. Afanasiev, B. Ivanov, A. Kalashnikova, K. Vahaplar, J. Mentink, A. Kirilyuk, T. Rasing, and A. Kimel, Nature Communications **3**, 666 (2012).

[86] R. John, M. Berritta, D. Hinzke, C. Müller, T. Santos, H. Ulrichs, P. Nieves, J. Walowski, R. Mondal, O. Chubykalo-Fesenko, J. McCord, P. M. Oppeneer, U. Nowak, and M. Münzenberg, Scientific Reports **7**, 4114 (2017).

[87] S. K. Kim and Y. Tserkovnyak, Physical Review B **92**, 020410 (2015).

[88] F. Schlickeiser, U. Ritzmann, D. Hinzke, and U. Nowak, Physical Review Letters **113**, 097201 (2014).

[89] X. S. Wang and X. R. Wang, Physical Review B **90**, 014414 (2014).

[90] J.-P. Tetienne, T. Hingant, J.-V. Kim, L. H. Diez, J.-P. Adam, K. Garcia, J.-F. Roch, S. Rohart, A. Thiaville, D. Ravelosona, and V. Jacques, Science **344**, 1366 (2014).

[91] J. Torrejon, G. Malinowski, M. Pelloux, R. Weil, A. Thiaville, J. Curiale, D. Lacour, F. Montaigne, and M. Hehn, Phys. Rev. Lett. **109**, 106601 (2012).

[92] W. Jiang, P. Upadhyaya, Y. Fan, J. Zhao, M. Wang, L.-t. Chang, M. Lang, K. L. Wong, M. Lewis, Y.-t. Lin, J. Tang, S. Cherepov, X. Zhou, Y. Tserkovnyak, R. N. Schwartz, and K. L. Wang, Physical Review Letters **110**, 177202 (2013).

[93] M. Kläui, P.-O. Jubert, R. Allenspach, A. Bischof, J. A. C. Bland, G. Faini, U. Rüdiger, C. A. F. Vaz, L. Vila, and C. Vouille, Physical Review Letters **95**, 026601 (2005).

[94] E. Martinez, L. Lopez-Diaz, L. Torres, C. Tristan, and O. Alejos, Physical Review B **75**, 174409 (2007).

[95] S. Emori, C. K. Umachi, D. C. Bono, and G. S. Beach, Journal of Magnetism and Magnetic Materials **378**, 98 (2015).

[96] E. Ramos, C. Lopez, M. Munoz, and J. L. Prieto, Physical Review B **91**, 214404 (2015).

[97] A. A. Thiele, A. H. Bobeck, E. D. Torre, and U. F. Gianola, Bell System Technical Journal **50**, 711 (1971).

[98] L. Thomas, R. Moriya, C. Rettner, and S. S. P. Parkin, Science **330**, 1810 (2010).

[99] D. G. Cahill, W. K. Ford, K. E. Goodson, G. D. Mahan, A. Majumdar, H. J. Maris, R. Merlin, and S. R. Phillpot, Journal of Applied Physics **93**, 793 (2003).

[100] M. Kläui, C. a. F. Vaz, J. a. C. Bland, W. Wernsdorfer, G. Faini, E. Cambril, L. J. Heyderman, F. Nolting, and U. Rüdiger, Physical Review Letters **94**, 1 (2005).

[101] G. Tatara, H. Kohno, and J. Shibata, Physics Reports **468**, 213 (2008).

[102] E. Martinez, L. Lopez-Diaz, O. Alejos, L. Torres, and C. Tristan, Physical Review Letters **98**, 267202 (2007).

[103] J. Leliaert, B. Van de Wiele, J. Vandermeulen, A. Coene, A. Vansteenkiste, L. Laurson, G. Durin, B. Van Waeyenberge, and L. Dupré, Applied Physics Letters **106**, 202401 (2015).

[104] E. Martinez, L. Lopez-Diaz, O. Alejos, and L. Torres, Journal of Applied Physics **106**, 043914 (2009).

[105] S. Lepadatu, M. C. Hickey, A. Potenza, H. Marchetto, T. R. Charlton, S. Langridge, S. S. Dhesi, and C. H. Marrows, Physical Review B **79**, 094402 (2009).

[106] Y. Togawa, T. Kimura, K. Harada, T. Matsuda, A. Tonomura, Y. Otani, and T. Akashi, Applied Physics Letters **92**, 012505 (2008).

[107] A. Yamaguchi, A. Hirohata, T. Ono, and H. Miyajima, Journal of Physics: Condensed Matter **24**, 024201 (2012).

[108] A. Yamaguchi, K. Yano, H. Tanigawa, S. Kasai, and T. Ono, Japanese Journal of Applied Physics **45**, 3850 (2006).

[109] M. Hayashi, *Current Driven dynamics of magnetic domain walls in permalloy nanowires*, Ph.D. thesis, Stanford University (2006).

[110] L. Lopez-Diaz, D. Aurelio, L. Torres, E. Martinez, M. A. Hernandez-Lopez, J. Gomez, O. Alejos, M. Carpentieri, G. Finocchio, and G. Consolo, Journal of Physics D: Applied Physics **45**, 323001 (2012).

[111] C.-Y. You, I. M. Sung, and B.-K. Joe, Applied Physics Letters **89**, 222513 (2006).

[112] K. J. Kim, J. C. Lee, S. B. Choe, and K. H. Shin, Applied Physics Letters **92**, 2013 (2008).

[113] P. E. Mijnarends, S. Sahrakorpi, M. Lindroos, and A. Bansil, Physical Review B **65**, 075106 (2002).

[114] A. J. Ramsay, P. E. Roy, J. A. Haigh, R. M. Otxoa, A. C. Irvine, T. Janda, R. P. Campion, B. L. Gallagher, and J. Wunderlich, Physical Review Letters **114**, 067202 (2015).

[115] N. L. Schryer and L. R. Walker, Journal of Applied Physics **45**, 5406 (1974).

[116] D.-s. Han, S.-k. Kim, J.-y. Lee, S. J. Hermsdoerfer, H. Schultheiss, B. Leven, and B. Hillebrands, Applied Physics Letters **94**, 112502 (2009).

[117] X.-g. Wang, G.-h. Guo, Y.-z. Nie, G.-f. Zhang, and Z.-x. Li, Physical Review B **86**, 054445 (2012).

[118] P. Yan, X. S. Wang, and X. R. Wang, Physical Review Letters **107**, 177207 (2011).

[119] J.-S. Kim, M. Stärk, M. Kläui, J. Yoon, C.-Y. You, L. Lopez-Diaz, and E. Martinez, Physical Review B **85**, 174428 (2012).

[120] G. E. W. Bauer, E. Saitoh, and B. J. van Wees, Nature Materials **11**, 391 (2012).

[121] S. Selzer, U. Atxitia, U. Ritzmann, D. Hinzke, and U. Nowak, Physical Review Letters **117**, 107201 (2016).

[122] C. Safranski, I. Barsukov, H. K. Lee, T. Schneider, A. A. Jara, A. Smith, H. Chang, K. Lenz, J. Lindner, Y. Tserkovnyak, M. Wu, and I. N. Krivorotov, Nature Communications **8**, 117 (2017).

[123] P. Yan, Y. Cao, and J. Sinova, Physical Review B **92**, 100408 (2015).

[124] W. Wang, M. Albert, M. Beg, M.-A. Bisotti, D. Chernyshenko, D. Cortés-Ortuño, I. Hawke, and H. Fangohr, Physical Review Letters **114**, 087203 (2015).

[125] S. K. Kim, O. Tchernyshyov, and Y. Tserkovnyak, Physical Review B **92**, 020402 (2015).

[126] U. Ritzmann, D. Hinzke, and U. Nowak, Physical Review B **89**, 024409 (2014).

[127] D. Hinzke, N. Kazantseva, U. Nowak, O. N. Mryasov, P. Asselin, and R. W. Chantrell, Physical Review B **77**, 094407 (2008).

[128] L. Berger, Journal of Applied Physics **58**, 450 (1985).

[129] D. D. Stancil and A. Prabhakar, *Spin Waves* (Springer US, Boston, MA, 2009).

[130] Y. Quessab, R. Medapalli, M. S. E. Hadri, M. Hehn, G. Malinowski, E. E. Fullerton, and S. Mangin, arXiv:1709.07645 (2017).

[131] K. Wagner, A. Kákay, K. Schultheiss, A. Henschke, T. Sebastian, and H. Schultheiss, Nature Nanotechnology **11**, 432 (2016).

[132] A. V. Chumak, V. I. Vasyuchka, A. A. Serga, and B. Hillebrands, Nature Physics **11**, 453 (2015).

[133] S. Parkin and S.-h. Yang, Nature Nanotechnology **10**, 195 (2015).

[134] K.-S. Ryu, L. Thomas, S.-H. Yang, and S. Parkin, Nature Nanotechnology **8**, 527 (2013).

[135] P. J. Metaxas, J. P. Jamet, A. Mougin, M. Cormier, J. Ferré, V. Baltz, B. Rodmacq, B. Dieny, and R. L. Stamps, Physical Review Letters **99**, 217208 (2007).

[136] P. Metaxas, in *Solid State Physics*, Vol. 62 (Academic Press, Cambridge, Massachusetts, 2010) pp. 75–162.

[137] V. Jeudy, R. D. Pardo, W. S. Torres, S. Bustingorry, and A. Kolton, arXiv1709.08009 (2017).

[138] J. Gorchon, S. Bustingorry, J. Ferré, V. Jeudy, A. B. Kolton, and T. Giamarchi, Physical Review Letters **113**, 027205 (2014).

[139] E. Martinez, L. Torres, N. Perez, M. A. Hernandez, V. Raposo, and S. Moretti, Scientific Reports **5**, 10156 (2015).

[140] Y. Yoshimura, K.-j. Kim, T. Taniguchi, T. Tono, K. Ueda, R. Hiramatsu, T. Moriyama, K. Yamada, Y. Nakatani, and T. Ono, Nature Physics **12**, 157 (2015).

[141] M. Voto, L. Lopez-Diaz, and L. Torres, Journal of Physics D: Applied Physics **49**, 185001 (2016).

[142] J.-V. Kim and M.-W. Yoo, Applied Physics Letters **110**, 132404 (2017).

[143] A. P. Mihai, A. L. Whiteside, E. J. Canwell, C. H. Marrows, M. J. Benitez, D. McGrouther, S. McVitie, S. McFadzean, and T. A. Moore, Applied Physics Letters **103**, 262401 (2013).

[144] J. Leliaert, B. Van de Wiele, A. Vansteenkiste, L. Laurson, G. Durin, L. Dupré, and B. Van Waeyenberge, Journal of Applied Physics **115**, 233903 (2014).

[145] A. Hrabec, J. Sampaio, M. Belmeguenai, I. Gross, R. Weil, S. M. Chérif, A. Stashkevich, V. Jacques, A. Thiaville, and S. Rohart, Nature Communications **8**, 15765 (2017).

[146] E. Jué, A. Thiaville, S. Pizzini, J. Miltat, J. Sampaio, L. D. Buda-Prejbeanu, S. Rohart, J. Vogel, M. Bonfim, O. Boulle, S. Auffret, I. M. Miron, and G. Gaudin, Physical Review B **93**, 014403 (2016).

[147] N. Perez, E. Martinez, L. Torres, S.-H. Woo, S. Emori, and G. S. D. Beach, Applied Physics Letters **104**, 092403 (2014).

[148] A. B. Kolton, A. Rosso, and T. Giamarchi, Physical Review Letters **94**, 047002 (2005).

[149] E. Agoritsas, V. Lecomte, and T. Giamarchi, Physica B: Condensed Matter **407**, 1725 (2012).

[150] J. H. Franken, M. Hoeijmakers, R. Lavrijsen, and H. J. M. Swagten, Journal of Physics: Condensed Matter **24**, 024216 (2012).

[151] T. A. Moore, P. Möhrke, L. Heyne, A. Kaldun, M. Kläui, D. Backes, J. Rhensius, L. J. Heyderman, J.-U. Thiele, G. Woltersdorf, A. Fraile Rodríguez, F. Nolting, T. O. Menteş, M. Á. Niño, A. Locatelli, A. Potenza, H. Marchetto, S. Cavill, and S. S. Dhesi, Physical Review B **82**, 094445 (2010).

[152] U.-H. Pi, Y.-J. Cho, J.-Y. Bae, S.-C. Lee, S. Seo, W. Kim, J.-H. Moon, K.-J. Lee, and H.-W. Lee, Physical Review B **84**, 024426 (2011).

[153] L. Thomas, M. Hayashi, X. Jiang, R. Moriya, C. Rettner, and S. S. P. Parkin, Nature **443**, 197 (2006).

[154] H. Y. Yuan and X. R. Wang, Physical Review B **92**, 054419 (2015).

[155] H. Yuan and X. Wang, The European Physical Journal B **88**, 214 (2015).

[156] X. Wang, P. Yan, J. Lu, and C. He, Annals of Physics **324**, 1815 (2009).

[157] E. Jué, C. K. Safeer, M. Drouard, A. Lopez, P. Balint, L. Buda-Prejbeanu, O. Boulle, S. Auffret, A. Schuhl, A. Manchon, I. M. Miron, and G. Gaudin, Nature Materials **15**, 272 (2015).

[158] S. Zhang and S. S.-L. Zhang, Physical Review Letters **102**, 086601 (2009).

[159] Nature Nanotechnology **12**, 185 (2017).

[160] J. L. Garcia-Palacios, arXiv:cond-mat/0701242 (2007).

[161] U. Atxitia, *Modeling of ultrafast laser-induced magnetization dynamics within the Landau-Lifshitz-Bloch approach*, Ph.D. thesis, Universidad Autonoma De Madrid (2012).

List of publications

1. Eduardo Martinez, Luis Torres, Noel Perez, Maria Auxiliadora Hernandez, Victor Raposo and **Simone Moretti**, *Universal chiral triggered magnetization switching*, Scientific Report **5**, 10156 (2015)

2. Tomek Schulz, Oscar Alejos, Eduardo Martinez, Kjetil MD Hals, Karin Garcia, Laurent Vila, Kyujoon Lee, Roberto Lo Conte, Gurucharan V Karnad, **Simone Moretti**, Berthold Ocker, Dafiné Ravelosona, Arne Brataas and Mathias Kläui, *Spin-orbit torques for current parallel and perpendicular to a domain wall*, Applied Physics Letters **107**, 122405 (2015)

3. Victor Raposo, **Simone Moretti**, Maria Auxiliadora Hernandez and Eduardo Martinez, *Domain wall dynamics along curved strips under current pulses: The influence of Joule heating*, Applied Physics Letters **108**, 042405 (2016)

4. Eduardo Martinez, Oscar Alejos, Maria Auxiliadora Hernandez, Victor Raposo, Luis Sanchez-Tejerina and **Simone Moretti**, *Angular dependence of current-driven chiral walls*, Applied Physics Express **9**, 063008 (2016)

5. **Simone Moretti**, Victor Raposo, Eduardo Martinez, *Influence of Joule heating on current-induced domain wall depinning*, Journal of Applied Physics **119**, 213902 (2016)

6. Michele Voto, Luis Lopez-Diaz, Luis Torres and **Simone Moretti**, *Disorder-induced domain wall velocity shift at high fields in perpendicularly magnetized thin films*, Physical Review B **94**, 174438 (2016)

7. **Simone Moretti**, Victor Raposo, Eduardo Martinez and Luis Lopez-Diaz, *Domain wall motion by localized temperature gradients*, Physical Review B **95**, 064419 (2017)

8. S. Ali Nasseri, **Simone Moretti**, Eduardo Martinez, Claudio Serpico and Gianfranco Durin, *Collective coordinate models of domain wall motion in perpendicularly magnetized systems under the spin hall effect and longitudinal fields*, Journal of Magnetism and Magnetic Materials **426**, 195 (2017)

9. Oscar Alejos, Victor Raposo, Maria Auxiliadora Hernandez, Luis Sanchez-Tejerina, **Simone Moretti** and Eduardo Martinez, *Micromagnetic analysis of geometrically*

controlled current-driven magnetization switching, AIP Advances **7**, 055909 (2017)

10. **Simone Moretti**, Michele Voto and Eduardo Martinez, *Dynamical depinning of chiral domain walls*, Physical Review B **96**, 054433 (2017)

Part V

Appendices

Appendix A

Thermodynamics of magnetic systems

A.1 Reminds of statistical mechanics

Consider a system composed of a single particle. The probability of finding the system in the state i of energy E_i is given by [11, 10]

$$p_i = \frac{\exp\left(-\frac{E_i}{k_B T}\right)}{\mathcal{Z}}\,, \tag{A.1}$$

where k_B is the Boltzmann constant and T the temperature of the system. $\mathcal{Z}$ is the partition function defined as

$$\mathcal{Z} = \sum_i \exp\left(-\frac{E_i}{k_B T}\right), \tag{A.2}$$

where the sum is over all possible states. The partition function ensures that $p_i < 1$. Then, by definition, the average magnetic moment of the system is given by

$$\langle \boldsymbol{\mu} \rangle = \sum_i p_i \boldsymbol{\mu_i} \ = \frac{\sum_i \boldsymbol{\mu_i} \exp\left(-\beta E_i\right)}{\mathcal{Z}}\,, \tag{A.3}$$

where $\boldsymbol{\mu}_i$ is the magnetic moment of the i state and $\beta = 1/(k_B T)$. If we consider a system of N non-interacting particles, the total partition function is $\mathcal{Z} = (\mathcal{Z}_i)^N$, where $\mathcal{Z}_i$ is the single particle partition function. Then, the total magnetic moment of this system can be calculated as

$$\langle \boldsymbol{\mu} \rangle_{\text{total}} = N \langle \boldsymbol{\mu} \rangle = \frac{N}{\mathcal{Z}_i} \sum_i \boldsymbol{\mu}_i \exp\left(-\beta E_i\right), \tag{A.4}$$

where $\langle \boldsymbol{\mu} \rangle$ represents the average magnetic moment of the single particle, as defined previously.

Analogously, the average energy of the single particle is given by

$$U = \langle E \rangle = \sum_i \frac{E_i \exp\left(-\beta E_i\right)}{\mathcal{Z}} = -\frac{\partial \log \mathcal{Z}}{\partial \beta}\,, \tag{A.5}$$

and the free energy F (Helmotz free energy) of the system is defined as

$$F \equiv U - TS\,, \tag{A.6}$$

where U is the internal energy of the system and S is its entropy. Since entropy can be written as [10] $S = k_B \log \mathcal{Z} + U$, the free energy is related to the partition function as

$$F = -k_B T \log \mathcal{Z}\,. \tag{A.7}$$

It follows that the free energy of N non interacting particles can be written as $F = -k_B T N \log \mathcal{Z}_i$.

It is possible to demonstrate that the total magnetic moment of a system consisting of N non interacting magnetic moments, subject to an external magnetic field $\mathbf{H}$, can be calculated as

$$\langle \boldsymbol{\mu} \rangle = -\frac{1}{\mu_0}\frac{\partial F}{\partial \mathbf{H}}\,. \tag{A.8}$$

In fact, by using Eq. (A.7) and the fact that $E_i = -\mu_0 \boldsymbol{\mu_i} \cdot \mathbf{H}$, Eq. (A.8) becomes

$$\langle \boldsymbol{\mu} \rangle = -\frac{1}{\mu_0}\frac{\partial F}{\partial \mathbf{H}} = \frac{N}{\mathcal{Z}_i}\sum_i \boldsymbol{\mu_i} \exp\left(\frac{\mu_0 \boldsymbol{\mu_i} \cdot \mathbf{H}}{k_B T}\right), \tag{A.9}$$

which is equal to Eq. (A.4) defining the total magnetic moment. Hence, the magnetization can be calculated as

$$\mathbf{M} = \frac{\langle \boldsymbol{\mu} \rangle}{\Delta V} = -\frac{1}{\mu_0 \Delta V}\frac{\partial F}{\partial \mathbf{H}} = \frac{\rho}{\mathcal{Z}_i}\sum_i \boldsymbol{\mu_i} \exp\left(\frac{\mu_0 \boldsymbol{\mu_i} \cdot \mathbf{H}}{k_B T}\right), \tag{A.10}$$

where $\rho = N/\Delta V$ is the particles density.

A.2 Reciprocity Theorem

Before stating the reciprocity theorem we shall state the following identity.

Theorem- Given the field $\mathbf{B}$ with the property $\nabla \cdot \mathbf{B} = 0$ and the field $\mathbf{H}$ with the property $\nabla \times \mathbf{H} = 0$, and assuming that both field tend to zero at infinity, then

$$\int \mathbf{H} \cdot \mathbf{B}\; d^3 r = 0\,, \tag{A.11}$$

where the integral is over the entire space.

Proof- Since $\nabla \times \mathbf{H} = 0$, we can express $\mathbf{H} = -\nabla\phi$, then

$$\int \mathbf{H}\cdot\mathbf{B}\; d^3r = -\int \nabla\phi\cdot\mathbf{B} d^3r = -\int \nabla\cdot(\phi\mathbf{B})\; d^3r + \int \phi\nabla\cdot\mathbf{B}\; d^3r = 0\,, \tag{A.12}$$

the second integral is zero since $\nabla\cdot\mathbf{B} = 0$ while the first term can be transformed into a surface integral which is zero since $\mathbf{B} = 0$ at infinity.

Theorem- Given the field $\mathbf{H}_1$, generated by the magnetization $\mathbf{M}_1$, and the the field $\mathbf{H}_2$, generated by the magnetization $\mathbf{M}_2$, then

$$\int \mathbf{H}_1\cdot\mathbf{M}_2\; d^3r = \int \mathbf{H}_2\cdot\mathbf{M}_1\; d^3r\,. \tag{A.13}$$

Proof- By writing $\mathbf{M}$ as $\mathbf{M} = \mathbf{B}/\mu_0 - \mathbf{H}$, Eq. (A.13) becomes

$$\int \mathbf{H}_1\cdot\left(\frac{\mathbf{B}_2}{\mu_0} - \mathbf{H}_2\right)\; d^3r = -\int \mathbf{H}_1\cdot\mathbf{H}_2 = \int \mathbf{H}_2\cdot\mathbf{M}_1\; d^3r\,, \tag{A.14}$$

since the second term is symmetric under the exchange of 1 ↔ 2 and we have used Eq. (A.11).

A.3 Stochastic processes

A generic stochastic differential equation can be written as [47]

$$\frac{dy_i}{dt} = A_i(\mathbf{y},t) + \sum_k B_{ik}(\mathbf{y},t)\xi_k(t)\,, \tag{A.15}$$

where $\mathbf{y} = (y_1, ..., y_n)$ are the system's variables and ξ_k are the random noise components. In the case of white noise, ξ_i has the properties

$$\begin{aligned} \langle\xi_i(t)\rangle &= 0\,, && \text{(A.16)}\\ \langle\xi_i(0)\xi_j(t)\rangle &= 2D\delta_{ij}\delta(t)\,, && \text{(A.17)} \end{aligned}$$

In general, and independently on the noise color, this kind of noise is called ”multiplicative” due to the form of Eq. (A.15), while, if $\partial B/\partial y = 0$, the noise is called ”additive”. Expanding Eq. (A.15) we can write

$$\begin{aligned} dy_i &= A_i(\mathbf{y},t)dt + \sum_k B_{ik}(\mathbf{y},t)\xi_k(t)dt \\ &= A_i(\mathbf{y},t)dt + \sum_k B_{ik}(\mathbf{y},t)\circ dW_k(t), \end{aligned} \tag{A.18}$$

where $dW_k(t) \equiv \xi_k(t)dt$ is a generic Wiener process [160] (if ξ_k has white noise properties). The integral of the stochastic term in Eq. (A.18) cannot be defined as a conventional Riemann integral but it can be defined in in two ways: (1) within the Stratonovich interpretation the integral of the X_t variable over the stochastic Wiener process W_t is defined as

$$\int_0^T X_t \circ dW_t \equiv \lim_{W_{t_{i+1}} \to W_{t_i}} \sum_{i=0}^{k-1} \frac{X_{t_{i+1}} + X_{t_i}}{2} (W_{t_{i+1}} - W_{t_i}) \,, \tag{A.19}$$

where $0 = t_0 < t_1 < ... < t_k = T$. Or (2) in the Ito interpretation, it is given by

$$\int_0^T X_t dW_t \equiv \lim_{W_{t_{i+1}} \to W_{t_i}} \sum_{i=0}^{k-1} X_{t_i} (W_{t_{i+1}} - W_{t_i}) \,. \tag{A.20}$$

The $\circ$ symbol is used to distinguish between the two interpretations. The Ito and Stratonovich interpretation are linked and it is possible to pass from one interpretation to the other. Furthermore, if the noise is additive, the two approaches coincides. In the following we shall use the Stratonovich interpretation.

A.3.1 Fokker-Planck equation

Given the stochastic differential equation (A.15), the non-equilibrium probability $P(\mathbf{y}, t)$ of finding the system in the state $\mathbf{y}$ at time t, satisfies the Fokker-Planck equation [47]:

$$\frac{\partial P}{\partial t} = -\sum_i \frac{\partial}{\partial y_i} \left[a_i^{(1)} P \right] + \sum_{ij} \frac{\partial^2}{\partial y_i \partial y_j} \left[a_{ij}^{(2)} P \right] \,, \tag{A.21}$$

where

$$a_i^{(1)} = A_i + D B_{jk} \frac{\partial B_{ik}}{\partial y_j} \,, \tag{A.22}$$

$$a_{ij}^{(2)} = D B_{ik} B_{jk} \,. \tag{A.23}$$

Therefore

$$\begin{aligned} \frac{\partial P}{\partial t} &= -\sum_i \frac{\partial}{\partial y_i} \left[\left(A_i + D \sum_{jk} B_{jk} \frac{\partial B_{ik}}{\partial y_j} \right) P \right] \\ &\quad + \sum_{ij} \frac{\partial^2}{\partial y_i \partial y_j} \left[D \left(\sum_k B_{ik} B_{jk} \right) P \right] \,, \end{aligned} \tag{A.24}$$

which can be re-written in the form of a continuity equation ($\partial P / \partial t = -\nabla \cdot \mathbf{J}_P$) for the probability distribution as

$$\begin{aligned} \frac{\partial P}{\partial t} &= -\sum_i \frac{\partial}{\partial y_i} \left\{ \left[A_i - D \sum_k B_{ik} \left(\sum_j \frac{\partial B_{jk}}{\partial y_j} \right) \right.\right. \\ &\quad \left.\left. - D \sum_{jk} B_{ik} B_{jk} \frac{\partial}{\partial y_j} \right] P \right\} . \end{aligned} \tag{A.25}$$

Equation for the average

Given the system described by the stochastic variables $\mathbf{y} = (y_1 ... y_n)$, the average value of any function $f(\mathbf{y})$ is given by

$$\langle f(\mathbf{y})\rangle = \int d\mathbf{y} f(\mathbf{y}) P(\mathbf{y})\,, \tag{A.26}$$

where the integral is over all possible values of $\mathbf{y}$. The equation of motion for $\langle f(\mathbf{y})\rangle$ is given by [160, 161]

$$\frac{d\langle f(\mathbf{y})\rangle}{dt} = \frac{\partial}{\partial t}\int d\mathbf{y} f(\mathbf{y}) P(\mathbf{y}, t) = \int d\mathbf{y} f(\mathbf{y}) \frac{\partial P(\mathbf{y}, t)}{\partial t}. \tag{A.27}$$

It is possible to demonstrate [160] that, when applying Eq. (A.27) to the function $f(y) = y_i$, it yields

$$\frac{dy_i}{dt} = \langle a_i^{(1)}(\mathbf{y}, t)\rangle. \tag{A.28}$$

Furthermore, if $\langle a_i^{(1)}(\mathbf{y}, t)\rangle$ is a linear function of $\mathbf{y}$, then

$$\frac{dy_i}{dt} = a_i^{(1)}(\langle \mathbf{y}\rangle, t). \tag{A.29}$$

Fokker-Planck equation for the stochastic LLG-Langevin equation

In the context of magnetization dynamics $\mathbf{y} = (m_x, m_y, m_z)$ and the Landau-Lifshitz (LL) Eq. (3.33), augmented with the stochastic thermal field $\mathbf{H}_{\text{th}}$ can be written in the form

$$\begin{aligned} \frac{dm_i}{dt} &= -\gamma_0 \left[\mathbf{m} \times \mathbf{H}_{\text{eff}} + \alpha \mathbf{m} \times (\mathbf{m} \times \mathbf{H}_{\text{eff}})\right]_i \\ &\quad -\gamma_0 \left[\epsilon_{ijk} m_j + \alpha \left(m_k m_i - m^2 \delta_{ik}\right)\right] H_{\text{th},k}\,, \end{aligned} \tag{A.30}$$

where we recall that $H_{\text{th},k}$ has white noise properties as ξ_k. Thus for the LL-Langevin equation

$$A_i = -\gamma_0 \left[\mathbf{m} \times \mathbf{H}_{\text{eff}} + \alpha \mathbf{m} \times (\mathbf{m} \times \mathbf{H}_{\text{eff}})\right]_i\,, \tag{A.31}$$

and

$$B_{ik} = -\gamma_0 \left[\epsilon_{ijk} m_j + \alpha \left(m_k m_i - m^2 \delta_{ik}\right)\right]. \tag{A.32}$$

Hence

$$\frac{\partial B_{ik}}{\partial m_j} = -\gamma_0 \left[\epsilon_{ijk} + \alpha \left(\delta_{ij} m_k + \delta_{kj} m_i - 2\delta_{ik} m_j\right)\right] \tag{A.33}$$

and

$$\sum_j \frac{\partial B_{jk}}{\partial m_j} = 2\gamma_0 \alpha m_k \,. \tag{A.34}$$

By using Eq. (A.34) it is possible to see that $\sum_k B_{ik}(\sum_j \partial B_{jk}/\partial m_j) = 0$ and, therefore, the second term on the RHS of Eq. (A.21) and (A.25) vanishes. For the third term, after some algebra, it is possible to obtain [47]

$$-D\sum_{jk} B_{ik}B_{jk}\frac{\partial P}{\partial y_j} = \frac{1}{2\tau_N}\left[\mathbf{m}\times\left(\mathbf{m}\times\frac{\partial P}{\partial \mathbf{m}}\right)\right] , \tag{A.35}$$

where $\tau_N^{-1} = 2D\gamma_0^2(1+\alpha^2)$ is the Néel (free-diffusion) time [47]. Finally, combining these results, the Fokker-Planck equation for the stochastic LL equation reads like

$$\begin{aligned} \frac{\partial P}{\partial t} &= \frac{\partial}{\partial \mathbf{m}}\cdot\left\{\left[\gamma_0 \mathbf{m}\times\mathbf{H}_{\text{eff}} + \gamma_0\alpha\mathbf{m}\times(\mathbf{m}\times\mathbf{H}_{\text{eff}})\right.\right. \\ &\qquad \left.\left. -\frac{1}{2\tau_N}\mathbf{m}\times\left(\mathbf{m}\times\frac{\partial}{\partial\mathbf{m}}\right)\right] P\right\} . \end{aligned} \tag{A.36}$$

At equilibrium, the system is expected to follow the Maxwell-Boltzmann distribution $P_0 \propto \exp -\beta E$ and, therefore, we impose that the latter is an equilibrium solution of the system ($\partial P_0/\partial t = 0$). Since the energy for the single elementary cell can be written as $E = -\mu_0 M_s \mathbf{m}\cdot\mathbf{H}_{\text{eff}}\Delta V$, it follows that $\partial P_0/\partial \mathbf{m} = \beta\mu_0 M_s \Delta V P_0 \mathbf{H}_{\text{eff}}$ and Eq. (A.36) becomes

$$\begin{aligned} \frac{\partial P_0}{\partial t} &= \frac{\partial}{\partial \mathbf{m}}\cdot\left\{\left[\gamma_0\alpha\mathbf{m}\times(\mathbf{m}\times\mathbf{H}_{\text{eff}})\right.\right. \\ &\qquad \left.\left. -\frac{\beta\mu_0 M_s}{2\tau_N}\mathbf{m}\times(\mathbf{m}\times\mathbf{H}_{\text{eff}})\right] P_0\right\} = 0 \,, \end{aligned} \tag{A.37}$$

where we have used the fact that first term on the RHS of Eq. (A.36) vanishes under these assumptions. Eq. (A.37) is satisfied by imposing

$$\gamma_0\alpha = \frac{\beta\mu_0 Ms}{2\tau_N} \Rightarrow D = \frac{2\alpha k_B T}{\mu_0\gamma_0 M_s(1+\alpha^2)\Delta V} , \tag{A.38}$$

from which D is obtained.

Appendix B

Landau-Lifshitz-Bloch equation

In this part we review the main passages, followed by Garanin [53], to derive the LLB equation (3.56). A more detailed description can be found in Ref. [53, 161]. The starting point is the atomistic LLG equation

$$\frac{d\mathbf{s}}{dt} = -\gamma_0 \mathbf{s} \times (\mathbf{H} + \mathbf{H}_{\mathrm{th}}) - \gamma_0 \alpha_0 \mathbf{s} \times (\mathbf{s} \times \mathbf{H}) \,, \tag{B.1}$$

where $\mathbf{s}$ is the normalized magnetic moment $\mathbf{s} = \boldsymbol{\mu}_s/\mu_s$ and $\mathbf{H}_{\mathrm{th}}$ is the stochastic thermal field with properties:

$$\langle H_{\mathrm{th},i} \rangle = 0 \,, \qquad \langle H_{\mathrm{th}}(0)_i H_{\mathrm{th}}(t)_j \rangle = \frac{2\alpha_0 k_B T}{\gamma_0 \mu_0 \mu_s} \delta_{ij} \delta(t) \,. \tag{B.2}$$

The amplitude of the noise $(2\alpha_0 k_B T/(\gamma_0 \mu_0 \mu_s))$ has been obtained as described in the previous section. $\mathbf{H}$ is the effective filed defined as $(\mu_0 \mu_s)^{-1} \delta \mathcal{H}/\delta \mathbf{s}$, where $\mathcal{H}$ is the Hamiltonian of the system. We consider an elementary cell containing N spins, whose dynamics is described by Eq. (B.1). The magnetization $\mathbf{m}$ of each cell is defined as

$$\mathbf{m} \equiv \langle \mathbf{s} \rangle = \int d\mathbf{m}' \mathbf{m}' f(\mathbf{m}') \,, \tag{B.3}$$

where $f(\mathbf{m}') = \exp\left[\mu_0 \mu_s \mathbf{m}' \cdot \mathbf{H}/(k_B T)\right]/\mathcal{Z}(\mathbf{m}')$ and $\mathcal{Z}(\mathbf{m}')$ is the partition function of the system (see also Appendix A). Thus, according to Eq. (A.27), the dynamics of the average moment is given by

$$\frac{d\langle \boldsymbol{s} \rangle}{dt} = \langle a_i^{(1)}(\mathbf{s}, t) \rangle \,. \tag{B.4}$$

It is possible to see that for the atomistic LLG Eq. (B.1)

$$a_i^{(1)} = -\gamma_0 \epsilon_{ijk} s_j H_k - \gamma_0 \lambda \epsilon_{ijk} \epsilon_{klm} s_j s_l H_m - 2\gamma_0 \frac{\lambda k_B T}{\mu_0 \mu_s} s_i \,. \tag{B.5}$$

Thus

$$\frac{d\langle s_i \rangle}{dt} = -\gamma_0 \epsilon_{ijk} \langle s_j \rangle H_k - \gamma_0 \lambda \epsilon_{ijk} \epsilon_{klm} \langle s_j s_l \rangle H_m - 2\gamma_0 \frac{\lambda k_B T}{\mu_0 \mu_s} \langle s_i \rangle \,, \tag{B.6}$$

and, in vectorial form, in terms of $\mathbf{m}$

$$\frac{d\mathbf{m}}{dt} = -\gamma_0 \mathbf{m} \times \mathbf{H} - \gamma_0 \lambda \langle [\mathbf{s} \times (\mathbf{s} \times \mathbf{H})] \rangle - 2\gamma_0 \frac{\lambda k_B T}{\mu_0 \mu_s} \mathbf{m}. \tag{B.7}$$

The behaviour of Eq. (B.7) is determined by the reduced field $\boldsymbol{\xi} = \mu_0 \mu_s \mathbf{H}/(k_B T)$ [53]. If $\boldsymbol{\xi} \gg 1$ (low temperature) the last term can be neglected and the average of the coupled moments $\langle s_j s_l \rangle$ can be decoupled, $\langle s_j s_l \rangle \sim \langle m_i m_l \rangle$, thus recovering the conventional LLG equation. On the other hand if $\boldsymbol{\xi} \ll 1$ (high temperature) the last term dominates and we recover the Bloch equation for the relaxation of $\mathbf{m}$ [53]. For intermediate values $\boldsymbol{\xi} \sim 1$ both terms contribute to the magnetization dynamics. Thus, in order to obtain a closed equation in terms of $\mathbf{m}$, the main issue is calculating the term $\langle s_j s_l \rangle$. This can be done by using the distribution function

$$f(\mathbf{m}, t) = \frac{\exp\left[\boldsymbol{\xi}(t) \cdot \mathbf{m}\right]}{\mathcal{Z}(\boldsymbol{\xi})}, \qquad \mathcal{Z}(\xi) = 4\pi \frac{\sinh \xi}{\xi}. \tag{B.8}$$

At equilibrium the magnetization is defined by (see also Section 2.4.2)

$$\mathbf{m} = B(\xi_0) \frac{\boldsymbol{\xi}_0}{\xi_0}, \tag{B.9}$$

where $\boldsymbol{\xi}_0$ is the equilibrium reduced field and $B(x)$ is the Langevin function [161, 11]. In particular, it is possible to demonstrate [53, 161] that

$$\begin{aligned} \langle s_i s_k \rangle &= \frac{1}{\mathcal{Z}(\xi)} \frac{\partial}{\partial \xi_k} \frac{\partial \mathcal{Z}(\xi)}{\partial \xi_i} \\ &= \frac{B(\xi)}{\xi} \left\{ \left(\frac{\xi}{B(\xi)} - 3 \right) \frac{\xi_k \xi_i}{\xi^2} - \delta_{ik} \right\}. \end{aligned} \tag{B.10}$$

For a ferromagnet it is possible to write the effective field as $\mathbf{H} = 2pJ_0/(\mu_0)\mathbf{m} + \mathbf{H}_{\text{ext}}$, where, for simplicity, we considered only the effect of the external field $\mathbf{H}_{\text{ext}}$. In principle, one could include also the anisotropy and the exchange between neighbouring cells [53]. J_0 is the atomistic exchange constant and p is the number of nearest neighbours. The first field is the internal exchange field, which dominates at $T < T_C$. For $T < T_C$ $\mathbf{H}_{\text{ext}}$ can be considered as a perturbation with respect to the internal exchange field. By using this approximation to calculate Eq. (B.10), after non-trivial algebra (see Ref. [53, 161] for more details), it is possible to finally obtain the LLB equation (3.56):

$$\frac{d\mathbf{m}}{dt} = -\gamma_0 \mathbf{m} \times \mathbf{H} - \frac{\gamma_0 \alpha_\perp}{m^2} \mathbf{m} \times (\mathbf{m} \times \mathbf{H}) + \frac{\gamma_0 \alpha_\parallel}{m^2} (\mathbf{m} \cdot \mathbf{H}) \mathbf{m}, \tag{B.11}$$

where

$$\mathbf{H} = \mathbf{H}_{\text{ext}} + \begin{cases} \frac{1}{2\chi_\parallel} \left(1 - \frac{m^2}{m_e^2}\right) \mathbf{m}, & T < T_C \\ -\frac{1}{\chi_\parallel} \left(1 + \frac{3}{5} \frac{T_C m^2}{(T - T_C)}\right) \mathbf{m}, & T > T_C \end{cases}, \tag{B.12}$$

$$\tilde{\chi}_\parallel = \frac{\partial m}{\partial H} = \frac{\mu_0 \mu_s}{J_0} \frac{B' \beta J_0}{1 - B' \beta J_0}, \tag{B.13}$$

and $m_e = B(\xi_0) = B(m_e \beta J_0)$ with $B'(x) = \partial B(x)/\partial x$. The damping parameters $\alpha_\perp$ and $\alpha_\parallel$ further depend on temperature as

$$\alpha_\perp = \lambda \left(1 - \frac{T}{3T_C}\right) , \quad \alpha_\parallel = \lambda \left(\frac{2T}{3T_C}\right) \text{ for } T < T_C \, , \tag{B.14}$$

$$\alpha_\perp = \alpha_\parallel = \lambda \left(\frac{2T}{3T_C}\right) \text{ for } T > T_C \, . \tag{B.15}$$

We recall that the aim of this appendix is simply to illustrate the procedure to obtain the LLB equation. For a detailed derivations we refer to Ref. [53, 161]

Appendix C

Extended one-dimensional models

C.1 Lagrangian approach

The Collective Coordinate (CC) model equations, derived in the main text directly from the LLG equation, can be obtained also by adopting a Lagrangian approach. Doring [64] first pointed out that the LLG equation in spherical coordinates, can be derived by the following Lagrangian ($\mathcal{L}$) and Rayleigh dissipative function ($\mathcal{F}$):

$$\begin{aligned} \mathcal{L} &= \mathcal{E} + \frac{\mu_0 M_s}{\gamma_0}\dot{\phi}\cos\theta\,, && \text{(C.1)} \\ \mathcal{F} &= \frac{\alpha\mu_0 M_s}{2\gamma_0}(\dot{\mathbf{m}})^2 = \frac{\alpha\mu_0 M_s}{2\gamma_0}\left(\dot{\theta}^2 + \sin^2\theta\dot{\phi}^2\right)\,, && \text{(C.2)} \end{aligned}$$

where $\mathcal{E}$ is the system energy density. The LLG equation can be obtained from the Euler-Lagrange-Rayleigh equations:

$$\frac{\delta\mathcal{L}}{\delta X} - \frac{d}{dt}\left(\frac{\partial\mathcal{L}}{\partial\dot{X}}\right) + \frac{\partial\mathcal{F}}{\partial\dot{X}} = 0\,, \tag{C.3}$$

where $X = \{\theta, \phi\}$. By using the ansatz (3.75) and integrating along the x direction , it is possible to obtain the Lagrangian $L = \int\mathcal{L}dx$ and dissipative function $F = \int\mathcal{F}dx$ in terms of the DW coordinates $\{q, \varphi, \Delta\}$. Then, the CC model equations can be obtained with the Euler-Lagrange-Reyleight equation where $X = \{q, \varphi, \Delta\}$.

Also the STT contributions can be added following a Lagrangian approach. The Zhang-Li STT introduces the following terms to the Lagrangian and dissipative function:

$$\mathcal{E}_{STT} = -\frac{\mu_0 M_s}{\gamma_0}bJ\phi\sin\theta\frac{\partial\theta}{\partial x}\,, \quad \mathcal{F}_{STT} = -\xi bJ\left(\frac{\partial\theta}{\partial x}\dot{\theta} + \sin^2\theta\frac{\partial\phi}{\partial x}\dot{\phi}\right)\,. \tag{C.4}$$

Analogously, for the SH torque, we need to add the following term:

$$\mathcal{F}_{SH} = -\mu_0 M_s c J^{\mathrm{HM}}(-\cos\phi\dot{\theta} + \sin\theta\cos\theta\sin\phi\dot{\phi})\,. \tag{C.5}$$

These terms are calculated from the LLG equations augmented with the corresponding torques. Following the same procedure, it is possible to derive the CC model equations as given in the main text.

C.2 Useful Integrals

C.2.1 Identities

The DW profile (Bloch profile)

$$\begin{aligned} \theta(x,t) &= 2\arctan\left[\exp\left(\frac{x-q(t)}{\Delta}\right)\right] && \text{(C.6)} \\ \phi(x,t) &= \varphi(t)\,, && \text{(C.7)} \end{aligned}$$

implies that

$$\begin{aligned} \frac{\partial\theta}{\partial x} &= \frac{2}{1+e^{2\left(\frac{x-q(t)}{\Delta(t)}\right)}}\frac{e^{\left(\frac{x-q(t)}{\Delta(t)}\right)}}{\Delta} = \frac{2/\Delta}{e^{-\left(\frac{x-q(t)}{\Delta(t)}\right)}+e^{\left(\frac{x-q(t)}{\Delta(t)}\right)}} \\ &= \frac{2/\Delta}{\tan\frac{\theta}{2}+\frac{1}{\tan\frac{\theta}{2}}} = \frac{2/\Delta\tan\frac{\theta}{2}}{\tan^2\frac{\theta}{2}+1} \\ &= \frac{2\sin\theta/2}{\cos\theta/2}\frac{\cos^2\theta/2}{\Delta} = \frac{\sin\theta}{\Delta}\,, && \text{(C.8)} \end{aligned}$$

where we have used the fact that

$$\begin{aligned} \tan(\theta/2) &= \exp\left(\frac{x-q(t)}{\Delta(t)}\right)\,, \\ \frac{1}{\tan(\theta/2)} &= \exp\left[-\left(\frac{x-q(t)}{\Delta(t)}\right)\right]\,. \end{aligned}$$

Additionally, since

$$\frac{\partial\theta}{\partial x} = \frac{2/\Delta}{e^{-(x-q)/\Delta}+e^{(x-q)/\Delta}} = \frac{\sin\theta}{\Delta} \tag{C.9}$$

and

$$\frac{2/\Delta}{e^{-(x-q)/\Delta}+e^{(x-q)/\Delta}} = \frac{1/\Delta}{\cosh\left[\frac{x-q}{\Delta}\right]}\,, \tag{C.10}$$

we have that

$$\sin\theta = \frac{1}{\cosh\left[\frac{x-q}{\Delta}\right]}\,. \tag{C.11}$$

C.2.2 Integrals

In developing the CC model equations, we need to solve the following integrals:

$$\int_{-\infty}^{\infty}\sin^2\theta(x-q)^2dx \quad \text{and} \quad \int_{-\infty}^{\infty}\sin^2\theta(x-q)dx \tag{C.12}$$

By using the identities introduced in the previous part, these integral become

$$\begin{aligned} \int_{-\infty}^{\infty} \sin^2\theta (x-q)^2 dx &= \Delta^2 \int_{-\infty}^{\infty} \left[\frac{1}{\cosh^2\left[\frac{x-q}{\Delta}\right]}\left(\frac{x-q}{\Delta}\right)^2\right] dx \\ &= \Delta^3 \int_{-\infty}^{\infty} \left[\frac{t^2}{\cosh^2(t)}\right] dt = \Delta^3 \frac{\pi^2}{6}\,, \end{aligned} \tag{C.13}$$

$$\begin{aligned} \int_{-\infty}^{\infty} \sin^2\theta (x-q) dx &= \Delta \int_{-\infty}^{\infty} \left[\frac{1}{\cosh^2\left[\frac{x-q}{\Delta}\right]}\left(\frac{x-q}{\Delta}\right)\right] dx \\ &= \Delta^2 \int_{-\infty}^{\infty} \left[\frac{t}{\cosh^2(t)}\right] dt = 0\,, \end{aligned} \tag{C.14}$$

where $t = (x-q)/\Delta$. Other common integrals are

$$\int_{-\infty}^{\infty} \sin\theta dx = \int_0^{\pi} \Delta d\theta = \pi\Delta\,, \tag{C.15}$$

$$\int_{-\infty}^{\infty} \sin^2\theta dx = \int_0^{\pi} \Delta \sin\theta d\theta = 2\Delta\,, \tag{C.16}$$

$$\begin{aligned} \int_{-\infty}^{\infty} \cos\theta d\mathrm{x} &= \lim_{b\to\infty} H_{ax} \left(\int_{-b}^{q-\Delta/2} \underbrace{\cos\theta}_{1} dx + \int_{q-\Delta/2}^{q+\Delta/2} \cos\theta dx + \int_{q+\Delta/2}^{b} \underbrace{\cos\theta}_{-1} dx \right) \\ &= \lim_{b\to\infty} q - \frac{\cancel{\Delta}}{\cancel{2}} + \cancel{b} - \cancel{b} + q + \frac{\cancel{\Delta}}{\cancel{2}} = 2q\,. \end{aligned} \tag{C.17}$$

Appendix D

CODE example

This appendix shows some example of the micromagnetic code. Fig. D.1 represents the calculation of the exchange field. The function is a kernel as indicated by the suffix ”global”. The structure **d_field** represents a 3D array of element which are indexed with (i, j, k). The structure ”Geo” includes the sample dimension, while the structure ”Mat” includes the material parameters. The index *idx* is defined in the main text and it indicates a specific thread in the GPU. The scalar field ”mask” includes information on the sample shape.

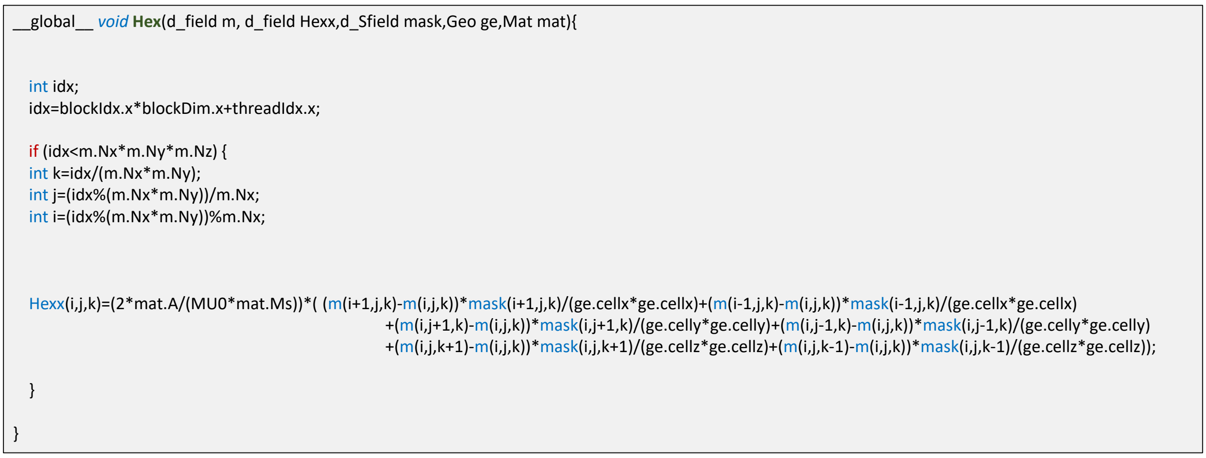

```
__global__ void Hex(d_field m, d_field Hexx,d_Sfield mask,Geo ge,Mat mat){


  int idx;
  idx=blockIdx.x*blockDim.x+threadIdx.x;

  if (idx<m.Nx*m.Ny*m.Nz) {
  int k=idx/(m.Nx*m.Ny);
  int j=(idx%(m.Nx*m.Ny))/m.Nx;
  int i=(idx%(m.Nx*m.Ny))%m.Nx;



  Hexx(i,j,k)=(2*mat.A/(MU0*mat.Ms))*( (m(i+1,j,k)-m(i,j,k))*mask(i+1,j,k)/(ge.cellx*ge.cellx)+(m(i-1,j,k)-m(i,j,k))*mask(i-1,j,k)/(ge.cellx*ge.cellx)
                                 +(m(i,j+1,k)-m(i,j,k))*mask(i,j+1,k)/(ge.celly*ge.celly)+(m(i,j-1,k)-m(i,j,k))*mask(i,j-1,k)/(ge.celly*ge.celly)
                                 +(m(i,j,k+1)-m(i,j,k))*mask(i,j,k+1)/(ge.cellz*ge.cellz)+(m(i,j,k-1)-m(i,j,k))*mask(i,j,k-1)/(ge.cellz*ge.cellz));

  }

}
```

Figure D.1: Extract from the micromagnetic code. Calculation of the exchange field.

Fig. D.2 represents the calculation of the demagnetizing field. Contrary to the exchange field, this is not a kernel but a normal function, which, in turns, calls several kernels. The first is related to the magnetization padding and initialization, as described in the main text. Then the magnetization is Fourier transformed and multiplied with the transformed demagnetizing factors. Finally, the demagnetizing field is transformed back and extracted.

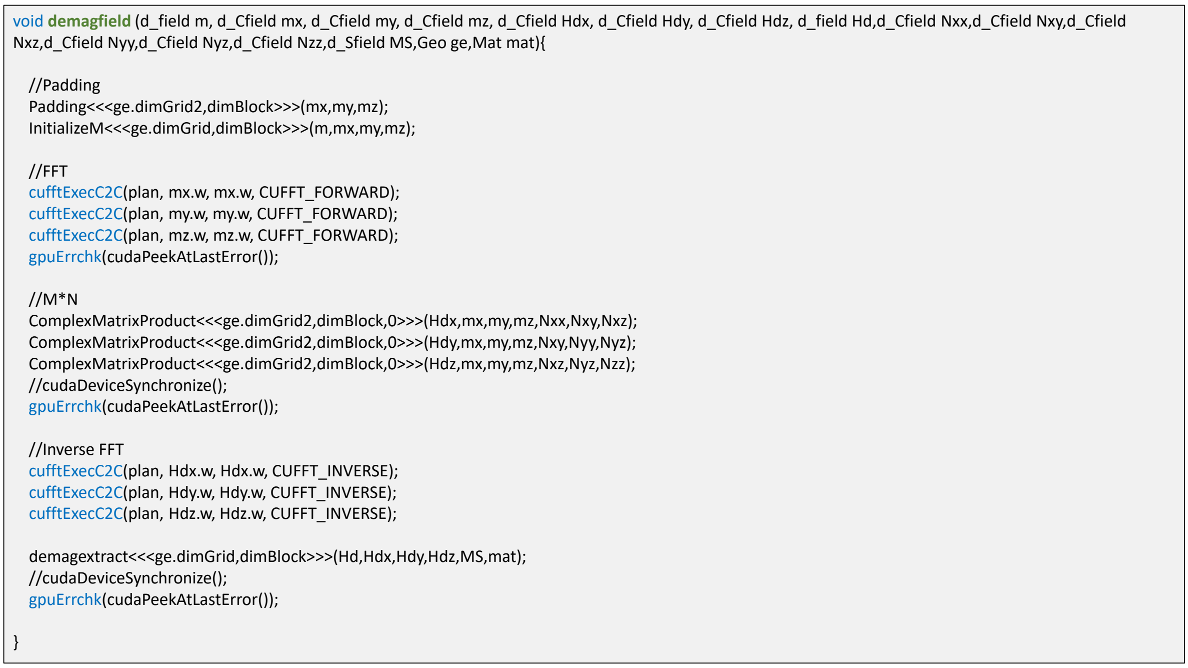

```
void demagfield (d_field m, d_Cfield mx, d_Cfield my, d_Cfield mz, d_Cfield Hdx, d_Cfield Hdy, d_Cfield Hdz, d_field Hd,d_Cfield Nxx,d_Cfield Nxy,d_Cfield
Nxz,d_Cfield Nyy,d_Cfield Nyz,d_Cfield Nzz,d_Sfield MS,Geo ge,Mat mat){

   //Padding
   Padding<<<ge.dimGrid2,dimBlock>>>(mx,my,mz);
   InitializeM<<<ge.dimGrid,dimBlock>>>(m,mx,my,mz);

   //FFT
   cufftExecC2C(plan, mx.w, mx.w, CUFFT_FORWARD);
   cufftExecC2C(plan, my.w, my.w, CUFFT_FORWARD);
   cufftExecC2C(plan, mz.w, mz.w, CUFFT_FORWARD);
   gpuErrchk(cudaPeekAtLastError());

   //M*N
   ComplexMatrixProduct<<<ge.dimGrid2,dimBlock,0>>>(Hdx,mx,my,mz,Nxx,Nxy,Nxz);
   ComplexMatrixProduct<<<ge.dimGrid2,dimBlock,0>>>(Hdy,mx,my,mz,Nxy,Nyy,Nyz);
   ComplexMatrixProduct<<<ge.dimGrid2,dimBlock,0>>>(Hdz,mx,my,mz,Nxz,Nyz,Nzz);
   //cudaDeviceSynchronize();
   gpuErrchk(cudaPeekAtLastError());

   //Inverse FFT
   cufftExecC2C(plan, Hdx.w, Hdx.w, CUFFT_INVERSE);
   cufftExecC2C(plan, Hdy.w, Hdy.w, CUFFT_INVERSE);
   cufftExecC2C(plan, Hdz.w, Hdz.w, CUFFT_INVERSE);

   demagextract<<<ge.dimGrid,dimBlock>>>(Hd,Hdx,Hdy,Hdz,MS,mat);
   //cudaDeviceSynchronize();
   gpuErrchk(cudaPeekAtLastError());

}
```

Figure D.2: Extract from the micromagnetic code. Calculation of the demagnetizing field.

Appendix E

Bubble vs linear domain wall

This section describes the differences between the field-driven dynamics of circular domain walls (DWs), as it occurs in bubble domains expansion, and linear DWs, as occurs in nanostrips. We show that the one-dimensional (1D) model, usually adopted for linear DWs, can also be used for circular DWs if the radius of the bubble is large enough. To describe the dynamics of circular domains it is convenient to adopt polar coordinates $\{r, \varphi\}$, as sketched in Fig. E.1. The magnetization can always be written as $\mathbf{m}(\mathbf{r}) = (\sin\theta\cos\phi, \sin\theta\sin\phi, \cos\theta)$ but θ and ϕ now depends on r and φ, rather than x and y. The bubble domain magnetization can be described by the following ansatz:

$$\theta(r) = 2\arctan\left[\exp\left(\frac{r - R_b}{\Delta}\right)\right], \tag{E.1}$$

$$\phi(\varphi) = \varphi + \beta, \tag{E.2}$$

where R_b is the DW position and Δ the DW width. Additionally, we are assuming the same DW angle β around the bubble. By adopting these coordinates the DW energy becomes

$$\begin{aligned} E &= t\int_0^{2\phi}\int_0^{R_t}\left\{A\left[\left(\frac{\partial\theta}{\partial r}\right)^2 + \frac{\sin^2\theta}{r^2}\right] - D\left[\frac{\partial\theta}{\partial r} + \frac{\cos\theta\sin\theta}{r}\right]\cos\beta\right. \\ &\quad \left. +(K_0 + K\sin^2\beta)\sin^2\theta\; - \mu_0 M_s H_z\cos\theta\right\} r dr d\varphi\,, \end{aligned} \tag{E.3}$$

where A is the exchange constant, D is the DMI constant, M_s is the saturation magnetization, K_0 is the effective anisotropy and K is the shape anisotropy as defined in Section 3.9.3. From Eq. (E.1) we have that $\partial\theta/\partial r = \sin\theta/\Delta$. Furthermore, since $\sin\theta \neq 0$ only for $r \approx R_b$, the variation of r can be neglected in the integral if $R_b \gg \Delta$ [38]. Within this approximation the DW energy per unit of length becomes

$$\frac{E}{t} = 2\pi R_b(\sigma_0 - \pi D\cos\beta + 2\Delta K\sin^2\beta) + \frac{4\pi A\Delta}{R_b} - 2\pi\mu_0 M_s H_z R_b^2\,, \tag{E.4}$$

where t is the sample thickness and $\sigma_0 = \sqrt{AK_0}$. The first term represents the DW energy. Contrary to linear DWs, this term is proportional to the bubble radius since an

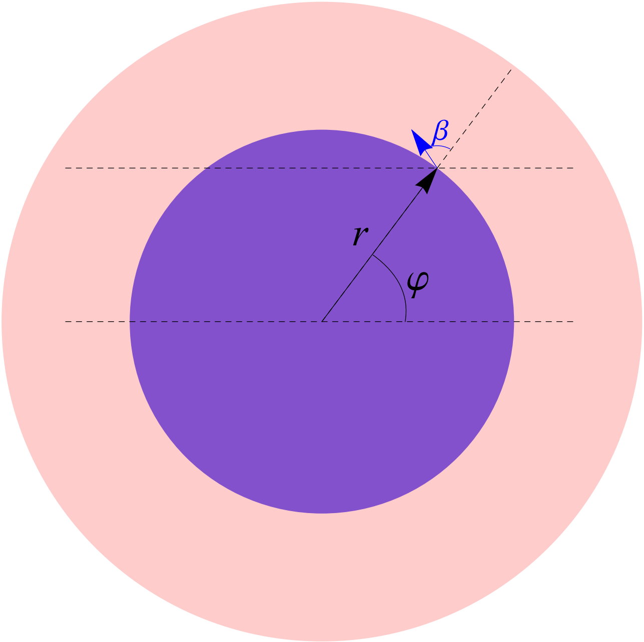

Figure E.1: Sketch of the polar coordinates used to describe circular DWs in bubble domains.

expansion of the bubble implies an increase of the DW length. However, the gain in the Zeeman energy is proportional to R_b^2 (see last term). The term proportional to $1/R_b$ represents the curvature energy cost of the bubble. Following the Lagrangian approach described in Appendix C.1, we have that the Lagrangian density and dissipative function density are given by

$$\frac{L}{t} = \frac{E}{t} + \frac{\mu_0 M_s}{\gamma_0} 2\pi\dot{\beta}(R_b^2 - R_t^2)\,, \tag{E.5}$$

$$\frac{F}{t} = \frac{2\pi\alpha\mu_0 M_s R_b}{\gamma_0}\left(\frac{\dot{R_b}^2}{\Delta} + \Delta\dot{\beta}^2\right)\,, \tag{E.6}$$

where R_t is total radius of the magnetic dot. By using the Euler-Lagrange-Rayleigh equations, it is possible to obtain the following equation for the dynamics of bubble radius $R_b(t)$ and the DW internal angle $\beta(t)$

$$\frac{\dot{R}_b}{\Delta} - \alpha\dot{\beta} = \gamma_0\left(H_K\frac{\sin 2\beta}{2} - \frac{\pi}{2}H_{\mathrm{DMI}}\sin\beta\right)\,, \tag{E.7}$$

$$\dot{\beta} + \alpha\frac{\dot{R}_b}{\Delta} = \gamma_0\left[H_z - \frac{1}{2\mu_0 M_s R_b}\left(\sigma_0 - \pi D\cos\beta + 2\Delta K\sin^2\beta - \frac{2A\Delta}{R_b^2}\right)\right]\,. \tag{E.8}$$

These equations are equivalent to the 1D model equations for the DW position q and internal angle ϕ obtained for a linear DW except for the terms proportional to $1/(2\mu_0 M_s R_b)$

in Eq. (E.8). These contributions are due to the DW surface tension and the curvature energy cost. Their effect vanishes as the bubble radius increases since the gain in the Zeeman energy increases as $\sim R_b^2$, while the DW energy cost scales as $\sim R_b$. The additional field

$$H_b(R_b) = \frac{1}{2\mu_0 M_s R_b}\left(\sigma_0 - \pi D\cos\beta + 2\Delta K_s \sin^2\beta - \frac{2A\Delta}{R_b^2}\right) \tag{E.9}$$

is plotted in Fig. E.2 for typical PMA sample parameters (see Chapter 11). Since typical experimental measurements involve bubbles with $r \geq 10\mu$m, the contribution of the additional H_b field is negligible since it is smaller that 1 mT. Explicitly, by imposing the condition $\mu_0 H_b < 1$ mT and neglecting the term proportional to $1/R_b^2$, which is relevant only for small radius, we have that $\mu_0 H_b$ is smaller that 1 mT for

$$\tilde{R}_b > \frac{\sigma_0 - \pi D\cos\beta + 2\Delta K_s \sin^2\beta}{2M_s} 10^3\,, \tag{E.10}$$

which, for the material parameters used in Chapter 11, yields $\tilde{R}_b \geq 7\ \mu$m. On the other hand, we would incur in an error if we try to simulate a bubble expansion measurement by simulating smaller bubbles, which have a larger effect of the H_b field.

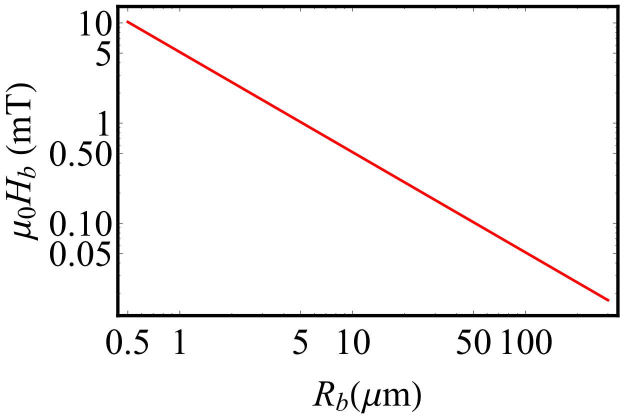

Figure E.2: H_b field as a function of the bubble radius R_B.

Appendix F

Maximum torque and equilibrium state

In this section we show in more detail how the maximum torque represents an indicator of the equilibrium state. Maximum torque is defined as

$$\frac{\tau_{\max}}{\gamma_0} = \mathrm{Max}\{-\frac{1}{1+\alpha^2}\mathbf{m}_i \times \mathbf{H}_{\mathrm{eff},i} - \frac{\alpha}{1+\alpha^2}\mathbf{m}_i \times (\mathbf{m}_i \times \mathbf{H}_{\mathrm{eff},i})\} = \frac{1}{\gamma_0}\mathrm{Max}\left(\frac{d\mathbf{m}_i}{dt}\right), \tag{F.1}$$

where the maximum is calculated over all cells labelled with $i = \{1, ..., N = N_x \cdot N_y\}$. MuMax3.9.3 [8] can provide this output automatically if selected. We perform the same simulations as indicated in Chapter 12, without any stopping condition, but simply running for $t = 20$ ns. Fig. F.1(a) shows the average m_z component for $\alpha = 0.2$ and $B_z = 10$ mT, while Fig. F.1(b) depicts the corresponding maximum torque. Once the system has reached equilibrium, the maximum torque has dropped to a minimum value. The same result is obtained for different damping but the final maximum torque is different. Numerically this value is never zero since it is limited by the numerical precision and by the system parameters, in particular by damping.

Fig. F.1(c) represents the maximum torque as function of applied field for different damping. The maximum torque is clearly independent on the applied field but depends on the damping value. Finally, Fig. F.1(d) shows the maximum torque as function of damping. The maximum torque decreases with damping and it saturates for $\alpha \geq 0.5$ since we have reached the minimum numerical precision of the code [8]. For higher damping the maximum torque oscillates around this minimum sensibility value, as shown in the inset of Fig. F.1(d). The value obtained with these preliminary simulations is used to set a threshold $\epsilon(\alpha)$ for the depinning field simulations in order to identify whether or not the system has reached an equilibrium. Furthermore, additional tests were performed, without setting any maximum torque condition, but simply running the simulations for a longer time ($t = 80, 160$ ns) and calculating the depinning field in order to ensure that the results obtained with these two methods were consistent, i.e., that we have actually reached an equilibrium state with the maximum torque condition.

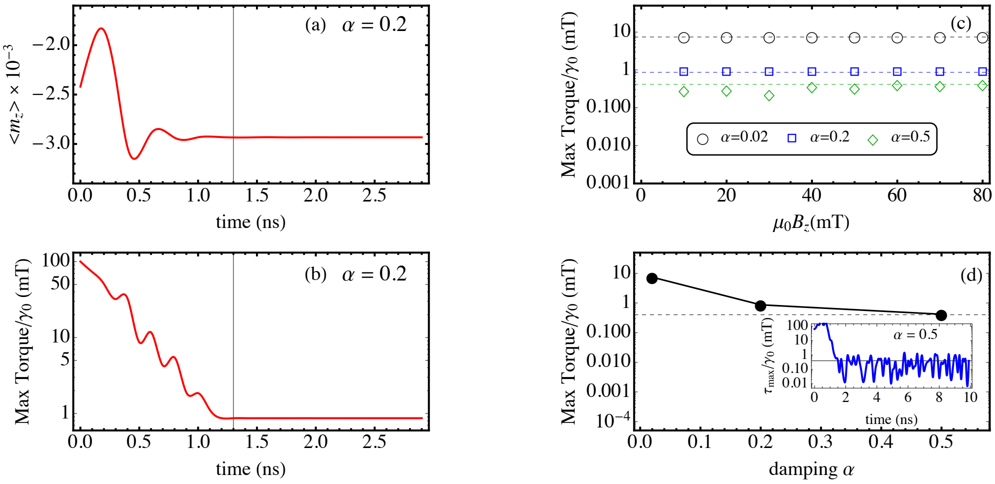

Figure F.1: (a) Average m_z as function of time. (b) Maximum torque/γ_0 ($\tau_{\max}$) as function of time. $\tau_{\max}$ rapidly decreases when the system is at equilibrium. (c) Maximum torque as function of applied field for different damping. (d) Maximum torque at equilibrium as function of damping. The inset shows the maximum torque as function of time for $\alpha = 0.5$.

NOTES